UNIVERSIDAD COMPLUTENSE DE MADRID

FACULTAD DE CIENCIAS FÍSICAS

TESIS DOCTORAL

Shape study of the N=Z waiting-point nucleus ^{72}Kr via beta decay

Estudio de la forma del núcleo N=Z y punto de espera ^{72}Kr a través de su desintegración beta

MEMORIA PARA OPTAR AL GRADO DE DOCTOR

PRESENTADA POR

José Antonio Briz Monago

Directores

María José García Borge
Enrique Nácher González

Madrid, 2014

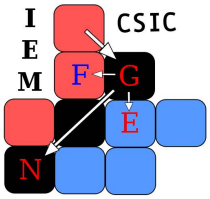

Grupo de Física
Nuclear Experimental

Shape study of the N=Z waiting-point nucleus ^{72}Kr via beta decay

Estudio de la forma del núcleo N=Z y punto de espera ^{72}Kr a través de su desintegración beta

José Antonio Briz Monago

Ph.D. thesis

Supervisors:

Prof. Maria José García Borge
Instituto de Estructura de la Materia (CSIC)

Dr. Enrique Nácher González
Instituto de Estructura de la Materia (CSIC) /
Instituto de Física Corpuscular (CSIC-Univ. Valencia)

September 25, 2013
Universidad Complutense de Madrid

Contents

Preface

It has been a long time since the human being has been interested in finding out the composition and nature of matter. The first hints come from the pre-Socratic Greek philosopher Democritus in the IV century B.C., who formulated the atomic theory that could be summarized saying that all materials could be subdivided into smaller and smaller pieces until one reaches the limit where no more divisions are possible, called the "atom".

This idea remained up to when the work of experimental scientists as J. Dalton, A. Avogadro, etc..., in the XIX century, introduced the scientific method to the investigation of the composition of matter. They formulated several phenomenological laws and models describing the properties of matter. Later, when the French physicist H. Becquerel discovered the radioactivity phenomenon in 1896 and the Polish physicist M. Curie worked to identify the radioactive substances from 1898, a new field of scientific research was born: **Nuclear Physics**. At the same time, the British physicist J.J. Thomson discovered that the so-called cathode rays were unique particles that he called "corpuscles" with a mass of perhaps one thousandth of the mass of hydrogen. The name of *electron* was later proposed by the Irish physicist G.F. Fitzgerald.

Later, in 1904, J.J. Thomson proposed the so-called *Plum pudding model* for the atomic structure which tells that the negatively-charged electrons were surrounded by a positively-charged soup in order to balance their electric charge and stay neutral.

The New Zealand-born physicist E. Rutherford studied the radiations discovered by Becquerel to classify them and study the composition of the atom. As part of these measurements, the famous experiment bombarding a thin Gold foil with alpha particles, ^{4}He, disproved the Plum pudding model. The experiment indicated the existence of a positively-charged atomic nucleus placed in a reduced space inside the atom leaving the electrons orbit around it. This model was concluded in accordance with the experimental angular distribution found for the scattered alpha particles in the collisions against the Gold atoms in the target and is commonly named as the *Rutherford model*. The experiment was carried out by H. Geiger y E. Marsden under the supervision of E. Rutherford in 1909 and published in 1911. The centenary of this publication was celebrated recently (August 2011) by means of the *"Rutherford Centennial Conference"* which took place in Manchester (United Kingdom) where the experiment was performed. This work meant the **discovery of the atomic nucleus**.

Several experimental studies were dedicated to the study of the atomic nucleus and its properties. As a result of this work, a massive particle in comparison with the electron but with positive electric charge (opposite to the one of electron) was discovered also by E. Rutherford in 1917 and published in 1919 when he found that the hydrogen nucleus was present in other

nuclei. Later, the English physicist J. Chadwick discovered a new particle present in the atomic nucleus, the neutron, which has no electric charge (neutral) and of similar mass than the proton.

Since then, the picture of the atomic nucleus stayed as a collection of neutrons and protons where the constituents interact with the close neighbours by the strong force and with the rest by means of the electromagnetic force.

From this moment on, a huge amount of both, theoretical and experimental studies have been devoted to improve our knowledge on the atomic nucleus in an interplay between both disciplines. On the one hand, when some new experimental results are found, theoreticians try to explain these results by means of a nuclear model. On the other hand, a theoretical model should have the ability to predict new properties which could be experimentally verified. Thus, with this active dialogue, the knowledge on the nuclear structure is progressing continuously.

Presently, the existence of around 3000 of the possibly more than 8000 different nuclei that should exist have been probed or identified. The properties of the majority of them have been studied but many others are still in progress and a lot of work is still to be done. Only around 300 nuclei are found in nature, the rest up to the 3000 known are the radioactive nuclei that suffer transformations consuming or emitting energy and probably they are the more interesting nuclei for being uncommon (exotic) and offering the possibility of finding new phenomena and physics.

At this stage, one could wonder why we are interested in the atomic nucleus, why it is so important and what is the interest to pursue its study. The answers to these questions probably lie in the fact that the nucleus, despite being 4-5 orders of magnitude smaller than the whole atom ($\approx 10^{-14}$ m vs. 10^{-10} m) contains the 99 % of the total mass of the atom and, consequently, of all the visible mass in the universe. The study of its properties is crucial in the human desire of understanding the universe. Additionally, the knowledge of the properties of the atomic nucleus is central in the understanding of extremely important processes with nuclear origin as the synthesis of all the elements present in the universe or the production of energy in the stars, including the Sun. However, one could become disappointed if only fundamental and non-practical reasons are given but the reality is more rich and much more interesting. Since the discovery of the subatomic world and its properties has also important applications as medical treatment such as radiation therapy, or medical imaging applications such as Positron Emission Tomography (PET), production of energy in nuclear power plants and many applications in industry.

The present work is located in the framework of fundamental knowledge, more concretely in the field of Nuclear Physics and more exactly Nuclear Structure. The main objectives of this field in the present time are "to understand and predict the properties of the atomic nucleus, to learn through its modelling about the underlying physics concepts and to extract the simple basic ingredients" as stated in the NuPECC Long Range Plan 2004. The Long Standing Questions to be addressed by the research in nuclear structure physics according with the latter publication are:

- What are the limits for existence of nuclei? Where are the proton and neutron drip lines situated? Where does Mendeleyev's table ends?
- How does the nuclear force depend on varying proton-to-neutron ratios?
- How to explain collective phenomena from individual motion?

- How are complex nuclei built from their basic constituents?

The study here presented aims at learning how the nuclear constituents organize in the bulk of the atomic nucleus, the properties of the nuclei located far from the stability line in the nuclear chart, and physics phenomena that arise when studying these so-called exotic nuclei. Furthermore, it also has implications in the astrophysical scenario as it will be presented. More precisely, this work consists of the study of the radioactive beta decay process of an N=Z nucleus, $^{72}_{36}Kr_{36}$, which is involved in stellar processes of production of heavier nuclei and emission of big amounts of energy. The aim is to find out both, macroscopic properties as its shape and microscopic properties as the internal structure including the ordering of its constituents inside. Of interest it is also to extract information on the radioactive decay process in which ^{72}Kr transforms into ^{72}Br including the improving the knowledge of the level scheme of the daughter nucleus. This study is performed by taking advantage of the high intensity beam provided by one of the most advanced international facilities for nuclear physics in the world, ISOLDE (CERN) in Switzerland. This work is the result of the big efforts of an international collaboration of nuclear physicists and local engineers participating in the preparation and data taking of the two measurements that will be presented.

1 Introduction

Contents

Along this chapter the scientific reasons that motivated this work will be presented in order to better understand the main questions that a scientist has to answer the fundamental questions **what?, why? how? what's for?** for the current study. The main basic knowledge on theory and physical quantities in which the present study is based will be introduced as well.

Let us start with an introduction of the main physical processes involved in the present study including a theoretical review describing the main properties of each of them before reviewing the motivation for the current work. The chapter will be finished with a review on the current knowledge on the nucleus of interest ^{72}Kr and its daughter nucleus in the beta decay process that we study, ^{72}Br.

1.1 Theoretical introduction

The information that one can obtain on the atomic nucleus is quite limited. One of the macroscopic properties that can be studied by different experimental techniques is the nuclear shape. Thus, one of the main motivations of this work will be to study the shape of the ^{72}Kr nucleus.

The way in which an experimentalist can study the level scheme of a certain nucleus is mainly through two types of physical processes. On the one hand one could perform in-beam gamma ray spectroscopy studies where the level scheme of the nucleus is examinated by performing nuclear reactions leading to the excited states in the nucleus of interest and then, studying the subsequent gamma rays emitted in the de-excitation process of the final nucleus. On the other hand, if the beta decay of the nucleus decaying into the one of interest occurs in Nature, one can fed via this beta decay the excited levels in the nucleus of interest. The fed levels in both cases can de-excite via the emission of gamma rays or conversion electrons, as we will see, if the fed level is bound for the emission of particles, or on the contrary it can emits a particle, which could be a proton, neutron, alpha, etc..., in order to reach a more stable nucleus.

Both techniques are widely used in the experimental nuclear physics field. The in-beam gamma-ray technique has the advantage that more excited levels in the nucleus of interest are fed as no restrictive selection rules are obeyed in the process and consequently, more transitions and levels could be studied. However, it has the disadvantage that less information can be directly extracted as the selection rules of beta decay could allow the scientist to assign spin and parity of the levels fed in the process.

Along this first section, the beta decay process will be reviewed as is the physical process used in the present work. The main properties of the process as well as its selection rules will be explained. Later, the properties of the de-excitation processes when the fed level in the daughter nucleus is fed will be briefly discussed, that is gamma de-excitation and internal conversion processes.

1.1.1 Beta decay

The atomic nucleus is composed by two types of particles called protons and neutrons that are referred generically as nucleons.

In the beta decay process one of the nucleons transforms into the other type of nucleon. At first sight, one could define two types of transformations, namely the transformation of a proton into a neutron and vice-versa. It turns out that the former can take place by two

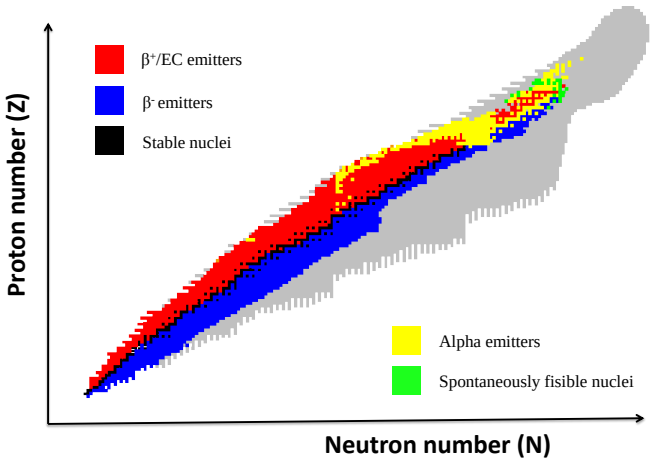

Figure 1.1: *Chart of nuclides, so-called Segré chart, where all the known nuclei are shown in a proton number (Z) versus neutron number (N) plot. In colour it is indicated the type of decay process that unstable nuclei suffer in order to try to get closer to the valley of stability. The stable nuclei are represented in black, while the grey colour indicates the nuclei theoretically predicted but not experimentally discovered yet.*

different processes, namely β^+ decay and electron capture (EC), while the latter is called β^- decay. If one considers a nucleus ${}^{A}_{Z}X_N$, the three processes can be expressed as:

$$\beta^- \text{ decay:} \quad {}^{A}_{Z}X_N \rightarrow {}^{A}_{Z+1}X'_{N-1} + e^- + \overline{\nu} \tag{1.1}$$

$$\beta^+ \text{ decay:} \quad {}^{A}_{Z}X_N \rightarrow {}^{A}_{Z-1}X''_{N+1} + e^+ + \nu \tag{1.2}$$

$$EC \text{ decay:} \quad {}^{A}_{Z}X_N + e^- \rightarrow {}^{A}_{Z-1}X''_{N+1} + \nu \tag{1.3}$$

As it can be observed in the previous expressions, the process is isobaric as it conserves the mass number A=Z+N. Another detail to be considered is the requirement that the EC decay process require the existence of atomic electrons as it consists of the capture of one of those, in a totally ionized atom the EC process cannot take place. It is important to note the fact that the processes β^+ and EC decay usually compete.

A Segré chart including the currently known nuclei is displayed in figure 1.1. There, all the known nuclei are displayed in a proton versus neutron number plot with their decay mode indicated in colour code. Most of the nuclei are unstable for beta decay processes, they correspond to the red and blue regions denoting the β^+/EC and β^- decay modes respectively. They decay to loose energy and in that way they get closer to the valley of stability, which is the region plotted as black dots in the figure and includes the stable nuclei that one can found in nature.

1.1.1.1 Energy balance

An important quantity is the energy released in the process and for this purpose the Q-value is defined. This quantity takes into account the available energy in the process so the released energy will be equal or smaller than the Q-value and the difference is due to the fact that the decay can occur to excited states in the daughter, i.e. the daughter nucleus keeps part

of the excitation energy that later release as de-excitation radiation which is in most of the cases of electromagnetic character.

For each process the Q-value is calculated in terms of the atomic masses as:

$$Q_{\beta^-} = M(^A_Z X_N)c^2 - M(^A_{Z+1}X'_{N-1})c^2 \tag{1.4}$$
$$Q_{\beta^+} = M(^A_Z X_N)c^2 - M(^A_{Z-1}X''_{N+1})c^2 - 2M_e c^2 \tag{1.5}$$
$$Q_{EC} = M(^A_Z X_N)c^2 - M(^A_{Z-1}X''_{N+1})c^2 - B_n \tag{1.6}$$

where M_e is the mass of the electron and B_n is the binding energy of the released electron. In terms of the tabulated mass excess defined as $\Delta M = M(^A_Z X_N)$-A, they reduce to:

$$Q_{\beta^-} = \Delta M(^A_Z X_N)c^2 - \Delta M(^A_{Z+1}X'_{N-1})c^2 \tag{1.7}$$
$$Q_{\beta^+} = \Delta M(^A_Z X_N)c^2 - \Delta M(^A_{Z-1}X''_{N+1})c^2 - 2M_{e^-}c^2 \tag{1.8}$$
$$Q_{EC} = \Delta M(^A_Z X_N)c^2 - \Delta M(^A_{Z-1}X''_{N+1})c^2 - B_n \tag{1.9}$$

A remarkable conclusion that one can extract from these expressions is that β^+ decay is not always energetically allowed. For the β^+ decay to be allowed, the mass difference between parent and daughter nucleus has to be bigger than twice the mass at rest of the electron (1022 keV/c^2). In the case of the EC decay this threshold in energy is much smaller as it is the binding energy of the electron and this quantity is in the order of some keV.

Another important fact is that these released energy (Q-E$_{exc}$)is shared by the outgoing particles. Thus, for β^- decay the energy is shared mainly by the electron and the antineutrino and in β^+ decay by positron and neutrino. A part of the energy can be taken by the nucleus which causes then daughter nucleus to remain in an excited level. In the case of the EC decay the energy is taken exclusively by the neutrino. Mathematically this can be expressed as:

$$Q_{\beta^-} = T_{e^-} + E_{\overline{\nu}} + E_{exc} \tag{1.10}$$
$$Q_{\beta^+} = T_{e^+} + E_{\nu} + E_{exc} \tag{1.11}$$
$$Q_{EC} = E_{\nu} + E_{exc} \tag{1.12}$$

This has the consequence that the electron spectrum is a continuous distribution ranging from zero up to the maximum available energy $E_{max} = Q_\beta - E_{exc}$ whose shape is shown, as an example with E$_{max}$=1.0 MeV, in figure 1.2.

1.1.1.2 Angular momentum and selection rules

The beta decay process must conserve the angular momentum and parity in the transformation from the initial to the final state. These conservation laws can be written as:

$$I_i = I_f + l_e + l_\nu + s_e + s_\nu \tag{1.13}$$
$$\pi_i = \pi_f \cdot (-1)^{l_e + l_\nu + s_e + s_\nu} \tag{1.14}$$

where I_i and I_f are the angular momenta of the initial and final nuclei, l_e and s_e are the angular momentum and spin of the electron/positron and l_ν and s_ν are the corresponding

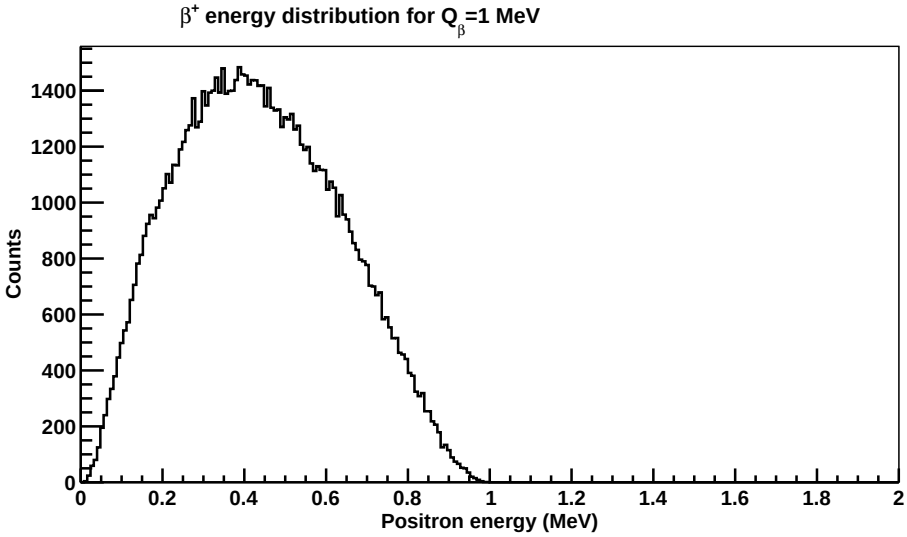

Figure 1.2: *Energy distribution of a β particle corresponding to a decay where the $E_{max} = Q_\beta - E_{exc}$=1.0 MeV. The maximum energy carried by the positron corresponds to the total energy available, 1 MeV, while the maximum of the distribution is placed at approximately one third of the maximum energy.*

for the antineutrino/neutrino. If one groups the momenta and spin of outgoing particles as $l_\beta = l_e + l_\nu$ and $s_\beta = s_e + s_\nu$ the resulting expression is:

$$I_i = I_f + l_\beta + s_\beta \tag{1.15}$$

$$\pi_i = \pi_f \cdot (-1)^{l_\beta + s_\beta} \tag{1.16}$$

The spin of electron (positron) and antineutrino (neutrino) is $1/2$ so they can couple with parallel or anti-parallel spins. In the former case $s_\beta = 1$ and the decay is called **Gamow-Teller decay** and in the latter $s_\beta = 0$ and it is known as **Fermi decay**.

The most extended approximation in the study of the beta decay process is to consider that the orbital angular momentum carried away by the outgoing particles is zero, namely $l_\beta = 0$. This is known as the **allowed approximation** and the transitions following this condition are called **allowed transitions**. These are the most likely transitions and experimentally easily measured because of their intensity.

There is a collection of conditions derived from the expressions 1.15 and 1.16 that summarize the possible values for angular momentum and parity of the initial and final states in order to satisfy the conservation laws. More exactly, they define the possible change in these quantities in the decay and they are known as **selection rules**. Table 1.1 summarizes the selection rules that have to be satisfied in the allowed transitions for Fermi and Gamow-Teller decays.

When the outgoing particles take some orbital angular momentum ($l_\beta \neq 0$), there are the so-called **forbidden transitions**, less probables than the allowed ones. It is important to note that this label of forbidden has nothing to do with the fact of being forbidden as they are not strictly forbidden but highly suppressed and they are called in that way for historical reasons. They are classified as first forbidden, second forbidden, and so on depending of the amount of angular momentum carried by the beta particle and neutrino (antineutrino). Thus, they are called first forbidden when $l_\beta = 1$, second forbidden when $l_\beta = 2$, etc... In the same way as allowed transitions, one can find forbidden transitions of Fermi or Gamow-Teller types.

	Fermi transition	Gamow-Teller transition
ΔI	0	0, $\pm$ 1 (except 0 $\rightarrow$ 0)
$\Delta\pi$	0	0
ΔT	0	0, $\pm$ 1 (except 0 $\rightarrow$ 0)
ΔT_Z	$\pm$ 1	$\pm$ 1

Table 1.1: *Selection rules for the angular momentum I, parity π, isospin T and third component of isospin T_z in allowed transitions of the β decay process.*

In table 1.1 there is also the selection rule for a quantity that has not been defined yet, which is called isospin. The isospin is a quantum number based on the fact that the strong interaction does not distinguish between neutron and proton. So in the absence of Coulomb and weak interactions the isospin should be conserved. The Isospin T was defined as a "spin" vector including neutrons and protons as two different states of the same particle, the nucleon. Thus, if one defines an arbitrary z axis, the neutrons would be the nucleons with isospin projection $T_z = +1/2$ along this z-axis and the protons would have isospin projection $T_z = -1/2$[1].

For a nucleus with N neutrons and Z protons, the isospin of the nucleus has to be obtained from the coupling of the isospin of the individual nucleons. Thus, the third component of the total isospin vector T_z is the sum of them, given by:

$$T_z = \frac{1}{2}(N - Z) \tag{1.17}$$

expressed in units of $\hbar$ which usually is omitted. The minimum value of T corresponds to the ground state and it is $|T_z|$ from 1.17. Consequently, the excited states should have $T \leqslant |T_z|$. value

For the case of $^{72}_{36}Kr_{36}$ decay the third component of the isospin vector is:

$$T_{gs}(^{72}Kr) = |T_z| = \frac{1}{2}(N - Z) = \frac{1}{2}(36 - 36) = 0 \tag{1.18}$$

and for the daughter nucleus $^{72}_{35}Br_{37}$ is:

$$T_{gs}(^{72}Br) = |T_z| = |\frac{1}{2}(N - Z)| = |\frac{1}{2}(37 - 35)| = 1 \tag{1.19}$$

If one checks the table 1.1, can conclude that for the decay of our interest the allowed Fermi transitions cannot occur as the selection rules require that there is no change in the value of the quantum number T and as seen in previous equations, there has to be a change in T while decaying from ^{72}Kr to ^{72}Br.

Another conclusion for this decay is that as the ground state spin and parity of ^{72}Kr is 0^+, all the allowed transitions will be Gamow-Teller $0^+ \rightarrow 1^+$. This fact allows us to directly assign the spin and parity of some very intensively fed levels in ^{72}Br to be 1^+.

[1] In some references one can find the opposite convention claiming that T_z(neutron)=-1/2 and T_z(proton)=-1/2 but with this convention the assumption that will be explained later that the operator τ^+ accounts for β^+ decays would not be fulfilled.

1.1.1.3 Beta decay transition probability

A very important quantity not mentioned yet is the transition probability λ which was studied by Fermi giving as a result the well-known **Fermi's golden rule** that mathematically can be expressed as:

$$\lambda = \frac{2\pi}{\hbar} \times |\langle \psi_f \varphi_e \varphi_\nu | V | \psi_i \rangle|^2 \times \rho(E_f) \tag{1.20}$$

where the wave functions ψ_i and ψ_f correspond to the nucleus in its initial and final states respectively, φ_e is the wave function of the electron (positron) and φ_ν is the corresponding to the antineutrino (neutrino).

The quantity $\rho(E_f)$ is the density of final states in the daughter nucleus and can be defined mathematically as:

$$\rho(E_f) = \frac{dn}{dE_f} \tag{1.21}$$

Let us develop a bit more on this concept and define **p** and **q** as the linear momentum of electron (positron) and antineutrino (neutrino) respectively for a β^- (β^+) decay. As the interest lies on the density of final states, one can consider a cartesian coordinates system where the magnitude of these linear momentum vectors is:

$$|\mathbf{p}| = (p_x^2 + p_y^2 + p_z^2)^{1/2}$$
$$|\mathbf{q}| = (q_x^2 + q_y^2 + q_z^2)^{1/2}$$

The number of states with a momentum between p and $p + dp$ where the electron is confined inside a volume V can be calculated as:

$$dn_e = \frac{4\pi p^2 dp V}{h^3} \tag{1.22}$$

where h^3 was introduced in order to keep dn_e as a dimensionless quantity. Equally for the neutrino (antineutrino) one ends up with:

$$dn_\nu = \frac{4\pi q^2 dq V}{h^3} \tag{1.23}$$

Resulting for the total number of final states:

$$d^2 n = dn_e \cdot dn_\nu = \frac{(4\pi)^2 p^2 dp q^2 dq V^2}{h^6} \tag{1.24}$$

For simplicity in the calculation, let us consider that the systems: electron (positron) and anti-neutrino (neutrino) can be describe as a free particle. In this case, their wave function takes the form:

$$\varphi_e = \frac{1}{\sqrt{V}} e^{ipr/\hbar}$$
$$\varphi_\nu = \frac{1}{\sqrt{V}} e^{iqr/\hbar}$$

The typical energy of an electron in the beta decay process is around 1 MeV and for this case: $p = 1.4\ MeV/c$ and $p/\hbar = 0.007\ fm^{-1}$. For the allowed approximation it was stated before that the electron and antineutrino do not carry any angular momentum. That means

that they are emitted in s-wave and, consequently, in a quite limited region (r $\ll$ 1). This makes $p \cdot r/\hbar \ll 1$ and supports the allowed approximation consisting of:

$$e^{ipr/\hbar} = 1 + \frac{ipr}{\hbar} + ... \cong 1$$
$$e^{iqr/\hbar} = 1 + \frac{iqr}{\hbar} + ... \cong 1$$

Making this approximation one ends up with the following result for the differential transition probability $d\lambda$:

$$d\lambda = \frac{2\pi}{\hbar} g^2 |M_{fi}|^2 (4\pi)^2 \frac{p \cdot dp \cdot q^2}{h^6} \frac{dq}{dE_f} \tag{1.25}$$

where we define the nuclear matrix element $M_{fi} = \int \psi_f^* \cdot O_x \cdot \psi_i$. The next step would be to integrate over all the possible states. For the neutrino momentum, q, the minimum value is 0 and the maximum has to be $q_{max} = (Q_\beta - T_e)/c$ according to the expressions 1.10 and 1.11 assuming $E_{exc} = 0$. The result of integrating the last expression for all possible states of the neutrino momentum is:

$$\lambda = \frac{g^2 |M_{fi}|^2}{2\pi^3 \hbar^7 c^3} \int_0^{p_{max}} F(Z', p) \cdot p^2 (Q - T_e)^2 dp \tag{1.26}$$

where Z' is the atomic number of the daughter nucleus of the decay. At this stage, one defines the quantity called Fermi integral f that takes care of the kinematics of the process:

$$f(Z', E_0) = \frac{1}{(m_e c)^3 (m_e c^2)^2} \int_0^{p_{max}} F(Z', p) \cdot p^2 \cdot (E_0 - E_e)^2 dp \tag{1.27}$$

where some quantities have been added to make f a dimensionless quantity. Introducing the Fermi integral, the transition probability turns into:

$$\lambda = \frac{g^2 |M_{fi}|^2}{2\pi^3 \hbar^7 c^3} (m_e c)^3 (m_e c^2)^2 \cdot f(Z', E_0) \tag{1.28}$$

As $\lambda = ln(2)/t_{1/2}$ one obtains the expression for the quantity known as **ft-value**:

$$ft_{1/2} = ln(2) \frac{2\pi^3 \hbar^7}{g^2 m_e^5 c^4 |M_{fi}|^2} \tag{1.29}$$

This parameter, also called ***comparative half-life*** and gives useful information on the probability of the beta decay to a certain level. It allows us to compare the beta decay probability in different nuclei as the differences found on its value should come from differences in the nuclear matrix elements. This quantity provides information on the degree of forbiddance of the decay transitions. Thus, fig. 1.3 shows the systematics experimentally found for β decay transitions for allowed 1.3(a) and forbidden 1.3(b) transitions as given in [Sin98]. One important fact is that no forbidden transitions has been found with a log(ft) value lower than 5. For this reason, this quantity is frequently used and the beta decay studies are usual to provide it for all the fed states.

The nuclear matrix element M_{fi} for a generic transition of mixed Fermi (F) and Gamow-Teller (GT) between state i in the parent and f in the daughter can be expressed as:

$$|M_{fi}|^2 = g_v^2 \cdot |M(F)|^2 + g_a^2 \cdot |M(GT)|^2 = g_v^2 \cdot B(F) + g_a^2 \cdot B(GT) \tag{1.30}$$

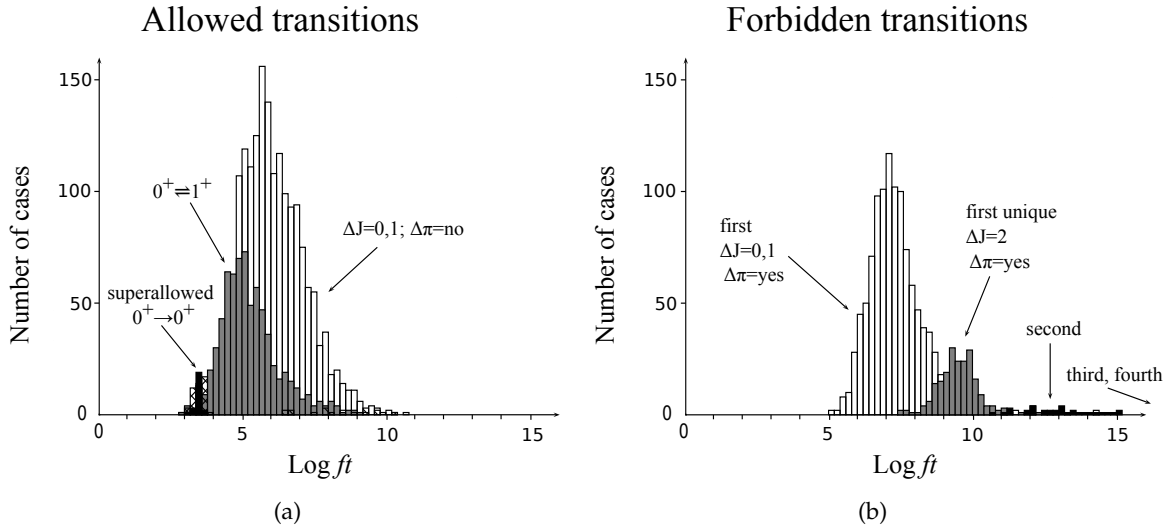

Figure 1.3: *Systematics for log(ft) values of β decay (a) allowed and (top) forbidden transitions experimentally found, as appears in [Sin98]. Forbidden transitions are located for log(ft)≥5.*

where the quantities $B(F)$ and $B(GT)$ Fermi are the Fermi and Gamow-Teller reduced transition probabilities defined as the squared of the corresponding matrix elements. Introducing this definition into expression 1.29 and grouping all the constants under $K = ln(2)\frac{2\pi^3\hbar^7}{m_e^5c^4}$ the result is:

$$ft_{1/2} = \frac{K}{g_v^2 B(F) + g_a^2 B(GT)} \tag{1.31}$$

or dividing by g_v^2:

$$ft_{1/2} = \frac{K/g_v^2}{B(F) + (g_a/g_v)^2 B(GT)} \tag{1.32}$$

where the constants take the values:

$$K' = \frac{K}{g_v^2} = 6143.6(17) \text{ [Har09]} \tag{1.33}$$

$$\frac{g_a}{g_v} = -1.2695(29) \text{ [Yao06]} \tag{1.34}$$

It is important to note that $t_{1/2}$ is the partial half-life of a certain level labelled f and it is not the same as the half-life of the nucleus, which is usually named as $T_{1/2}$. The relationship between them is:

$$t_{1/2} = \frac{T_{1/2}}{I_\beta} \tag{1.35}$$

where I_β is the β-feeding to the level f and the $T_{1/2}$ is the half-life of the decaying nucleus.

Let us review the already presented reduced transition probabilities $B(F)$ and $B(GT)$. They were defined as the square of the corresponding nuclear matrix elements:

$$B(F) = \frac{g_v^2}{4\pi}|\langle\psi_f|\tau_\pm|\psi_i\rangle|^2 \tag{1.36}$$

$$B(GT) = \frac{g_a^2}{4\pi}|\langle\psi_f|\sigma\tau_\pm|\psi_i\rangle|^2 \tag{1.37}$$

where the operators involved in each type of decay are included and the transition probabilities B(F) and B(GT) are expressed in units of $\frac{g_v^2}{4\pi}$ and $\frac{g_a^2}{4\pi}$ respectively following the convention given in ref. [BM98]. This convention assures than the B(GT) of the neutron decay into proton is 3, in $\frac{g_a^2}{4\pi}$ units. Let us comment on some important aspects of every operator.

- **Isospin operator** $\tau_{\pm}$: it changes the third component of the isospin T_z of the initial state ψ_i by increasing (τ_+ present in the β^+/EC decay) or decreasing (τ_- acting in the β^- decay) in one unit but not modifying the isospin vector T. Mathematically: $\Delta T_z = \pm 1$.

- **Spin operator** σ: acting on an initial state ψ_i it changes the amount of total angular momentum I in one unit, mathematically: $\Delta I = \pm 1$.

As a conclusion, the Fermi decay can only modify the third component of isospin T_z as in this decay only isospin operator takes part and the Gamow-Teller decay can modify both the third component of isospin T_z as well as the spin of the nucleus I.

In the case of the β^+/EC decay of ^{72}Kr, as the Fermi transitions cannot occur in allowed approximation, the ft-value from equation 1.32 becomes:

$$ft_{1/2} = \frac{K'}{\frac{g_a^2}{g_v^2} B(GT)} \tag{1.38}$$

and, consequently, for the reduced transition probability one obtains:

$$B(GT) = K' \left(\frac{g_v}{g_a}\right)^2 \frac{I_\beta(E)}{fT_{1/2}} = K' \left(\frac{g_v}{g_a}\right)^2 \frac{1}{ft_{\frac{1}{2}}} \tag{1.39}$$

The purpose of the TAS measurement will be to measure the $I_\beta(E)$ within the Q_β-window. Considering that the value of f is tabulated and the half-life of ^{72}Kr decay is known as well as the constants K', and the ratio g_v/g_a one can obtain the $B(GT)$ value as a function of the excitation energy in the daughter nucleus, ^{72}Br.

1.1.2 De-excitation processes

Once the parent nucleus β decays excited levels in the daughter nucleus are fed as shown in fig. 1.4. These excited states usually de-excites quickly to reach the state of minimum energy, the ground state. The most frequent process to de-excite is the gamma emission, that is the emission or electromagnetic radiation (or photons) in the energy range 100 keV up to approximately 10 MeV. However, there exists another less frequent process but quite relevant in the mass region of our interest, the internal conversion or emission of conversion electrons. It consists of the emission of an atomic electron of the more internal shells as a result of the interaction with the electromagnetic field of the nucleus in the excited state.

Let us review briefly the main characteristics of both processes as are of primordial relevance in the present work.

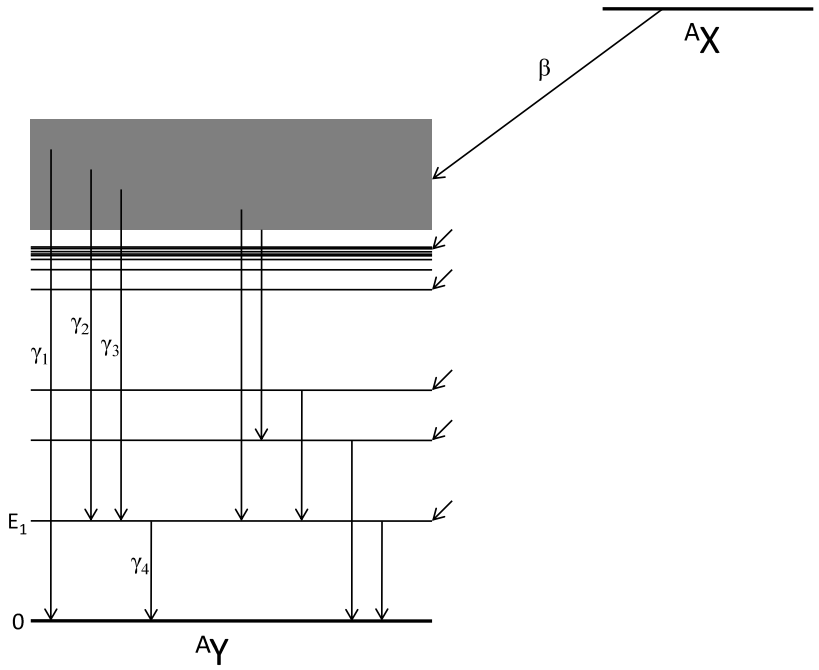

Figure 1.4: *Example of the level scheme corresponding to a β decay of nucleus ^{A}X leading to the nucleus ^{A}Y.*

1.1.2.1 Gamma de-excitation

As already commented, the gamma de-excitation is the most general process for a bound excited state in the daughter nucleus to reach the state of minimum energy, the ground state. Basically, it consists of the emission of gamma radiation (photons) to decrease the excitation energy of the nucleus. The path to reach the ground state could be a single step process if only one gamma ray is emitted or a multi-step process in which case several consecutive gamma rays are emitted, producing the so-called *gamma de-excitation cascade*.

If one considers the nucleus to have a rest mass M and that the gamma de-excitation process occurs between an initial state of energy E_i and the final state with energy E_f the energy and linear momentum conservation laws lead us to expressions 1.40 y 1.41.

$$E_i = E_f + E_\gamma + T_R \tag{1.40}$$

$$0 = \mathbf{p_R} + \mathbf{p}_\gamma \tag{1.41}$$

where T_R y p_R are the kinetic energy and the linear momemtum of the recoil nucleus, in our case of interest ^{72}Br. It follows that $p_R = p_\gamma$. In addition, if one defines $\Delta E = E_i - E_f$ and we use the expression $E_\gamma = cp_\gamma$ the resulting equation is 1.42.

$$\Delta E = E_\gamma + \frac{E_\gamma^2}{2Mc^2} \tag{1.42}$$

From where we can obtain an expression for the energy of the emitted gamma radiation by clearing up from the last expression:

$$E_\gamma = Mc^2\left[-1 \pm \left(1 + 2\frac{\Delta E}{Mc^2}\right)^{1/2}\right] \tag{1.43}$$

The typical values for the energy differences between levels, ΔE, are of the order of MeV and the atomic masses, Mc^2, are of the order of $A \cdot 10^3$ MeV. For nuclei with low mass numbers, A, the corrections over the energy difference between levels, ΔE, are important. For example, for ^{14}C, the gamma transition between the first excited and the ground states the result is:

$$\Delta E = 6093.8 \text{ keV} \quad (1.44)$$
$$E_\gamma = 6092.377 \text{ keV} \quad (1.45)$$

Therefore, the energy difference between then is not negligible:

$$\Delta E - E_\gamma = 1.423 \text{ keV} \quad (1.46)$$

In our case of interest, ^{72}Br, as an example for the most intense transition, E_γ=309.9 keV, we obtain:

$$\Delta E = 309.92 \text{ keV} \quad (1.47)$$
$$E_\gamma = 309.91845 \text{ keV} \quad (1.48)$$

Being the difference:

$$\Delta E - E_\gamma = 0.00155 \text{ keV} \quad (1.49)$$

As we can see, the difference is much lower and far smaller than the energy resolution of the experimental detectors that we will use, usually it is of the order of 1 keV as we will see.

Due to this, in the present work, as a good approximation, we will assume:

$$\Delta E \cong E_\gamma \quad (1.50)$$

that is that the energy of the gamma ray emitted is the same than the energy difference between initial and final states in the de-excitation process.

The gamma radiation is, as we already know, electromagnetic radiation emitted by the nucleus which can be considered as a electric charge distribution not totally symmetric and an electric current due to the movement of the electrically charged constituents of the nucleus, and that, depending on the nucleus it should be described through the multipolar radiation field including the dipolar, quadrupolar, octupolar, etc..., terms.

Without entering into details, the main characteristics of these radiation useful for our interest can be summarizes as follows:

1. The parity of the emitted radiation is given by:

$$\pi(ML) = (-1)^{L+1} \quad (1.51)$$
$$\pi(EL) = (-1)^{L} \quad (1.52)$$

where M or E inform of the magnetic or electric character of the radiation and L gives the multipolar order. This expression means that electric and magnetic multipoles of the same order have opposite parity.

2. The radiated power, where σ = E or M in order to use a generalized expression:

$$P(\sigma L) = \frac{2(L+1)c}{\epsilon_0 L[(2L+1)!!]^2}\left(\frac{\omega}{c}\right)^{2L+2}[m(\sigma L)]^2 \tag{1.53}$$

where $m(\sigma L)$ is the amplitude of the multipolar moment of L order, being dipolar for L=1, quadrupolar for L=2, octupolar for L=3, etc... The double factorial is $(2L+1)!! = (2L+1)(2L-1)\cdots 3\cdot 1$.

In order to carry these expressions into a quantum treatment we should quantize the radiation sources, that is, the multipolar moments. Basically, the only relevant modification would be to express the multipolar moment as the matrix element $m_{fi}(\sigma L)$ between the initial state ψ_i and the final one ψ_f of the multipole operator $m(\sigma L)$, that is:

$$m_{fi}(\sigma L) = \int \psi_f^* m(\sigma L)\psi_i dv \tag{1.54}$$

Thus, we would end up with:

$$P(\sigma L) = \frac{2(L+1)c}{\epsilon_0 L[(2L+1)!!]^2}\left(\frac{\omega}{c}\right)^{2L+2}[m_{fi}(\sigma L)]^2 \tag{1.55}$$

A physical quantity of interest is the probability per time unit λ in the form of photons with energy given by $E = \hbar\omega$ which takes the value:

$$\lambda(\sigma L) = \frac{P(\sigma L)}{\hbar\omega} = \frac{2(L+1)}{\epsilon_0 \hbar L[(2L+1)!!]^2}\left(\frac{\omega}{c}\right)^{2L+1}[m_{fi}(\sigma L)]^2 \tag{1.56}$$

In order to evaluate the matrix element m_{fi} we make the assumption that the **independent particle model** is valid, which means that we will assume that the process consists of the change of a proton from a shell to other in the framework of the spherical shell model without altering the rest of the nuclear system.

For electric transitions, we consider that the wave functions extend up with a constant value up to a matter radius R and they are zero for distances beyond R, $r > R$, being the nuclear radius $R = R_0 A^{\frac{1}{3}}$. All together, the resulting expression is:

$$\lambda(EL) \cong \frac{8\pi(L+1)}{L[(2L+1)!!]^2}\frac{e^2}{4\pi\epsilon_0\hbar c}\left(\frac{E}{\hbar c}\right)^{(2L+1)}\left(\frac{3}{L+3}\right)^2 c(R_0 A^{\frac{1}{3}})^{2L} \tag{1.57}$$

and if we include the value of the constants the result is:

$$\lambda(E1) = 1.0\times 10^{14} A^{\frac{2}{3}} E^3 \tag{1.58}$$

$$\lambda(E2) = 7.3\times 10^{7} A^{\frac{4}{3}} E^5 \tag{1.59}$$

$$\lambda(E3) = 34\times A^2 E^7 \tag{1.60}$$

$$\lambda(E4) = 1.1\times 10^{-5} A^{\frac{8}{3}} E^9 \tag{1.61}$$

For magnetic transitions, following the same assumptions we obtain:

$$\lambda(ML) \cong \frac{8\pi(L+1)}{L[(2L+1)!!]^2}\left(\mu_p - \frac{1}{L+1}\right)^2\left(\frac{\hbar}{m_p c}\right)^2\left(\frac{e^2}{4\pi\epsilon_0\hbar c}\right) \times \tag{1.62}$$

$$\times\left(\frac{E}{\hbar c}\right)^{2L+1}\left(\frac{3}{L+2}\right)^2 c(R_0 A^{\frac{1}{3}})^{2L-2} \tag{1.63}$$

Usually, the factor $(\mu_p - \frac{1}{L+1})^2$ is replace by 10, giving as a result the following values:

$$\lambda(M1) = 5.6 \times 10^{13} E^3 \tag{1.64}$$

$$\lambda(M2) = 3.5 \times 10^{7} A^{\frac{2}{3}} E^5 \tag{1.65}$$

$$\lambda(M3) = 16 \times A^{\frac{4}{3}} E^7 \tag{1.66}$$

$$\lambda(M4) = 4.5 \times 10^{-6} A^2 E^9 \tag{1.67}$$

The main conclussions that we can extract are:

1. Lower multipole orders dominate since when the multipolar order increases the transition probability decreases.
2. For a given multipole order, electric transition is 2 orders of magnitude more likely than the magnetic one.

Angular momentum and selection rules of gamma de-excitation

The angular momentum conservation law requires:

$$\mathbf{I}_i = \mathbf{L} + \mathbf{I}_f \tag{1.68}$$

where **L** is the angular momentum vector of the emitted gamma radiation. The module of this vector is restricted to be lower or equals than $I_i + I_f$ and larger or equals than $|I_i - I_f|$. The electric or magnetic character of the radiation is given from the relative parity between initial and final states. As we saw in expressions 1.51 and 1.52, electric and magnetic transitions of the same order have opposite parity. Therefore, examining if there is change of parity or not between initial and final states, and knowing the order of the transition, we can determine the character of the radiation emitted.

A summary of the selection rules for gamma emission could be:

$$|I_i - I_f| \leq L \leq I_i + I_f \text{ no L=0} \tag{1.69}$$

$$\Delta\pi = no \quad \text{even electric or odd magnetic order} \tag{1.70}$$

$$\Delta\pi = yes \quad \text{odd electric or even magnetic order} \tag{1.71}$$

Using the Weisskopf estimation, [Wei51], the following considerations could be extracted:
1. Usually the lower multipole order dominates, for example: λ(M1)/λ(E2)$\simeq 10^6 \mathrm{A}^{-4/3}\mathrm{E}^{-2}$
2. The selection rules forbid the competition of transitions of the same order of different character (electric and magnetic). Anyway, for the same multipole order, the electric transition is more likely than the corresponding magnetic one. As an example: λ(E1)/λ(M1) $\simeq 2{\cdot}\mathrm{A}^{2/3}$.
3. The emission of a multipole $L+1$ is 5 orders of magnitude less probable than the multipole of order L.

4. Since the competing multipoles in one transition are the electric of order L and the magnetic of order $L+1$ and viceversa, we should remember that:

$$\frac{\lambda(EL')}{\lambda(ML)} \approx 10^{-3} \tag{1.72}$$

$$\frac{\lambda(ML')}{\lambda(EL)} \approx 10^{-7} \tag{1.73}$$

which means that, for example, when competition between E1 and M2 transitions, the E1 is 10^7 times more likely than the M2 and if the competition would be between E2 and M1, the E2 is 10^3 times more probable than the M1, if one looks at the expressions 1.59 y 1.64.

1.1.2.2 Internal conversion or conversion electron emission

The internal conversion, or so-called conversion electron emission, is an electromagnetic process which competes with gamma de-excitation. The electromagnetic field of the nucleus interacts with the atomic electrons provoking that one of them (usually from the inner shells), is emitted from the atom. It is good to remark that is not a two step process as one could think in which a gamma ray is emitted and the interaction of this photon with the atomic electron would cause the emission of the electron as this process has an almost zero probability of occurrence.

The energy of de-excitation of the nucleus, ΔE, in invested in freeing the atomic electron, where the binding energy of the electron B_e is needed, and the rest of energy is carried by the electron in form of kinetic energy, T_e. Thus, the kinetic energy of the outgoing electron will be:

$$T_e = \Delta E - B_e \tag{1.74}$$

The binding energy of the atomic electron, B_e, depends on the shell occupied by the electron before the process occurs. Thus, the kinetic energy of the electron will be different depending on the initial shell where the electron was previously. In this way, we will have electrons coming from K, L, M, etc..., shells, corresponding to the principal quantum number n=1,2,3,...

Further, if we observe with enough energy resolution, we could resolve sub-structures corresponding to electrons occupying different subshells in the atom. Thus, we could distinguish $2s_{1/2}$, $2p_{1/2}$ and $2p_{3/2}$ electrons, which are named, respectively as L_I, L_{II} y L_{III} and conversion electrons M_I, M_{II},M_{III}, M_{IV} and M_V for the atomic shells $3s_{1/2}$, $3p_1/2$, $3p_{3/2}$, $3d_{3/2}$ and $3d_{5/2}$.

Experimentally, the energy difference between the subshells is quite low, of the order of tenths of keV and as we will see later, the energy resolution of our detectors are or the order of 1 keV so we cannot resolve these electrons and even, in some cases, we will not be able to distinguish between electrons from L and M shells, when their energy difference is lower than the energy resolution of the experimental device.

As a consequence of the internal conversion process, a vacancy in the atomic shell is left where the electron was located and a subsequent X-ray emission follows the internal conversion process when electrons from upper shells occupy the vacancy in order to decrease the total energy of the atom. Experimentally we will observe the characteristic X-rays of the nucleus but when an EC decay process occurs also the X-rays of the daughter nucleus are emitted and we cannot distinguish them as they have exactly the same energy.

Any level can de-excite by means of gamma emission or internal conversion. Therefore, the total probability of de-excitation will be given by:

$$\lambda_t = \lambda_\gamma + \lambda_e \tag{1.75}$$

The proportion between the probability of internal conversion and gamma emission is defined as internal conversion coefficient or simply **conversion coefficient**, α, with the aim of quantifying their relative intensities.

$$\alpha = \frac{\lambda_e}{\lambda_\gamma} \tag{1.76}$$

Thus, the total de-excitation probability can be defined as a function of only the gamma de-excitation probability as:

$$\lambda_t = \lambda_\gamma + \lambda_e = \lambda_\gamma \cdot (1 + \alpha) \tag{1.77}$$

As it was already mentioned, depending on the initial shell occupied by the electron the electron transition can be distinguished, the total conversion coefficient α_T or simply α, can be defined as the sum of all their components:

$$\alpha = \alpha_K + \alpha_L + \alpha_M + \alpha_N + ... \tag{1.78}$$

where the sub-index K, L, M, N, etc..., indicates the electron shell.

If one aims to obtain the intensity of the de-excitation transition one should measure both, the contribution from the gamma de-excitation and the one from internal conversion. With this aim, it is important to measure the conversion coefficients, α. In the same way as defined for the total transition probability, the total intensity of the transition between two levels can be determined from the expression:

$$I_T = I_\gamma + I_e = I_\gamma(\alpha_T + 1) = I_e(1 + \frac{1}{\alpha_T}) \tag{1.79}$$

since the conversion coefficient can be expressed in the form

$$\alpha_T = \frac{I_e}{I_\gamma} \tag{1.80}$$

which is the expression that we will use during chapter 3 in order to determine them experimentally.

The probability of the internal conversion process depends, mainly, of the following quantities:

1. **Transition energy**. While increasing the transition energy the internal conversion intensity decreases.

2. **Transition multipolarity**. As much larger the transition multipolarity is larger the internal conversion probability will be.

3. **Atomic number (Z)**. The more intense the electric field created by the nucleus is, the larger the internal conversion probability will be.

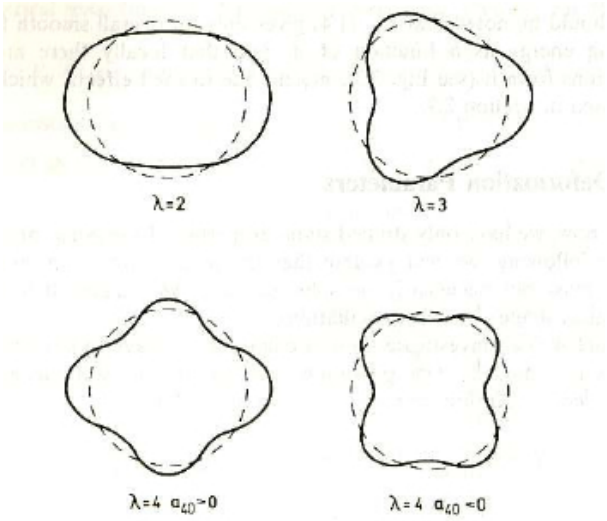

Figure 1.5: *Nuclear distortions from spherical shape for quadrupole ($\lambda = 2$), octupole ($\lambda = 3$) and hexadecapole ($\lambda = 4$) deformations.*

1.1.3 Nuclear shapes and deformations

The surface of a nucleus can be described by the vector pointing from the origin to the surface, which mathematically is:

$$R = R(\theta, \phi) = R_{av}\left(1 + \alpha_{00} + \sum_{\lambda=1}^{\infty}\sum_{\mu=-\lambda}^{+\lambda} \alpha_{\lambda\mu} Y_{\lambda\mu}(\theta, \phi)\right) \tag{1.81}$$

where R_{av} is the radius corresponding to the sphere with the same volume than as the ellipsoidal nucleus, usually taken as $R_{av} = R_0 A^{1/3}$, $\alpha_{\lambda\mu}$ are the coefficients of the spherical harmonics $Y_{\lambda\mu}$. The parameter α_{00} only describes changes in the nuclear volume while the rest of parameters represent deviations from the spherical shape of the nucleus. Thus, $\lambda = 1$ represents the translation of the centre of mass. The next order, $\lambda = 2$, already gives spectroscopic information as it describes the quadrupole deformation corresponding to prolate (rugby-ball shaped) or oblate (lentil shaped). Higher orders in λ than 2 describe more exotic deformations as the octupole deformation ($\lambda = 3$) which can be visualized as a pear shaped object. Recently, a new article has been published on the determination of static pear-shaped deformation for ^{224}Ra [Gaf13]. Fig. 1.5 shows how deformations of orders $\lambda = 2, 3, 4$ look like in comparison with the non-deformed spherical shape.

The assumption of axial symmetry is usually taken for well deformed nuclei. Taking the z-axis as the symmetry axis, the deformation parameters $\alpha_{\lambda\mu}$ vanish except for $\mu = 0$ and due to this the notation $\alpha_{\lambda 0} = \beta_\lambda$ is used. For our purposes, only quadrupole deformations $\lambda = 2$ will be considered.

Under these assumptions, eq. 1.81 is simplified to:

$$R(\theta, \phi) = R_{av}\left(1 + \beta_2 Y_{20}(\theta, \phi)\right) \tag{1.82}$$

β_2 is the quadrupole deformation parameter which is related to the nuclear shape as:

$$\beta_2 = \frac{4}{3}\sqrt{\frac{\pi}{5}}\delta \tag{1.83}$$

where $\delta = \frac{\Delta R}{R_{av}}$ is the parameter relating ΔR, the difference between the semi-length of the axes of symmetry (z-axis) and the semi-length of one the perpendicular axes (both are equally long in axially symmetric approximation) of the nuclear ellipsoid (when quadrupole deformed), and the average radius R_{av}. Generally, when referred to without subscript, β, means β_2. Thus, a **negative value for** β_2 indicates an **oblate deformation** (lentil shape) and a **positive value a prolate deformation** (rugby ball shape).

The Nilsson quadrupole deformation parameter ε_2 in terms of the δ parameter, can be expressed as:

$$\varepsilon_2 = \delta + \frac{1}{6}\delta^2 + \frac{5}{18}\delta^3 + \frac{37}{216}\delta^4 + ... \tag{1.84}$$

The relation linking ε_2 and β_2 is:

$$\beta_2 = \sqrt{\pi/5}\left(\frac{4}{3}\varepsilon_2 + \frac{4}{9}\varepsilon_2^2 + \frac{4}{27}\varepsilon_2^3 + \frac{4}{81}\varepsilon_2^4 + ...\right) \tag{1.85}$$

In the same way as β_2, a positive value for ε_2 refers to a prolate deformed nucleus and a negative value to an oblate nucleus.

A very useful quantity is the so-called intrinsic quadrupole moment Q_0 defined as:

$$Q_0 = \int d^3r\rho(r)(3z^2 - r^2) \tag{1.86}$$

and it is related with β_2 in the by [Kra87, Cas00]:

$$Q_0 = \frac{3}{\sqrt{5\pi}}R_{av}^2 Z\beta_2(1 + 0.16\beta_2) \tag{1.87}$$

up to second order in β_2. R_{av} is estimated from the formula $R_{av} = R_0 A^{1/3}$ as already commented for eq. 1.81.

The spectroscopic quadrupole moment Q is related to the intrinsic quadrupole moment Q_0 by:

$$Q = Q_0\frac{3K^2 - J(J+1)}{(J+1)(2J+3)} \tag{1.88}$$

where J is the total nuclear angular momentum (or spin) and K is its projection on the symmetry axis (z-axis).

A commonly employed notation to represent deformations in a more general way, not only the axially symmetric deformations, is the Lund convention. It makes use of β_2 and γ parameters, see fig. 1.6. γ gives information on the triaxial deformation. The relation between spherical harmonics parameters from eq. 1.81 and these new parameters is:

$$\alpha_{21} = \beta_2 cos\gamma \tag{1.89}$$

$$\alpha_{22} = \alpha_{2-2} = \frac{1}{\sqrt{2}}\beta_2 sin\gamma \tag{1.90}$$

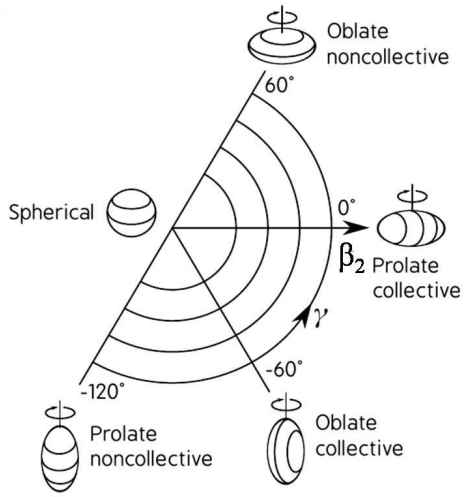

Figure 1.6: *Lund convention using the nuclear deformation parameters β_2 and γ and the resulting deformations for the nucleus [Nil55].*

Due to the symmetries of equations 1.81 and 1.90 it is sufficient by using the region $\beta_2 > 0$ and $0° \leq \gamma \leq 60°$. When $\gamma = 0°$ a prolate deformation is obtained and $\gamma = 60°$ an oblate deformation is resulting for the nuclear shape. The intermediate values of the γ parameter corresponds to triaxial deformed shapes.

1.2 Motivation

In the next sections the main reasons for performing the present study of the β-decay of ^{72}Kr will be explained. Firstly, the shape coexistence phenomenon will be presented and its presence in the mass region of interest. A brief overview on the systematics on shapes in neighbouring krypton isotopes and the theoretical predictions for the ^{72}Kr shape will be presented. In the following section, the astrophysical motivation for studying ^{72}Kr will be explained. Afterwards, the previous studies on the deformation of neighbouring nuclei by using the same technique that the present study are presented together with their main results. The theoretical approach used to compared with the experimental data in these studies, and also in the current work, are presented and briefly described.

1.2.1 Shape coexistence

The observation of atomic nuclei exhibiting eigenstates with different shapes is the evidence of the so-called **shape coexistence** phenomenon [Hey11]. This behaviour is familiar in molecules where different geometrical arrangements of widely spaced atomic nuclei cause different shapes for the molecule. However, the atomic nucleus does not have a substructure with widely spaced subunits and this fact makes this phenomenon unique in finite many-body quantum systems. There appears to be a possibility that it occurs in all nuclei and to explain the disappearance (*"collapse"*) of shell structure of nuclei far from closed shells.

Shape coexistence is governed by two opposing tendencies. On the one hand, the stabilizing effect of closed shells and subshells causing the nucleus to show a spherical shape. On

the other hand, the residual interactions between protons and neutrons which drives the nucleus towards a deformed shape. This latter term is proportional to the number of interacting neutrons times the number of interacting protons.

The shape coexistence phenomenon was first proposed to occur in the ^{72}Kr mass region for ^{72}Se in the work of [Ham74]. They found an exceptionally low energy of the 0_2^+ state and a strong B(E2; $0_2^+ \rightarrow 2_1^+$)= $0.32(6)\ e^2b^2 = 36(7)$ single-particle units, in comparison with the neighbouring $^{74-78}$Se isotopes. Additionally, they determined a strong B(E2; $2_2^+ \rightarrow 0_2^+$) of the same order as the one for the transition $2_2^+ \rightarrow 2_1^+$. The behaviour of the $\frac{2I}{\hbar^2}$ vs. $\hbar\omega^2$ where I is the moment of inertia was strange for low-spin. For this representation, they assumed the 0_1^+ and 2_1^+ states to belong to the same band as the rest 4^+, 6^+, 8^+, etc..., and found a sharp behaviour of the curve indicating a change in the structure of the nucleus. This behaviour was quite different from that found for yrast bands except for ^{186}Hg where similar coexistence evidence was found. These features motivated the suggestion of a coexisting spherical ground state (0_1^+) with a deformed excited state (0_2^+).

Later, a similar pattern of de-excitation was found in the nucleus of interest, ^{72}Kr, suggesting shape coexistence [Var87]. The fact that the strongest line not being the lowest in energy was surprising as in the isotopes ^{74,76,78}Kr the strongest and lowest in energy transitions is the $2_1^+ \rightarrow 0_1^+$.

This idea was supported by later works as the G. de Angelis and collaborators [de 97]. They proposed the level scheme of ^{72}Kr shown in figure 1.7(a). They found a exceptionally larger moment of inertia for high spin levels than expected for an oblate deformed nucleus, $I \approx 17\hbar^2 MeV^{-1}$, which is 20 % larger than expected. From this, they inferred that the shape at high spin is prolate deformed. Furthermore, they found irregularities in the low-spin region as can be seen in figure 1.7(b). In this figure, one can observe a quite exceptional delay in the crossing frequency for the band crossing towards S-band. Successful selfconsistent Total Routhian Surface (TRS) calculations for this region [Naz85, Rud97], predict this crossing at $\hbar\omega = 0.55$ but as can be seen in figure 1.7(b) this does not occur. This delay was proposed to be due to additional correlations in the T=0 channel or coupling to vibrational degrees of freedom or both.

A new isomeric 0^+ state understood as a shape isomer was proposed at an excitation energy of 671(2) keV in [Bou03]. They reported, from a conversion electron spectroscopy experiment, a lifetime of $\tau = 38(3)ns$ and the reduced electric monopole (E0) strength $\rho(E0)^2$ was determined to be $\rho^2(E0) = 72(6) \times 10^{-3}$. In the article, a two-level mixing calculation for the coexisting 0^+ states was performed giving as a result a mixing amplitude of 10% for the dominantly oblate ground state, 0_1^+, and the first excited state 0_2^+ which is understood as mainly prolate.

1.2.1.1 Systematics in the region

The mass region N=Z and A≈ 70-80 is where the heavier nuclei with neutrons and protons occupying the same orbitals that can be studied experimentally.

The systematics in the region could be very useful to understand what is particular in ^{72}Kr and what is a general feature in the mass region. For this purpose, the systematics of the low-lying states in the even-even ^{72,74,76,78}Kr isotopes is shown in figure 1.8. The position of

[2] the reduced electric monopole strength $\rho(E0)$ is related to the reduced E0 transition strength B($E0$) by means of the expression [Rei77]: B($E0$;$0_1^+ \rightarrow 0^+$)=$e^2R^4\rho^2(E0)$, where e is the electron electric charge and R is the radius of the nucleus often assumed as R=$R_0A^{-1/3}$ with R_0=1.20 fm and A the atomic mass.

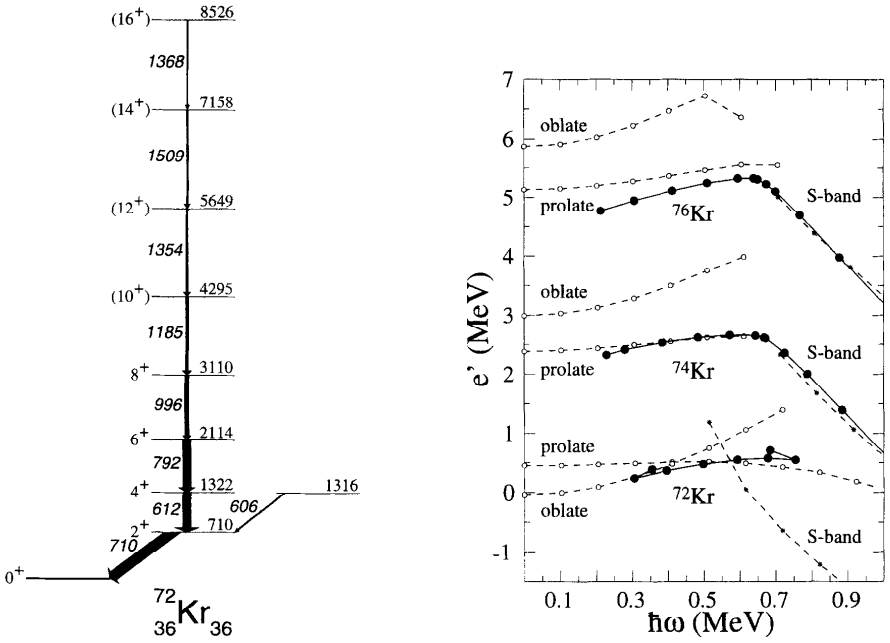

(a) (b)

Figure 1.7: *(a) Proposed excitation level scheme of ^{72}Kr in [de 97]. (b) Experimental (filled circles) and theoretical (empty circles) routhians with respect to the rotational frequency for oblate and prolate yrast bands and S-band for ^{72,74,76}Kr as shown in ref. [de 97].*

the first excited 0^+ state is decreasing in energy up to ^{74}Kr and then it increases again. The only isotope where the 0^+ state is the first excited one is for ^{72}Kr, as in the rest of them the first excited is the first 2^+ state belonging to the ground state band.

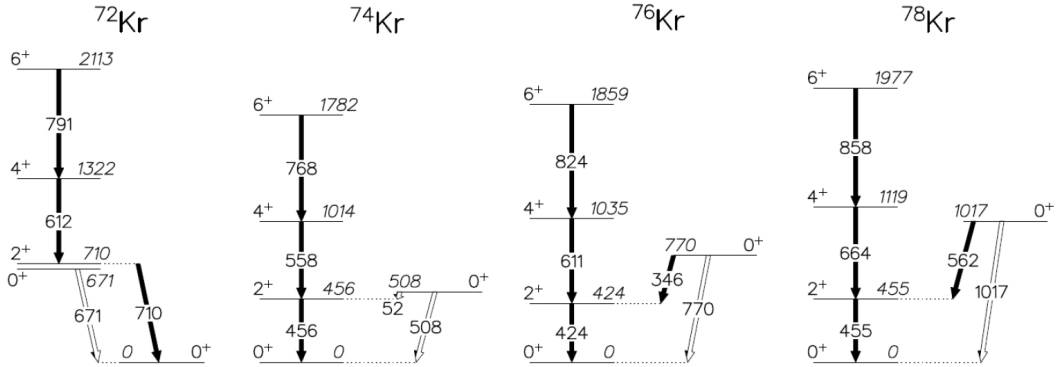

Figure 1.8: *Systematics of low-lying states in ^{72,74,76,78}Kr taken from [Cle11]. The position of the first excited 0^+ state understood as the band head of a different deformation is given. Note as ^{72}Kr is the only one having as the first excited state the 0^+_1 while for the rest is the 2^+_1 state.*

Figure 1.9 shows the experimental and theoretical calculations using the macroscopic-microscopic model [Mö09] on the positioning of the shape isomers with respect to the ground

states. One can realize how the ground state of all these krypton isotopes are prolate except for ^{72}Kr where oblate deformation is expected and some experimental pieces of evidence have suggested.

One of the main purposes of this work is to determine the sign of the deformation of ^{72}Kr by measuring the experimental B(GT) distribution of the ^{72}Kr β^+/EC decay and comparing with the predicted B(GT) distributions from P. Sarriguren calculations to confirm the oblate character of the ground state of ^{72}Kr.

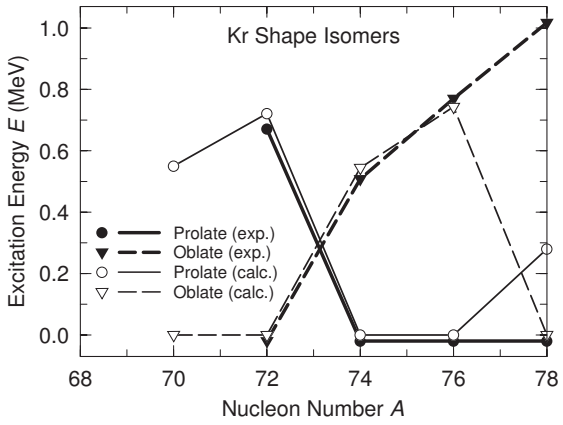

Figure 1.9: *Systematics of shape isomers states in ^{72,74,76,78}Kr as given in [Mö09]. Experimental energies and theoretical values from that work are given.*

1.2.2 Astrophysical interest

From the astrophysical point of view, ^{72}Kr is interesting for taking part in the rp-process of stellar nucleosynthesis. The rp-process is the mechanism leading to the X-ray bursts, that are generated by a thermonuclear runaway in the hydrogen-rich environment of an accreting compact object (typically a neutron star) which is fed from a binary companion (typically a red giant). The ignition is located on the surface of the neutron star in extreme conditions with high densities, around $10^{6-7}g/cm^3$ and temperatures, in the order of 10^9K.

The rp-process is much more faster than its competing process, namely β decay, and it produces rapid nucleosynthesis on the proton-rich side of the chart of nuclides toward heavier proton-rich nuclei and is the cause of the energy observed in the X-ray bursts. The path of the rp-process is shown in figure 1.10.

Having a look in more detail to the region around the nucleus of interest, ^{72}Kr, shown in figure 1.11 one sees as a sequence of proton capture processes (red arrows) that leads the process towards nucleus as ^{72}Kr where the next nucleus in this sequence is unbound, ^{73}Rb. This causes the raise of the competence between the two proton capture (green arrow) which is a very unlikely process and the beta decay (blue arrows) which is a much slower process. The nuclei where this takes place, as ^{72}Kr, are known as "waiting points" of the rp-process due to the consequent slowing down of the global process at this nuclei.

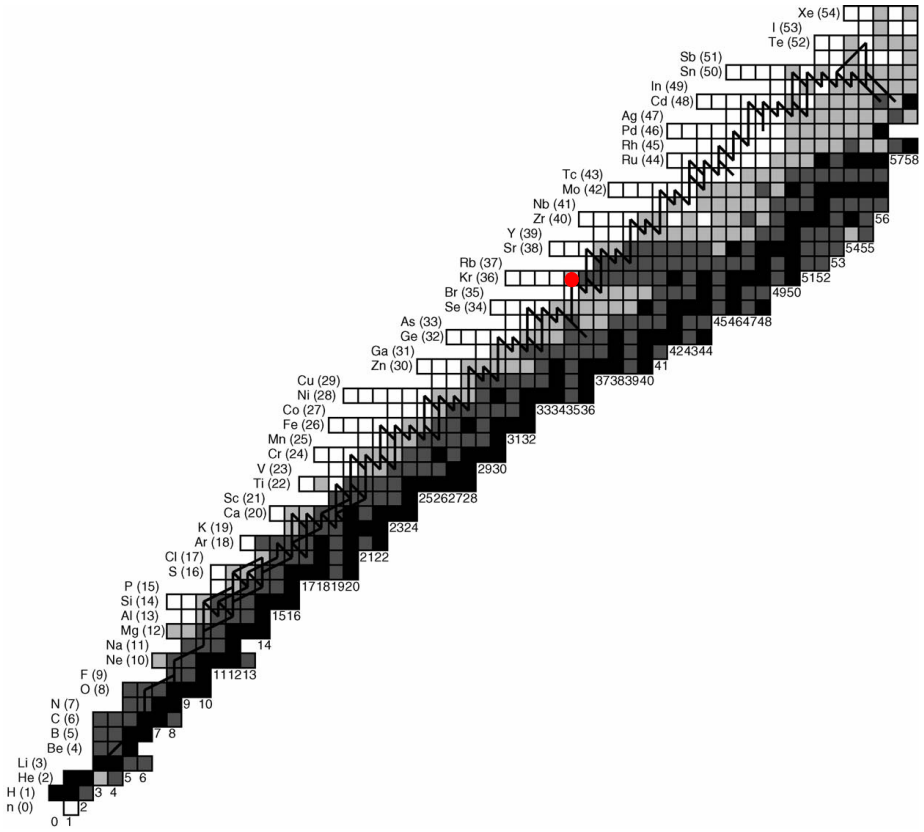

Figure 1.10: *Path of the rp-process along the chart of nuclides taken from H. Schatz work [Sch06]. Stable nuclei are shown in black and the path followed by the rp-process is indicated with a black line. The placement of the nucleus of interest, ^{72}Kr is indicated with a red dot. Figure 1.11 shows a zoomed view of the surrounding region of ^{72}Kr.*
Image credit: [Sch06]

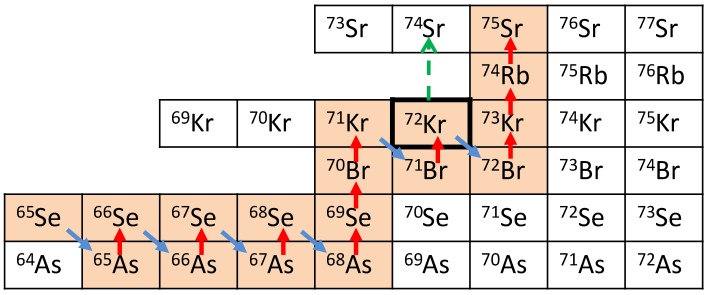

Figure 1.11: *Path of the rp-process in the mass region of the chart of nuclides around ^{72}Kr. The proton capture process (red arrows) is leading the process till nucleus where next in the path is unbound, such as ^{73}Rb which is the following one to ^{72}Kr. This provokes a slowing down in the process as the possibilities are a two proton capture (green arrow), a much unlikely process, or the beta decay (blue arrows) which is a much slower process. The nuclei where this takes place, as ^{72}Kr, are known as "waiting points" of the process.*

The beta decay process of the waiting point nuclei has to be studied carefully as their main properties play a key role in the astrophysical network calculations. These calculations follow the time evolution of the isotopic abundances to determine the amount of energy released by nuclear reactions and to find the reaction path for the rp process. The half-lives of waiting point nuclei are very important to determine the time scale of the nucleosynthesis process and the isotopic abundances. However, while the half-lives give only a limited information of the decay, different B(GT) distributions may lead to the same half-life, and it is of paramount importance to calculate the energy released in the β-decay process.

Specially important are the weak decay rates of neutron-deficient medium-mass nuclei under stellar conditions as they play a relevant role in the understanding light curves observed in type I X-ray bursts.

1.2.3 Nuclear deformation studies based on β decay measurements

The measurement of the B(GT) distributions for the N=Z and A$\simeq$70-80 region of the chart of nuclides was performed in a series of experiments at the ISOLDE facility. Previous studies on neighbouring nuclei have been already published as the cases of ^{76}Sr [Ná04b], ^{74}Kr [Poi04] and ^{78}Sr [Pé13].

The motivation for this campaign of measurements was based on two main reasons, on the one hand the performance of detailed studies of these beta decay processes enriching the knowledge on the level schemes of the daughter nuclei. The information obtained included level spin-parities, transition multipolarities, beta feeding distributions, etc...

On the other hand, Gamow-Teller (GT) β^+/EC decay strength distributions for N=Z nuclei in this mass region were found to depend sensitively on the nuclear shape [Ham95]. The deformed Hartree-Fock (HF) calculations of the latter reference were done using a quasiparticle Tamm-Dancoff approximation (TDA) including Skyrme-type interactions. Several energy minima are obtained located at different quadrupole moment, Q_2, and their corresponding GT strength distributions were quite different, see fig. 1.12.

A similar type of calculations, in this case HF plus quasiparticle random phase approximation QRPA plus BCS, performed by P. Sarriguren and co-workers [Sar99, Sar01] also found

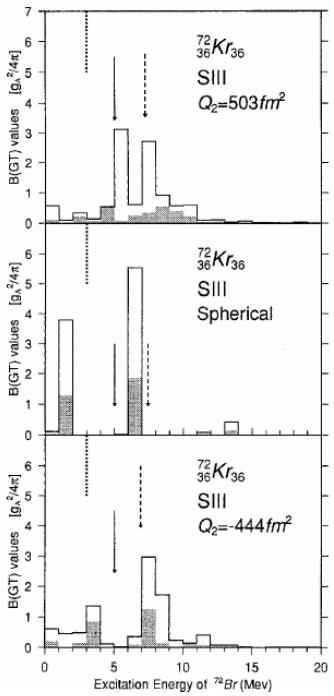

Figure 1.12: *Predictions on the B(GT) for the β^+/EC decay of ^{72}Kr from Hartree-Fock calculations in Tamm-Dancoff approximation [Ham95]. The B(GT) shows to be sensitive to the nuclear shape as different B(GT) distributions are found for assuming different deformations of ^{72}Kr ground state.*
Image credit: [Ham95]

several minima in potential energy curves for nuclei in the mass region A≈70-80 corresponding to different value for the deformation parameter β_2. Next section will be dedicated to explain the theoretical approach they followed.

The experimental campaign was devoted to measure the B(GT) distributions by means of the Total Absorption Spectroscopy technique that will be explained in detail in chapter 2. The potential energy curves obtained in [Sar99] for Sr and Kr isotopes are shown in figures 1.13, 1.14. They were obtained by using two different types of Skyrme forces as effective interactions in the calculations, the SG2 which has been successfully tested against spin and isospin excitations in both, spherical and deformed nuclei, and the Sk3 interaction, which is one of the oldest and simplest parametrizations designed to fit ground state properties of spherical nuclei and nuclear matter properties.

In most of the cases, at least two energy minima were found. Paying special attention to the case of interest, ^{72}Kr, one can see how two minima corresponding to opposite signs of the quadrupole moment are given. Their energy are spaced in around 1 MeV which is a hint of shape coexistence.

The B(GT) distributions for these isotopes calculated for the energy minima are plotted in fig. 1.15. The Q_β window of the decay is indicated with a solid line. Remarkable differences are found for the ^{72,74}Kr and ^{76,78,80}Sr isotopes.

Three experimental works have been already published from our experimental campaign [Poi04, Ná04b, Pé13]. The study of the ^{76}Sr case ended up with a nice match between the experimental data and the predictions for the prolate deformation of the ground state as can be seen in fig. 1.16(b). The case of ^{74}Kr does not match with any of the theoretical B(GT) distri-

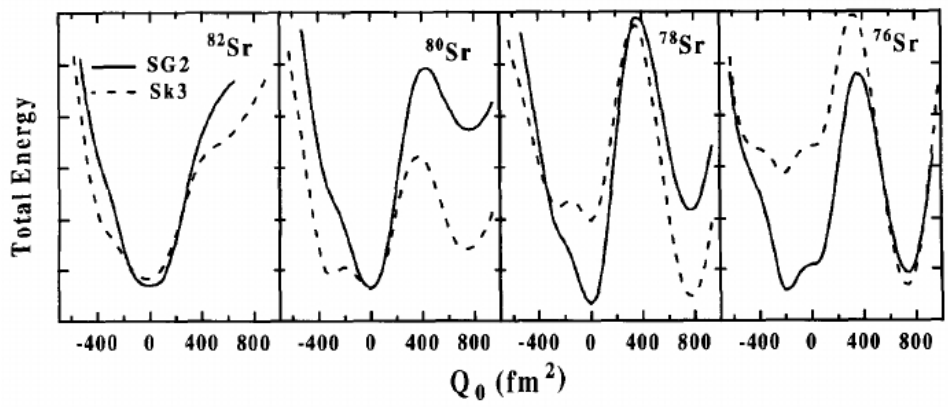

Figure 1.13: *Total energy curves with respect to the mass quadrupole moment for ^{82,80,78,76}Sr isotopes. The results correspond to a constrained HF+BCS calculation using SG2 (solid lines) and Sk3 (dashed lines) forces [Sar99]. Absolute values of total energy are not given but the tick-to-tick distances is kept to be 1 MeV. Image credit: [Sar99]*

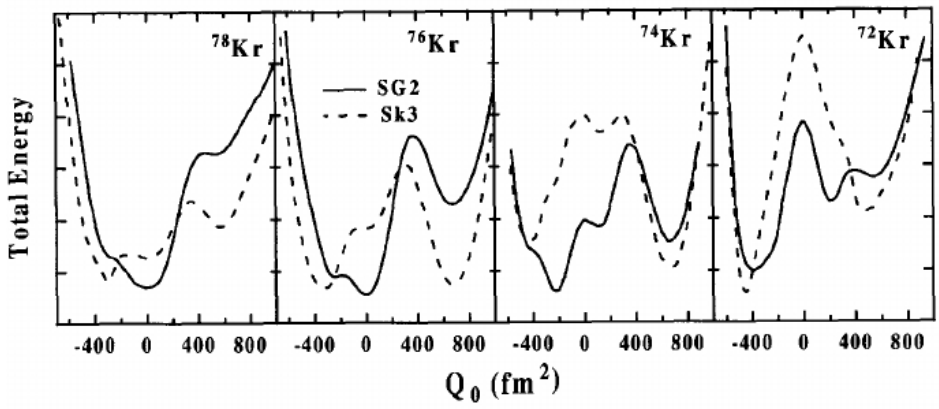

Figure 1.14: *Same as fig. 1.13 for ^{78,76,74,72}Kr isotopes.*

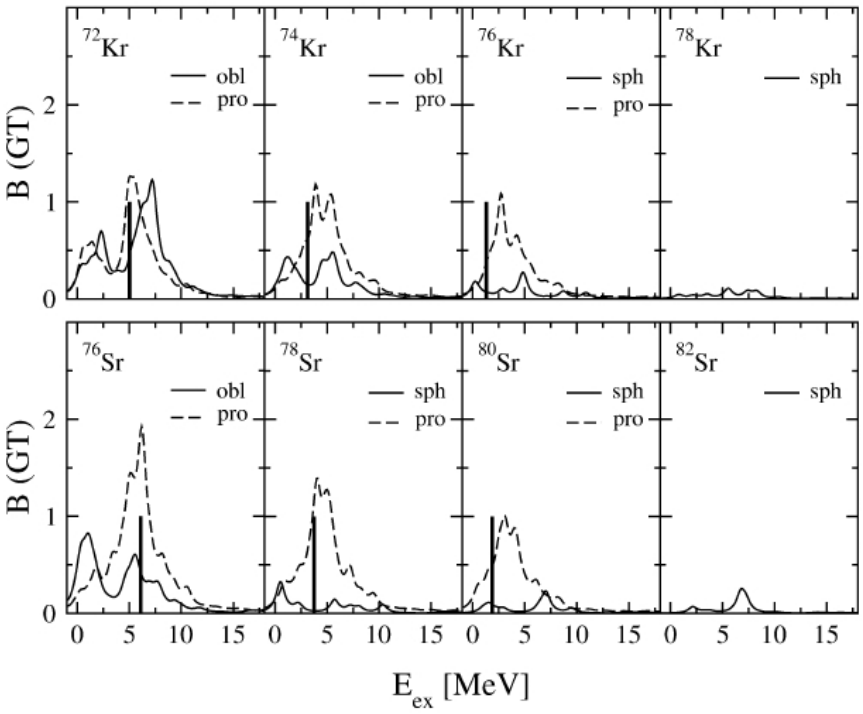

Figure 1.15: *Predicted B(GT) distributions for ^{72,74,76,78}Kr and ^{76,78,80,82}Sr isotopes from [Sar01] calculated for the energy minima found in figs. 1.14 and 1.13. For every nuclei, a vertical line indicates the Q_β energy window available experimentally.*

butions 1.16(a) confirming the idea of shape mixing for the ground state also proposed both, theoretically [Pet00] and experimentally [Bec99, Cle07]. Experimentally, around 50 % mixing amplitude is proposed. The recently published results for ^{78}Sr show a good agreement with the predicted B(GT) distribution for prolate deformation. Fig. 1.16(c) shows the comparison with spherical and prolate predictions using three different Skyrme forces (SG2, Sk3 and SLy4).

1.2.3.1 Self-consistent Hartree-Fock QRPA calculations

Next, a summary of the main ingredients of the theoretical formalism explained in detail in ref. [Sar99, Sar01, Sar09].

The method consists on a selfconsistent formalism based on a deformed Hartree-Fock calculation (mean field obtained) with a Skyrme interaction including pairing correlations in the BCS approximation. Once the states of the parent and daughter nuclei are calculated using the HF method, one solves the Quasiparticle Random Phase Approximation, QRPA, equations with a separable residual interaction derived from the same Skyrme force.

This microscopic calculation uses a self-consistent method in the sense that with a two-body density dependent effective interaction one derives: 1) the self-consistent mean field generating the single particle energies, wave functions and occupations of the ground state, 2) the particle-hole Landau-Migdal interaction averaged over the nuclear volume generating the QRPA modes. In this way, the same two-body interaction is used to develop the QRPA excitations consistently with the quasiparticle basis and ground state.

The density-dependent HF approximation gives a very good description of ground state properties for both, spherical and deformed nuclei [Flo73, Que78, Bon85].

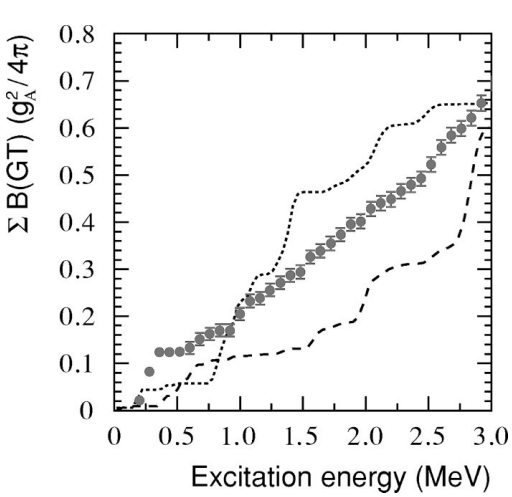

(a)

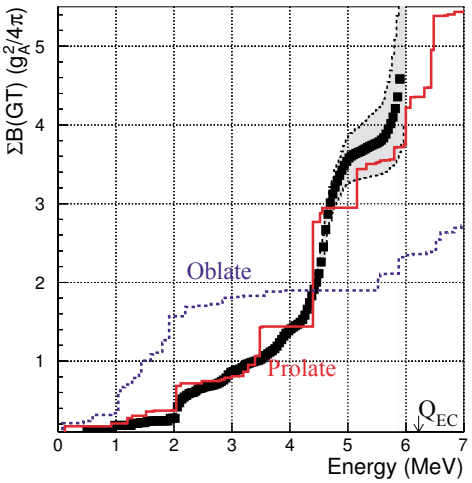

(b)

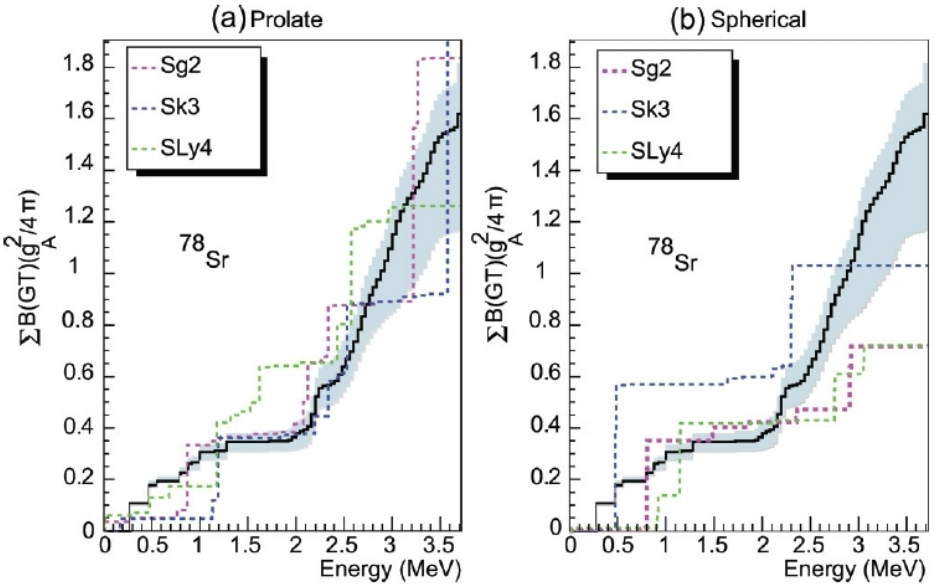

(c)

Figure 1.16: *(a) Comparison of experimental accumulated B(GT) distribution with theoretical predictions from [Sar01] for oblate (dotted line) and prolate (dashed line) deformation of the ^{74}Kr ground state [Poi04]. (b) Same as (a) for ^{76}Sr where oblate is plotted with blue line and prolate in red [Ná04b]. (c) Same as (a) for ^{78}Sr where the comparison is done using two panels, left one for prolate energy minimum and right one for the spherical case [Pé13]. Three Skyrme-type forces are included in (c): SG2, Sk3 and SLy4 whose properties are described in the text.*

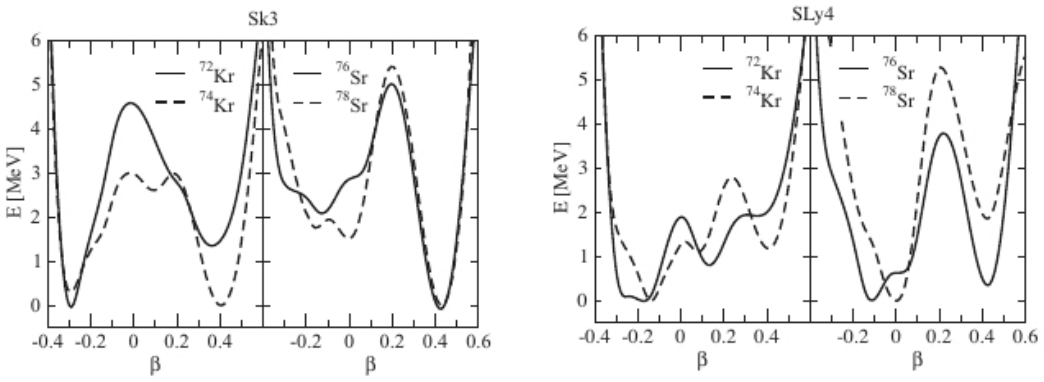

Figure 1.17: *(a) Potential energy curves obtained for $^{72,74}Kr$ (left) and $^{76,78}Sr$ (right) from a constrained HF plus BCS calculations using Sk3 Skyrme-type force [Sar09]. (b) Same as (a) but using the SLy4 Skyrme force. For more details see text. β is the quadrupole deformation parameter which is usually noted as β_2.*

The solution of the HF equation is found using the McMaster procedure based in the formalism developed in [Vau72, Vau73] assuming time reversal and axial symmetry.

The energy surfaces are analyzed as a function of the quadrupole deformation. To achieve this, constrained HF calculations are performed with a quadratic constraint [Flo73]. The HF energy is minimized under the constraint of keeping fixed the nuclear deformation. The Gamow-Teller strengths are calculated for the minima found in the energy surfaces.

Most recent calculations [Sar09] were performed by using two different types of Skyrme forces, one of the oldest parametrizations called Sk3 [Bei75] which has proved to be successful in the description of many nuclear properties of spherical and deformed nuclei, and the SLy4 force [Cha98], one of the most recent parametrizations which includes selected properties of unstable nuclei in the fitting procedure.

The results from these calculations for the potential energy curves with respect to the quadrupole deformation parameter β_2 for several nuclei in the mass region, including the nucleus of interest ^{72}Kr, are shown in figure 1.17. For the case of interest, ^{72}Kr, the results from the Sk3 force predict the ground state to be oblate with a deformation parameter of around $\beta_2 \approx -0.3$ and another minimum at around 1.2 MeV of excitation energy with a strong prolate deformation, $\beta_2 \approx 0.38$. From the SLy4 force two nearby minima are found with oblate deformation with approximate deformations of $\beta_2 \approx -0.18$ and -0.27 and another prolate minimum at an excitation energy of around 0.6 MeV with a deformation parameter of $\beta_2 \approx +0.16$.

One key assumption of these calculations is that the ground state of the parent nucleus and the populated states in the daughter nucleus must have similar shapes since the β-decay connecting different shapes is disfavoured.

A standard quenching factor of 0.77 is included in the calculations in order to include in an effective way all the correlations not properly considered in this approach [Ber82].

The corresponding B(GT) distributions for the prolate and oblate minima in figure 1.17 are shown in figure 1.18. In the figure, the experimental determination of the B(GT) via the high resolution spectroscopy study in [Piq03] is shown.

One of the main goals of the present study is to determine the B(GT) distribution in the ^{72}Kr decay by means of the Total Absorption Spectroscopy technique as it was done in

previous works [Poi04, Ná04b, Pé13]. In this way, the right B(GT) distribution will be extracted without the influence of some experimental difficulties that will be presented in chapter 2 usually linked with the High Resolution measurements.

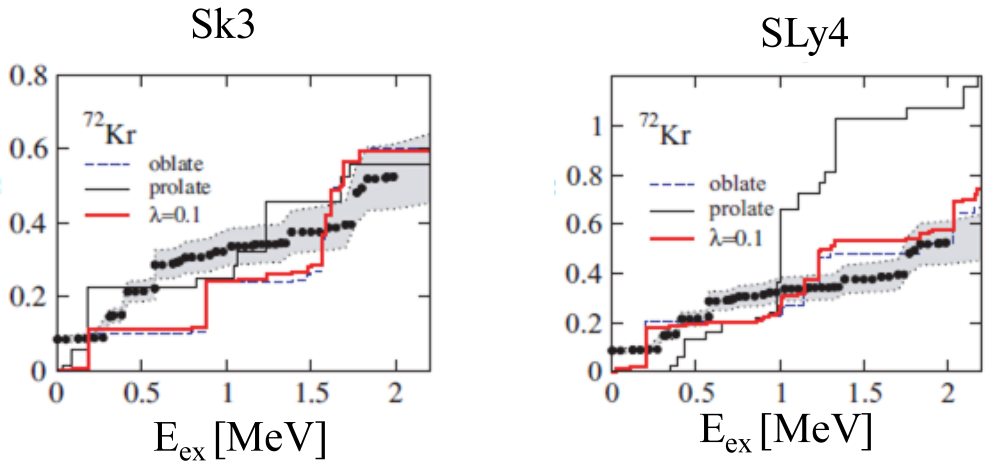

Figure 1.18: *Comparison of experimental B(GT) distribution of ^{72}Kr beta decay determined from high resolution spectroscopy [Piq03] with theoretical predictions for oblate, prolate and mixing amplitude $\lambda = 0.1$ deformations of the ground state of ^{72}Kr by using two different Skyrme-type two-body interactions Sk3 (left) and SLy4 (right) as given in [Sar09]. The mixing amplitude of $\lambda = 0.1$ was reported by experimental studies in [Kor01, Bou03].*

1.2.3.2 Variation After Mean-field Projection In Realistic model spaces approach

Another type of self-consistent approach that has been applied to the mass region of interest is the so-called excited Variation After Mean-field Projection In Realistic model spaces (VAMPIR) variational approach described by A. Petrovici and co-workers in [Pet96, Pet00]. It is based on the use of a *complex* Hartree-Fock-Bogoliubov transformations and a relatively large model space.

The most recent publication of the results from this approach is [Pet11] where the B(GT) distributions of the β-decay of ^{72}Kr and ^{68}Se are compared to experimental data. This comparison is shown in figure 1.19. For nuclei in this mass region a ^{40}Ca core is used and oscillator orbits $1p_{1/2}, 1p_{3/2}, 0f_{5/2}, 0f_{7/2}, 1d_{5/2}$ and $0g_{9/2}$ for both, neutrons and protons. The effective two-body interaction is constructed from a nuclear matter G-matrix based on the Bonn one-exchange potential (Bonn A/Bonn CD) [Pet09]. The calculations labelled with an "ext-space" are using an extended model space including, in addition to the previously mentioned levels, the $2s_{1/2}, 1d_{3/2}$ and $0g_{7/2}$ orbitals for neutrons and protons.

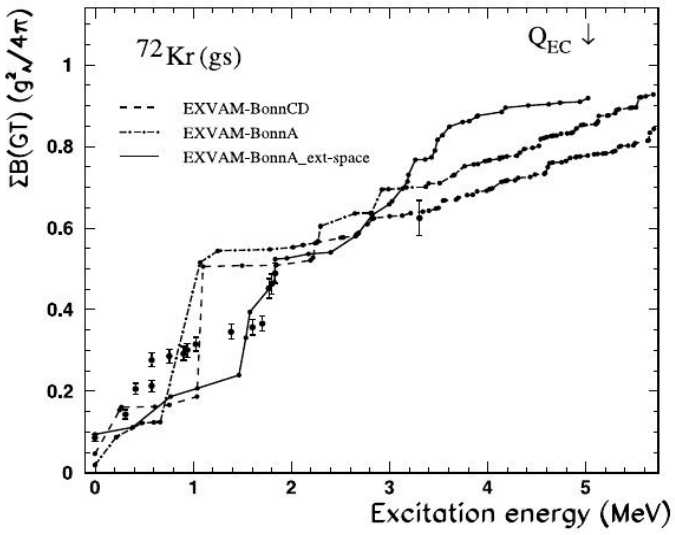

Figure 1.19: *Comparison of experimental B(GT) distribution in the beta decay of ^{72}Kr from [Piq03] with the predictions from excited VAMPIR calculations using Bonn A and Bonn CD potentials and an extended model space "ext-space" as given in [Pet11].*

As shown in figure 1.19 the reproduction of the experimental data taken with High Resolution technique [Piq03] is fairly good with this approach. However, the present study tries to improve the experimental determination of the B(GT) distribution as the one reported in [Piq03] suffers from experimental systematic error inherent to the high resolution technique as it will be explained in chapter 2.

1.2.4 Theoretical predictions on ^{72}Kr shape

The first prediction on the ground state deformation of Kr isotopes was done in 1972 by F. Dickmann and collaborators [Dic72] where indications of oblate deformed ground states were reported for the region of ^{72}Kr and neighboring nuclei.

A microscopic calculation study performed by W. Nazarewicz [Naz85] predicted a quadrupole deformation parameter $\beta_2 = -0.31$ and a quadrupole moment of $Q_2 = -2.12e \cdot b$ for the ^{72}Kr ground state and a first excited state prolate deformed at excitation energy of around 0.26 MeV with $\beta_2 = 0.37$ and $Q_2 = 3.15e \cdot b$.

Liquid drop model calculations performed by P. Möller and collaborators [Mö95] predict a vast majority of prolate deformed ground state nuclei in the chart of nuclides. Fig. 1.20 shows the value of the quadrupole deformation parameter β_2 for N=Z nuclei in the mass region from A=20 to A=100. Most of them are predicted to be prolate deformed except two cases, ^{70}Br and the nucleus of interest of this study, ^{72}Kr. Strong shape changes are predicted from ^{68}Se to ^{70}Br and from ^{72}Kr to ^{74}Rb as the deformation changes from prolate to oblate and back to prolate respectively with strong deformation parameters as shown in fig. 1.20. There, a deformation parameter β_2 is found to be -0.349 for the ^{72}Kr ground state.

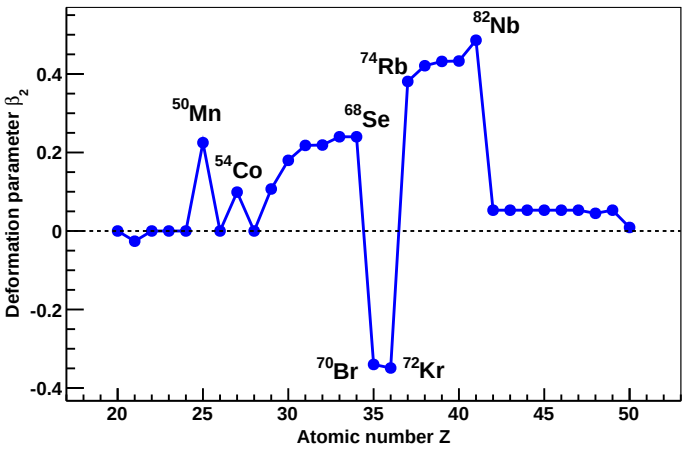

Figure 1.20: *Predicted values for the quadrupole deformation parameter β_2 as a function of the Z number for N=Z nuclei [Mö95]. The most deformed cases are labelled. Only two cases seem to be oblate deformed, ^{70}Br and ^{72}Kr, the nucleus of interest of the present study.*

Predictions of shape coexistence

An attractive point of the nucleus of interest, ^{72}Kr is the fact that it is the "poster child" nucleus of nuclear shape isomers [Mö09], which means that it is a good example of shape coexistence as can be seen in fig. 1.21. It shows the potential energy surface for ^{72}Kr obtained via a macroscopic-microscopic calculations performed by P. Möller and colleagues [Mö09]. It can be seen that several energy minima are found close in energy corresponding to different deformations, the ones shown in the upper part of the figure. Each minima is indicated with a marker of the same colour that the corresponding deformation shown in the upper part. The potential energy surface is plotted following the Lund convention that was already presented with the slight difference that instead of β_2 as deformation parameter the Nilsson quadrupole deformation parameter ε_2 has been used.

If one remembers the definitions given in earlier section 1.1.3, $\gamma = 0°$ gives a prolate deformation while $\gamma = 60°$ corresponds to oblate deformation.

The absolute minimum of potential energy in the plot (predicted ground state) is obtained for an oblate deformation where an energy a bit lower than 3 MeV is found (blue point in the plot). The blue ellipsoid in the upper plot displays how the nuclear shape would be for this minimum corresponding to a deformation parameter $\epsilon_2 \approx 0.28$ which is equivalent to $\beta_2 \approx 0.22$.

Another minimum located at a prolate deformation for an energy around 3.6 MeV (600 keV of excitation energy with respect to the ground state) is found and represented as a green point in the plot. The green ellipsoid in the upper part is the approximate shape corresponding to this minimum with a deformation parameter $\epsilon_2 \approx 0.35$ which is equivalent to $\beta_2 \approx 0.28$.

The third minimum found is located at a triaxial deformation plotted as a red point in the plot. This minimum has an energy of around 4.6 MeV (so is around 1 MeV higher than the ground state). Finally, a fourth minimum is found at spherical deformation corresponding to a potential energy of around 6 MeV which means 3 MeV of excitation energy above the predicted ground state.

Thus, several energy minima are predicted for ^{72}Kr each of them corresponding to a different quadrupole (even triaxial) deformation. All of them are quite close in energy but

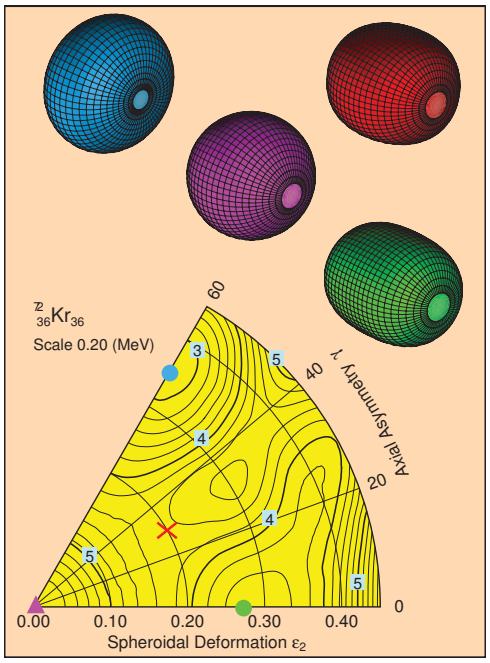

Figure 1.21: *Potential energy surfaces for ^{72}Kr with respect to ε_2 and γ parameters obtained from a macroscopic-microscopic calculation [Mö09]. Equipotential lines are distanced 0.2 MeV. The numbers indicate the energy in MeV corresponding to the line on top of which they are placed.*

specially the two lower states, the predicted ground state (oblate) and the first excited state (prolate) are only 600 keV of energy difference. This scenario is typical for the shape coexistence phenomenon and due to the proximity in energy of these states, a strong mixing between these states is expected.

Nuclei having oblate shape at low spins are rare in nature as the prolate deformation is the mostly found experimentally. However, the case of ^{72}Kr is predicted to show oblate deformation for the ground state and prolate deformation for the band starting at the first excited state, which is a 0^+ at 671(2) keV as proposed by [Bou03]. This is an unique case in nature showing shape coexistence whose study offer the possibility of studying and learn about the not yet known mechanism which makes the ground state of a nucleus such as ^{72}Kr to be oblate deformed.

1.3 Previous knowledge on ^{72}Kr nucleus

In the next sections, the available knowledge on both, the level scheme of ^{72}Kr and the β-decay scheme of ^{72}Kr will be presented. For the decay scheme, the main experimental works will be summarized with the main contributions done by every work.

1.3.1 Excitation scheme of ^{72}Kr

Recalling the previously mentioned work of G. de Angelis and collaborators [de 97], they proposed the excitation band up to a tentative spin of 12^+, see fig. 1.22.

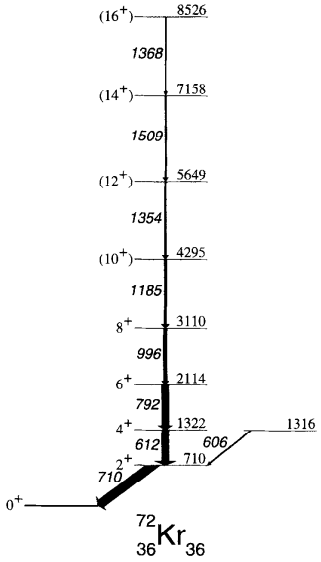

Figure 1.22: *Proposed level scheme of ^{72}Kr from [de 97].*

An experimental observable accounting for information on the shape of the nucleus is the $B(E2)$ values. The $B(E2)$ value is a measurement of the intensity of the electric quadrupole radiation, E2, and it is defined as:

$$B(E2; J_i \rightarrow J_f) = \frac{1}{2J_i + 1} \langle \psi_f || E2 || \psi_i \rangle^2 \tag{1.91}$$

It is important to note that two main standards are used, the Weisskopf unit (W.u.) and the single-particle rate. They correspond, respectively, to $2^+ \rightarrow 0^+$ and $0^+ \rightarrow 2^+$ transitions. The W.u. is defined as 1 $W.u. = 5.94 \times 10^{-}6A^{4/3}e^2b^{23}$. Single-particle rates are a factor 5 larger than W.u. as $J_i = 0$ in contrast with $J_i = 2$ for W.u.

Thus, the absolute $B(E2; 0_1^+ \rightarrow 2_1^+)$ is related to the deformation parameter β_2 by means of the expression:

$$\beta_2 = \frac{4\pi}{3ZR_0^2} \sqrt{B(E2; 0_1^+ \rightarrow 2_1^+)/e^2} \tag{1.92}$$

where R_0 is usually taken as $R_0 = 1.2A^{1/3}$ fm.

In 2006, A. Gade and colleagues [Gad05] measured the $B(E2; 0_1^+ \rightarrow 2_1^+)$ for ^{72}Kr to be:

$$B(E2; 0_1^+ \rightarrow 2_1^+) = 4997(647)e^2fm^4 = 280.85 \text{ single-particle units} = 57(8)W.u. \tag{1.93}$$

which gives a value for the deformation parameter of:

$$\beta_2(^{72}\text{Kr}) = 0.33 \tag{1.94}$$

which is a value for the module of the parameter and, despite being in agreement with theoretical calculations predicting oblate deformation of the ground state, no experimental information is extracted for the sign of the deformation from these studies and cannot be concluded that the ^{72}Kr ground state is oblate deformed.

[3] $1\ e^2b^2 = 10^4e^2fm^4$

Later, an erratum publication [Gad06] admitted the possibility of an additional source of systematic error coming from the assumption that 100 % of ^{72}Kr in the beam came in the ground state while a not negligible amount of the nucleus could be produced in the first 0^+ state which is a shape isomer. In that experiment the ratio of production between both isomers was not measured but another experiment with the same primary beam and target but different beam energy (73 MeV/nucleon instead of 140 MeV/nucleon) reported a $5.5(12)(7)\%$.

Furthermore, as already explained in section 1.2.1, a shape isomer 0^+ state was identified at 671(2) keV of excitation energy with a lifetime of $\tau = 38(3)ns$ and a reduced electric monopole strength $\rho(E0)^2 = 72(6) \times 10^{-3}$, see [Bou03].

1.3.2 Excitation scheme of ^{72}Br

1.3.2.1 β-decay studies of ^{72}Kr

In the following, the most important works on the description of the level scheme of the daughter nucleus in the β^+/EC decay of ^{72}Kr, namely ^{72}Br, are analyzed. A brief summary of the main results from every one including the level scheme of ^{72}Br deduced from each of them as well as a short description of the work is included.

1. **C.N. Davids and collaborators [Dav73]**. Impinging a 52 MeV ^{16}O ion beam on a ^{58}Ni target they obtained ^{72}Kr and studied its beta decay at Brookhaven National Laboratory located in Upton, New York (U.S.A.). They measured the gamma radiation by means of two of Ge(Li) detectors. The main results of this work were:

   - The half life for ^{72}Kr nucleus of $T_{1/2} = 17.4 \pm 0.4\ s$ from the time evolution of its more intense gamma transitions.
   - The half life of the gamma line 101.3 $\pm$ 0.4 keV turns out to be $T_{1/2} = 21.9 \pm 1.9\ s$ so they did not assigned it to ^{72}Kr declaring its origin as unknown.
   - Direct beta feeding was found to levels at 162, 310, 415 and 576.6 keV of excitation energy in ^{72}Br. These levels were assigned a spin-parity 1^+ as being allowed transitions from the parent ground state well-known to be an 0^+ state as it is an even-even nucleus ground state.
   - The 124.4 keV transition was not firmly placed and, consequently, the direct beta feeding to the ground state was left dependent on the position of this 124.4 keV transition, ranging from 2 ± 11 to $9 \pm 15\%$. The starting level of this transition was assigned to be 1^+ as well for being directly fed by a β decay allowed transition.
   - the feeding intensities were not corrected by electron conversion as they were not studied as well as the multipolarities of the transitions were not determined.
   - The resulting level scheme from this work is shown in figure 1.23(a).

2. **H. Schmeing and collaborators [Sch73]**. The beta decay of ^{72}Kr was studied at Chalk River facility in Ontario (Canada). ^{72}Kr was produced in the reaction $^{58}Ni(^{16}O, 2n)^{72}Kr$ by means of a 55 MeV ^{16}O beam impinging on a ^{58}Ni target. Their main results were:

   - The ^{72}Kr half life was measured to be: 16.7$\pm$0.6 s.
   - The ground state beta feeding was determined to be 54%. This leads to the assignment of the ^{72}Br ground state spin-parity to be 1^+.

- The Q_{EC} value was found to be: $Q_{EC} = 5057 \pm 135$ keV.
- In the same way as Davids work [Dav73], they assigned spin-parity 1^+ to all the levels directly fed. These states were placed at excitation energies of 162, 310, 415 and 576.5 keV and the starting level of the 124 keV transition was placed in the level scheme as shown in figure 1.23(b).
- Other 3 possible weak gamma transitions of energies 438±2 keV, 559±2 keV and 147±1 keV were identified.
- The level scheme proposed in this work is shown in figure 1.23(b).

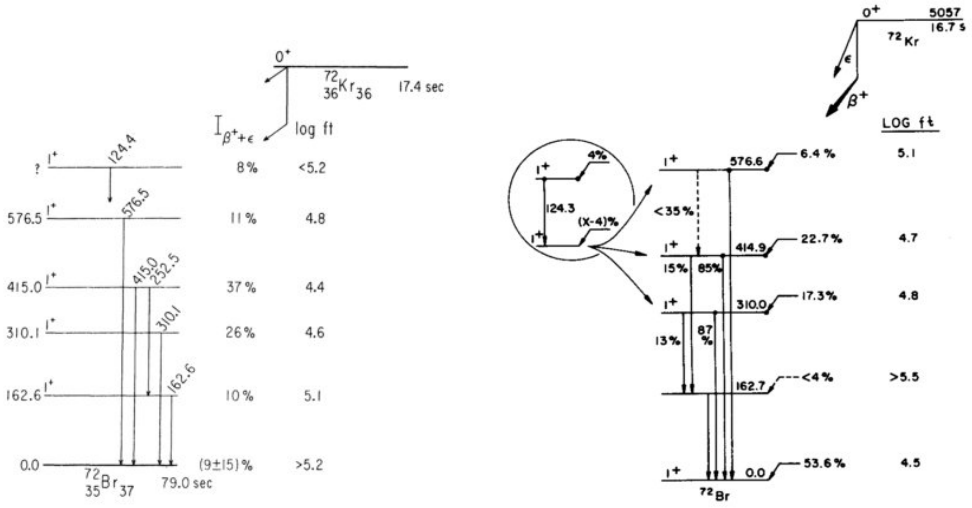

(a) (b)

Figure 1.23: *(a) Level scheme of ^{72}Br deduced from the beta decay study performed in [Dav73]. (b) Same as (a) but from [Sch73].*

3. **I. Piqueras et al. [Piq03]**. The experiment was performed at ISOLDE (CERN) in Geneva, Switzerland. It consisted on the study of the beta decay of ^{72}Kr by means of $\beta\gamma$ and $\beta\gamma\gamma$ coincidences done by using 2 different measuring stations: 2 HPGe detectors and a β detector on one side and 1 gas-Si telescope, 1 HPGe and 1 Si(Li) detector on the other side. A ^{72}Kr beam was produced by impinging a 1 GeV proton beam on a 37 g/cm^2 niobium target. The results of this measurement can be summarized as:

   - Identification of 27 new levels in the daughter level scheme, that is ^{72}Br.
   - Measurement of the ^{72}Kr half-life resulting $T_{\frac{1}{2}} = 17.1 \pm 0.2s$ by means of the time evolution of the more intense gamma lines in the daughter nucleus in time intervals of 3.5 s.
   - Assignment of the spin-parity of ^{72}Br ground state to be $J^\pi(gs) = 1^+$ from an intense direct beta feeding to the ground state of ^{72}Br (∼33%).
   - An upper limit for the beta-delayed proton emission from ^{72}Kr was established to be 10^{-6}.
   - The low-energy part of the level scheme of ^{72}Br can be seen in figure 1.25.

Apart from the previous studies on the ^{72}Kr decay, the next work is indicated as it has important implications in the discussion of the spin and parity of the ^{72}Br ground state.

4. **W.E. Collins and collaborators [Col74]**. They studied the β^+/EC of the daughter nucleus ^{72}Br at Oak Ridge National Laboratory in Tennessee (U.S.A.). By means of a 42-46 MeV ^{16}O ions beam impinging on a ^{58}Ni target they obtained ^{72}Br. Their results can be summarized as:

   - Direct beta feeding found to 2^+ states located at 862 and 1316.7 keV excitation energy with intensities 23.2 and 20 % respectively and to a 4^+ state at 1636.8 keV with an intensity of 5 % in ^{72}Se. These results suggested the ^{72}Br ground state spin to be 3.

   - The ^{72}Br half life was measured: $T_{1/2} = 1.31 \pm 0.04\ min$.

   - 32 transitions were assigned to the ^{72}Se level scheme.

The currently available information on the ^{72}Br level scheme can be summarized as shown in the level schemes in figures 1.24 and 1.25. The first of them, fig. 1.24, is just a compilation of the previously explained works of [Dav73], [Sch73] and [Gar82]. The second, fig. 1.25, is the result of the more recent work of Piqueras et al. [Piq03].

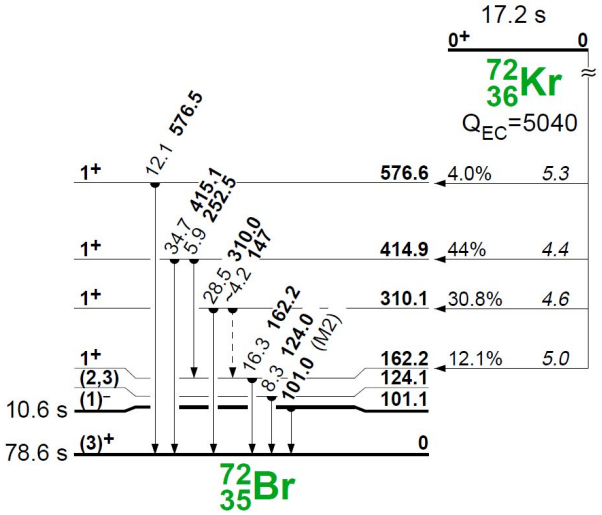

Figure 1.24: *Information on the ^{72}Br level scheme as appears in [Fir96]. It is a compilation of the works already described of references [Dav73], [Sch73] and [Gar82].*

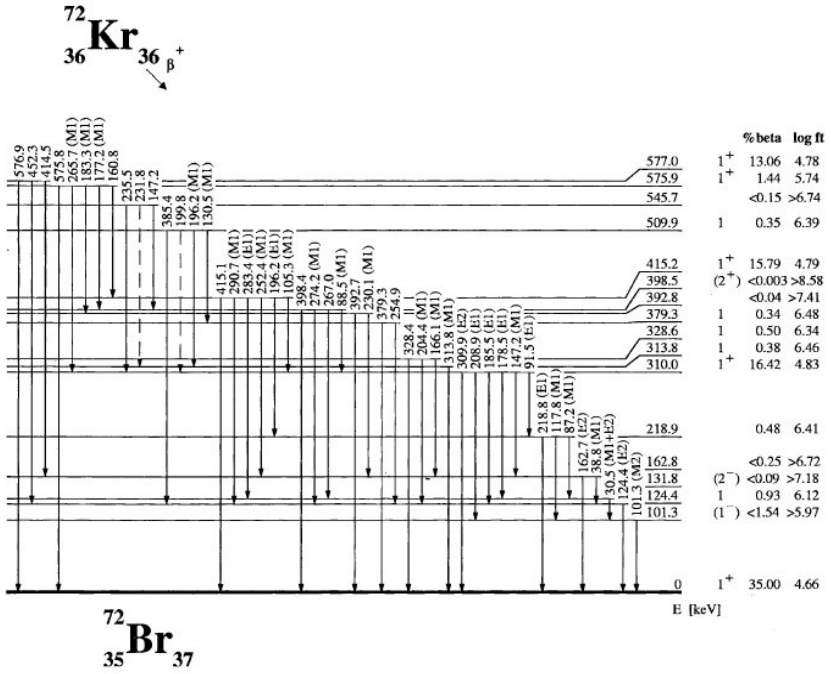

Figure 1.25: *Knowledge on the ^{72}Br level scheme in the low-energy region taken from [Piq03]. As described in the text, this work consists of beta decay studies of ^{72}Kr by means of high resolution spectroscopy with HPGe, Si(Li), gas-Si telescope and β detectors.*

1.3.2.2 In-beam γ-ray spectroscopy of ^{72}Br

In the following, the main studies of in-beam gamma ray spectroscopy of ^{72}Br are summarized to know the main properties of the ^{72}Br scheme obtained through this technique.

- **G. Garcia Bermudez and collaborators [Gar82]**. They studied ^{72}Br excited states obtained from the ^{58}Ni(^{16}O,np)^{72}Br reaction in the energy range of 40 to 55 MeV at Brookhaven National Laboratory in Upton, New York (U.S.A.). The obtained results were:

  - The half life of the isomeric state located at 101.0 keV was found to be 10.3±0.6 s. Previously, as already mentioned, Davids and collaborators [Dav73], found 21.9 s as the half life of the 101 keV transition that can be explained if one considers the 101 keV an isomeric level with a half-life of around 10 seconds as it is delayed by the decay of ^{72}Kr, see figure 1.27.

  - A more detailed level scheme of ^{72}Br was built as the excited states of ^{72}Br were populated by the reaction, for which the restrictive selection rules of β-decay do not apply, see section 1.1.1. Thus, they were able to populate higher spin states such as J=2,4,6, etc...

  - The level scheme deduced is shown in figure 1.26.

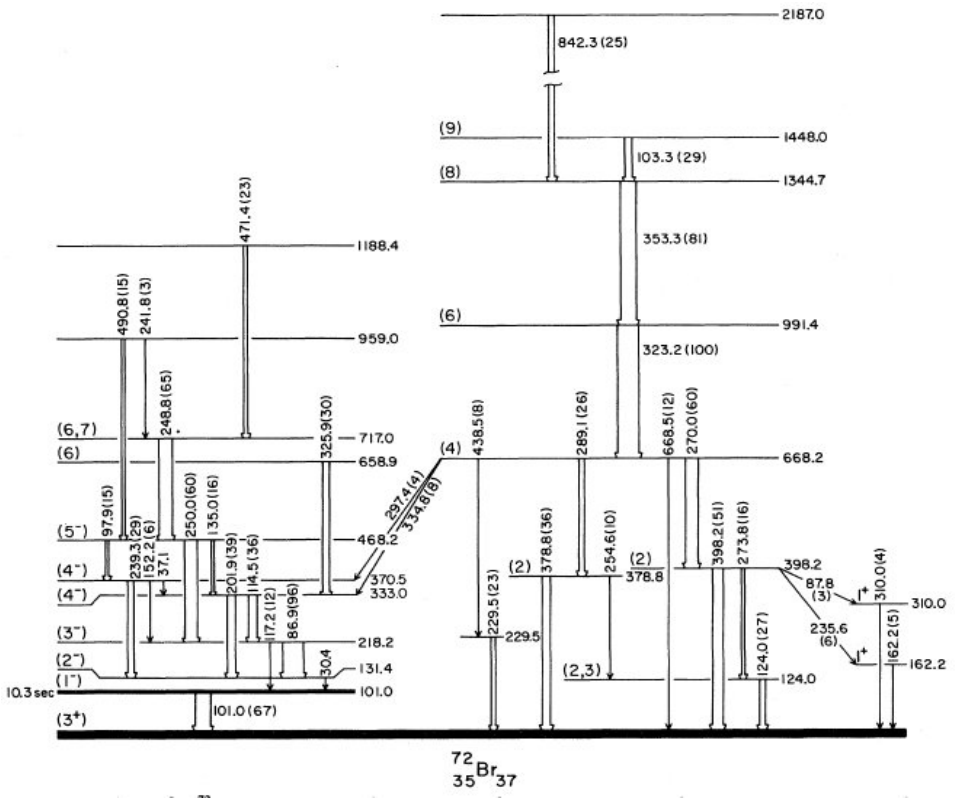

Figure 1.26: *Proposed level scheme of ^{72}Br from high-spin studies from ^{58}Ni(^{16}O,np)^{72}Br reaction in [Gar82].*

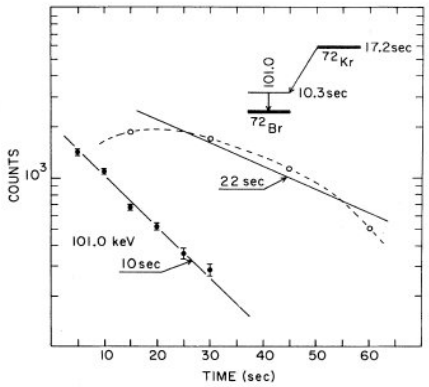

Figure 1.27: *Decay curve of the de 101 keV line and a fit with a half-life of $T_{\frac{1}{2}} = 10$ s considering it as an isomeric state in ^{72}Br taken from [Gar82]. Due to this, the 10 s half-life is delayed by the 17.1 s decay half-life of the parent nucleus ^{72}Kr feeding this level. The dotted line at the right is the result of the previous assumption on the 101 keV transition. If one fits the time evolution directly to a exponential decay the result is a half-life of around 22 seconds as it was obtained in the previous work of [Dav73].*

1.3.3 Mass measurements of ^{72}Kr and ^{72}Br

The measurement of the atomic masses is important for several applications [Bla06] as the determination of nuclear binding energy, the verification of nuclear models, the verification

of the Standard Model (the Conserved-Vector-Current, CVC, hypothesis and the unitarity of the Cabibbo-Kobayashi-Maskawa, CBM, quark mixing matrix), for metrology standards as the definition of the kilogram or the determination of fundamental constants, and to test quantum electrodynamics and fundamental charge, parity and time reversal symmetry.

As far as the present study concerns, the mass measurements of the parent nucleus of the decay, that is ^{72}Kr, and the daughter, ^{72}Br, determine the available energy in the process as it has been already presented in the section 1.1.1. This energy can be invested in kinetic energy of the neutrino/antineutrino, positron/electron or excitation energy in the daughter nucleus in β^+/β^- decays and between neutrino and excitation energy in the daughter in the EC decay as already explained.

The measurement of the ^{72}Kr mass was performed by D. Rodríguez and collaborators [Rod04] using the ISOLTRAP Penning trap mass spectrometer installed at ISOLDE facility, in the CERN accelerator complex, in Geneva, Switzerland. This experimental device includes a radio-frequency quadrupole trap for ion beam cooling and bunching, a Penning trap for further cooling and isobaric separation and a ultra-high-vacuum hyperboloidal Penning trap for the mass measurement with a micro-channel-plate detector.

They determined the mass excess, D which was defined in the section 1.1.1 as the difference between the atomic mass expressed in u units and the mass number A, for the ground state of ^{72}Kr to be:

$$\text{D}(\,^{72}\text{Kr}) = \text{M(in u)} - \text{A} = -53940.6\ (80)\ \text{keV} \tag{1.95}$$

The case of ^{72}Br was more recently measured by P. Herfurth and collaborators [Her11]. This experiment was also performed at ISOLDE facility by means of the ISOLTRAP mass spectrometer. The resulting value for the mass excess of the ground state of ^{72}Br is:

$$\text{D}(\,^{72}\text{Br}) = \text{M(in u)} - \text{A} = -59067.4\ (67)\ \text{keV} \tag{1.96}$$

Therefore, the Q-value for the β^+/EC decay of ^{72}Kr (see eq. 1.9) results to be:

$$Q_{EC} = \text{D}(\,^{72}\text{Kr, keV}) - \text{D}(^{72}\text{Br, keV}) = \text{M}(^{72}\text{Kr}) - \text{M}(^{72}\text{Br}) = 5126.8(104)\ \text{keV} \tag{1.97}$$

This value is the same than the one provided in the most recent compilation of atomic mass references of G. Audi and collaborators [Aud12] and the associated tables in [Wan12a, Wan12b]. The value reported in [Wan12b] is Q_{EC}=5127(10) and this is the value adopted in this work.

2

Experimental methodology

Contents

In this chapter I present the available experimental tools in order to achieve the goals pursued in this study.

The main option to perform beta decay studies is via High Resolution Spectroscopy technique. This allows us to construct the level scheme from the detected γ-rays and the study of their coincidences. In order to determine from the constructed level scheme the beta decay properties we have to assume that all the gamma radiation belonging to the decay has been identified. This is difficult to be fully achieved with the high resolution system. With the aim to obtain the population to the different states in the daughter nucleus from a certain knowledge on the low energy part of the decay scheme, the Total Absorption Spectroscopy technique is used.

Let us describe the main features of both experimental techniques more in detail along this chapter.

2.1 High Resolution gamma Spectroscopy

As mentioned in the previous chapter, the main purpose of the current work is the study of the beta decay of ^{72}Kr in order to both, enrich the knowledge on the level scheme of the

daughter nucleus, ^{72}Br, and determine the beta strength distribution in order to get information on the deformation exhibited by the ground state of the parent nucleus, ^{72}Kr.

The study of the level scheme populated by beta decay is usually performed by measuring the subsequent β-delayed γ radiation emitted in the de-excitation of the daughter nucleus. This is due to the fact that the beta decay is a 3-body process, nucleus, positron/electron and neutrino/anti-neutrino. The nucleus can end up in an excited state and the other two particles are emitted. The available energy, named Q_β, is shared by the three particles and, as a consequence, the β-particle spectrum is continuous as already presented in the previous chapter.

The gamma radiation is usually detected by using semiconductor materials, such as HPGe or historically Ge(Li) as nowadays is an obsolete type of detector. The energy resolution of this type of detectors is quite good (in the order of 1-2 keV as can be seen in table 4.3). This is the so-called **High Resolution Spectroscopy** technique.

Several previous works have studied the level scheme of the daughter nucleus of interest, ^{72}Br, and they have been presented in chapter 1. Those works studied different aspects of the level scheme such as level energy, their spin and parities, the intensity of transitions linking the levels as well as its multipolarity, etc...,

A specially detailed work on this beta decay was performed by I. Piqueras and collaborators [Piq03] which will be referred constantly along the present work. In that work, the level scheme was enriched with 27 new levels, the B(GT) distribution was determined in the low excitation energy part of the level scheme, the half-life of the parent nucleus was more precisely measured and strong direct beta feeding to the ground state (33 %) was proposed using intensity balance arguments.

All those works were performed with the High Resolution Spectroscopy technique, which makes use of HPGe detectors and it takes advantage of the good energy resolution of this type of detectors to accurately identify the individual energy of the gamma transitions connecting levels. The usual way of building up a level scheme is by the study of the gamma rays in coincidences to place the levels. The measured quantities are the energy and intensity of the individual gamma rays. Then, using intensity balance arguments one can assign the beta population to each level, from now on beta feeding (β-feeding). This is done as the amount of direct beta population needed to balance the incoming and outgoing gamma intensities for each level assuming that we have detect all of them.

This technique has been historically the most widely employed to carry out beta decay studies. It usually succeeds for most of the cases but it suffers from experimental difficulties due to three main factors:

1. High level density for high excitation energies.
2. High fragmentation of the gamma de-excitation pattern of highly excited levels.
3. Low detection efficiency of HPGe detectors (also the obsoletes Ge(Li) detectors) for high-energy γ-rays.

These conditions cause that much of the β-feeding to high excitation energy levels remains unobserved, see fig. 2.1. This leads the experimentalist to wrongly assign the β-feeding to lower excitation energy levels than the real ones. This has the consequence of introducing a large systematic error in the determination of B(GT) distributions and total B(GT) values obtained via High Resolution Spectroscopy technique. This is the so-called **Pandemonium effect** which was firstly pointed out by J. C. Hardy et al. [Har77]. In that work, they simulated the beta decay of a fictional nuclide (called Pandemonium) using statistical models and they

proved that much of the de-excitation intensity remains unobserved as demonstrated by the latter analysis of the simulated γ-ray spectrum.

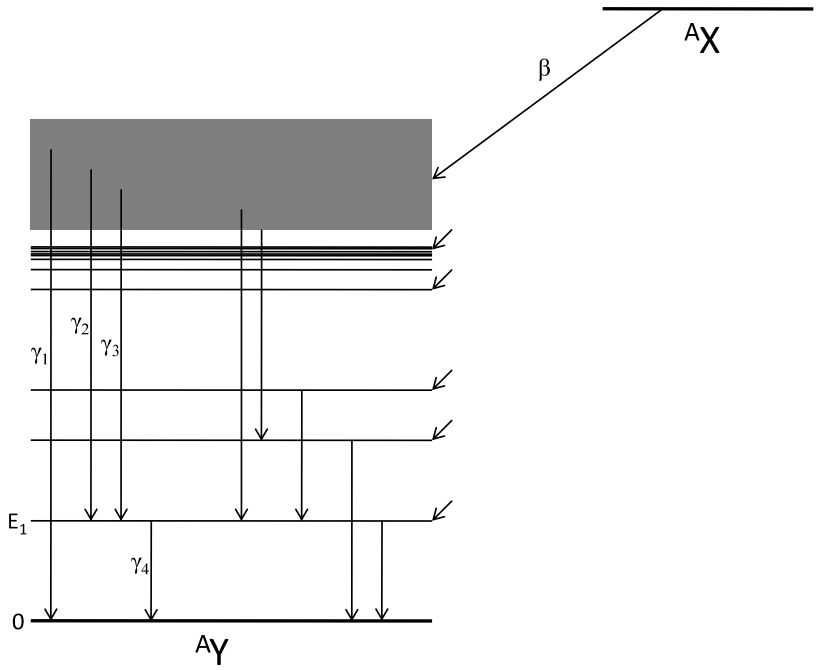

Figure 2.1: *Example of the level scheme corresponding to a β decay of nucleus ^{A}X leading to the nucleus ^{A}Y. The level density usually increases with excitation energy and this makes the beta feeding distribution to be very fragmented at high excitation energies. This, combined with a high fragmentation of the gamma de-excitation pattern and the low detection efficiency of HPGe detectors for high-energy γ-rays makes that, in most cases, γ_1, γ_2 and γ_3 keep undetected. This would cause the wrong assignment of feeding to level at excitation energy E_1 provoking an overestimation of feeding at this level and an underestimation of feeding at higher excitation levels. This is the so-called Pandemonium effect [Har77].*

This experimental difficulty lead us to perform the study by using a different technique which is presented in the next section.

2.2 Total Absorption Spectroscopy

The Total Absorption Spectroscopy (TAS) is a technique based in the use of a large crystal of a highly efficient scintillation material which is sensitive to the full γ de-excitation cascades instead of the individual gamma rays emitted from the fed levels in the daughter nucleus. In an ideal case, the detection of the full cascades would allow us to extract the β-feeding distribution.

This can be done by using a (near) 4π angular coverage NaI(Tl) scintillation mono-crystal detector which ideally absorbs all the γ-rays emitted in the de-excitation cascade starting at the directly fed levels in the beta decay, see figure 2.2. With such a device, instead of obtaining peaks in the energy spectrum corresponding to each of the single gamma ray emitted one ends up with a peak at the excitation energy of the directly fed level.

The use of this highly efficient detector together with the capability of obtaining the energy of the full de-excitation cascade, allows for a precise determination of the decay feeding distribution as a function of the excitation energy.

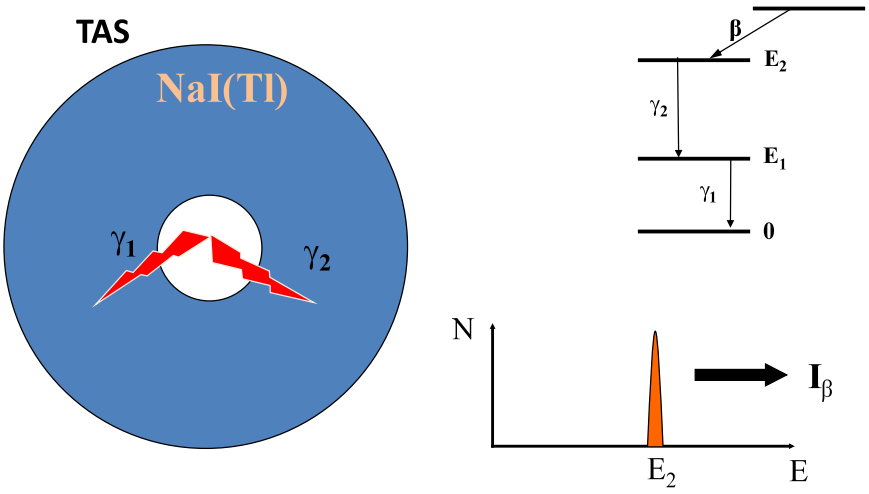

Figure 2.2: *Simplified representation of how an ideal Total Absorption Spectrometer works. The individual gamma-rays emitted by the source are added and the resulting spectra shows a peak at the added energy. Thus, by measuring the total gamma intensity one could directly deduce the beta feeding to the level located at the same excitation energy than the gamma energy detected.*

The detector is a single scintillation crystal whose scintillation light is collected by several photo-multipliers and whose signals are added to form the total signal for every decay event. This is done after a careful test of the alignment of the photo-multipliers responses is performed.

The ideal case of a TAS measurement makes use of a detector which covers the whole 4π solid angle subtended from the source and which fully absorbs all the gamma-rays coming from the source. The real detector does not cover the full 4π solid angle as one needs to introduce the radioactive sample to be studied in the geometrical center of the detector and move it away when its activity decreases being not useful any more. For this reason a hole has to be drilled to the 4π TAS detector and the angular coverage decreases.

Additionally, for different reasons, mainly the identification of contaminants in the measurements and the selection of the EC or β^+ components of the decays, one has to make use of ancillary detectors such as a plastic scintillator for β-particles detection and a HPGe telescope detector for X- and γ-rays. They have to be placed close to the sample in order to show good detection efficiencies and be useful. This makes the efficiency of the TAS detector even lower and enhances the probability of loosing individual gamma-rays in the de-excitation cascade.

The fact that the real TAS detector is not 100% efficient for gamma cascades makes it necessary to determine its response function to the decay of interest, including all different types of radiation involved, and apply a deconvolution procedure explained in the next section.

2.2.1 Operating principles of TAS data analysis

The analysis of the Total Absorption Spectroscopy (TAS) experimental data, d, consists of the procedure which allow us to extract the beta feeding distribution, f, on the energy window of the daughter nucleus. It is important to note that both, the experimental data d and the feeding distribution f are discretized in bins (divisions) of a certain width.

On the one hand, the case of the experimental data is related with the fact that one is using digital electronics and the ADC stores the data with discrete numbers.

On the other hand, the decay scheme of the daughter nucleus is discretized due to several reasons, mainly because the knowledge of the level scheme in the daughter is restricted up to a certain excitation energy. In the case of interest is, at most, up to 2 MeV, and as one has to cover the whole Q_{EC}-window one has to discretize the energy region from at least 2 MeV up to 5.127(10) MeV, the Q_{EC} of ^{72}Kr decay. For this, one discretizes the whole decay scheme of the daughter as shown in fig. 2.3. The bin width was chosen in both cases to be 40 keV to simplify the analysis. These reasons imply that the feeding distribution, f, resulting from the analysis is a discretized distribution in bins of 40 keV width.

The quantity that links both variables, d and f, is the response matrix of the detector to the current beta decay of interest, R. Mathematically this is expressed by:

$$d_i = \sum_j R_{ij} f_j \tag{2.1}$$

where i and j indexes indicate the discretization of both variables that has been mentioned above. d_i is the content of bin i in the energy spectrum resulting as the sum over the response of the detector R_{ij} to all the possible fed bins j which can contribute to the data bin i. The levels fed in bin j contribute to the data bin i if the element R_{ij} of the response matrix is not zero.

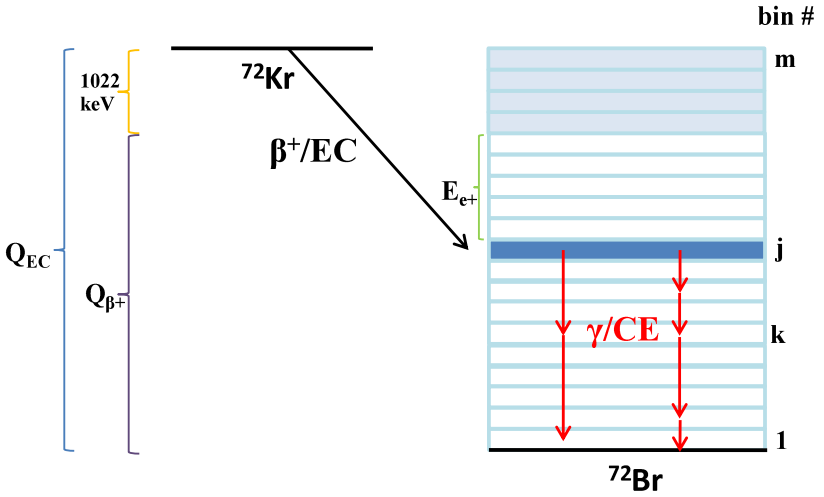

Figure 2.3: *Discretized level scheme of the daughter nucleus, ^{72}Br for the TAS data analysis. The bin width was chosen as 40 keV in the analysis for both, the level scheme, f_j and the experimental spectrum d_i. The decay scheme extends up to the Q_{EC}=5127(10) keV of the decay of interest.*

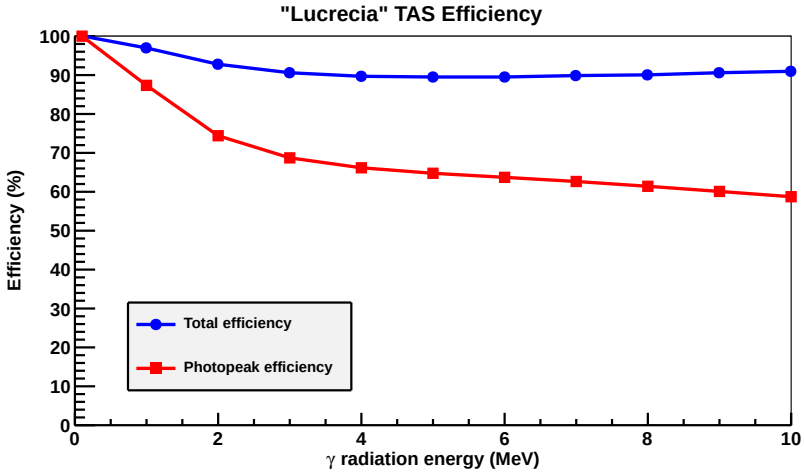

Figure 2.4: *Total and photopeak efficiencies of "Lucrecia" Total Absorption Spectrometer obtained from simulations performed using a GEANT4 code including the experimental set-up. As can be seen, the total efficiency is higher than 90 percent in the whole energy range (0-10 MeV gamma radiation energy). The photopeak efficiency is lower, specially for relatively high energy, namely from 2 MeV on. It is good to remember at this point that the efficiency of the TAS detector for the detection of beta feeding to a level is higher than the photopeak shown in the figure. The use of the TAS response matrix and the deconvolution algorithm is able to include as detected events those γ-rays not fully absorbed. Additionally, it is good to point out that the individual gamma-rays that will be detected in our experiment will have small energies as we detect the full cascade and the Q_{EC}=5.127(10) MeV.*

In an ideal case, if the total absorption spectrometer had a 100 $\%$ efficiency and the resolution of the detector was infinitely good (resolution equals to zero) one could identify every beta feeding via the de-excitation gamma-ray emission following the decay so the response function R_{ij} would be a matrix where the response to a feeding at a certain level, f_j, would be entirely located at one division in the spectrum (bin i), R_{ij}=1 for every pair of specific values of i and j. Thus, the normalized spectrum would represent the feeding distribution directly.

The real case is not so wonderful, as usual, because the detector efficiency is smaller than 100 $\%$ as shown in figure 2.4, the resolution of the NaI(Tl) crystal is quite far from zero (FWHM $\approx$ 90 keV at at 1.5 MeV gamma-rays) and the non-linearity of the response of the detector to the radiation energy adds extra complications. Thus, the response of the detector to the feeding of a certain level to have contributions at lower energies than the excitation energy of the level, the resolution merges the peaks corresponding to close levels, etc... All these reasons makes the analysis tougher as there is a relationship between data in bin 5, for example, with the feeding to a level at bin 50. This relationship is given by the Response Matrix.

As the aim is to obtain the feeding distribution, one has to extract the f variable from expression 2.1, and, consequently, to invert the response matrix R_{ij}. As the relation in eq. 2.1 is linear, this is the so-called **linear inverse problem**. In a general case, maximum values of the indexes i and j are different so the response matrix is not a squared matrix and, consequently, not invertible. But event if it was a squared matrix this would not guarantee the matrix to be regular.

In addition, one should be aware that, under certain conditions, a completely unreasonable β-feeding distribution could reproduce fairly well the experimental data. This is the so-called **ill-conditioned or ill-posed problem** inherent to the inverse problem that it is faced

in this analysis. The way to overcome this problem is to include in the analysis some initial information on the coherence of the solution when the statistical problem is established.

In order to solve these difficulties one has to make use of numerical algorithms to find the feeding distribution. Several algorithms for solving the inverse problem in the β-decay total absorption spectroscopy have been contemplated and they are discussed in [Tai07a]. The conclusion of that study is that either the Maximum Entropy (ME) or the Expectation- Maximisation algorithms are well suited for the analysis of the TAS spectra [Tai07a].

Both algorithms can be applied to the present analysis and, as the second one was already applied to previous TAS analysis this work will make use of it again. The Expectation-Maximisation algorithm has been applied to the problem of image reconstruction in emission and transmission tomography as well by assuming that the data follows the Poisson statistics, see ref. [She82] and [Lan84].

The **Expectation-Maximization (EM)** algorithm is an iterative general method for maximum likelihood estimation of parameters from an incomplete set of data as described in [Dem77]. It consists of two steps: firstly, calculate the **expectation** of the log-likelihood for the current values of the parameters, and, secondly, perform the **maximisation** of the expectation by finding the values of the parameters which maximize the likelihood.

The same algorithm is obtained via the use of the Bayes theorem in ref. [D'A95], which states that the causes, the feeding distribution in bins, f_j, in the present case, which produce an effect, which is the experimental data d_i in this work, are related via the Bayes formula:

$$P(f_j|d_i) = P(d_i|f_j)P(f_j) \tag{2.2}$$

adding a normalization term to guarantee the normalization of the probability to the unity:

$$P(f_j|d_i) = \frac{P(d_i|f_j)P(f_j)}{\sum_{j=1}^{m} P(d_i|f_j)P(f_j)} \tag{2.3}$$

where $P(f_j|d_i)$ represents the final conditional probability that the feeding to a level at bin j, f_j, is the cause of the contribution to the data bin i, d_i. $P(f_j)$ is really $P(f_j/\sum_{j=1}^{m} f_j)$ meaning the normalized initial probability of feeding a certain level at bin j and $P(d_i|f_j)$ is the probability that the feeding of a level at bin j contributes to the data bin i, being equivalent to the definition of the response matrix R_{ij} already defined earlier.

The expression 2.2 can be explained as following *if one observes a single event (effect), d_i, the probability that it has been due to the j-th (cause), f_j, is the probability of the cause to occur, $P(f_j)$, times the probability that the cause produces the effect, $P(d_i|f_j)$*. The eq. 2.3 is just the previous including the probability normalized.

Obviously, the $P(f_j|d_i)$ depends on the initial probability of the causes used in the method. However, the Bayes formula has the capability of increasing the knowledge of $P(f_j)$ as one increases the statistics in the experimental data spectrum. If one has no a priori information on the $P(f_j)$ the process of inference can be started from a uniform distribution.

The Bayes formula 2.3 provides us with a way of obtaining a better estimation of the feedings based on the measurements. This idea can be applied using the following expression, where the expected value of the feeding is named $\hat{f}_j$ and the expected value of the data as $\hat{d}_i$:

$$\hat{f}_j = \frac{1}{\sum_i R_{ij}} \sum_{i}^{n} P(f_j|d_i)\hat{d}_i \tag{2.4}$$

the index j extends from 0 up to the last bin m in the Q_β-window of the decay as shown in fig. 2.3.

Replacing the value of $P(f_j|d_i)$ given in equation 2.3 in the last expression 2.4 and making the association of $P(d_i|f_j)$ with the response matrix R_{ij} one gets:

$$f_j^{s+1} = \frac{1}{\sum_i R_{ij}} \sum_i^n \frac{R_{ij} f_j^s d_i}{\sum_k R_{ik} f_k^s} \tag{2.5}$$

In the expression 2.5 one obtains a more accurate estimation of the feeding in the s+1 iteration f_j^{s+1} from a previous estimation f_j^s by means of the data d_i and the response matrix R_{ij}.

This last expression represents the iterative method that will be used in the analysis procedure of deconvolution of the experimental TAS spectrum in order to deduce the beta feeding distribution.

2.2.2 Analysis procedure

The objective of the experiment is to obtain the B(GT) distribution over the whole Q_β of the decay. The case of interest, that is the ^{72}Kr decay, is a β^+/EC decay so the total B(GT) will have two components, namely EC and β^+.

Experimentally, one can distinguish the β^+ and EC components by using a plastic scintillator to detect the positrons coming from β^+ decay and the HPGe detector for detecting the X-rays coming from the EC component of the decay. So if one imposes the condition of detecting one positron in the plastic scintillator one can extract the TAS spectrum corresponding to the β^+ decay component and if one does the same with the X-rays of the daughter nucleus in the HPGe spectrum the TAS spectrum from the EC decay can be obtained.

Due to this capability of selecting components three different analysis can be performed:

- **Analysis of β^+ component:** if one gates the experimental TAS data with the condition of coincidence with a signal in the plastic scintillator one can select those events coming from the β^+ decay of ^{72}Kr. In reality one is not only getting events coming from this decay but also from the beta decay of the descendants: ^{72}Br, ^{72}Se and ^{72}As. The contribution from the descendants have to be removed by subtracting them once a dedicated measurement is done. Through this analysis one would end up with the feeding from the β^+ component of the decay.

- **Analysis of EC component:** by gating the TAS data with a signal of the X-rays detected in the HPGe detector only the events coming from the EC decay of ^{72}Kr are selected. This is due to the nature of the EC decay, where an atomic electron is absorbed and an X-ray is emitted after the cascade of more excited electrons to fill this vacancy occurs. Consequently, if one analyses these data one will obtain the feeding from the EC component of the decay.

- **Analysis of β^+/EC decay:** by analyzing directly the TAS spectra one will obtain the total feeding of the decay. The same result should be obtained as if one adds the feeding components extracted separately via the two previous analysis. Mathematically:

$$f(total) = f(\beta^+) + f(EC) \tag{2.6}$$

This last analysis has the added problem of the subtraction of room background contaminants apart from the decay of descendants: daughter, granddaughter and so. The room background can vary with time and it is hard to obtain a good estimation of a proper background of every measurement as a kind of time trace should be taken at regular time intervals.

These analysis are generally applicable for every β^+/EC decay but, in the case of the ^{72}Kr decay, there is an important component of conversion electrons in the de-excitation of the excited levels of ^{72}Br as it will be shown in chapter 3. If a certain level de-excites by ejecting an atomic electron instead of a gamma ray, the emission of an X-ray follows the filling of the electronic hole. This is a drawback that prevents us from using the analysis of the EC component because when we are gating on the X-rays we are not only selecting events coming from EC decay but also from β^+ decay and the electron conversion in the de- excitation of the daughter nucleus. This is the reason why this work is only going to be performed via the β^+ analysis.

2.2.2.1 Response function for β and γ radiation

The first step in the analysis is to obtain the response function of our spectrometer to the radiation connected to the decay to be studied. In our case, β radiation and the subsequent γ radiation have to be taken into account. This has to be done for the energy range covering from 0 to Q_β=5127(10) keV of our decay.

Ideally, one would obtain experimentally the response of our detection system for the β and γ radiation by emitting this radiation from the measurement point of our tape station. So we would need to produce monoenergetic β and γ radiation corresponding to the energy range 0-5127 keV in steps of 40 keV, which is the size of the energy bin chosen. This is experimentally impossible so we need to think in an alternative way of obtaining the response function.

The solution is to simulate the response function using Monte Carlo methods. It was possible to use a reliable simulation code of the experimental set-up and with the appropriate physical properties of the interactions involved in the decay one could obtain a reasonably good response function of our system. The procedure is described in detail in [Can99a].

The deposited energy by the gamma or beta radiation in the NaI(Tl) crystal is invested in liberating the so-called delta rays, which are freed electrons with enough energy to travel along the crystal producing ionization and therefore more electrons. At the end of their path this secondary electrons and all the other freed electrons produce atomic excitations in the crystal. The de- excitation of the latter emits scintillation light. The expression for the scintillation efficiency of a NaI(Tl) crystal L/E_e, which relates the energy of the delta ray E_e with the amount of scintillation light produced L, is eq. 2.7, and it is given in ref. [Pre69].

$$\frac{L}{E_e} = \frac{a_1(1 - e^{-a_2 E_e}) + a_3 E_e + a_4 E_e^2}{a_5 + a_6 E_e + a_7 E_e^2} \tag{2.7}$$

where the values of the parameters are $a_1 = 1.6(2)$, $a_2 = 0.058(8)$, $a_3 = 0.580(4)$, $a_4 = 0.00490(2)$, $a_5 = 0.25(2)$, $a_6 = 0.479(4)$, $a_7 = 0.00494(2)$.

Simulations of our experimental set-up were performed with the help of a GEANT4 code. Te geometrical model of the detector includes all the components of the TAS experimental set-up that will be detailed in the chapter 4: the "Lucrecia" Total Absorption Spectrometer with its shielding components, plastic scintillator detector for β detection, HPGe detectors

(coaxial and planar ones), transporting tape, rollers, beam pipe, etc... Every component in the set-up can affect the final response function and must be included.

The complete configuration is shown in figure 2.5 where the aluminum pieces of the TAS encapsulation have been hidden to show the ancillary detectors and components located in the hole of the TAS detector.

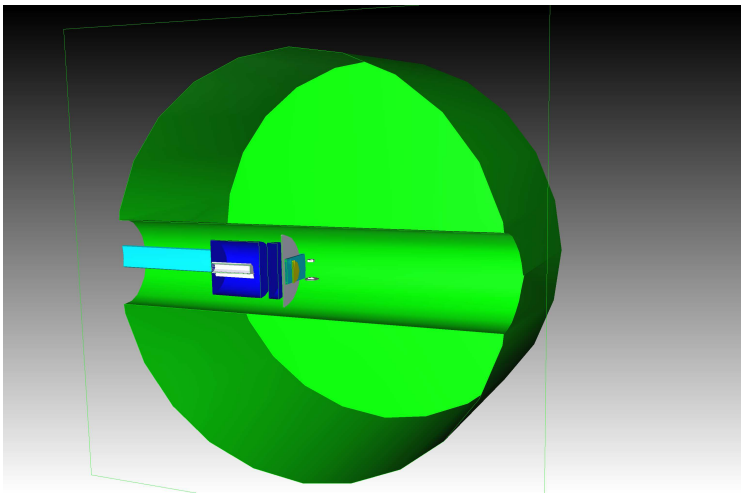

(a)

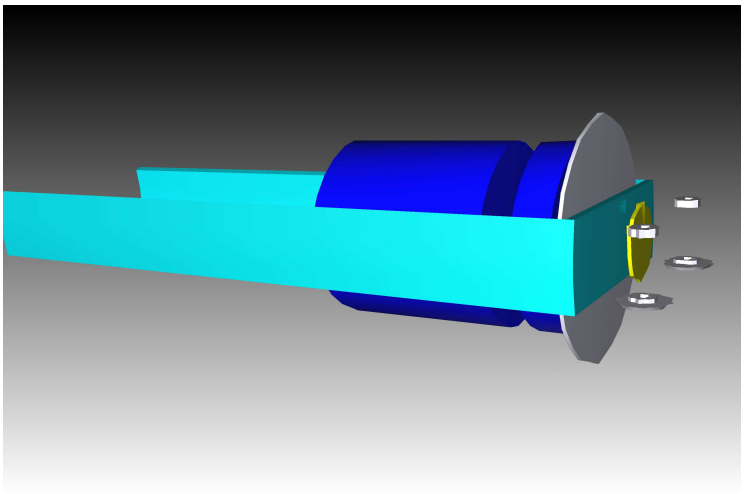

(b)

Figure 2.5: *TAS setup as included in GEANT4 simulations to obtain the response function. (a) shows a transversal section where the NaI(Tl) crystal is shown in green with the transversal hole and the ancillary detectors and other components are plotted. (b) shows a closer view of the rest of components located in the hole of the TAS detector. The HPGe telescope in blue, the beryllium window of the HPGe detector in white, the beta detector, its light guides in cyan and the rollers to guide the transport tape in white are shown.*

Before obtaining the response function one has to check that the code fairly reproduces the experimental spectra of several reference radiation sources.

For this purpose one uses standard calibration sources whose decay scheme is well known and one could compare with the simulated spectrum easily. As an example, the comparison of experimental beta gated spectra taken with a ^{24}Na source and the corresponding simulated one is shown in figure 2.6.

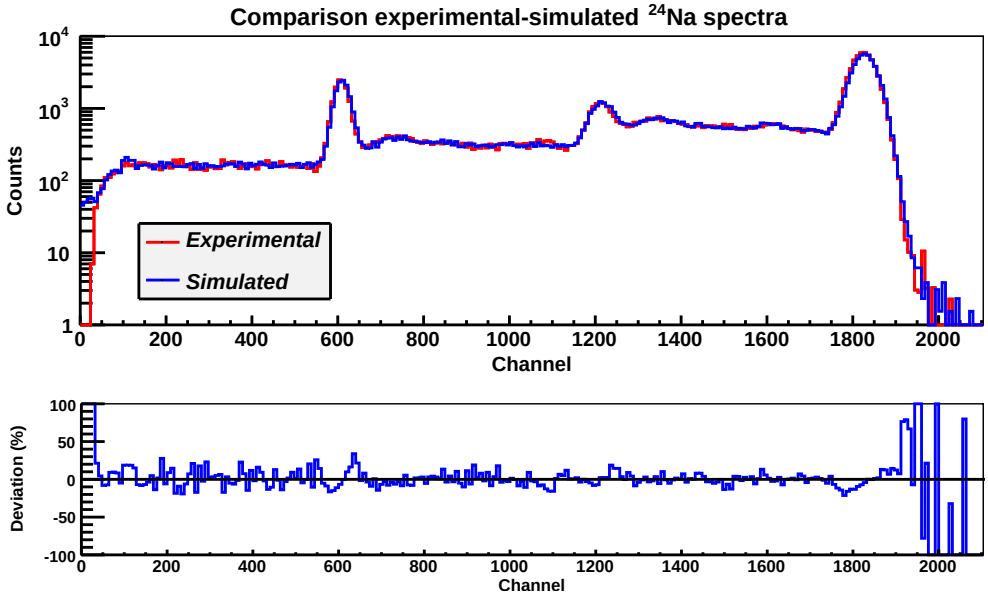

Figure 2.6: *Comparison of experimental and simulated TAS spectra corresponding to a ^{24}Na source in the upper panel and the residuals in the lower. The experimental spectrum is beta gated (coincidence condition impose with a signal in the beta detector) in order to reject all the possible background contaminations. Also, the pile-up of the measurement has been subtracted from the experimental one. The simulated spectrum has been obtained as the widening of the deposited energy by the light calibration given by equation 2.8. The deviations from experiment are quite limited in the whole energy range up to when the statistics is around 1 count and the percentage deviations are enlarged from fluctuations.*

Several considerations have to be made:

- the experimental spectrum has been obtained by imposing the coincidence condition with a signal in the beta detector to reject any background contamination.
- The pile up has been subtracted from the experimental spectrum by using the procedure described in chapter 4.
- The simulated spectrum has been widened to account for the fact that experimental resolution of the TAS detector is worse than the simulated one.

The last point is done because the simulations do not include the increase of energy resolution from to the statistical nature of the light production and its collection in the photomultiplier (pmt), of the light-to-electric signal conversion in the pmt, and the latter treatment of the signal. All these contributions could be included in the so-called **instrumental width** σ^2_{instr} which relates the simulated and experimental ones by means of the equation:

$$\sigma_{exp}^2 = \sigma_{sim}^2 + \sigma_{instr}^2 \tag{2.8}$$

The experimental width σ_{exp} is obtained from the measurements with standard calibration sources, as ^{137}Cs, ^{60}Co, etc... The simulated width σ_{sim} is taken from the simulations of the same standard calibration sources. Then, a fit between both set of data gives us the resulting instrumental width as its difference for each transition.

The result for our decay data is a set of response spectra for gamma radiation in the energy range from 0 till the Q_{EC} of the decay and a set of responses for positrons in the same energy range in steps of 40 keV (same as bin width of the analysis). As an example, figure 2.7 shows two examples of these sets of responses, the figure 2.7(b) shows the response for a gamma radiation of 3 MeV while the figure 2.7(a) is the response to positrons of 1 MeV of kinetic energy.

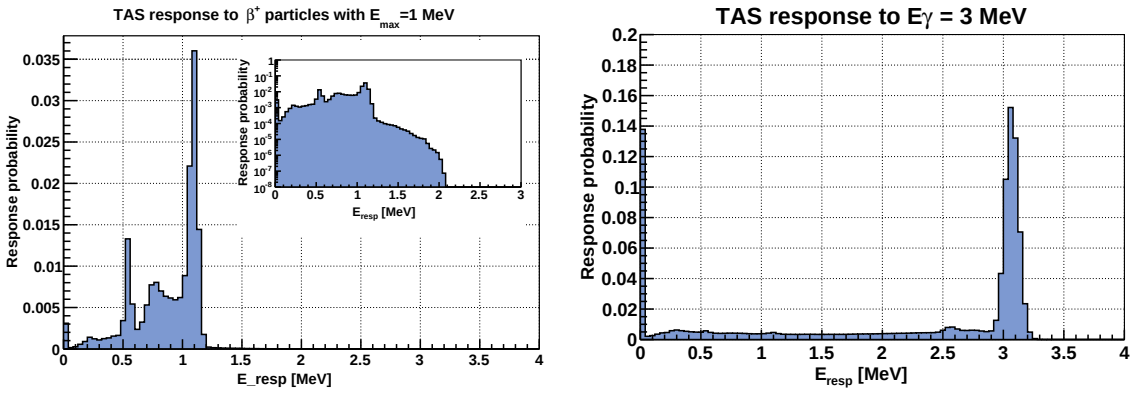

(a) (b)

Figure 2.7: *Response functions of TAS detector to (a) positrons of E_{max}=1 MeV and (b) E_γ= 3 MeV. The inset of figure (a) shows the same spectrum in logarithmic scale to show the higher energy tail of the distribution that in linear scale is not visible and is due mainly to bremsstrahlung of the positron while it stops. Counts in channel number 0 in both spectra represent those events depositing less than 40 keV, which mainly are the events not interacting and depositing an energy 0.*

2.2.2.2 Branching Ratio Matrix

Once one knows how the TAS detector responses to general β and γ radiation, the next step is preparing a matrix with the information of the decay scheme of the decay daughter. This is done in order to find out the energy and type of radiation involved in the decay of each single ^{72}Kr nucleus.

As it is shown in figure 2.8 if the decay of the parent nucleus feeds one excited state located at E_2 (MeV) of excitation energy, we need to know all the possible gamma de-excitation paths with its branching ratios. In this example, level at E_2 can de-excite by means of two different paths:

- One, it has a probability of BR1 (%) to reach the ground state in the daughter nucleus by emitting a γ-ray of energy E_2.

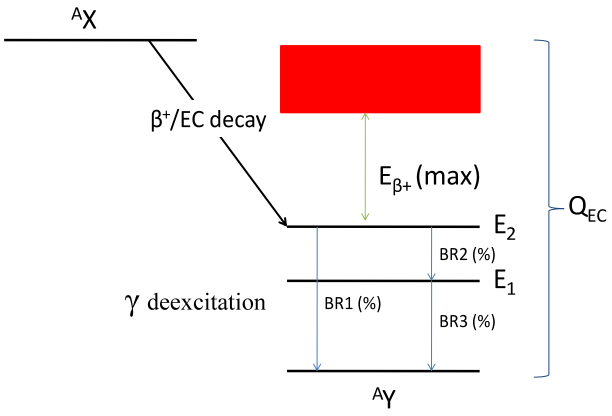

Figure 2.8: *Schematic example of a β^+/EC decay. Once the β decay or electron capture occurs one excited state is fed (in the picture, level at E_2 of excitation energy). The de-excitation from this level can occur following different paths, such as the emission of a γ radiation of E_γ=E_2 to reach the ground state or the emission of a γ radiation of E_γ=E_2-E_1. Each of this two paths occurs with a probability given by a branching ratio BR1 and BR2 respectively. The Branching Ratio Matrix includes all the possible γ transitions with their branching ratio.*

- Second, it will de-excite through the emission of a γ ray of energy E_2-E_1 and reaching the level at E_1 of excitation energy. This occurs with a probability of BR2 (%) and following this radiation it will emit another γ ray of energy E_1 in order to reach the ground state.

In summary, in both cases, and considering a β^+ decay, it would be emitted a positron with an energy given by the Fermi distribution with an endpoint of Q_{EC}-E_2. In addition to the positron, in the case of the de-excitation through the first path it would emit a γ radiation of energy E_2 and in the second case, it would emit two γ radiations of energies E_2-E_1 and E_1.

The response of our detector to these two different de-excitation paths would be different and this is the reason why we need to include in our analysis the Branching Ratio Matrix.

The previous is just a simple example to visualize which is the procedure. However, the real situation is much more complex as usually there are more possible paths to de-excite through 1 direct transition to the ground state, 2 transitions, 3 or even more transitions to reach the ground state.

Additionally, one should be aware of the conversion electron (CE) process that is present in the decay of interest in competition with the mentioned gamma de-excitation process. The TAS detector is not sensitive to low-energy conversion electrons (where the probability of conversion electrons is maximum as for high energy transitions is very unlikely the process to occur) so one has to include the intensity going by CE. This is done by including the experimental conversion coefficients, that will be measured via the experiment described in chapter 3 and whose results are included in the chapter 5, in the response matrix. Thus, one considers in the response that the total intensity of every transition in the branching ratio is multiplied by (1+α_T). Later this aspect will be explained more in detail.

The information required is the excitation energy of each level, spin and parity of the level and the branching ratios of the different decay paths from every level. The ideal case considers that the whole level scheme of our decay daughter is well known. The problem is

that in our case, despite there are some spectroscopy studies of the level scheme of ^{72}Br (as it was shown before), the knowledge of the level scheme is not complete. In such a case, the best way to proceed is to separate the level scheme in two parts, the known part of the level scheme, where discrete levels with the available information on its spin-parities, excitation energy, branching ratios for the de-excitation to lower levels and the corresponding conversion coefficients (if known) are included, and the unknown part of the level scheme with a set of unknown averaged levels at higher energies are located.

Known part of ^{72}Br level scheme

The current knowledge on the ^{72}Kr level scheme can be found in the reference [Piq03] or in the more recent Nuclear Data Sheets compilation for mass A=72: [Abr10]. The low energy part is shown in figure 2.9.

The list of levels coming from these references is shown in table 2.1. It includes the needed information in this analysis: excitation energy, spin and parity of each level, and the energy, branching ratio and conversion coefficient for every de-excitation radiation starting at this level.

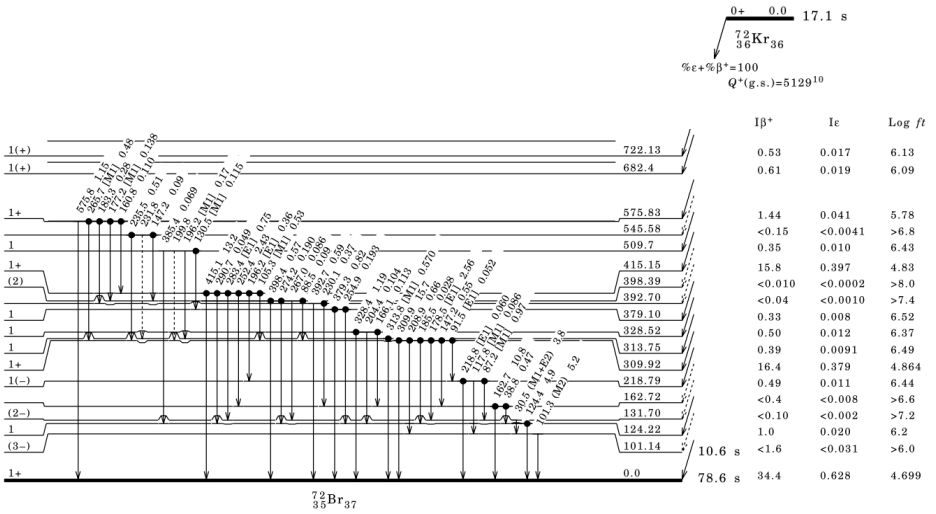

Figure 2.9: *Low energy region of ^{72}Br level scheme taken from [Abr10] which is a compilation of the information for A=72. The original work is the spectroscopy study of the ^{72}Kr decay performed by I. Piqueras et al. [Piq03].*

Table 2.1: *List of levels and gamma transitions in ^{72}Br from the beta decay study of ^{72}Kr in ref. [Piq03]. The information displayed is the energy of each level, its Spin and Parity (if known), all the gamma transitions starting at every level with their branching ratio (%) and the conversion coefficient (if provided in ref. [Piq03]).*

E_{level} (keV)	Spin	Parity	E_γ	Branching Ratio (%)	Conv. Coeff. (α)
0.0	1.0	+1.0	0.0	0.0	0.00
101.3	1.0	-1.0	101.3 (3)	100.0	1.145
124.4	1.0		124.4 (2)	100.0	0.06332
131.8	2.0	-1.0	30.5(5)	100.0	30.0
162.8			38.8 (2)	4.2	0.00
162.8			162.7 (1)	95.8	0.00
218.9			87.2 (5)	86.8	0.167
218.9			117.8 (5)	7.8	0.0733
218.9			218.8(5)	5.4	0.00
310.0	1.0	+1.0	91.5(5)	0.3	0.1102
310.0	1.0	+1.0	147.2(1)	2.8	0.00
310.0	1.0	+1.0	178.5(5)	13.1	0.01519
310.0	1.0	+1.0	185.5(7)	0.1	0.00
310.0	1.0	+1.0	208.9(3)	3.4	0.00
310.0	1.0	+1.0	309.9(1)	80.3	0.00
313.8	1.0		313.8(3)	100.0	0.00
328.6	1.0		166.1(7)	8.0	0.00
328.6	1.0		204.4(2)	7.3	0.00
328.6	1.0		328.4(2)	84.6	0.00
379.3	1.0		254.9(5)	19.0	0.00
379.3	1.0		379.3(5)	81.0	0.00
392.8			230.1(3)	38.8	0.00
392.8			392.7(2)	61.2	0.00
398.5	2.0	+1.0	88.5(5)	9.5	0.00
398.5	2.0	+1.0	267.0(5)	9.3	0.00
398.5	2.0	+1.0	274.2(3)	20.4	0.00
398.5	2.0	+1.0	398.4(2)	60.8	0.00
415.2	1.0	+1.0	105.3(1)	3.1	0.0995
415.2	1.0	+1.0	196.2(5)	2.1	0.01152
415.2	1.0	+1.0	252.4(2)	14.1	0.00
415.2	1.0	+1.0	283.4(4)	4.4	0.00
415.2	1.0	+1.0	290.7(4)	0.3	0.00
415.2	1.0	+1.0	415.1(2)	76.0	0.00
509.9	1.0		130.5(5)	32.1	0.0557
509.9	1.0		196.2(5)	48.6	0.0191
509.9	1.0		385.4(5)	19.3	0.00
545.7			147.2(1)	15.6	0.00
545.7			235.5(4)	84.4	0.00
575.9	1.0	+1.0	160.8(6)	5.1	0.00
575.9	1.0	+1.0	177.2(5)	6.4	0.0248
575.9	1.0	+1.0	183.3(5)	13.1	0.00
575.9	1.0	+1.0	265.7(2)	22.3	0.00
575.9	1.0	+1.0	575.8(4)	53.1	0.00
577.0	1.0	+1.0	414.5(5)	48.0	0.00
577.0	1.0	+1.0	452.3(3)	5.4	0.00
577.0	1.0	+1.0	576.9(4)	46.6	0.00

Continued on next page

Table 2.1 – continued from previous page

E_{level} (keV)	Spin	Parity	E_γ	Branching Ratio (%)	Conv. Coeff. (α)
682.5	1.0	+1.0	519.5(5)	50.1	0.00
682.5	1.0	+1.0	682.5(5)	49.9	0.00
708.3	1.0	+1.0	132.5(5)	6.1	0.00
708.3	1.0	+1.0	379.3(5)	3.4	0.00
708.3	1.0	+1.0	489.2(5)	6.2	0.00
708.3	1.0	+1.0	545.3(3)	28.6	0.00
708.3	1.0	+1.0	583.3(5)	21.5	0.00
708.3	1.0	+1.0	708.0(3)	34.1	0.00
722.2	1.0	+1.0	146.2(4)	2.0	0.00
722.2	1.0	+1.0	307.0(5)	16.2	0.00
722.2	1.0	+1.0	412.1(2)	33.0	0.00
722.2	1.0	+1.0	559.7(4)	42.3	0.00
722.2	1.0	+1.0	722.3(4)	6.5	0.00
755.7	1.0	+1.0	427.1(3)	4.9	0.00
755.7	1.0	+1.0	631.3(5)	21.2	0.00
755.7	1.0	+1.0	755.5(4)	73.9	0.00
796.1			380.8(2)	34.5	0.00
796.1			485.9(5)	25.2	0.00
796.1			633.5(5)	25.3	0.00
796.1			671.7(5)	7.0	0.00
796.1			795.7(5)	8.0	0.00
902.3	1.0	+1.0	356.3(5)	5.6	0.00
902.3	1.0	+1.0	504.0(7)	19.1	0.00
902.3	1.0	+1.0	592.5(4)	4.1	0.00
902.3	1.0	+1.0	777.5(5)	23.8	0.00
902.3	1.0	+1.0	901.9(5)	47.3	0.00
939.5	1.0	+1.0	541.1(5)	7.3	0.00
939.5	1.0	+1.0	546.7(5)	7.8	0.00
939.5	1.0	+1.0	610.4(4)	5.5	0.00
939.5	1.0	+1.0	815.1(2)	22.2	0.00
939.5	1.0	+1.0	939.2(3)	57.2	0.00
1027.9	1.0	+1.0	451.4(5)	9.7	0.00
1027.9	1.0	+1.0	482.5(5)	7.8	0.00
1027.9	1.0	+1.0	629.8(5)	8.1	0.00
1027.9	1.0	+1.0	635.2(5)	37.5	0.00
1027.9	1.0	+1.0	648.8(5)	9.7	0.00
1027.9	1.0	+1.0	699.5(5)	13.9	0.00
1027.9	1.0	+1.0	865.3(5)	5.2	0.00
1027.9	1.0	+1.0	1027.7(5)	8.2	0.00
1154.30	1.0		739.2(3)	47.0	0.00
1154.30	1.0		844.5(5)	42.7	0.00
1154.30	1.0		991.2(5)	10.3	0.00
1173.2	1.0	+1.0	774.5(8)	23.9	0.00
1173.2	1.0	+1.0	844.5(5)	31.5	0.00
1173.2	1.0	+1.0	954.6(5)	44.6	0.00
1323.0	1.0	+1.0	994.3(5)	45.9	0.00
1323.0	1.0	+1.0	1160.1(5)	54.1	0.00
1386.08	1.0	+1.0	484.7(5)	21.9	0.00
1386.08	1.0	+1.0	590.6(5)	19.5	0.00

Continued on next page

Table 2.1 – continued from previous page

E_{level} (keV)	Spin	Parity	E_γ	Branching Ratio (%)	Conv. Coeff. (α)
1386.08	1.0	+1.0	810.1(2)	13.0	0.00
1386.08	1.0	+1.0	840.3(5)	15.7	0.00
1386.08	1.0	+1.0	1058.0(5)	15.4	0.00
1386.08	1.0	+1.0	1076.0(5)	5.0	0.00
1386.08	1.0	+1.0	1167.1(5)	1.0	0.00
1386.08	1.0	+1.0	1386.0(4)	8.4	0.00
1605.0	1.0	+1.0	1029.0(2)	39.9	0.00
1605.0	1.0	+1.0	1441.9(7)	4.5	0.00
1605.0	1.0	+1.0	1481.3(5)	27.0	0.00
1605.0	1.0	+1.0	1605.1(6)	28.6	0.00
1704.1	1.0	+1.0	801.7(5)	35.4	0.00
1704.1	1.0	+1.0	908.0(7)	55.6	0.00
1704.1	1.0	+1.0	1541.0(7)	9.0	0.00
1772.3	1.0	+1.0	617.9(3)	8.0	0.00
1772.3	1.0	+1.0	869.9(5)	5.1	0.00
1772.3	1.0	+1.0	976.6(5)	23.8	0.00
1772.3	1.0	+1.0	1049.9(6)	19.6	0.00
1772.3	1.0	+1.0	1373.3(5)	8.3	0.00
1772.3	1.0	+1.0	1392.6(5)	8.1	0.00
1772.3	1.0	+1.0	1609.2(6)	11.7	0.00
1772.3	1.0	+1.0	1648.0(7)	13.7	0.00
1772.3	1.0	+1.0	1771.9(6)	1.7	0.00
1799.6	1.0	+1.0	1222.4(7)	21.4	0.00
1799.6	1.0	+1.0	1636.9(5)	27.8	0.00
1799.6	1.0	+1.0	1675.0(6)	39.5	0.00
1799.6	1.0	+1.0	1799.6(6)	11.3	0.00
1835.7	1.0	+1.0	1039.5(3)	39.4	0.00
1835.7	1.0	+1.0	1457.0(5)	20.8	0.00
1835.7	1.0	+1.0	1672.7(4)	5.0	0.00
1835.7	1.0	+1.0	1711.2(3)	32.0	0.00
1835.7	1.0	+1.0	1835.8(6)	2.8	0.00
1943.5	1.0	+1.0	1943.5(7)	100.	0.00
1950.0	1.0	+1.0	1950.0(7)	100.	0.00
1988.4	1.0	+1.0	1988.4(10)	100.	0.00
3304.9	1.0	+1.0	3304.8(10)	100.	0.00

Unknown part of ^{72}Br level scheme

The knowledge on the ^{72}Br level scheme up to 2 MeV of excitation energy is quite detailed as it is shown in table 2.1. However, from this energy up to the Q_{EC}= 5127 keV, there is no available information on level positions (except for one isolated level at 3304.9 keV), spin and parities as well as branching ratios in the de-excitation path of these levels.

In order to overcome this lack of information one turns to statistical models. These describe average properties of the nucleus such as level densities for the placement of the excited levels and gamma strength functions for the description of the de-excitation pattern.

The present procedure is explained in detail in ref. [Tai07b].

Excited levels

The level density functional is used for the description of the excited levels including their spin, parity and excitation energy. The back-shifted Fermi gas model formula given in [Dil73] is chosen to fit the number of excited levels in ^{72}Br and, in this way, be able to deduce the position of the excited levels in the decay scheme. It can be mathematically expressed as eq. 2.10 the spin-dependent expression and 2.11 for total level density.

$$\rho(J,\pi,E_{exc}) = \rho(J,\pi)\rho(E_x) \tag{2.9}$$

$$\rho(E_{exc},J) = \frac{1}{24\sqrt{2}} \cdot \frac{2J+1}{\sigma^3 a^{1/4}} \cdot \frac{e^{2[a(E_{exc}-\Delta)]^{1/2}-J(J+1)/2\sigma^2}}{(E_{exc}-\Delta+t)^{5/4}} \tag{2.10}$$

$$\rho(E_{exc}) = \frac{1}{12\sqrt{2}} \cdot \frac{1}{\sigma a^{1/4}} \cdot \frac{e^{2[a(E_{exc}-\Delta)]^{1/2}}}{(E_{exc}-\Delta+t)^{5/4}} \tag{2.11}$$

where Δ and a are the parameters to be fitted to reproduce the data corresponding to the number of levels up to a certain excitation energy level that for our case are given in table 2.2, and E_{exc} is the excitation energy, σ is the spin cut-off parameter calculated as $\sigma^2 = 0.0150 \cdot A^{5/3} \cdot t$ and t is the thermodynamic temperature which can be obtained from: $E_{exc} - \Delta = at^2 - t$.

The number of accumulated number of levels for the ^{72}Br case: A=72 and Z=35 obtained via Hartree-Fock BCS calculations as described in [Gor01] [Dem01] can be accessed via the web [Bel]. Thus, the number of levels up to a certain value of excitation energy in ^{72}Br are obtained, see table 2.2.

E_{exc} (MeV)	N (accum)
0.5	7
2.0	124
5.0	6940

Table 2.2: *Accumulated number of levels for different values of the excitation energy in the nucleus ^{72}Br obtained from the web [Bel] which are based in the microscopic statistical model described in [Gor01] and [Dem01].*

The result of the fit of data in table 2.2 to eq. 2.11, provide us with the following values for the fitting parameters a and Δ:

$$a = 10.697 \tag{2.12}$$

$$\Delta = -0.839 \text{ MeV} \tag{2.13}$$

The placement of the levels is done by assuming that the level are spaced following the Wigner distribution 2.14:

$$P_W(x) = \frac{1}{2}\pi x e^{-\pi x^2/4} \tag{2.14}$$

where $x = d/\langle d \rangle$ and the value of $\langle d \rangle$ is obtained by solving:

$$1 = \int_{E_{prev}}^{E_{prev}+\langle d \rangle} \rho(J,\pi,E_x) dE_x \tag{2.15}$$

note as E_{prev} refers to the excitation energy of the previously placed level.

Thus, levels are placed in the unknown part of the level scheme following the density functional. To check the sensitivity of the analysis to different level schemes, two different analysis will be performed and compared: one considering the limit of the known scheme at 1 MeV and another moving this limit up to 2 MeV.

Branching ratios for de-excitation of each level

The next step is to determine the branching ratios of the de-excitation path starting at each of the previous levels defined by the statistical model. In order to do this, one can use gamma-ray strength functions which characterize the average electromagnetic properties of excited nuclei. The Giant Dipole Resonance (GDR) model is useful for this purpose as it is explained in [Kop90]. Only E1, M1 and E2 transition multipolarities are considered in our analysis.

The average γ radiation width $\langle\Gamma_\gamma\rangle$ from a level of spin-parity J^π located at excitation energy E_x to levels located in a energy interval $E - E + \Delta E$ is given as:

$$\langle\Gamma_\gamma\rangle = \frac{1}{\rho(J,\pi,E_x)} \sum_{XL} \sum_{J_f^{\pi_f}} \int_{E_x-E-\Delta E}^{E_x-E} E_\gamma^{2L+1} \cdot f_{XL}(E_\gamma) \times \rho(J_f,\pi_f,E_x-E_\gamma) dE_\gamma \tag{2.16}$$

where X is a generic notation of the character electric ($X = E$) or magnetic ($X = M$) of the transition, L is the multipolarity of the transition, E_γ is the energy of the latter, $\rho(J,\pi,E_x)$ is the level density given by eq. 2.11 with the value of the parameters in expressions 2.12, $J_f^{\pi_f}$ is the spin-parity of the final level and $f_{XL}(E_\gamma)$ is the corresponding strength function for this transition defined as is shown next.

For the dominant E1 mode two resonances each one with generalized Lorentzian shape are used while for M1 and E2 resonances a Lorentzian shape is considered [Kop90]. Their mathematical expressions are:

$$f_{E1}(E_\gamma,T) = 8.68\times10^{-8}\cdot\sigma_r\Gamma_r \times \left(\frac{E_\gamma\Gamma(E_\gamma)}{(E_\gamma^2-E_r^2)^2+E_\gamma^2\Gamma(E_\gamma)^2} + \frac{2.8\pi^2T^2\Gamma_r}{E_r^5}\right) \tag{2.17}$$

$$f_{M1}(E_\gamma) = 8.68\times10^{-8}\frac{\sigma_r E_\gamma\Gamma_r^2}{(E_\gamma^2-E_r^2)^2+E_\gamma^2\Gamma_r^2} \tag{2.18}$$

$$f_{E2}(E_\gamma) = 5.22\times10^{-8}\frac{\sigma_r E_\gamma^{-1}\Gamma_r^2}{(E_\gamma^2-E_r^2)^2+E_\gamma^2\Gamma_r^2} \tag{2.19}$$

where E_r (MeV), Γ_r (MeV) and σ_r (mb) are the resonance parameters which are given next. T is the nuclear temperature defined as $T = \sqrt{B_n - E_\gamma/a}$ including B_n, which is the neutron binding energy (B_n=10.1 MeV for ^{72}Br [Abr10]) and a is the Fermi gas level density parameter found to be 10.77 as given in eq. 2.12. $\Gamma(E_\gamma)$ can be written as:

$$\Gamma(E_\gamma) = \Gamma\frac{E_\gamma^2+4\pi^2T^2}{E_r^2} \tag{2.20}$$

The values of E_r, Γ_r and σ_r are obtained from the global systematics that can be found at RIPL database [kfa]:

E1:
E_r =22.610241 MeV Γ_r=10.039134 MeV σ_r=82.126938 mb
E_r =15.839375 MeV Γ_r=5.0871310 MeV σ_r=162.07236 mb

M1:
E_r=9.8694315 MeV Γ_r=4.0 MeV σ_r=9.5751619 mb

E2:
E_r=15.165224 MeV Γ_r=5.2460003 MeV σ_r=1.9391215 mb

Here, two E1 giant resonances were taken into account as we are dealing with a deformed nucleus (^{72}Br) and the systematics for these cases requires the use of two resonances [kfa]. The quadrupole deformation parameter β_2 of the daughter nucleus, ^{72}Br, is required to deduce the giant resonance parameters for E1 resonances. The value of β_2 has been obtained from theoretical predictions [Mö95] resulting $\beta_2 = -0.333$.

Expressions 2.17, 2.18 and 2.19 give the branching ratio of a transition of energy E_γ connecting two excited levels in the unknown part of the level scheme or a level in the unknown part with one in the known part given by the table 2.1.

This is the way on how we estimate the position of the levels and the gamma de-excitation branching ratios of the unknown part of the level scheme. With all this information one is able of building the whole level scheme of the daughter nucleus including known and guessed levels together with their de-excitation branching ratios.

The **Branching Ratio Matrix** is just a way of collecting all this information in a Matrix where the levels are placed in excitation energy, which is usually divided in 40 keV width bins, and the branching ratios tells how a certain bin is de-excites.

2.2.2.3 Response Matrix

The next step in the analysis is to construct the Response Matrix of the TAS detector to the decay of interest. For this, one needs the response function of the detector to the individual types of radiation involved in the decay. These particles include positrons coming from the beta decay in our case and the gamma radiation following the decay in order the daughter nucleus to de-excites till its ground state. Also the Branching Ratio Matrix is needed as it is shown next.

The Response Matrix R_j is calculated as the addition of the response to positrons, e_j, only in the case of β^+ decay, and the response to the cascade of gamma radiation from the fed level to reach the ground state, r_j.

$$R_j = e_j \otimes r_j \tag{2.21}$$

The response to positrons, e_j, has to be included in the response matrix only in β^+ decay as in EC decay no positron is emitted. The endpoint energy of the positron is E_{e^+} when the fed level is the $j-th$, as shown in fig. 2.3 indicated with a green brace.

The response to the de-excitation cascade, r_j, is obtained as the convolution of the branching ratio matrix b_{jk} which tells the path followed from the initial state till the ground state, and the response to gamma radiation, g_{jk}, of the energy given as the energy difference between levels j and k:

$$r_j = \sum_{k=1}^{k=j-1} b_{jk} g_{jk} \otimes r_k \tag{2.22}$$

where k extends from bin number 1 (ground state) up to the bin lower than the fed level j, as can be graphically seen in fig. 2.3.

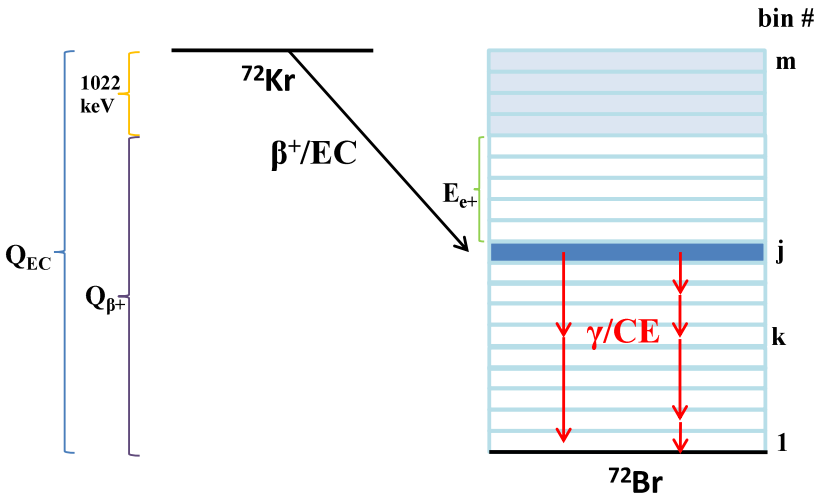

Figure 2.3: *Discretized level scheme of the daughter nucleus, ^{72}Br for the TAS data analysis. The bin width was chosen as 40 keV in the analysis for both, the level scheme, f_j and the experimental spectrum d_i. The decay scheme extends up to the Q_{EC}=5127 keV of the decay of interest.*

In order to include the conversion electron intensities in the de-excitation cascade, the g_{jk} components have to be modified including the conversion coefficient, α_{jk}, of the transition from level j to k:

$$g_{jk} \rightarrow \frac{1}{1+\alpha_{jk}} g_{jk} + \frac{\alpha_{jk}}{1+\alpha_{jk}} I \tag{2.23}$$

where I is the identity matrix. In this step, the assumption that conversion electron and X-ray/Auger electron emitted in the conversion electron process do not penetrate the TAS sensitive material and, consequently those responses are not included. This assumption is valid as the energy of this radiation is quite low and the encapsulation material of TAS detector and beam-pipe described in chapter 4 can easily absorb them.

Fig. 2.11(b) shows the response of the TAS detector to an event of β^+ decay of ^{72}Kr which directly feeds a level located at excitation energy in the energy range 3000-3040 keV (bin number 75). This figure shows how the TAS spectrum looks like for the mentioned event of decay. Obviously, this is a probability distribution so the contribution to the spectrum would be just one count calculated as a random number following this distribution law. Anyway, for a high statistics measurement one would obtain a spectrum with exactly the shape shown in Fig. 2.11(b) if only one level at 3 MeV excitation energy in the daughter nucleus is fed.

The generalization of the previous figure for feeding at all the possible final states in ^{72}Br gives as a result the Response Matrix to the decay of interest. Fig. 2.11(a) shows the Response Matrix of the "Lucrecia" TAS spectrometer calculated for the decay of interest, ^{72}Kr β^+ decay, in a 2-dimensional plot. It consists of the plot of the probability distribution of contributing a given channel in the experimental spectrum when a certain level of ^{72}Br is fed via the decay.

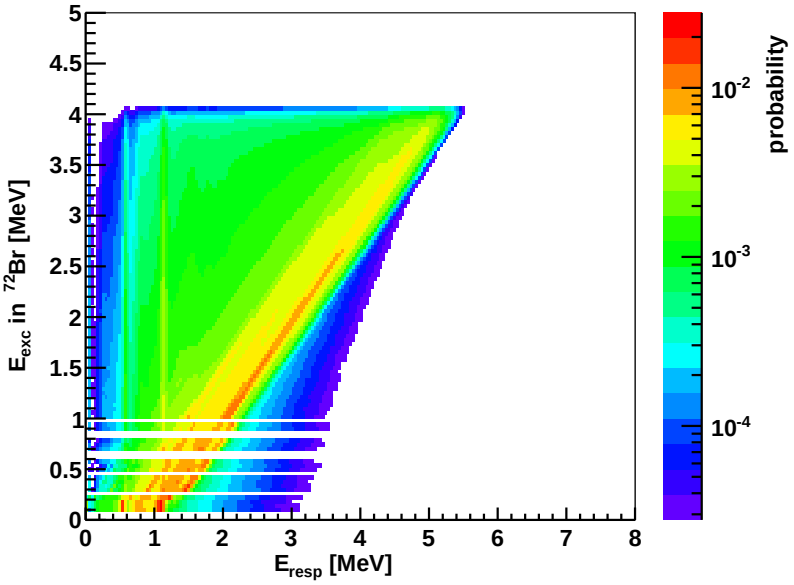

(a)

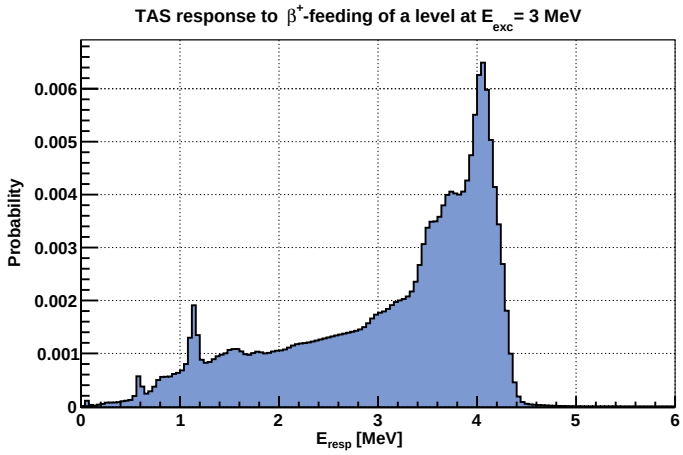

(b)

Figure 2.11: *(a) Bi-dimensional plot of the Response Matrix of the "Lucrecia" TAS spectrometer to the β^+ decay of ^{72}Kr. The probability distribution is plotted versus excitation energy in ^{72}Br and the response energy in the TAS detector. Note that the Z-axis is plot in logarithmic scale (b) shows a projection of the matrix corresponding to β-feeding to a level located at E_{exc}=3 MeV. This is the convolution of responses to 1 MeV positrons 2.7(a) and the γ de-excitation of the level at E_{exc} = 3 MeV.*

2.2.2.4 Contaminants subtraction

Contaminants is the usual way we call to all the contributions to the spectra not coming from the beta decay of interest, in this case β^+/EC decay of ^{72}Kr. The main contributions as contaminants are the decay of descendants: daughter, granddaughter, etc..., as already commented and the background radiation and the contribution of pile up signals of our detection system.

The followed procedure will explained in detail in section 4.2.2.1. The aim of this subtraction is to obtain a clean spectrum containing only contribution coming from the decay of interest. Thus, one can proceed with the deconvolution of the spectrum in order to find the feeding distribution.

2.2.2.5 Deconvolution of spectra through the EM algorithm

The deconvolution of the experimental spectra is the task of solving the inverse problem already presented and whose mathematical expression is given in eq. 2.1. As it was already explained in section 2.2.1, the way of solving this equation system is to use the Expectation-Maximization (EM) algorithm. This is a quickly convergent algorithm that, as we will see later, provides with good likelihood fits after few iterations.

The iterative expression that relates the feeding to a certain bin is given by the expression 2.5 for the iteration $s+1$.

$$f_j^{s+1} = \frac{1}{\sum_i R_{ij}} \sum_i^n \frac{R_{ij} f_j^s d_i}{\sum_k R_{ik} f_k^s} \tag{2.5}$$

where s extends up to an aimed χ^2 value or after a certain number of iterations as it will be explained in chapter 4.

The result of this deconvolution process would be a feeding distribution at each bin j in the energy range from 0 up to the Q_{EC} of the decay.

2.3 ISOLDE facility

Once we know the procedure of analyzing the TAS data is presented, the next section is devoted to describe the facility where the experiment was carried out and how the ^{72}Kr beam was produced and lead to our experimental setup. This procedure is the same for both experiments, the conversion electron study and the TAS measurement as they both were performed at the ISOLDE facility at CERN. The only difference between both experiments from the facility point of view was that the location of the experimental setup was different in both cases and the beam transport had to be performed through different beam lines, see figure 2.12.

2.3.1 Description of the facility

The experiments were performed at the ISOLDE (Isotope Separation On-Line DEvice) facility one of the experiments of the CERN facilities. These are located in the outskirts of the city of Geneva (Switzerland) right at the border between Switzerland and France.

A general overview of the ISOLDE facility is shown in figure 2.12. The 1.4 GeV proton beam coming from the Proton Synchrotron (PS) Booster accelerator is directed towards two different target stations: the so-called General Purpose Separator (GPS) or the High Resolution Separator (HRS) target depending on which mass separator will be used in the experiment.

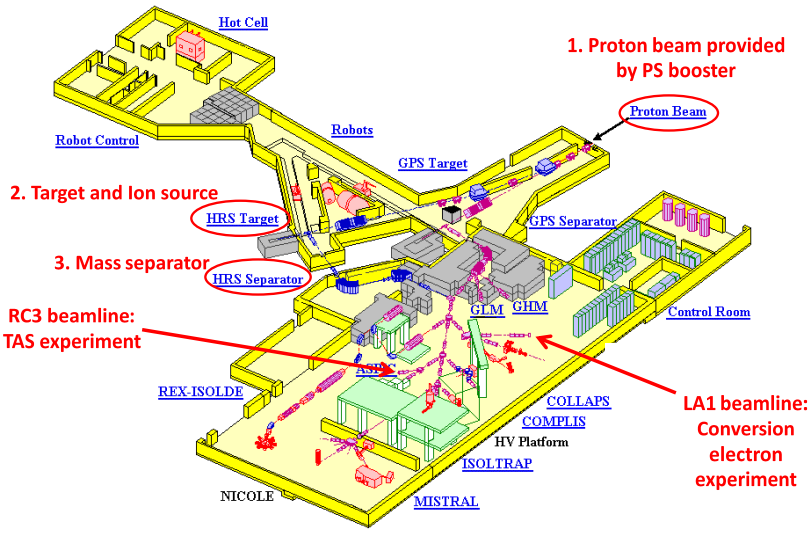

Figure 2.12: *General overview of the ISOLDE facility. The main components involved in the beam preparation and leading to our experimental set-ups are indicated in red. The incoming direction of proton beam is indicated, the position of the Target plus Ion Source and the HRS mass separator are marked in red. The location of the experimental set-ups for the two experiments, the conversion electron experiment described in chapter 3 was performed at LA1 beamline, and the Total Absorption Spectroscopy experiment described in chapter 4 was located at the TAS beamline.*

The method to produce exotic beams at ISOLDE is the so-called Isotope Separation On-Line technique (ISOL) which gives the name to the facility. In this method, a proton beam of maximum intensity of 2 μA coming from the PS-Booster of CERN facility at E = 1.4 GeV im-

pinges on a heavy target at ISOLDE. This target is coupled to an ion source to produce ionized fragments via chemical procedures. Later, a mass separator is used to select the nucleus of interest from the wide variety of nuclei that can be produced at ISOLDE. In particular, more than 600 isotopes of almost 70 elements (Z=2 to 88) have been produced at ISOLDE at intensities up to 10^{11} atoms per μA proton beam.

2.3.2 Production of ^{72}Kr beam

The proton beam from the Proton Synchrotron Booster (PS-Booster) is a 1.2 s periodic pulsed beam of an intensity of the order of 3×10^{13} protons per pulse (ppp) with a beam energy of 1.4 GeV. The maximum average intensity of the beam is 2 μA. Every proton pulse has an internal structure due to the way of operation of PS-Booster.

As can be seen in figure 2.13 where the whole CERN accelerator complex is represented, the initial proton beam from LINAC2 (plotted in pink) is accelerated in the Booster up to 1.4 GeV and then the resulting proton beam can be lead either towards the Proton Synchrotron for further acceleration processes or towards the ISOLDE facility, which is the case of these experiments.

The Booster is composed by 4 Synchrotron rings which provide 4 different proton pulses which all together form the proton beam provided by the PS-Booster. These four pulses are separated by 120 ns gap and the duration of each pulse is 230 ns. This means that the PS-Booster output beam has a total duration of 1.28 μs.

The repetition period of the Booster proton beam is 1.2 seconds meaning that every 1.2 seconds one proton beam is ejected from the Booster. There is a higher level structure called Super-Cycle, which includes a certain number of proton pulses provided by the Booster that can vary depending on the demand of proton pulses by the other users, that is the LHC experiments, n-TOF facility, etc... In the time when the data analysed here was taken, the Super-Cycle consisted of 12 proton pulses for the TAS measurement and 28 pulses for the conversion electron spectroscopy measurement, which means that the duration of the Super-Cycle was 14.4 and 33.6 seconds respectively.

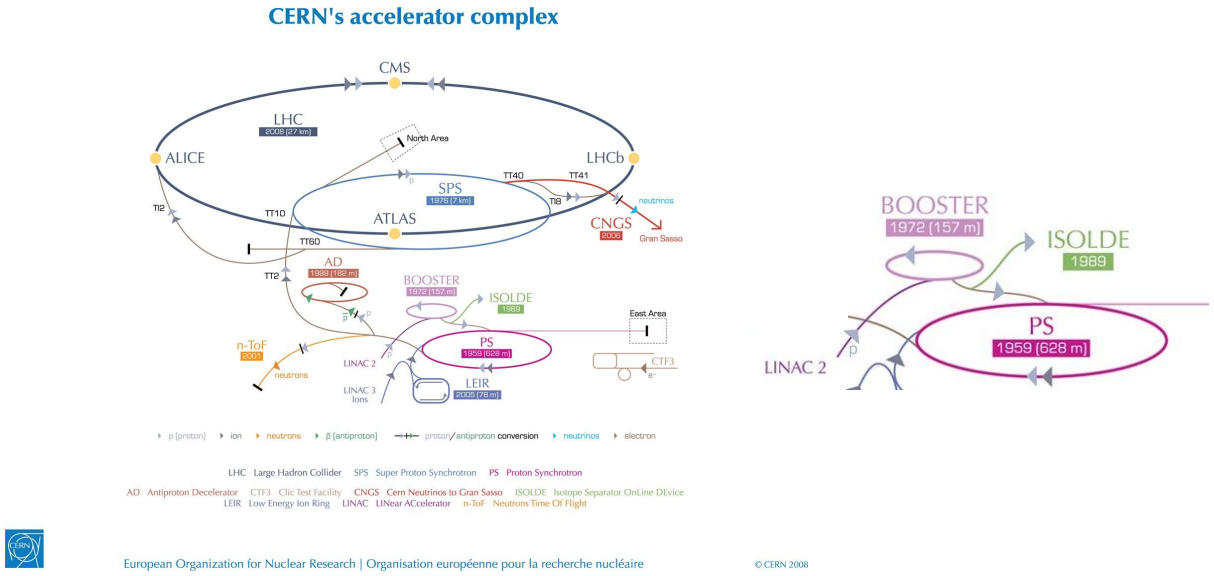

Figure 2.13: *Full CERN accelerator complex as it was in 2008 and the region related with ISOLDE is expanded at the right side to better observe it. The proton beam from LINAC2 (pink) is accelerated in the Booster synchrotron up to 1.4 GeV of energy. Then, this proton beam is directed towards the ISOLDE facility where it is used to imping on a heavy target.*

In general, the 1.4 GeV proton beam impinges on a thick heavy target at the ISOLDE facility. When it impacts on the target, most of the cases uranium carbide (UC_x) with a big amount of ^{238}U, three kind of reactions happen:

- **Spallation**: when some neutrons and protons are stripped out of the target nuclei and nuclei of masses close to the target material are produced.
- **Fission**: in this case, the target nucleus is split in two similar fragments (symmetric fission) and two near half- mass of the target nucleus are produced. Additionally, some nucleons are emitted as a result of the reaction.
- **Fragmentation**: when the resulting nuclei of the reaction have quite different masses (asymmetric fission). Apart from them, some nucleons are also released.

In the TAS experiment, the target used was made of 43 g/cm^2 Nb and in the conversion electron spectroscopy experiment it was a 26 g/cm^2 Nb target. In both cases, for producing the nuclei of interest, ^{72}Kr, the reaction that takes place in the target is the spallation:

$$^{93}_{41}Nb_{52}(p, 16n\ 6p)^{72}_{36}Kr_{36} \tag{2.24}$$

The fragments produced in the reactions, not only ^{72}Kr, go out of the target container by *diffusion* processes to the surface of the target material. Then they are transported by *effusion* to the ion source and there, they are ionized to +1 charge state (in most of the cases) in the ion source. Ideally, the combination of target and ion source should be able to produce an ion beam which only contains isotopes from one chemical element so this combination is a key point in the production of significant high yields for exotic nuclei like the ^{72}Kr. The high intensity of the proton beam allows the high yield and the combination of target plus ion source gives chemical

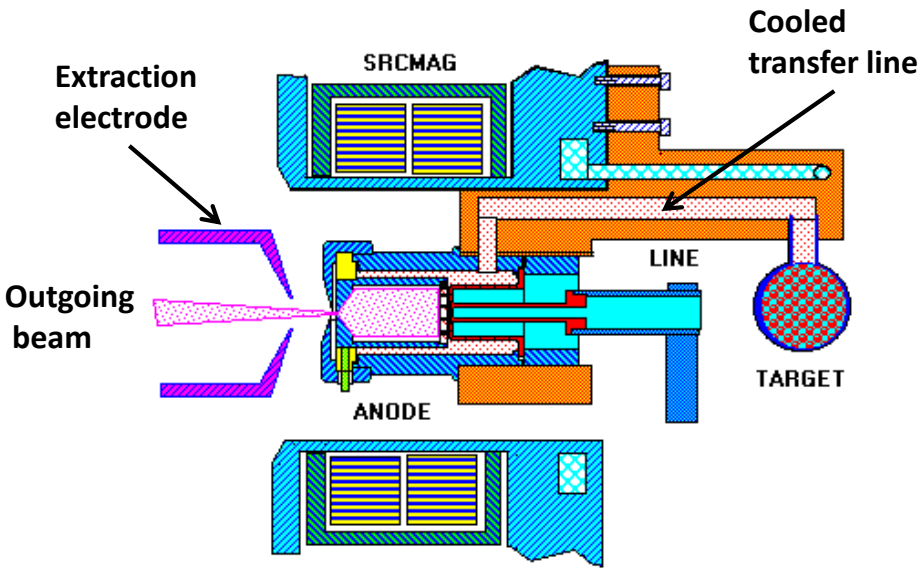

Figure 2.14: *Plasma Ion Source with cooled Transfer Line taken from ref. [Is]. The diffused out particles from the target travel along the cooled transfer line up to reach the Plasma Ion Source. Then the ionized fragments are extracted through the extraction electrode which applies a 60 kV voltage.*

selectivity which, in many cases is enough for the separation in others, a laser is needed when the properties of a chemical element are similar to the neighbour.

There are 3 main types of ion sources available at ISOLDE facility, the **surface ion source** is the most simple as it is only a metal tube (called line) made of, for example, tungsten or tantalum, which has a higher work function than the atom to be ionized. This line is usually heated up depending on the line's material up to 2400 ^{0}C.

When the nucleus of interest cannot be ionized through surface ionization it is usually ionized with the **plasma ion source**. The plasma is produced by a gas mixture, typically Xe or Ar, that is ionized by electrons being accelerated between the transfer line and the extraction electrode by supplying an anode voltage of around 130 V. An additional magnetic field (SRCMAG) is used in order to optimize the process.

In the case of noble gas isotopes, as the ^{72}Kr of interest, the plasma ion source set-up is modified in the way that the transfer line in between target and gas plasma is cooled by a continuous water flow to suppress the transport of less volatile elements and reduce via this mechanism the isobaric contamination in the ISOLDE ion beams that are released to the mass separator. In fig. 2.14 how the Plasma Ion Source with cooled transfer line looks like is shown.

Once the beam is ionized and extracted from the ion source with a maximum extraction potential of 60 kV, the next step will be to separate by mass in order to select only the isotopes we are interested in. For this purpose, ISOLDE has two separators:

- The **General Purpose Separator (GPS)** has one bending magnet and an electrostatic switch-yard allowing the simultaneous extraction of three mass separated beams. Its mass resolving power is $\Delta M/M = 2400$, see figure 2.15(a).

- The **High Resolution Separator (HRS)** consists of two bending magnets with an elaborated ion-optical system for higher order corrections. Its mass resolving power exceeds $\Delta M/M = 5000$, see figure 2.15(b).

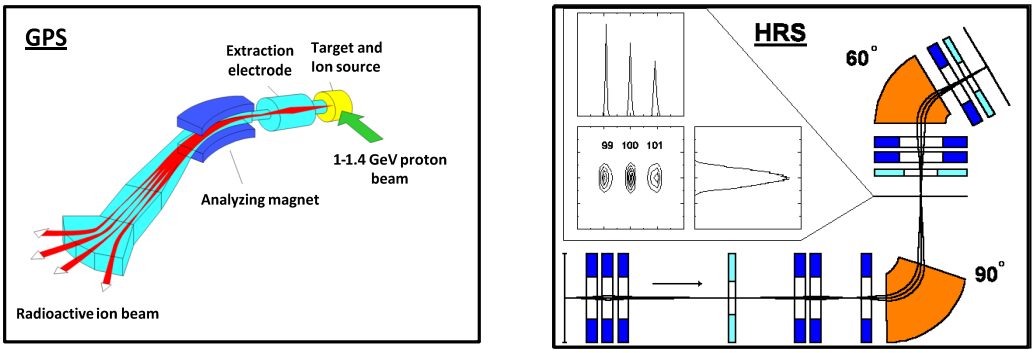

(a) (b)

Figure 2.15: *Mass separators available at the ISOLDE facility. (a) General Purpose Separator (GPS) and a sketch on the steps from the proton beam impinging the ISOLDE target until it is delivered to the experimental beam lines where the users place the setup. (b) High Resolution Separator (HRS) mode of operation. HRS provides us with better resolving power, being $\Delta M/M$ = 5000 vs. 2400 for the GPS. Our measurements made use of the HRS.*

The IS370 experiment, devoted to the measurement with the Total Absorption technique, and its addendum (IS370-A) to measure the conversion coefficients of low energy transitions, were carried out using the HRS separator which provides better isotopic separation and, consequently, a cleaner ^{72}Kr beam.

A brief summary of the conditions in each of the experiment analysed in this work are described next, giving an estimation of the amount of ^{72}Kr ions available in the experimental setup.

Conversion electron experiment

In the conversion electron experiment described in chapter 3, the conditions of the experiment, from the ISOLDE facility point of view were the following:

- a 26 g/cm^2 niobium (Nb) target was used,
- the Plasma ion source with the cooled transfer line was used,
- the Super-Cycle from PS-Booster was composed by 28 proton pulses and 14 from them were assigned to ISOLDE with an intensity of 3×10^{13} protons per pulse,
- the Super-Cycle was 33.6 s long as every cycle comes 1.2 s after the previous one, so
- the proton current was kept at 2 μA for most of the measurements,
- the estimated yield of ^{72}Kr is 2×10^3 ions per μC,
- the transmission from the separator till the experimental chamber was around 30%, measured using stable beam of ^{80}Kr,

- the estimated amount of ^{72}Kr reaching the experimental setup is around 600 ^{72}Kr ions/μC (30% of 2000 ^{72}Kr ions produced),
- the production rate of ^{72}Kr at the experimental chamber is around **1200 ^{72}Kr ions/s** (600 ^{72}Kr ions/$\mu C \times 2$ μA proton current).

Total Absorption Spectroscopy experiment

In the TAS experiment described in chapter 4, the properties of the elements involved in the ISOLDE facility were:

- a 43 g/cm^2 niobium (Nb) target was used,
- the Plasma ion source with the cooled transfer line was used,
- the Super-Cycle from PS-Booster was composed by 14 proton pulses and 7 from them were assigned to ISOLDE.
- the Super-Cycle was 16.8 s long as every cycle comes 1.2 s after the previous one,
- the proton current was kept at 2 μC for most of the measurements,
- the estimated yield of ^{72}Kr is 2×10^3 ions per μC,
- a system of three collimators (36, 4 and 4 mm width) is placed around 92 cm before the collection point of the setup (downstream) to define a 6×8 mm^2 beam spot in the center of the crystal to avoid contamination in the surrounding areas of the collection point,
- the transmission from the separator till the experimental chamber was around 26%, measured using stable beam of ^{40}Ar in the collection point,
- the estimated production of ^{72}Kr at the experimental setup is around 520 ^{72}Kr ions/μC (26% of 2000 ^{72}Kr ions produced),
- the production rate of ^{72}Kr at the experimental chamber is around **1040 ^{72}Kr ions/s** (520 ^{72}Kr ions/$\mu C \times 2$ μA proton current).

One issue to be remarked is that the transmission from the separator till the experimental setup was, in both experiments, performed by using stable beams of ^{80}Kr and ^{40}Ar as indicated above. The reason is that the production of these isotopes is much higher and can be measured with the Faraday cups available in the facility while the productions of ^{72}Kr radioactive beam is below the detection threshold of these components and no beam intensity can be measured.

The yields were obtained through the most intense gamma lines in the de-excitation of ^{72}Br, more exactly the 124 keV, 162.7 keV, 309.9 keV, 414.5+415.1 keV doublet and 575.9+576.8 keV doublet.

Once the radioactive beam has been transmitted to the experimental setup, the beam is provided by the facility and now the experimental setups of both experiments will be detailed. Chapters 3 and 4 are devoted to each of the two experiments performed, that is chapter 3 for the conversion electron measurement and chapter 4 for the TAS experiment. In what follows, the two experiments will be described and the subsequent data analysis will be presented. Afterwards, in chapter 5 the results from these experiments will be presented.

3

Conversion electron spectroscopy

Contents

The IS370-A experiment, which is an addendum to the IS370 experiment, is devoted to the study of the low-spin structure of the ^{72}Br fed through the beta decay of ^{72}Kr. In the following, the experiment and the data analysis will be described.

3.1 Experimental setup

The ^{72}Kr beam selected in the HRS mass separator at ISOLDE was lead to the experimental setup. A picture of the experimental station is shown in figure 3.1. The experimental setup includes a tape transport system which collects the sample in the **Collection point** and moves it to the **Measuring point** in the next step of the synchronous system.

The measuring point was surrounded by 2 high purity germanium (HPGe) detectors and a Miniorange spectrometer plus Si(Li) detector in order to measure the radiation emitted by the radioactive sample. In this study the interest lies in measuring γ radiation and conversion electrons in order to study the conversion coefficients in the de-excitation process of the excited states in ^{72}Br fed by β decay of the ^{72}Kr beam implanted on the tape.

Next, the main characteristics of all the components in the experimental setup of the IS370-A experiment are detailed in order to know how the study of the conversion coefficients was experimentally carried out.

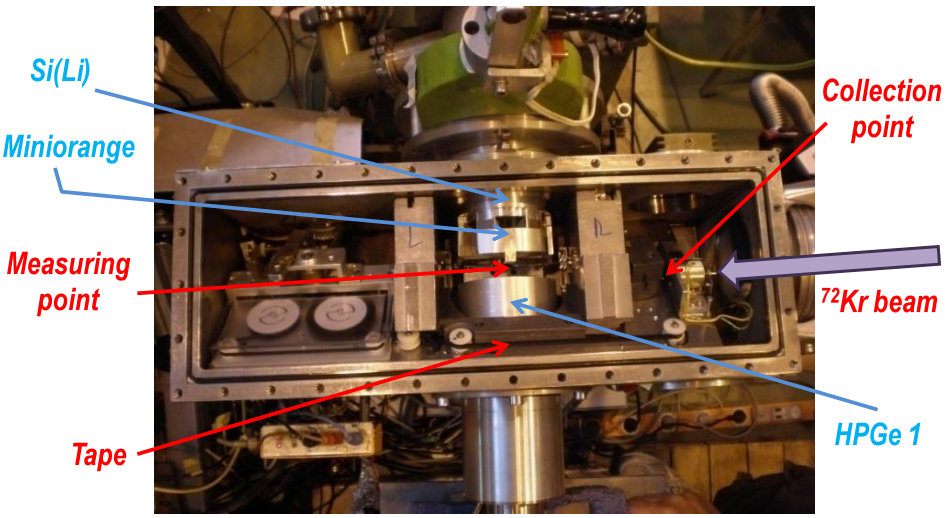

Figure 3.1: *Top view of the experimental setup of the IS370-A experiment at ISOLDE (CERN). The transportation tape collects the ^{72}Kr nuclei in the collection point. After a step of tape movement, this sample is located in the measuring point where is surrounded by the electron spectrometer, composed by a Miniorange spectrometer and a Si(Li) detector and the HPGe 1 detector. There are two lead pieces, labeled with L and R in the picture, in order to shield the measurement position of radiation coming from outside as, for example, the collection point or the rollers where the tape was stored after a collection-measurement cycle was completed (white rollers at the left part of the station).*

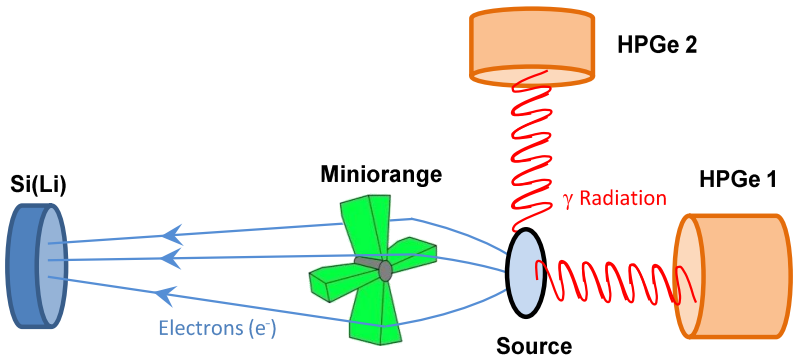

Figure 3.2: *Sketch showing a transversal cross section of the experimental setup of the IS370-A experiment. As it is shown, the Si(Li) detector and the two HPGe detectors are located in the same plane in perpendicular position one from each other. The source is placed in the measuring point where it is surrounded by detectors.*

3.1.1 Detection of γ radiation

The detection of γ radiation is performed by using HPGe detectors. The reason for using this kind of detectors is their very good energy resolution in comparison with scintillators (0.5-2 keV in the energy range 0-2 MeV in which this study is interested, see table 3.1) and higher photo-peak efficiency than silicon detectors as the probability of photoelectric effect per atom is proportional to the Z number of the material following the relationship given in equation 3.1.

$$P_{\text{Phot. effect}} = K \times \frac{Z^n}{E_\gamma^{3.5}} \tag{3.1}$$

where 4<n<5. As the Z value of Ge is higher than Si (32 vs. 14) the probability of producing an electron from photoelectric process (photo-electron) and consequently a photo-peak detection, is higher for Ge than for Si detectors.

HPGe 1

HPGe 1 detector is an EURISYS n-type semi-planar detector. The front diameter is 69.9 mm, its front surface is 38.4 mm^2 and the operation voltage is -3000 V. The front face has a diameter of 90 mm and includes a Be window 0.3 mm thick.

The detector was placed inside the chamber by using a cover cap made of aluminum, that is the one visible inside the chamber in fig. 3.1. In the front side of the cap there is a mylar foil in order not to strongly suppress the low-energy gamma radiation. The purpose of placing this cap was both, to close the chamber and place the HPGe 1 detector as close to the sample as possible.

The front window of the HPGe 1 detector was placed 2 cm from the mylar foil of the cap. The distance from the cap to the measuring point was, approximately, 2 cm but it is not well known. This distance will be more exactly deduced from the simulations used to reproduce the absolute efficiency curve that was obtained in the efficiency calibration process. So, as a rough estimation, it was considered that the source-detector distance was 4 cm. The solid angle covered by this detector is given by the expression 3.2.

$$\Omega = 2\pi(1 - cos\ \theta) \tag{3.2}$$

where θ is the angle that the detector subtends from the source point of view, see fig. 3.3. This angle is easily obtained from the following equation:

$$tan\ \theta = \frac{R}{d} = \frac{6.99/2\ \text{cm}}{4\ \text{cm}} \tag{3.3}$$

and θ turns out to be 41.15° and the solid angle covered by the detector:

$$\Omega = 0.1235 \times 4\pi \tag{3.4}$$

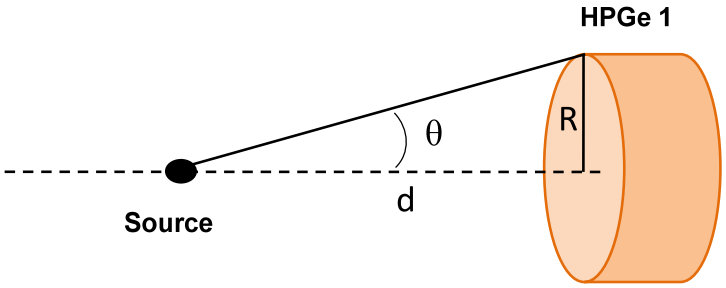

Figure 3.3: *Solid angle covered by the HPGe 1 detector from the source point of view schematically shown. The distance d is known to approximately be 4 cm and R is the half-diameter of the front side of the detector. The front diameter is 6.99 cm so R is 6.99/2 cm. The solid angle is calculated from eq. 3.2.*

So, geometrically it is obtained approximately a 12 % of the whole 4π solid angle. I will return to this point, when the simulated absolute efficiency is fitted to the experimental one, in order to obtain the real source-detector distance and, consequently, the real solid angle coverage.

The effective energy range for this detector is from 10 to 1250 keV, as shown in fig. 3.4. The energy resolution is quite good, $\Delta E \leq 1$ keV in the energy region up to 300 keV and better than 1.8 keV in the whole energy range. The main γ transitions of the ^{241}Am and ^{152}Eu sources are listed in table 3.1 together with the energy resolution provided by both HPGe detectors.

HPGe 2

The other HPGe detector is an n-type HPGe detector belonging to the dismounted TESSA array (for further information see [Twi83]). It is located in vertical position and it cannot be seen in fig. 3.1 as it was removed when the picture was taken). The geometrical configuration of the setup including this detector can be seen in figure 3.2. The detectors identified from here on as HPGe 1 and HPGe 2 are located perpendicular to each other and with respect to the Si(Li) detector.

The operation voltage is -2750 V. The effective energy range is chosen to be from 16 to 950 keV, as shown in figure 3.4. The energy resolution provided by this detector is around 2 keV see table 3.1 values for several intense transitions of the calibration sources.

The fact that the energy resolution is worse for HPGe 2 than for HPGe 1, as shown in the lower-center spectra in fig. 3.4, is one important disadvantage that, in addition to others

Source	E_γ (keV)	HPGe 1 Resolution (keV)	HPGe 2 Resolution (keV)
^{241}Am	59.5412(1)	0.7057(6)	2.053(14)
^{152}Eu	121.7817(3)	0.847(2)	1.99(4)
^{152}Eu	244.6975(8)	1.002(10)	2.18(17)
^{152}Eu	344.279(1)	1.133(5)	2.44(6)
^{133}Ba	356.0134(6)	1.151(5)	2.41(5)
^{152}Eu	778.9045(24)	1.603(17)	2.19(8)
^{152}Eu	964.079(18)	1.82(2)	

Table 3.1: *The main gamma transitions of ^{241}Am, ^{133}Ba and ^{152}Eu sources are listed. The energy resolution of HPGe 1 and 2 detectors for these gamma transitions are shown. The 964 keV transition is not observed in detector HPGe 2 because is beyond its effective energy range (16-950 keV.)*

that will be discussed later lead us to make the choice of the HPGe 1 for the measurement of gamma transition intensities in the current conversion coefficients study and to just use the HPGe 2 as a support detector for other less important tasks.

3.1.2 Detection of conversion electrons

The detection of charged particles is commonly performed with silicon detectors as they are simple to operate, e.g. generally they do not need to be cooled down at low temperatures, at the same time they keep good energy resolution, stability of operation and have thin entrance windows. These windows are important in charged particles detection as they cause a not-desirable energy loss in the full-energy identification procedure (mainly at low energies). In the case of electron detection, silicon detectors are more suitable also as the electron backscatter process is less frequent than in germanium detectors.

When an electron passes through a material it deposits energy mainly by means of two processes: collision losses (ionization and excitation) and radiation losses (bremsstrahlung). The former varies little with energy while the latter is approximately proportional to the energy. The **critical energy** of a material is defined as the energy where the radiation losses equal the collision losses. This means that for energies higher than the critical one, the radiation losses dominates so the detector material should be chosen with high critical energy for electron detection as bremsstrahlung radiation can escape from the detector. An approximate expression given by Bethe and Heitler [Bet53] is:

$$E_c = \frac{1600 m_e c^2}{Z} \tag{3.5}$$

So, for a material of low Z, such as Si (Z=14) with respect to Ge (Z=32), the critical energy would be higher (around 2.3 times higher) and the relative importance of radiation losses is smaller. As the collision losses are the ones employ to obtain the spectrum, for the electron spectroscopy is more suitable to use silicon than germanium detectors.

Another advantage of the silicon material is that the leakage current is lower as the band-gap energy width is higher (1.11 vs. 0.66 eV in germanium), so the thermally generated electron-hole pairs per volume unit is fairly smaller for silicon as the needed energy for

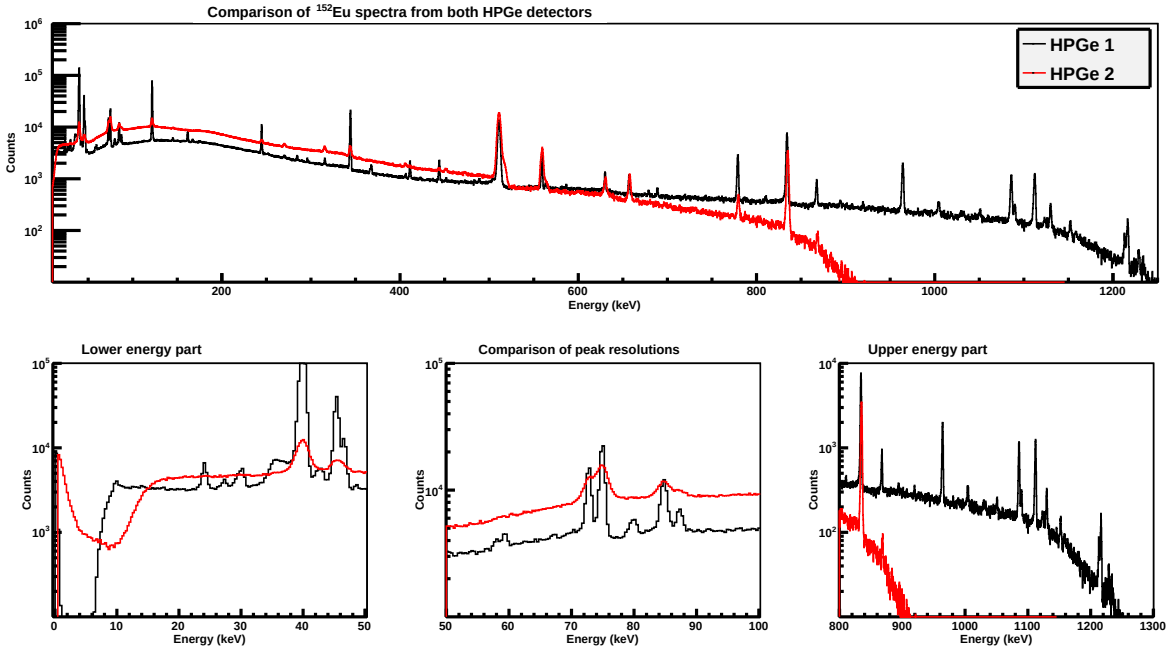

Figure 3.4: *Comparison of the ^{152}Eu spectra obtained with the HPGe 1 and 2 detectors. In the upper part, a general overview of the spectra is shown. In the three lower figures, three different energy regions are shown, from left to right side, the lower energy part of the spectra up to 50 keV where one can see the lower energy threshold. In the middle, the comparison in the interval 50-100 keV shows the difference in energy resolution of the two detectors for lead X-rays. On the right hand side, the upper energy part of the spectra from 800 up to 1300 keV is shown. It can be noticed that the energy range covered by the HPGe 1 detector is larger as well as it has a better energy resolution.*

the creation of electron-hole pair is higher (3.76 vs. 2.96 eV in germanium). This implies a better energy resolution using equivalent electronic components with respect to germanium detectors. In spite of being smaller than in germanium detectors, the compensated region is sufficiently large so that at room temperature the fluctuations in the leakage current can be a significant source of noise, especially for low energy studies of electrons or X-rays where the detector signals are quite small. In order to solve this issue, most of the silicon detectors are cooled to the liquid nitrogen temperature.

The main drawback of using pure silicon detectors is that the depletion depth that can be reached by reverse biasing a silicon diode detector is limited to 1 or 2 mm. If one requires thicker detectors, as in the case under study at least, 3 mm are needed in order to have high probability of full absorption for electrons of 1.5 MeV as indicated in ref. [Ber69]. For this work this type of detectors cannot be used and one must attend to detectors built through the lithium drifting process, Si(Li), that allows to achieve thicknesses of up to 5 or 10 mm.

Once the detector thickness is larger than the maximum penetration distance of electrons in the detector's material, the response function of the detector consists of a full-energy peak plus a continuum of lower amplitude events. The full-energy peak corresponds to the electrons fully stopped in the active volume of the detector and those which bremsstrahlung photons generated along its path are completely absorbed in the detector. The continuum comes from the events where partial energy loss happens, this can be either backscattering of electrons that come back through the incident surface without having deposited all their energy, or the escape of bremsstrahlung photons generated in the way of the electron through the detector's material. In the case of heavier charged particles, such as protons or α particles, the collision with atomic electrons does not produce so frequent backscattered particles due to the difference in mass of colliding particles while in the case of electron detection the collision occurs between equally massive particles (electron with electron).

Additionally, peaks corresponding to the full-energy deposition show a **tail at lower energies** than the peak position which is due to the incomplete charge collection in the Si(Li) crystal as a consequence of charge trapping process in the crystal structure as it is explained in detail in ref. [Vis07]. Apart from this, as it is explained in ref. [Dam82], the incomplete energy deposition in the detector due to three causes: 1.- backscattered electrons, 2.- penetration in the depletion layer and 3.- the electromagnetic radiation (bremsstrahlung), is the responsible of the low energy tails (LET) of the full energy peaks of electron spectroscopy performed with silicon detectors.

In order to independently measure the conversion electrons on the Si(Li) detector and the gamma radiation in the HPGe one, a central piece of a heavy material has been placed to efficiently suppress the gamma radiation reaching the Si(Li) detector. Thus one obtains a cleaner electron spectrum. The drawback is that this piece not only stops the gamma radiation but also the low-energy electrons in which this study is interested.

This is solved by placing a system of permanent magnets which acts as an electromagnetic lens focusing electrons towards the silicon detector and deviating the positrons emitted by the source, in the case of β^+ decay emitters, outside of the silicon detector. For more details see ref. [Van72] and [Van75]. In this way, one obtains a clean electron spectrum with almost no gamma peaks in the spectrum.

In subsequent paragraphs the main properties of the Miniorange spectrometer are described in detail.

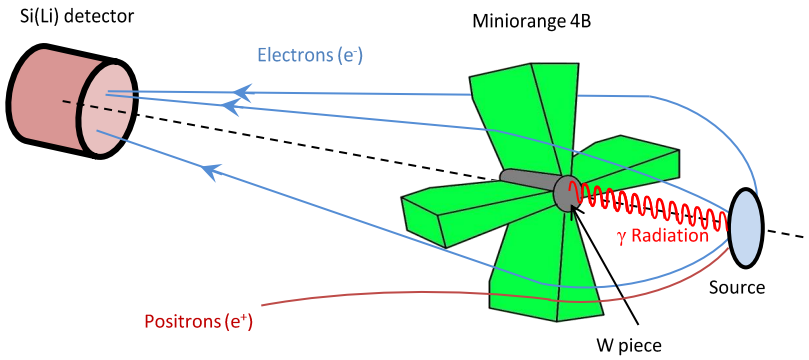

Figure 3.5: *Sketch of the Miniorange spectrometer composed by a Si(Li) detector and a set of magnets. The central piece of tungsten stops the direct gamma and X-rays coming from the source while the set of magnets focuses the electrons (and de-focuses the positrons) to the Si(Li) detector in order to improve the electron detection efficiency (avoiding positrons to reach the detector).*

3.1.2.1 Miniorange spectrometer

In order to measure the conversion electrons a Miniorange spectrometer and a Si(Li) detector surrounding the sample was placed, in the same plane as the two HPGe detectors, at 90 and 180 degrees with respect to them, as can be seen in fig. 3.2. The **Miniorange spectrometer** is described in Ref. [Pé11] and references therein. It is composed by a central piece made of tungsten (W) and a set of magnets to optimize the efficiency in a certain energy range.

The Miniorange spectrometer has a double purpose:

- To avoid that the X-rays and gamma radiation coming from the source could reach the Si(Li) detector smudging the spectrum and making harder the task of peak identification and the extraction of peak areas correctly. As shown in figure 3.8, the electron spectrum is quite complicated by itself as every electron peak is asymmetric and shows a tail at low energies for the reasons already explained. and consequently the energy loss on it too. For this reason, non-desirable radiation needs to be removed. To this aim, a **piece** made of tungsten or so-called wolfram, W, is placed in the center of the spectrometer, see figure 3.5.

- To improve the electron detection efficiency (so-called electron transmission), several **$SmCo_5$ magnets** (in green in fig. 3.5) are located around the central piece in order to deviate and focus the electrons on the Si(Li) detector. At the same time, it de-focuses positrons emitted by β^+/EC decay sources as, for example, the ones emitted in the decay of ^{72}Kr.

The working principle of the Miniorange spectrometer is illustrated in fig. 3.5. There are several sets of magnets to optimize the electron transmission in different energy ranges. The configurations are named by D1/D2/NT where D1 is the distance between the reference origin and the Si(Li) detector, D2 is the distance between the central W piece of the Miniorange and the radioactive source and NT specifies the number of magnets, N, and the type of them, T. The description of the distances is shown in figure 3.6. There are two different types of magnets, A and B, whose sizes are given in figure 3.7.

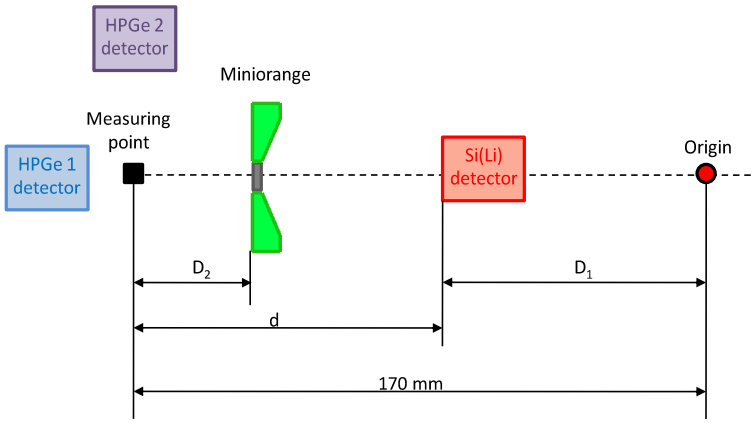

Figure 3.6: *Graphical representation of the side view of the experimental setup including the description of the distances D1 and D2 used to label every Miniorange configuration as D1/D2/NT. N gives the number of magnets included in the configuration and T the type as the ones shown in figure 3.7.*

The Si(Li) detector has a frontal surface of 300 mm^2 and a thickness of 4 mm. It includes a polyethylene window, aluminized in both faces and 260 $\mu g/cm^2$ thick. This window is placed 4 mm far from the front face of the liquid-nitrogen-cooled detector to prevent the impurities to be deposited in the front window of the detector in spite of having the detector in vacuum. The energy resolution of the Si(Li) detector at several energies is indicated in table 3.2.

One important detail to be considered is the fact that by using a Miniorange spectrometer, the electrons detected by the Si(Li) detector are impinging at oblique angles. This has the disadvantage that a larger fraction of the incoming electrons are scattered back out of the detector in comparison with normal incident electrons. In practice, the continuum in the response function that has been explained before is enhanced in this experimental conditions with respect to normal incidence. So, in the present work less full-energy peak efficiency will be obtained in comparison with normal incidence. This disadvantage of the current setup has to be assumed in order to suppress the gamma and X-ray radiation from the source and get a cleaner spectrum at low energies.

Source	E_e (keV)	Si(Li) Resolution FWHM (keV)
^{75}Kr	74.82(6)	1.14(7)
^{75}Kr	118.96(8)	1.06(2)
^{75}Kr	273.3(2)	1.52(19)
^{207}Bi	481.694(2)	1.87(7)
^{207}Bi	975.652(3)	3.40(6)

Table 3.2: *Some conversion electron transitions corresponding to the ^{207}Bi calibration source and ^{75}Kr decay produced on-line in the experiment. The resolution of Si(Li) detector is given. The peaks have been fitted using the expression 3.10 in order to reproduce the low-energy tail of every peak due to the incomplete energy deposition.*

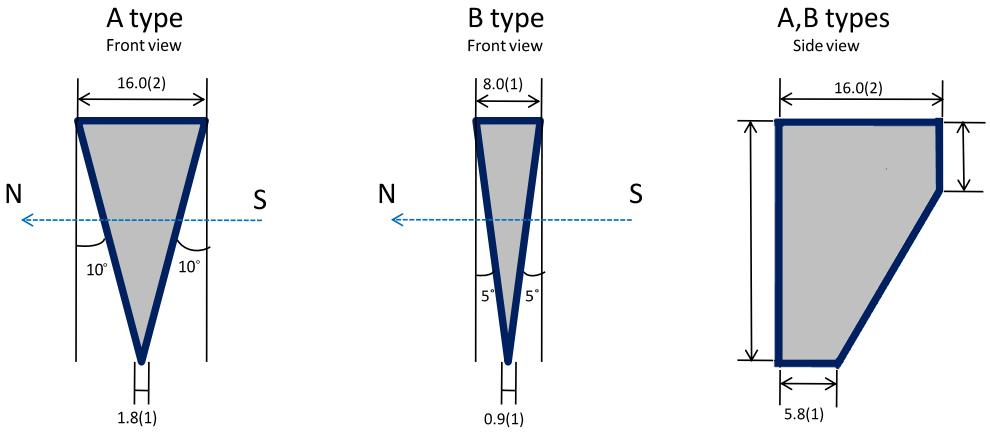

Figure 3.7: *Types of magnets used in the Miniorange spectrometer. All the dimensions are given in mm. As it is shown, the A type magnet is bigger than B type and both lateral profiles are identical. In both front views it is displayed the direction of the magnetic field created by each magnet by showing where the North (N) and South (S) poles of the magnet are located.*

D1/D2/NT	Effective energy range E(keV)	Beam or calibration source used with this configuration
125/8/3B	20-170	^{76}Kr (calib) and ^{72}Kr
85/8/4B	60-200	^{75}Kr (calib) and ^{72}Kr
125/8/6A	300-1100	^{74}Kr, ^{207}Bi (calib) and ^{72}Kr
110/8/6A	400-1100	^{74}Kr, ^{207}Bi (calib) and ^{72}Kr

Table 3.3: *Configurations of the Miniorange magnets used in the IS370-A experiment ordered as a function of increasing effective energy. Apart from the effective electron energy range of each configuration, it is shown the beam used with each configuration of the magnets. In addition to the ^{72}Kr beam, that is the subject of this study, other krypton isotopes as ^{74,75,76}Kr were used as beam in order to perform the calibrations of every Miniorange configuration.*

3.2 Analysis

The first step in the analysis procedure is the characterization of all the detectors, more exactly, the calibration in energy and efficiency of the different data channels, used in the experiment in order to have them ready for the extraction of results later on.

The system composed by detector and the associated electronic chain provides analogue signals that are converted in numbers in the data acquisition system at the end, the so-called channel number or division, which has no physical interest. One has to convert these values in physical observables, for example, energy. This process is known as calibration.

In the current experiment, the interest lies on **calibrating the response of every detector to energy**, with the aim of knowing the exact energy of every transition in the spectrum, **and efficiency**, in order to deduce from the measured quantities the total emitted particles by the source and, consequently, the absolute intensities for every detected radiation.

The energy calibration is the procedure to obtain the equation to convert the channel number (provided by every electronic data channel) to the energy deposited by the incident particle in the detector (a physical quantity of interest).

The number of counts in every peak in the spectrum is just the number of detected particles but not the total emitted particles with this energy, which is the important physical quantity independent of the experiment. This transformation is known as the efficiency calibration.

Source	A(ref) (kBq)	Date (ref)	$T_{1/2}$ (years)	A (Bq) (14/07/2008)	T_{real} (s)	T_{live} HPGe 1 (s)	T_{live} HPGe 2 (s)	T_{live} Si(Li) (s)
^{133}Ba	11.6	01/03/2007	10.51(5)	10600(60)	849	600	550	618
^{152}Eu	11.8	01/03/2007	13.537(6)	11000(50)	1815	1280	1199	1326
^{241}Am	40	01/01/2008	432.2(7)	39912(5)	793	562	484	579
^{207}Bi	30	02/06/2006	31.55(5)	28636(2)	2170	1671	1617	1742

Table 3.4: *Information of the standard calibration sources that were used to perform the energy calibration of HPGe and Si(Li) detectors during the experiment. The uncertainty in the activity is calculated through the propagation of the uncertainties of the independent variables $T_{1/2}$, t_0 and t using the expression 3.7 as it is detailed in the text.*

The activity, A (Bq), of every source in the date of the measurement is calculated from the activity of reference given by the manufacturer and the radioactive decay law (eq. 3.6).

$$A(t) = A(t_0) \times e^{-\lambda(t-t_0)} = A(t_0) \times e^{\frac{-ln2\cdot(t-t_0)}{T_{1/2}}} \tag{3.6}$$

The uncertainty on the calculated activity of every source was obtained by propagating the uncertainties on the half life of the source ($T_{1/2}$), on the reference time (t_0) which depends on the source but has been considered as the precision given for the date, and on the measurement time, t, that has been considered to be one day. The propagation of the uncertainties has been performed following the expression 3.7 that is valid for the case of all the included variables are independent between themselves.

$$\Delta A = \sqrt{\left(\frac{\partial A}{\partial T_{1/2}}\right)^2 \cdot \Delta T_{1/2}^2 + \left(\frac{\partial A}{\partial t_0}\right)^2 \cdot \Delta t_0^2 + \left(\frac{\partial A}{\partial t}\right)^2 \cdot \Delta t^2} \tag{3.7}$$

3.2.1 Energy calibrations

In order to perform the energy calibration of HPGe detectors, several standard γ radiation sources were used, the information of everyone is shown in table 3.4. The list of transitions used in the energy calibration of HPGe 1 are shown in table 3.5 while table 3.6 contains the ones used for HPGe 2 calibration.

The type of detectors used for spectroscopy purposes are chosen, apart from other considerations, because they exhibit linear response to the energy deposited by the incident particle. This means that the analytic expression for the energy calibration is a linear dependence so the calibration equations include two parameters, the slope and offset.

The calibration equation obtained for HPGe 1:

$$E(keV) = 0.045189(4) \times channel + 0.05(3) \tag{3.8}$$

and for HPGe 2:

$$E(keV) = 0.03493(2) \times channel + 0.56(11) \tag{3.9}$$

Source	E_γ(ref) (keV)	Position (channel number)	E_γ (measured) (keV)	E_γ(measured)-E_γ(ref) (keV)
^{241}Am	26.3448(2)	582(2)	26.4(1)	0.0(1)
^{241}Am	33.196(1)	736(2)	33.3(1)	0.1(1)
^{133}Ba	53.1625(6)	1175(2)	53.1(1)	0.0(1)
^{241}Am	59.5412(1)	1317(2)	59.6(1)	0.0(1)
^{133}Ba	79.6139(13)	1762(4)	79.7(2)	0.1(2)
^{133}Ba	80.9971(12)	1791(2)	80.97(6)	-0.02(6)
^{152}Eu	121.7817(3)	2693(2)	121.8(1)	0.0(1)
^{133}Ba	160.6109(17)	3553(8)	160.6(2)	0.0(2)
^{133}Ba	223.2373(14)	4938(8)	223.2(2)	0.0(2)
^{152}Eu	244.6975(8)	5413(4)	244.7(1)	0.0(1)
^{133}Ba	276.3997(13)	6115(8)	276.4(1)	0.0(1)
^{133}Ba	302.8510(6)	6700(4)	302.8(1)	0.0(1)
^{152}Eu	344.2785(13)	7618(2)	344.3(1)	0.0(1)
^{133}Ba	356.0134(6)	7877(4)	356.0(1)	0.0(1)
^{133}Ba	383.8480(12)	8493(4)	383.9(1)	0.0(1)
^{152}Eu	443.9650(3)	9824(8)	444.0(4)	0.0(4)
^{152}Eu	688.670(5)	15240(8)	688.7(2)	0.1(2)
^{152}Eu	867.373(3)	19195(12)	867.5(2)	0.1(2)
^{152}Eu	964.079(18)	21333(8)	964.1(4)	0.0(4)
^{152}Eu	1085.869(24)	24028(8)	1085.8(2)	0.0(2)
^{152}Eu	1112.069(3)	24608(8)	1112.1(2)	0.0(2)

Table 3.5: *List of gamma transitions used in the **energy calibration of the HPGe 1 detector**. In the first column the calibration source is given. Second one shows the reference value for the energy, E_γ(ref), of the chosen transitions for the energy calibration from Ref. [Art96] for ^{152}Eu transitions, from Ref. [Rab95] for the ^{133}Ba ones and Ref. [Bas06] for ^{241}Am transitions. In the third column, the measured position for each transition in the spectra is shown and in the last column, the deviation of the energy calibration from the reference value is indicated. The deviations are plotted in figure 3.10(a). Expression 3.8 is used to transform values from column 3 to column 4.*

Source	E_γ(ref) (keV)	Position (channel number)	E_γ (measured) (keV)	E_γ(measured)-E_γ(ref) (keV)
^{133}Ba	30.850(2)	870(8)	30.9(3)	0.08(30)
^{133}Ba	35.2(1)	990(12)	35.2(4)	-0.05(40)
^{152}Eu	39.906(2)	1128(4)	40.0(2)	0.06(20)
^{152}Eu	45.5(1)	1289(16)	45.6(6)	0.09(60)
^{241}Am	59.5412(1)	1691(8)	59.6(3)	0.09(30)
^{133}Ba	80.9971(12)	2300(8)	80.9(3)	-0.09(30)
^{152}Eu	121.7817(3)	3469(12)	121.7(4)	-0.06(40)
^{152}Eu	244.6975(8)	6985(32)	244.5(11)	-0.16(110)
^{133}Ba	276.3997(13)	7891(16)	276.2(6)	-0.20(60)
^{133}Ba	302.8510(6)	8646(8)	302.6(3)	-0.29(30)
^{133}Ba	344.2785(13)	9831(16)	344.0(6)	-0.33(60)
^{133}Ba	356.0134(6)	10165(16)	355.6(6)	-0.39(60)
^{152}Eu	656.487(5)	18802(16)	657.3(7)	0.84(70)
^{152}Eu	778.9045(24)	22290(24)	779.2(10)	0.26(100)

Table 3.6: *List of gamma transitions used in the **energy calibration of the HPGe 2 detector**. In the first column the calibration source is shown, in the second the reference value for the energy of the transition from [Art96] for ^{152}Eu transitions, from [Rab95] for the ^{133}Ba ones and [Bas06] for ^{241}Am transitions, while in the third column is the measured position for each transition in the spectra and in the last column, the deviation of the energy calibration from the reference value. The deviations are plotted in figure 3.10(b). Expression 3.9 is used to transform values from column 3 to column 4.*

The calibration of charged particle detectors, such as the Si(Li) detector of this setup, has to be performed with the same kind of radiation than the measurement of interest. For this reason, in the current study one needs electron-emitting radiation sources.

The standard source of ^{207}Bi has several intense conversion electron transitions but all of them are located at around 500 and 1000 keV as it can be observed in figure 3.23. This is useful for the calibration of the detector in the medium-high energy range of this study. The information from the ^{207}Bi source used in the calibrations is shown in table 3.4.

one has to make use of the online sources such as ^{74,75,76}Kr isotopes in order to correctly perform the energy calibration of the Si(Li) detector.

The electron transition peaks that appear in the Si(Li) detector exhibit a tail at low energies as already mentioned For this reason, the usual gaussian plus linear background model function that were used in the calibration of HPGe detectors is not useful to analyse the Si(Li) spectra. Instead, the function given in the work of Mattoon et al. in ref. [Mat09] is used to fit the peaks of the energy spectrum. Its mathematical expression is given in eq. 3.10.

$$F(x) = c_1 \frac{1}{\sigma\sqrt{2\pi}} e^{-(x-\mu)^2/2\sigma^2} + c_2 \cdot e^{[(x-\mu)/\beta + \sigma^2/2\beta^2]} erfc\Big(\frac{x-\mu}{\sqrt{2}\sigma} + \frac{\sigma}{\sqrt{2}\beta}\Big) + c_3 \cdot erfc\Big(\frac{x-\mu}{\sqrt{2}\sigma}\Big) \quad (3.10)$$

As an example, the fit of one of the most intense transitions in ^{207}Bi decay is shown in figure 3.8. It is the 569K electron transition located at 481 keV energy. The parameter σ provides information on the width of the peak as shown in fig. 3.9 and, consequently, on the resolution of the detector. The resolution has been considered to be the Full Width at Half-Maximum (FWHM), as usual, where: FWHM=2.35·σ although the fit to the peak is not exactly a single gaussian function. Some values on the resolutions of the Si(Li) detector are shown in table 3.2.

The need of some calibration points in the low energy region obliged us to use several internal calibration sources (in-beam measurements) such as some krypton isotopes like ^{74}Kr,

Miniorange configuration	Source	Transition	E_γ ref. (keV)	E_e ref. (keV)	E_e meas. (keV)	$\Delta E = E_e$(ref.) -E_e(meas.) (keV)
125/8/3B	^{76}Kr	45K	45.48(2)	32.01(1)	30.9(3)	1.1(3)
125/8/3B	^{76}Kr	45L	45.48(2)	43.70(2)	43.6(3)	0.1(3)
85/8/4B	^{75}Kr	88K	88.29(6)	74.82(5)	75.4(3)	-0.5(3)
85/8/4B	^{75}Kr	88L	88.29(6)	86.51(6)	87.1(3)	-0.6(3)
85/8/4B	^{75}Kr	132K	132.43(8)	119.77(11)	119.3(2)	0.4(3)
85/8/4B	^{75}Kr	141K	141.19(10)	127.72(11)	128.9(4)	-1.2(4)
85/8/4B	^{75}Kr	132L	132.43(8)	130.78(12)	130.9(4)	-0.2(4)
85/8/4B	^{75}Kr	132M	132.43(8)	132.20(13)	132.9(4)	-0.7(4)
85/8/4B	^{75}Kr	286K	286.5(2)	273.0(2)	272.0(5)	1.0(6)
110/8/6A	^{74}Kr	D634K	634.3(2) + 634.8(1)	622.04(10)	624.2(7)	-2.2(7)
125/8/6A	^{74}Kr	D634K	634.3(2) + 634.8(1)	622.04(10)	624.1(7)	-2.1(7)
110/8/6A	^{74}Kr	D634L	634.3(2) + 634.8(1)	633.04(10)	635.3(7)	-2.3(7)
125/8/6A	^{74}Kr	D634L	634.3(2) + 634.8(1)	633.04(10)	635.7(7)	-2.6(7)
110/8/6A	^{207}Bi	569K	569.698(2)	481.693(2)	481.3(5)	0.4(5)
110/8/6A	^{207}Bi	569L	569.698(2)	553.837(2)	553.6(6)	0.3(6)
110/8/6A	^{207}Bi	569M	569.698(2)	565.847(2)	566.0(6)	0.2(6)
110/8/6A	^{207}Bi	1063K	1063.656(3)	975.651(3)	974.7(8)	1.0(8)
110/8/6A	^{207}Bi	1063L	1063.656(3)	1047.795(3)	1046.9(8)	0.9(8)
125/8/6A	^{207}Bi	569K	569.698(2)	481.693(2)	480.8(5)	0.9(5)
125/8/6A	^{207}Bi	569L	569.698(2)	553.837(2)	553.0(6)	0.8(6)
125/8/6A	^{207}Bi	569M	569.698(2)	565.847(2)	565.1(6)	0.7(6)
125/8/6A	^{207}Bi	1063K	1063.656(3)	975.651(3)	975.6(8)	0.1(8)
125/8/6A	^{207}Bi	1063L	1063.656(3)	1047.795(3)	1047.5(8)	0.3(8)
125/8/6A	^{207}Bi	1063M	1063.656(3)	1059.805(3)	1060.0(12)	0.2(12)

Table 3.7: *List of transitions used to perform the energy calibration of Si(Li) detector. Reference values for the energy of electron transitions have been taken from [Sin06] for ^{74}Kr transitions, [Far99] for ^{75}Kr, [Sin95] for ^{76}Kr and [Mar93] for lines from ^{207}Bi. The double line in the table is to separate the transitions used for calibration in the low-energy range, i.e. from 0 to 400 keV, and the high-energy range (400 up to 1100 keV). The deviations between reference energies for the electron transitions and the measured ones are given in the last column and illustrated in figures 3.11(a) and 3.11(b). The transition labeled as D634 is the doublet 634.3 + 634.7 keV that has its K and L components, and they are named as D634K and D634L. These transitions have been used as a single one as they cannot be resolved. The energy of the doublet has been obtained as a weighted average by their intensities.*

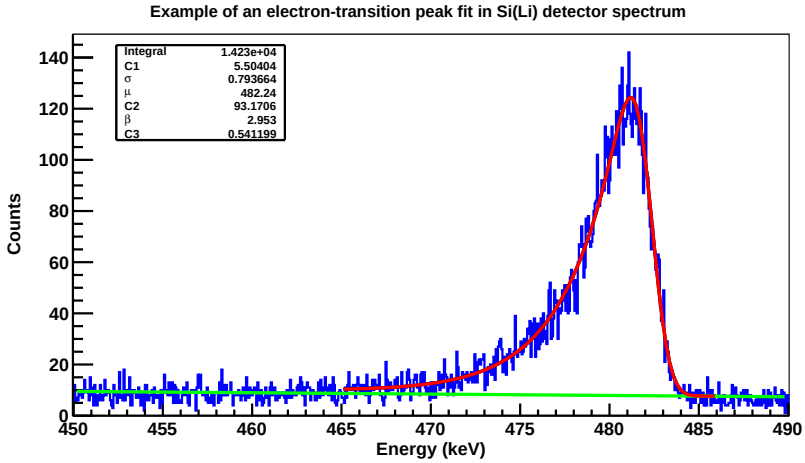

Figure 3.8: *The fit to the 569K electron transition of 481 keV energy to the function given in eq. 3.10. The fit parameter values are shown at the up-right side.*

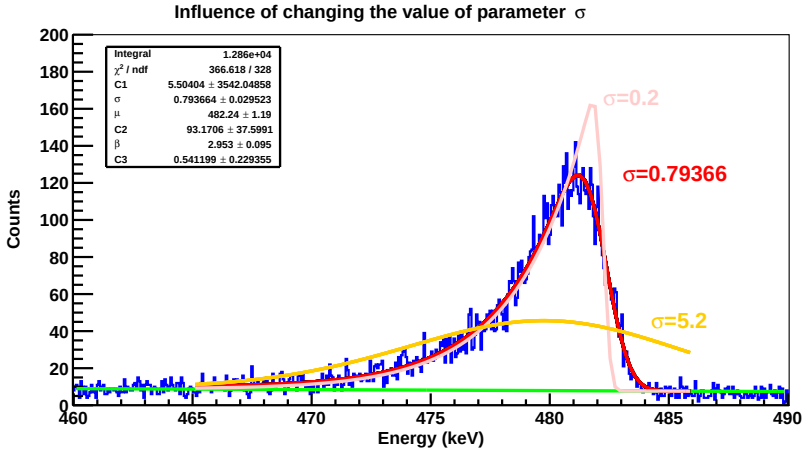

Figure 3.9: *Example illustrating the influence of varying the value of parameter σ in the fit to the peak shown in figure 3.8. As a conclusion, this parameter provides information on the resolution of the detector as when it is changed to higher values the width of the function increases causing the resolution to be worse. However, when changed to lower values the resolution would be better as the width of the function is lower. So, this parameter can be taken as equivalent to the usual parameter σ of a gaussian function taken to express resolutions by obtaining the FWHM of the peak as FWHM=2.35·σ.*

^{75}Kr and ^{76}Kr. These isotopes have to be produced by the reactions happened in the target when the proton beam impinges on it. They have electron transitions whose conversion coefficients are well known. As it will be seen later, these sources will be needed for the efficiency calibration of the Si(Li) detector as well.

The list of transitions involved in the energy calibration of the Si(Li) detector can be observed in table 3.7. A preliminary calibration with an unique energy range was performed but the deviations from tabulated values were so high that a new calibration was performed dividing in two different energy ranges:

- 0-400 keV: The equation of calibration in this energy region obtained is 3.11.

$$E(keV) = 6.194(9) \times 10^{-2} \cdot channel + 3.73(17) \text{ keV} \tag{3.11}$$

- 400-1100 keV: The equation of calibration in this energy region obtained is 3.12.

$$E(keV) = 6.289(3) \times 10^{-2} \cdot channel + 3.3(3) \text{ keV} \tag{3.12}$$

Figures 3.10 and 3.11 show the energy differences between the known energy for every transition taken from the references indicated in figure and table captions and the energy obtained with the calibration equations for the HPGe and Si(Li) detectors respectively. As can be observed in figure 3.10, the HPGe 2 detector shows larger deviations from the reference energies as well as larger uncertainties in the peak position as its energy resolution is worse as shown in table 3.1.

In the case of the HPGe 1, one can see that the larger deviations obtained in the full energy range are less than 0.2 keV, around 0.1 keV in the worst cases, and in the HPGe 2 the deviation can reach up to 1 keV. For this reason, the HPGe 1 detector is favored for single measurements.

For the case of Si(Li) detector, it can be seen that in the low-energy region the deviations from the reference values are smaller or around 1 keV while in the high-energy region there is the same tendency except for the 634 keV doublet transitions where around 2 keV deviation is found. These discrepancy in the values are acceptable in the current work as the transitions of interest are not closer than 2 keV but it has to be taken into account during the analysis.

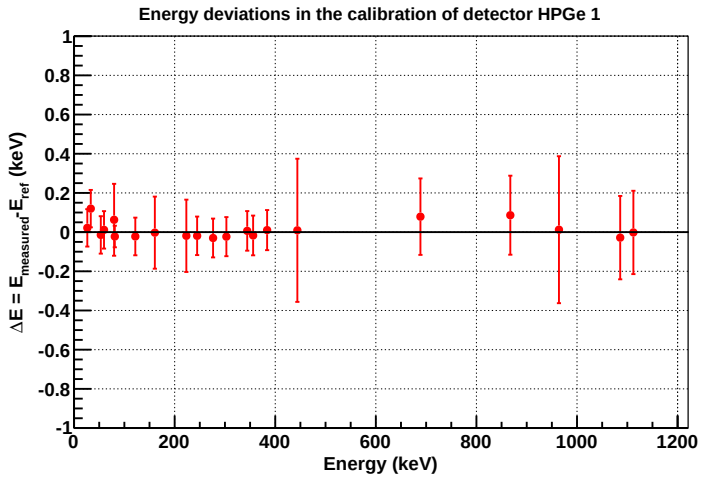

(a)

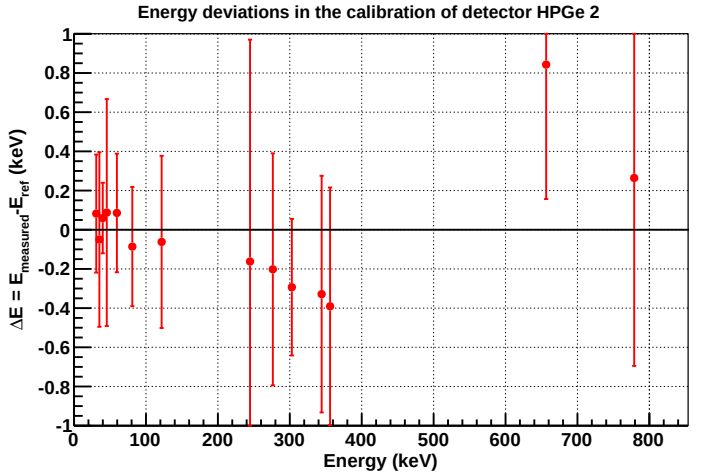

(b)

Figure 3.10: *(a) Difference of the calibrated energies for the transitions included in the energy calibration of HPGe 1 detector with respect to the reference values from [Art96] and [Rab95]. Plotted values are from the table 3.5. (b) Same as (a) but for HPGe 2 with the values in table 3.6 and taking the reference values from the same sources.*

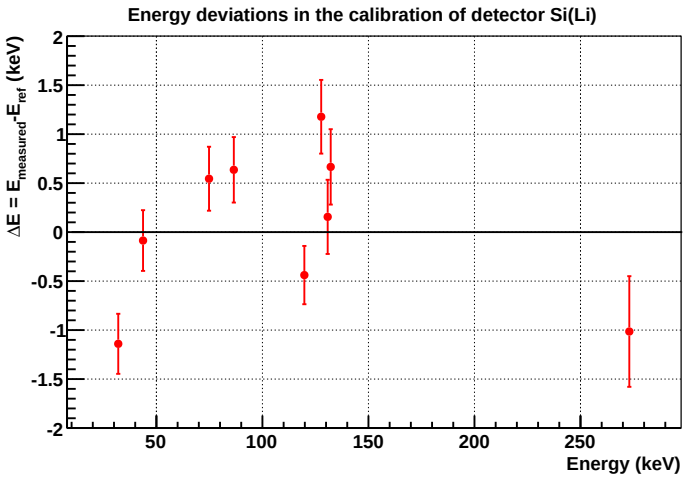

(a)

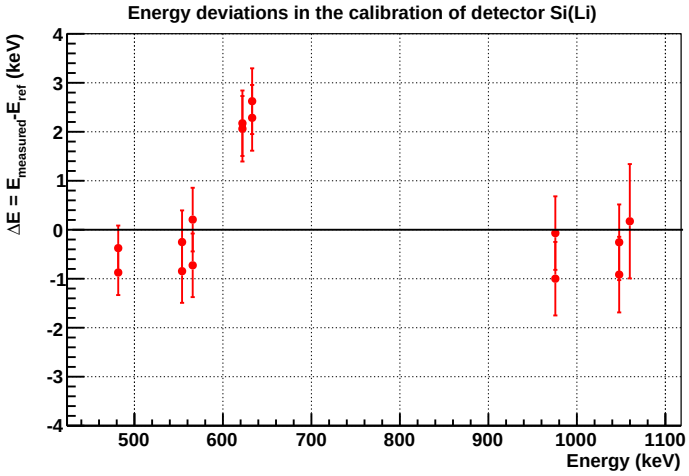

(b)

Figure 3.11: *Difference of the calibrated energies for the transitions included in the energy calibration of Si(Li) detector with respect to the reference values from [Sin06], [Far99], [Sin95] and [Mar93]. It has been performed in two different energy ranges, 0-400 keV (a) and 400-1100 keV (b). Plotted values are from the table 3.7.*

3.2.2 Efficiency calibrations of HPGe 1 and HPGe 2

Before going into details let us review some basic concepts.

One can define three different types of detector efficiency. It is known as **absolute efficiency** the proportion between the number of detected particles and the ones emitted by the source, mathematically can be expressed as:

$$\epsilon_{abs} = \frac{N_{detected}}{N_{emitted}} \tag{3.13}$$

The **geometrical efficiency** is defined as the ratio of the number of particles reaching the detector to the ones emitted by the source, that is:

$$\epsilon_{geom} = \frac{N_{reaching}}{N_{emitted}} \tag{3.14}$$

Finally, it is known as **intrinsic efficiency** the proportion between the number of detected particles with respect to the number of particles which reach the detector:

$$\epsilon_{int} = \frac{N_{detected}}{N_{reaching}} \tag{3.15}$$

All these three efficiencies are related by means of the following expression:

$$\epsilon_{abs} = \epsilon_{geom} \times \epsilon_{int} \tag{3.16}$$

The intrinsic efficiency is a characteristic of the detector which only depends on the physical properties of the detector material and its size (and the window in front) while the geometric efficiency only depends on the geometric configuration of the source-detector system (solid angle coverage by the detector view by the source).

On the other hand, one can define the **total efficiency** and the **photo-peak efficiency** depending on whether it is considered the deposition of part of the energy or the full energy in the detector, respectively. Mathematically, it can be expressed as follows:

$$\epsilon_{total} = \frac{N_{detected}}{N_{emitted}} \tag{3.17}$$

$$\epsilon_{photo-peak} = \frac{N_{photo-peak}}{N_{emitted}} \tag{3.18}$$

Photopeak efficiency is the magnitude of interest for us, because when the data collection involves several transitions, the γ-rays that have deposited only part of their energy in the detector volume are indistinguishable in the spectrum as they form a continuum region where contributions of γ-rays of different incident energy are mixed.

region of the spectrum piled up for all the incidents energies.

The only way to distinguish different incoming radiation is looking at the photo-peak where all the energy of the incoming photon is deposited. From now on, for simplicity, it will be used the term efficiency to refer to **absolute photo-peak efficiency**.

The calibration sources used are the same as in the energy calibration (shown in table 3.4). They were placed in the measurement position that is shown in fig. 3.1 with the help of a

Source	E_γ reference (keV)	I_γ(measured) (10^4 counts)	I_γ(expected) (10^4 counts)	Efficiency I_γ(measured)/I_γ(expected)
^{241}Am	13.9(1)	7.5(5)	299(17)	0.025(2)
^{241}Am	17.8(1)	14.6(2)	440(30)	0.033(2)
^{241}Am	20.8(1)	4.0(2)	110(7)	0.036(3)
^{241}Am	26.3448(2)	2.239(18)	54(3)	0.041(2)
^{133}Ba	30.851(2)	28.5(2)	607(64)	0.047(5)
^{133}Ba	35.2(1)	6.25(13)	141(15)	0.044(5)
^{152}Eu	45.5(1)	10.68(7)	210(20)	0.051(5)
^{133}Ba	53.1625(6)	0.580(13)	14.0(15)	0.041(4)
^{241}Am	59.5412(1)	39.04(6)	810(40)	0.048(2)
^{133}Ba	79.6139(13)	0.88(2)	16.7(18)	0.053(6)
^{133}Ba	80.9971(12)	9.47(4)	220(20)	0.044(5)
^{152}Eu	121.7817(3)	18.6(2)	400(40)	0.046(4)
^{133}Ba	160.6109(17)	0.159(15)	4.1(4)	0.039(5)
^{133}Ba	223.2373(14)	0.09(2)	2.9(3)	0.030(8)
^{152}Eu	244.6975(8)	2.43(2)	107(10)	0.023(2)
^{133}Ba	276.3997(13)	0.828(15)	46(5)	0.0182(19)
^{133}Ba	302.853(1)	1.918(17)	117(12)	0.0164(17)
^{152}Eu	344.279(1)	6.61(3)	370(30)	0.0177(16)
^{133}Ba	356.0134(6)	5.54(2)	390(40)	0.0140(15)
^{133}Ba	383.848(12)	0.822(12)	57(6)	0.0144(15)
^{152}Eu	443.965(3)	0.513(13)	44(4)	0.0116(11)
^{152}Eu	688.67(5)	0.092(8)	12.1(11)	0.0076(10)
^{152}Eu	778.905(2)	1.242(14)	183(17)	0.0065(6)
^{152}Eu	867.373(3)	0.295(9)	60(5)	0.0049(5)
^{152}Eu	964.079(18)	0.970(12)	206(19)	0.0047(4)
^{152}Eu	1085.869(24)	0.591(9)	144(13)	0.0041(4)
^{152}Eu	1112.069(3)	0.630(9)	192(17)	0.0033(3)

Table 3.8:
*Transitions used in the efficiency calibration of **HPGe 1 detector**. The first column shows the standard source used and in the second one the tabulated energy of every transition. The third column contains the measured intensity and the fourth the expected intensity taking as reference the gamma intensity from [Art96] for ^{152}Eu transitions, [Rab95] for ^{133}Ba transitions and [Bas06] for ^{241}Am transitions and the activity of each source from the table 3.4. The values for the absolute photo-peak efficiency appear in the last column and are obtained by dividing the values from 3^{rd} and 4^{th} columns. These values are the experimental points used in the efficiency curve shown in figure 3.13 (blue dots). Note that the expected intensities are estimated for the live time of the measurement.*

source holder that was supported on the magnets of the Miniorange with the aim of reproducing exactly the measurement position where the tape places the radioactive sample collected in the previous step of the movement.

The efficiency calibration of the HPGe 1 detector is shown in figure 3.13. The experimental values are taken from table 3.8 and represented by blue dots. The fit of these data points has been performed by using three different models.

1. The orange line is a **logarithmic series function** described by Z. Kis et al. in Ref. [Kis98]. The mathematical expression proposed by them is a polynomial in the natural logarithm, ln, of the relative energy E/E_0 and is given in eq. 3.19 where N is the maximum order considered in the fit. Each extra power-order term added to the fit improves the results but in order not to complicate the case the fit has been considered until 4^{th} order (i=0,..,4) and the value of the parameters obtained is shown in table 3.9.

$$ln\epsilon = \sum_{i=1}^{N} a_i \left(ln\frac{E}{E_0} \right)^{i-1} \tag{3.19}$$

Parameter	Value (Uncertainty)
a_0	-8.00(10)
a_1	2.07(4)
a_2	0.017(7)
a_3	-0.0665(12)
a_4	0.00482(13)

Table 3.9: *Value of the fitting parameters corresponding to the equation 3.19 of the experimental absolute efficiency data that appears in table 3.8 and are plotted in figure 3.13.*

2. The red line corresponds to the combination of expressions 3.20 and 3.21. The first one belongs to the work of **Gallagher** and collaborators [Gal74] on the efficiency of Si(Li) detectors in the energy range from 3.3 up to 136 keV so this is the approximate valid energy range for this expression. The second expression is the result from a systematic study of the efficiency of 60 Ge(Li) and HPGe detectors. This work was done by **Jäckel** and colleagues and further details can be found in [Jä87]. The energy range validity of this expression is, approximately, from 50 keV up to energy values where the losses due to the escape peaks of gamma radiation begin, that is, around 2500 keV. The combination of these two equations is needed to cover the whole reachable energy range with the detectors of the IS370-A experimental setup, which is from 20 up to 1300 keV as it was mentioned in the descriptions of the HPGe 1 and 2 detectors.

   The values of the a_i and b_i parameters and their uncertainties obtained in the fit of the experimental data are listed in tables 3.9(a) and 3.9(b). The matching point of the two expressions has been found to be in E=146 keV by imposing the conditions of continuity of the composed function and its derivative in the matching point in order to guarantee both, the continuity and smoothness of the resulting function.

$$\varepsilon(E) = b_1 \times exp(b_2 E^{b_3})[1 - exp(b_4 E^{b_5})] \tag{3.20}$$

$$ln\ \varepsilon(E) = 2(a_1 + a_2x + a_3x^2) \cdot \frac{arctan[exp(a_4 + a_5x + a_6x^3)]}{\pi} - 25 \text{ where x=ln(E)} \quad (3.21)$$

(a) Obtained values for the Gallagher function parameters, eq. 3.20, in the efficiency calibration of HPGe 1 detector

Parameter	Value (Uncertainty)
b_1	3.74771
b_2	-1.61957
b_3	0.21(11)
b_4	-0.0046(12)
b_5	1.27(12)

(b) Obtained values of the Jäckel function coefficients, eq. 3.21, for the efficiency calibration of HPGe 1 detector.

Parameter	Value (Uncertainty)
a_1	28.0(3)
a_2	-0.75(2)
a_3	-0.040(4)
a_4	2.3(4)
a_5	-0.14(13)
a_6	-0.0008(11)

Table 3.10: *Absolute efficiency calibration using equations 3.20 and 3.21 for the **HPGe 1 detector**.*

3. Finally, the violet line describes the result obtained from a **Monte Carlo simulation** performed by means of a **GEANT4** code [GEA] of the detector. The geometry of the simulations is shown in figure 3.12 where it can be observed the main components included as the HPGe crystal (blue), a thin beryllium foil (yellow), a mylar foil (red) located in the cap and the gamma radiation (green) coming from the measuring point at 2 cm from the mylar foil located at the end of the endcap.

   The simulation was mainly carried out to check the efficiency of the detector in the energy region from 80 to 150 keV where the conversion coefficients studied in this work mainly occur. Furthermore, in this region the two empirical curves show different behavior and the matching point of Gallagher and Jäckel expressions is placed. In general, it is always important to perform simulations to cross-check the results. cross-check. Furthermore, as the distance from the mylar foil located in the cover cap of the HPGe 1 detector to the measuring point was not known, the results of the simulation will help us to estimate this distance.

   In the simulation, gamma radiation from the source position was generated in 10 keV steps from 10 keV up to 150 keV and in 50 keV steps for higher energies.

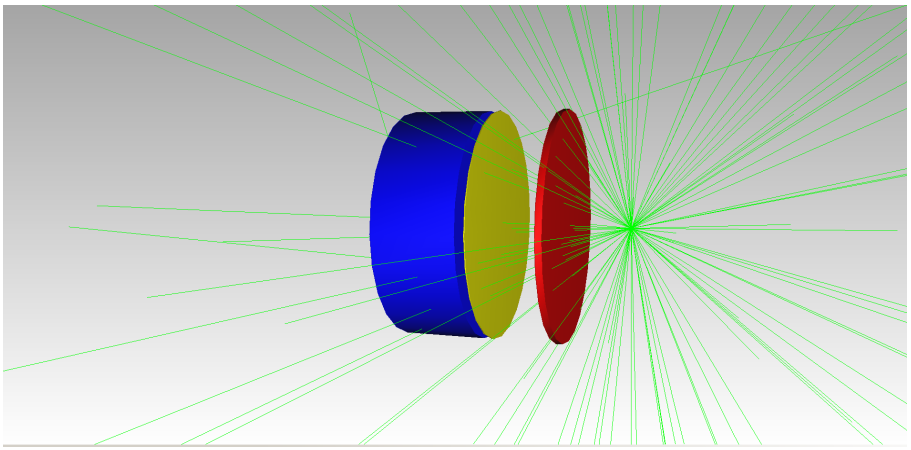

Figure 3.12: *Geometrical configuration of the GEANT4 simulations performed to obtain the absolute photo-peak efficiency of the **HPGe 1 detector**. The gamma radiation is plotted in green while the mylar foil is in red. The beryllium window of the detector is represented in yellow and the germanium crystal appears in blue. The distance detector-mylar foil is known to be 2 cm but the distance mylar foil-source is not known and it is defined as 2 cm to perform the simulations. An estimation of the real value will be obtained through the fit of the simulated absolute efficiency to the experimental one (see text).*

The exact source-detector distance was not known so an initial cap-source distance of 20 mm (2 cm) was used in the simulations. Later, a geometrical factor f was introduced to scale the efficiency curve to the experimental data.

The violet curve shown in figure 3.13 is the result obtained for the simulations fitted to the experimental dots in blue by using the scaling parameter f. The value of the parameter f which better fits the simulation to the experimental data is f=0.463. This means that the real cap-source distance is larger than the 20 mm assumed in the GEANT4 simulation. With this result, one knows that the real solid angle covered by the detector is 0.463 times smaller than the initial one so:

$$\Omega' = 0.463 \times \Omega = 0.463 \times 2\pi(1 - cos\ \theta) = 2\pi(1 - cos\ \theta') \tag{3.22}$$

Thus, the value of the real θ' angle is θ'= 26.76º and the real detector-source distance is:

$$d' = \frac{R}{tan\ \theta'} = 69.3\ mm \tag{3.23}$$

where, as the detector-cap is known to be 23 mm, the cap-source distance is:

$$D = (69.3 - 23)\ mm = 46.3\ mm \approx 4.6\ cm \tag{3.24}$$

instead of the 2 cm that were used in the code.

Figure 3.13 shows the three efficiency curves. The composed model of Gallagher plus Jäckel function is very similar to the simulated efficiency. In order to compare the fits of the 3 models, one can check the χ^2 values of the fits in table 3.11. The best statistical value is obtained with the simulated curve and the other two expressions have quite similar χ^2 values. One could use any of the three expressions as they produce similar χ^2 values, but the Gallagher plus Jäckel curve will be chosen for the analysis as it is closer to the data points in the energy

region from 80 up to 150 keV where most of the experimental conversion coefficients to be studied are located.

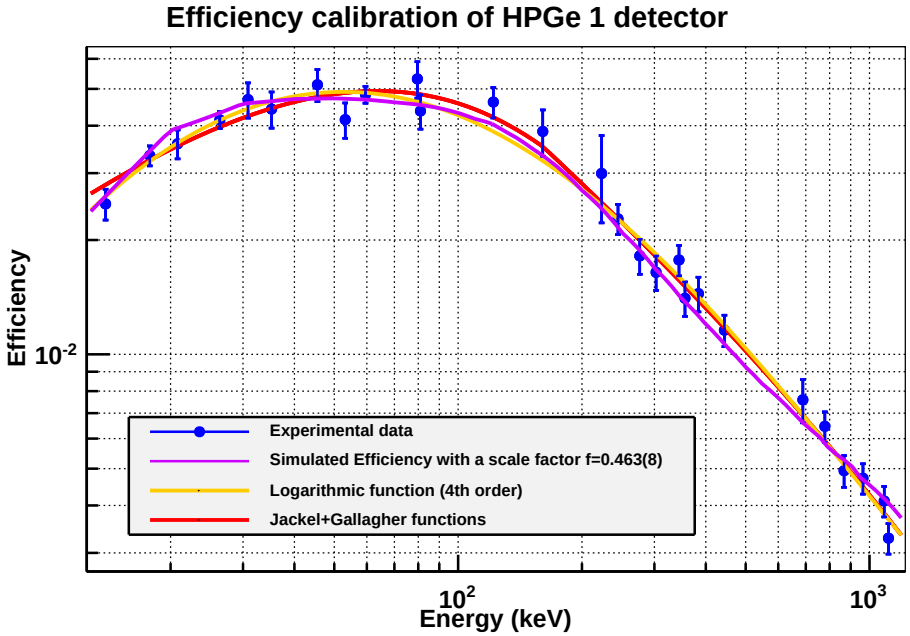

Figure 3.13: *Efficiency calibration of **HPGe 1 detector**. The experimental data in table 3.8 are the blue dots. The plot shows 3 different fits to the experimental points: the red line is a fit to a logarithmic series at 4th order as described in [Kis98], the orange line is the fit of a combination of equations 3.20 and 3.21 and the violet line is the simulated efficiency of the detector carried out with a GEANT4 code [GEA] describing the geometry of the setup where the detector-source distance was fitted (see text for further details).*

Function	χ^2	Numerator degrees of freedom (ndf)	χ^2/ndf
Gallagher + Jäckel	18.7	17	1.1
Logarithmic series 4^{th} order [Kis98]	19.7	22	0.90
GEANT4 simulation	26.9	26	1.03

Table 3.11: *Comparative table of the goodness of the fits performed for the 3 different functions employed in the efficiency calibrations for **HPGe 1 detector**. Note that the χ^2 values obtained are close to the unity indicating the goodness of the fits. As it can be observed, the best value of the ratio χ^2/ndf is reached with the simulation curve while Gallagher+Jäckel and logarithmic curves fit similarly well to the data.*

In order to be cautious with the value provided for the efficiency curve of this detector in the final analysis, a 10 percent uncertainty will be considered for every estimated efficiency in the analysis as shown in figure 3.14 where the green shaded region indicates a 10% uncertainty over the whole curve. In this figure, the final curve including its uncertainty is shown in comparison with the experimental data that lead us to obtain it. As can be seen, the uncertainty region considered guarantees that almost every data point from calibration sources is covered.

errors of each parameter of the fit gives uncertainties as small as 1 percent of the efficiency. 3.14 where the final curve and uncertainty region is shown.

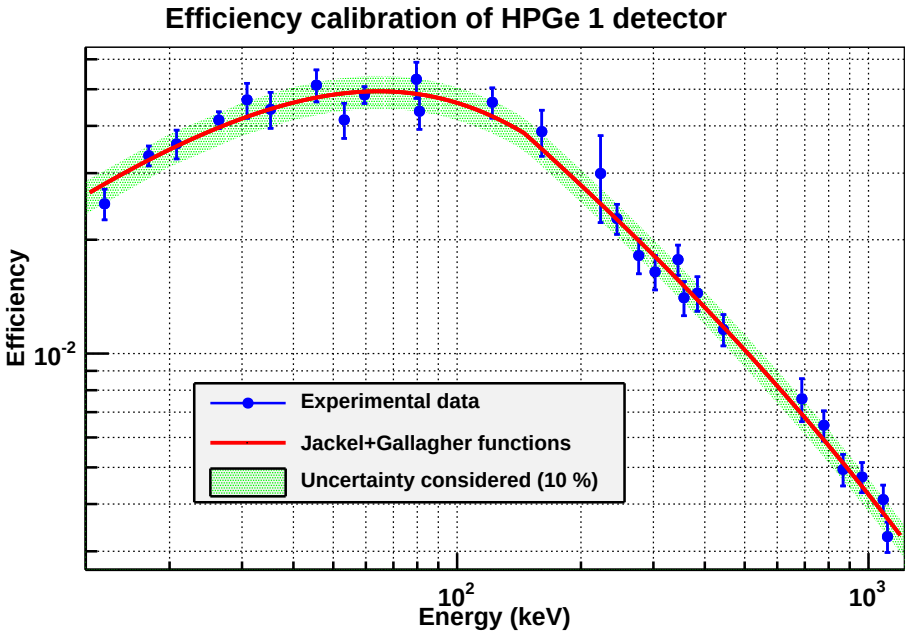

Figure 3.14: *Final efficiency calibration of **HPGe 1 detector** obtained by fitting the experimental data (blue dots) to Gallagher [Gal74] and Jäckel [Jä87] functions. The shaded region shows the uncertainty takes into account for the interpolation of the efficiency of this detector (10% of the efficiency value).*

In the case of HPGe 2, the experimental data is listed in table 3.12. As for this detector there are no many points available for the fit it have been tried only with the Jäckel function 3.21 which is valid for the energy range from 60 up to 1333 keV. The result of the fit is shown in figure 3.15. The curve reproduces the experimental data fairly well in the whole energy range. This result is enough for the current analysis as this detector is not going to participate in the determination of crucial observables and it has been mainly used for doing cross-checks.

The values obtained for the coefficients of the Jäckel expression are shown in table 3.13.

Source	E_γ reference (keV)	I_γ(measured) (10^3 counts)	I_γ(expected) (10^4 counts)	Efficiency I_γ(measured)/I_γ(expected)
^{133}Ba	30.851(2)	28.2(3)	556(15)	0.00507(13)
^{133}Ba	35.2(1)	11.0(3)	129(4)	0.0085(3)
^{152}Eu	39.906(2)	57.8(5)	780(3)	0.0074(2)
^{152}Eu	45.5(1)	19.1(5)	195(7)	0.0098(4)
^{241}Am	59.5412(1)	56.1(4)	696(8)	0.0081(1)
^{133}Ba	80.9971(12)	14.0(3)	199(3)	0.00705(15)
^{152}Eu	121.7817(3)	32.2(5)	374(3)	0.00862(15)
^{152}Eu	244.6975(8)	5.2(3)	99.3(9)	0.0053(3)
^{133}Ba	276.3997(13)	1.99(17)	42(2)	0.0048(5)
^{133}Ba	302.853(1)	3.71(17)	106.6(9)	0.00348(16)
^{152}Eu	344.279(1)	13.0(3)	350(3)	0.00370(9)
^{133}Ba	356.0134(6)	13.46(19)	361(3)	0.00373(6)
^{152}Eu	778.9045(24)	2.29(7)	171.1(15)	0.00134(4)

Table 3.12: *Transitions used in the efficiency calibration of the **HPGe 2 detector**. In the first column it is shown the radioactive source for every transition, in the second one the known energy of the transition. The third column shows the measured intensity for every transition, that is, the peak area measured. The fourth column indicates the expected intensity for every transition obtained from the transition intensity of references [Art96] for ^{152}Eu transitions, [Rab95] for ^{133}Ba transitions and [Bas06] for ^{241}Am transitions, the activity of each source indicated in table 3.4 and the live time of each measurement. Last column just shows the absolute efficiency for every transitions which is simply the ratio between measured and expected intensities shown in former two columns. These values are used in the fit shown in figure 3.15. Note that the expected intensities are estimated for the live time of the measurement.*

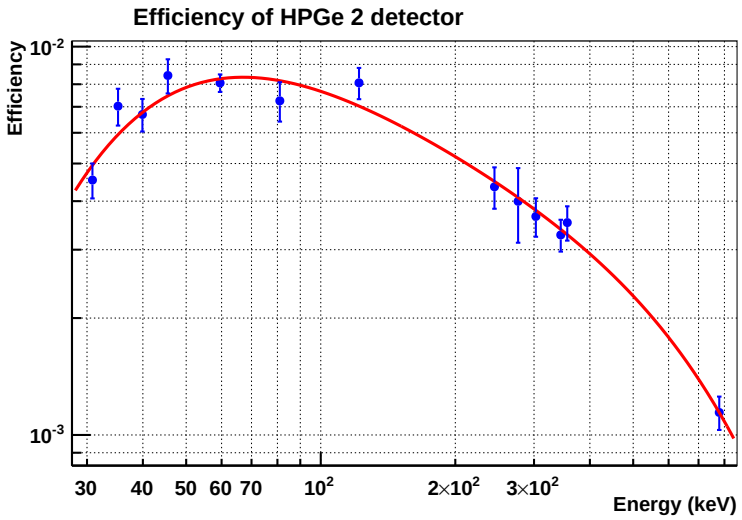

Figure 3.15: *Efficiency calibration of **HPGe 2 detector**. Experimental data are shown in blue dots and correspond to the values in table 3.12. The fit function used is the jackel equation 3.21 and the values for the fit parameters can be seen in table 3.13.*

Parameter	Value (Uncertainty)
a_1	-28.2(5)
a_2	30.64(14)
a_3	-3.12(2)
a_4	1.171(19)
a_5	-0.412(4)
a_6	0.00516(11)

Table 3.13: *Obtained values for the fit parameters of the eq. 3.21 to reproduce the experimental data for the efficiency of **HPGe 2 detector** shown in table 3.12. The resulting value for the parameter χ^2/NDF parameter was found to be 8.2/7 being 1.11, relatively close to the wanted value of the unity.*

3.2.3 Efficiency calibration of Si(Li) detector: Transmission curves

Once the efficiency calibration for HPGe 1 and HPGe 2 detectors are obtained, the next step in the analysis is to calibrate in efficiency the electron detection system: the Miniorange spectrometer plus Si(Li) detector.

In the case of the Miniorange spectrometer the efficiency to measure the full energy of the incoming particles (electrons in the present work) depends on two different components. On the one hand, the transmission efficiency of particles towards the Si(Li) detector, that is, the amount of electrons that the Miniorange spectrometer can deviate and focus towards the front surface of the Si(Li) detector. On the other hand, just the intrinsic efficiency of the Si(Li) detector for particle detection, i.e. once the particles impinge on the detector, how many of them are detected with the full energy deposited and contribute to the full-energy peak. The first component has much higher influence on the total efficiency of the system so from now on, the efficiency of the whole system composed of the Miniorange spectrometer and the Si(Li) detector will be called **transmission**.

electrons transmitted from the source to the Si(Li) detector

The efficiency of the electron spectrometer (Miniorange plus Si(Li) detector) is the proportion between the electrons detected: $I_e(detected)$ and the number of electrons emitted by the source $I_e(emitted)$, mathematically is expressed as follows:

$$\tau_e = \frac{I_e(detected)}{I_e(emitted)} \tag{3.25}$$

Each Miniorange configuration has its characteristic transmission curve so the calibration has to be evaluated for every magnet configuration. The method to obtain this curve consists of the following steps that have to be carried out for every transition:

1. **Absolute gamma intensity I_γ:** For a given transition between states i and j one can have a gamma transition of energy $E_\gamma = E_i - E_j$. The area of the gamma peak corresponding to the transition of interest is obtained from the HPGe 1 spectrum. As in the procedure there are different detectors involved (HPGe 1 and Si(Li)), it is required to correct the peak areas by the dead time of each detector. For this purpose the peak area is divided by the live time of the measurement in this data channel (t_γ). Then, the absolute gamma intensity of this transition (I_γ) is obtained dividing the peak area by the photo-peak effi-

ciency of each detector (ϵ(E$_\gamma$)). This leads us to the following expression:

$$I_\gamma = \frac{A_\gamma}{\epsilon(E_\gamma) \cdot t_\gamma} \tag{3.26}$$

the measurement in the data channel associated with the HPGe 1 detector.

2. **Absolute or emitted electron intensity I$_e$(emitted):** By using the conversion coefficient of the transition of interest (α) the intensity of the emitted electrons is calculated:

$$I_e(emitted) = \alpha \times I_\gamma = \frac{\alpha \cdot A_\gamma}{\epsilon(E_\gamma) \cdot t_\gamma} \tag{3.27}$$

3. **Detected electron intensity I$_e$(detected):** it is determined by correcting the electron-peak area in the Si(Li) detector (A$_e$) by deadtime, that is, dividing by the live time of the data channel (t$_e$) as it was done with the gamma transition counts.

$$I_e(detected) = \frac{A_e}{t_e} \tag{3.28}$$

4. **Electron transmission τ_e:** is obtained by means of the expression:

$$\tau_e = \frac{I_e(detected)}{I_e(emitted)} = \frac{A_e/t_e}{\alpha \times A_\gamma/(\epsilon(E_\gamma) \times t_\gamma)} = \frac{A_e \times \epsilon(E_\gamma) \times t_\gamma}{t_e \times \alpha \times A_\gamma} \tag{3.29}$$

Through the previous procedure one obtains experimental points of transmission vs. energy of the electron. As for the future data analysis is needed a interpolation of these data for the exact energies of the studied electron transitions, one has to obtain an interpolation curve which connects the experimental data points obtained previously. It is important to note that this curve is just an interpolation in between experimental data and not a proper fit of the data with physical meaning, so, in principle, the data points have not to be fitted to any mathematical model.

This interpolation curve in the full energy range of validity of every magnet system (labeled by D1/D2/NT as it was explained before) is called the **transmission curve**. In order to obtain the transmission curve of every Miniorange configuration, several mathematical expressions will be used but it is important to remember that this is just a way of guiding the eye and, in the analysis of the data will be the way to obtain the transmission for a certain electron energy in between the points used to deduce the transmission curve.

Before moving forward, it is necessary to clarify the meaning of the concept "$Tot - K$" that will be frequently used from now on. As it was explained before, the electron transitions that one can observe experimentally are named as K, L, M, etc..., depending on the original atomic shell of the electron which is ejected. Thus, K corresponds to the electrons from atomic shells with main quantum number n equals to zero, L to shells with n=1, M to shells with n=2, and so on.

The total conversion coefficient, α_T is the sum of all different electron transitions, eq. 3.30 . One can have the K-shell, L-shell, M-shell, etc... electron transitions in the spectra and, consequently measured the α_K, α_L, α_M, etc..., conversion coefficients.

$$\alpha_T = \alpha_K + \alpha_L + \alpha_M + \alpha_N + ... \tag{3.30}$$

Note as the energy of every conversion electron emitted in the de-excitation transition from the level i to j is:

$$E_e = E_i - E_j - B_e \tag{3.31}$$

where B_e is the binding energy of the electron in the shell where it was placed.

The electron binding energies for the case of bromine are shown in table 3.14. As can be seen, the energy difference in between K and L shell electrons is around 12 keV while between L and M electrons is around 1.5 keV and from M to N even smaller (around 0.2 keV). This means that the energy difference in the spectrum between electrons from K-shell and L-shell will be the same than their electron binding energies, see eq. 3.31.

As one can check in table 3.2, the best energy resolution provided by the Si(Li) detector is around 1.5-1.6 keV. This means that one will be able to discriminate K-shell from L-shell conversion electrons but will be harder to do this between L-shell and M-shell and impossible for M-shell and N-shell. So we define two types of conversion coefficients:

- α_K corresponding to K-shell electrons, and
- α_{Tot-K} corresponding to the rest of electron transitions, namely L-, M- and N-shell transitions.

Electron shell	Binding energy (keV)
K	13.4737
L_1, L_2, L_3	1.7820, 1.5960, 1.5499
M_1, M_2, M_3, M_4, M_5	0.2565, 0.1893, 0.1815, 0.0701, 0.069
N_1, N_2 N_3	0.0273, 0.0052, 0.0046

Table 3.14: *Electron binding energies for bromine (Z=35).*

The method to set the uncertainties used in this work is the propagation of the uncertainty of every physical quantity. This can be mathematically expressed for a generic physical quantity z which depends on two independent physical quantities x and y, such as z=q(x,y), as follows:

$$\Delta z = \sqrt{\left(\frac{\partial q}{\partial x}\right)^2 \cdot (\Delta x)^2 + \left(\frac{\partial q}{\partial y}\right)^2 \cdot (\Delta y)^2} \tag{3.32}$$

Thus, one has to apply this expression to our case given in equation 3.29, where the transmission τ depends on the variables A_e, ϵ, t_γ, t_e, α and A_γ in order to obtain the uncertainty for the transmission of the Miniorange system for a given electron transition.

Before starting with the determination of the transmission curves it is proper to remember the labeling of every Miniorange configuration that was done in section 3.1 where a sketch displaying the distances was given in fig. 3.6 and the sizes of each type of magnet was shown in fig. 3.7.

85/8/4B Miniorange

As stated before, during the experiment several Miniorange configurations were used in order to maximize the electron transmission in different energy ranges. In table 3.3, the four Miniorange configurations used in the experiment are shown and its approximate effective energy range for the electron detection.

In the case of 85/8/4B, the energy range is from 60 to 200 keV. The only external calibration source of electrons available, ^{207}Bi, does not have any electron transitions in this energy range as can be seen in table 3.23. For this reason, internal calibrations with ^{75}Kr beam were performed as some low-energy transitions in its decay have well-known conversion coefficients, see Ref. [Bea95, Far99].

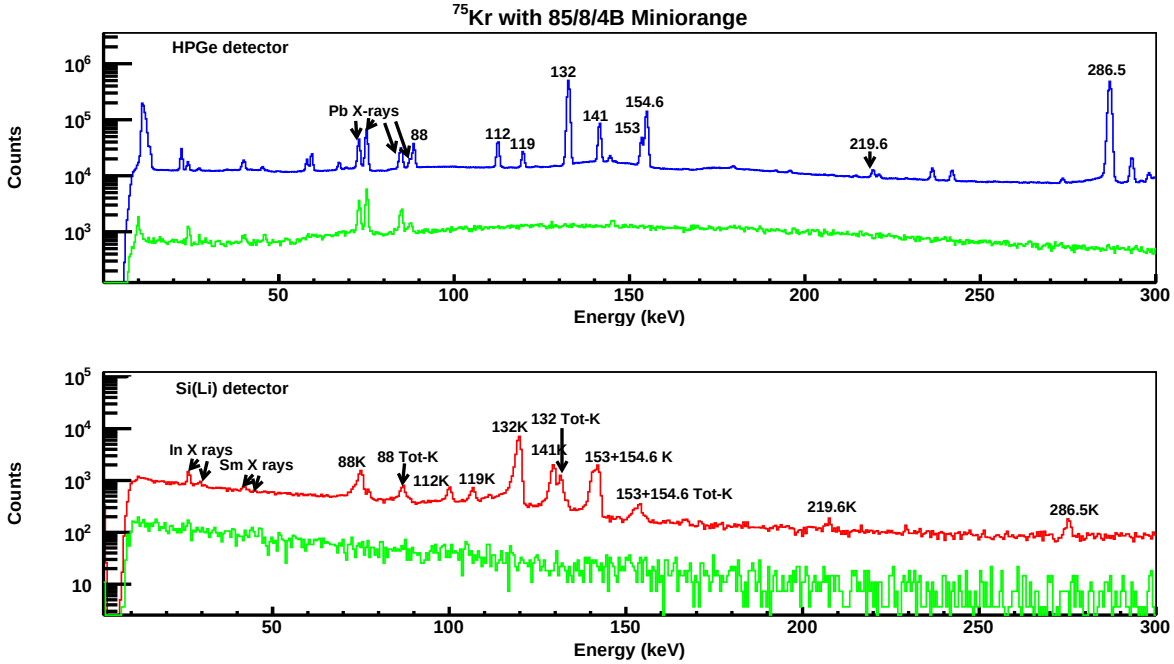

Figure 3.16: *Spectra taken with the Miniorange configuration 85/8/4B and ^{75}Kr as beam. In the upper part, the spectra from the HPGe detector measured with beam (blue) and without beam (green) are plotted in order to visually identify the peaks coming from the ^{75}Kr beam and the ones corresponding to the background radiation. Both spectra are normalized to the live time of the measurements. In the lower part, the spectra from the Si(Li) detector with beam (red) and without beam (green) are illustrated. The peaks used to obtain the transmission curve are labeled and listed in table 3.18.*

The spectra registered with both detectors, HPGe and Si(Li), in the ^{75}Kr measurement are shown in fig. 3.16. The corresponding spectra taken without beam are plotted in order to easily identify the peaks from the ^{75}Kr decay and the ones from the background radiation. In table 3.18 it appears the list of transitions used to obtain the transmission curve for the 85/8/4B spectrometer.

The data have been separated in three energy ranges in the fitting procedure to better describe the experimental data:

- The first energy range is **50-120 keV** and has been fitted with the expression 3.33, a gaussian plus constant function. The resulting values for the coefficients can be seen in table 3.15.

$$\tau_e(E) = \tau_0 + \frac{A}{\sigma \cdot \sqrt{\pi/2}} \times e^{-2\cdot[(E-C)/\sigma]^2} \tag{3.33}$$

Coefficient	Value
τ_0	0.0014
A	20.32
σ	41.12
C	203.99

Table 3.15: *Values of the different parameters for expression 3.33 obtained in the fit of the data listed in table 3.18 corresponding to the Miniorange configuration 85/8/4B in the energy range from 0 up to 120 keV.*

- The second range is **120-140 keV** and it has been fitted to the expression 3.33 as well. The obtained coefficient values are shown in table 3.16.

Coefficient	Value
τ_0	0.001
A	1.128
σ	13.06
C	130.5

Table 3.16: *Same as Table 3.15 for the energy range 120-140 keV.*

- The third range is **140-300 keV** and the data have been fitted to the equation 3.34. The values of the coefficients are shown in table 3.17.

$$\tau_e(E) = \tau_0 + e^{a_0 + a_1 E} \tag{3.34}$$

Coefficient	Value
τ_0	8.76×10^{-4}
a_0	0.647
a_1	-0.0307

Table 3.17: *Same as Table 3.15 for expression 3.34 in the energy range from 140 up to 300 keV.*

The global result for the transmission of the Miniorange configuration 85/8/4B is shown in figure 3.17.

Nucleus	E_γ (keV)	Electron shell	E_e (keV)	α [Bea95]	α [Roe74, Cob72]	α considered	τ_e
^{75}Br	88.29(6)	K	74.82(6)	1.5(2)	1.07(27)	1.35(16)	0.0029(5)
^{75}Br	88.29(6)	L+M	86.51(6)	0.282(45)	0.21(7)	0.25(3)	0.0047(5)
^{75}Se	112.1(1)	K	99.7(1)	0.076(13)		0.076(13)	0.0086(13)
^{75}Br	119.5(1)	K	106.0(1)	0.084(14)		0.084(14)	0.015(2)
^{75}Br	132.43(8)	K	118.96(8)	0.032(5)	0.032(3)	0.032(3)	0.024(3)
^{75}Se	141.3147(22)	K	128.66	0.034(5)		0.034(5)	0.0351(18)
^{75}Br	153.15(5)	K	139.68(5)	0.032(5)	0.026(5)	0.026(5)	0.0263(18)
^{75}Br	154.66(9)	K	141.19(9)	0.022(4)			
^{75}Br	153.15(5)	L	151.37(5)	0.0044(11)	0.005(2)	0.005(2)	0.017(5)
^{75}Br	154.66(9)	L	152.88(9)	0.0029(7)			
^{75}Br	219.6(3)	K	206.1	0.07(3)		0.07(3)	0.0046(19)
^{75}Se	286.5(2)	K	273.8	0.0036(11)	0.0028(4)	0.0029(4)	0.0013(2)

Table 3.18:
List of transitions taken into account to obtain the transmission curve of the 85/8/4B configuration of the Miniorange spectrometer. The electron transitions 153.15K and 154.66K are not distinguishable for us (the energy resolution of the Si(Li) detector is worse than 1.5 keV at these energies, see table 3.2). Therefore, they have been considered as a doublet transition located at the weighted-average energy of them, that is 154.241 keV, and with a conversion coefficient obtained as the weighted average of the two coefficients. Similar procedure has been followed for the L components of this doublet. doublet transition. The values of the conversion coefficients have been taken from [Bea95] (5^{th} column), [Roe74] for ^{75}Br transitions and [Cob72] for the 286.5 keV transition of ^{75}Se (6^{th} column). When values are provided in both references, the weighted average by their uncertainties are considered in the calculation (7^{th} column).

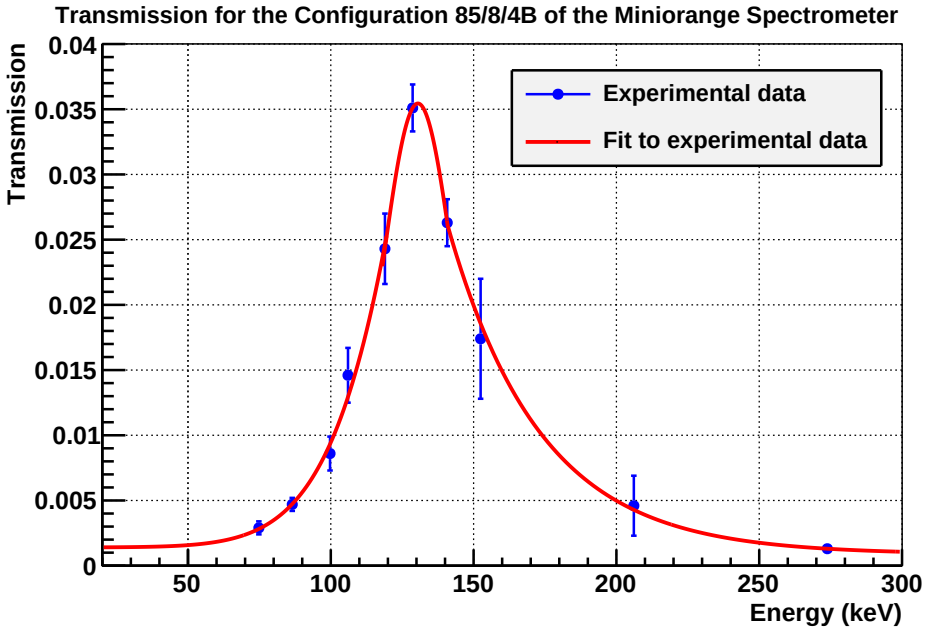

Figure 3.17: *Transmission curve for the configuration 85/8/4B of the Miniorange spectrometer. The experimental data are the values from table 3.18. As in the current analysis it is necessary to obtain the transmission for the whole energy range, the experimental data have been fitted in order to interpolate the value of the transmission. The error bars have been estimated to be 20% of the the transmission value (± 20 %) in order to be of similar amplitude than the experimental data points.*

125/8/3B Miniorange

The effective energy range for electron detection of this configuration is, approximately, from 20 up to 200 keV. The spectra taken with a ^{76}Kr beam is shown in figure 3.18 for the HPGe 1 and Si(Li) detectors. As it can be seen, there are only three useful converted transitions to obtain the transmission curve: the 45K, 45Tot-K and 103K transitions. These 3 data points are not enough to define a proper curve.

It is important to note the background contamination in the Si(Li) spectrum coming from the indium X-rays as its contribution is added to the peak area corresponding to the 45.5K transition. The estimation of this contamination has been determined from the green spectrum plotted in the lower part of the figure 3.18 which corresponds to a background measurement performed just before the ^{76}Kr one.

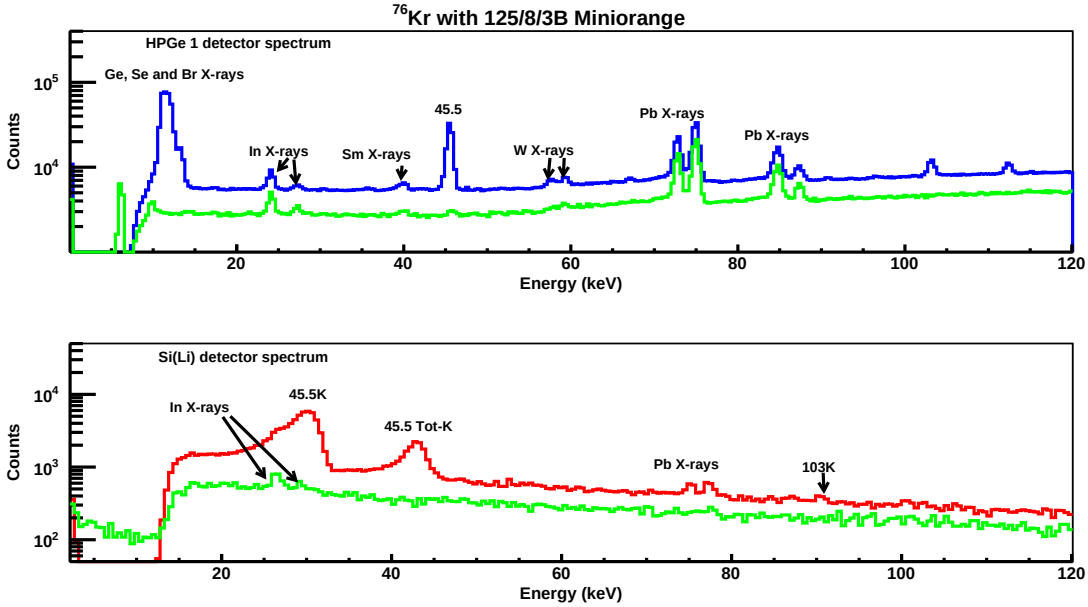

Figure 3.18: *Spectra taken using the Miniorange configuration 125/8/3B with the HPGe 1 detector (top) and Si(Li) detector (bottom) with a ^{76}Kr beam. In the Si(Li) spectrum it can be noticed that only 3 electron transitions can be used to obtain the transmission curve as the rest of transitions observed in the spectrum are coming from X-rays of some surrounding components in the setup. Green spectra are the same detector spectra for a background measurement carried out just before the real measurement in order to identify possible background contaminants as, for example, indium and lead X-rays seen in both spectra. These background spectra are scaled in order to correspond to the same live time that the in-beam measurement. The indium X-rays have been subtracted from the 45.5K peak area in the Si(Li) spectrum in order to calculate the transmission for this energy.*

Fortunately, the study of the conversion coefficients in the beta decay of ^{75}Kr done by J. Bea and collaborators [Bea95] was performed with the same Miniorange spectrometer and with the same magnets configuration. The transmission curve for this configuration was carried out using a ^{77}Kr beam. The transmission points obtained by them is shown with blue squared dots in fig. 3.18.

The list of transitions used to obtain the transmission curve is shown in table 3.19 and it includes the three available transitions from the ^{76}Kr measurement of the measurement of this

work (first three rows in the table), and the transitions from J. Bea et al. work (from 4^{th} row on).

Nucleus	E_γ (keV)	Transition	E_e (keV)	α [Par73]	τ_e
^{76}Br	45.48	K	32	0.96(9)	0.028(4)
^{76}Br	45.48	L+M	45	0.13(1)	0.049(6)
^{76}Br	103.3	K	89.8	0.10(1)	0.007(2)
^{77}Kr	66.52	K	52.2	-	0.0455
^{77}Kr	66.52	L	64.6	-	0.0283
^{77}Kr	66.52	M	66.2	-	0.021
^{76}Br	103.3	K	89.8	-	0.01
^{77}Br	105.87	K	92.4	-	0.0082
^{77}Br	105.87	L	104.1	-	0.0064
^{77}Br	129.64	K	116.2	-	0.0052
^{77}Br	146.59	K	133.1	-	0.0037
^{77}Kr	178.78	K	164.5	-	0.0019

Table 3.19: *Transitions used to obtain the transmission curve for the Miniorange 125/8/3B. The three transitions from ^{76}Br are from the measurement of IS370-A experiment with a ^{76}Kr beam that can be seen in the spectra 3.18. The conversion coefficients needed to obtain the transmission for these transitions are taken from the work of Paradellis et al. [Par73]. The rest of transitions are taken from the work of J. Bea and collaborators [Bea95] which was performed with the same Miniorange spectrometer. These data are plotted in fig. 3.19.*

In order to be able to interpolate the value of the transmission with this Miniorange in the whole effective energy range (20-200 keV), the experimental data have been fitted to mathematical models as explained earlier in the text. To better adjust to the experimental data the fit has been carried out in three different energy ranges.

- The first energy range is from **20 to 50 keV** and the function considered in this region to be fitted is eq. 3.35 with the values of the parameters shown in table 3.20.

$$\tau_e(E) = \tau_0 + \frac{A}{\sigma \cdot \sqrt{\pi/2}} \times e^{-2\cdot[(E-C)/\sigma]^2} \tag{3.35}$$

Coefficient	Value
τ_0	0.0
A	0.050
σ	13.53
C	46.35

Table 3.20: *Values of the coefficients of expression 3.33 obtained in the fit of the data in table 3.19 corresponding to the Miniorange configuration 125/8/3B in the energy range from 20 up to 50 keV.*

- The second one is from **50 to 90 keV** and it has been fitted to the eq. 3.36, obtaining as a result the values of the parameters expressed in table 3.21.

$$\tau_e(E) = \tau_0 + \tau_1 \cdot E + \frac{A}{\sigma \cdot \sqrt{\pi/2}} \times e^{-2\cdot[(E-C)/\sigma]^2} \tag{3.36}$$

Coefficient	Value
τ_0	0.031
τ_1	-2.63 $\times$ 10^{-4}
A	0.9
σ	11.97
C	48.17

Table 3.21: *Same as Table 3.20 using the expression 3.36 in the energy range 50-90 keV.*

- The third energy range is from **90 up to 200 keV** and the function to fit is eq. 3.37. The values for the coefficients in this expression obtained through the fit are shown in table 3.22.

$$\tau_e(E) = a_0 + a_1 \cdot E + e^{(c_0 + c_1 \cdot E)} \tag{3.37}$$

Coefficient	Value
a_0	-0.018
a_1	5.27$\times$$10^{-5}$
c_0	-3.04
c_1	-8.83$\times$$10^{-3}$

Table 3.22: *Same as Table 3.20 using the expression 3.37 in the energy range 90-200 keV.*

The experimental data as well as the fitting functions are plotted in fig. 3.19.

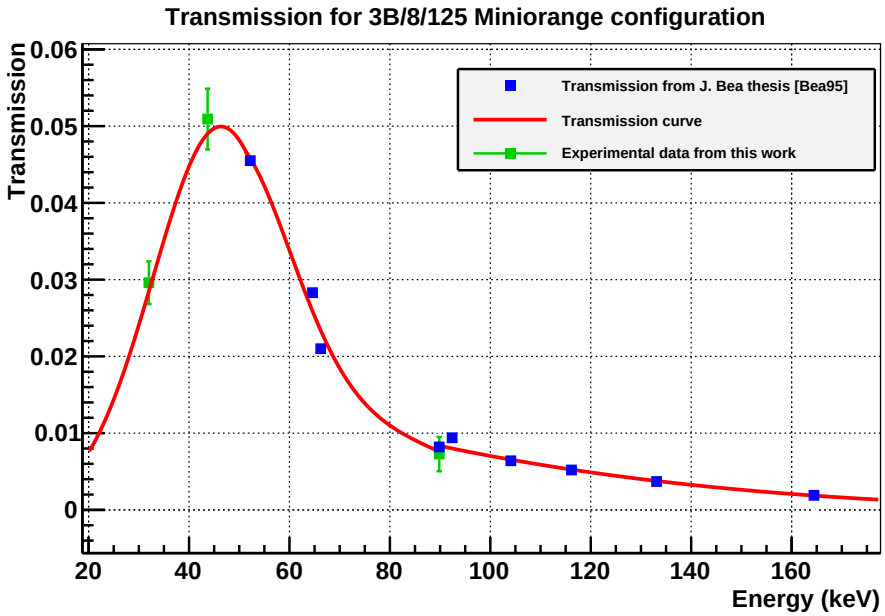

Figure 3.19: *Transmission curve for 125/8/3B Miniorange. The data considered are listed in table 3.19 where only three experimental points (green dots) belong to the measurement of IS370-A experiment. The rest of the data are taken from [Bea95] (blue dots). Mathematical expressions for interpolation are obtained in three energy ranges as explained in the text.*

110/8/6A Miniorange

This configuration provides us with best electron efficiency for higher energies. The effective energy range of this configuration is approximately from 400 up to 1200 keV.

In this case one can use the transitions from ^{207}Bi source as their energy are in the effective energy range for this configuration. The level scheme for the ^{207}Bi decay is shown in figure 3.20 and the conversion coefficients for the two more intense transitions are given in table 3.23. The experimental spectrum taken with this Miniorange configuration together with the one taken with the next configuration are shown in fig. 3.23. One can clearly observe the K, L and M components for each of the two transitions in both spectra but with different transmission with each configuration.

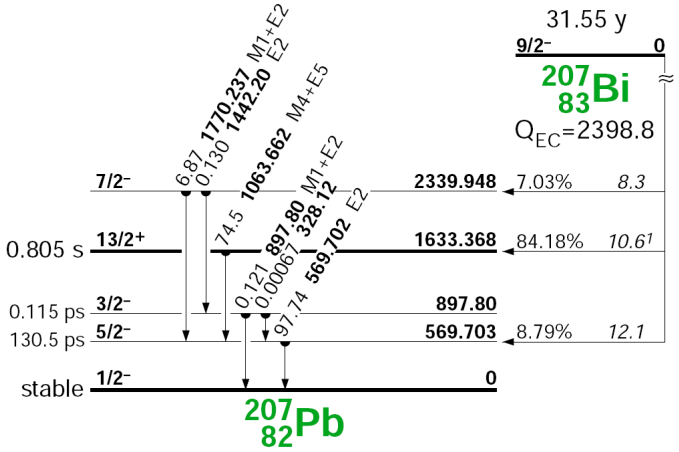

Figure 3.20: *Decay scheme of ^{207}Bi take from [Fir96]. The most intense transitions are the 1063.662 and 569.702 keV transitions and as their multipolarities are quite high, M4+E5 and E2 respectively, they both show conversion eletrons as can be seen in figure 3.23 that will be used for calibration purposes of the Si(Li) detector and to obtain the transmission curves of the Miniorange spectrometer. The conversion coefficients for these transitions is shown in table 3.23.*

		Conversion coefficients (α)		
E_γ (keV)	Intensity (%)	α_K	α_L	α_M
569.698(2)	97.74(3)	0.0155(5)	0.00433(15)	0.001085(5)
1063.656(3)	74.5(2)	0.097(2)	0.0247(14)	0.0060(4)

Table 3.23: *Information on the most intense gamma transitions in the ^{207}Bi source. The corresponding conversion coefficients of each transitions taken from [Mar93] are provided as well.*

The measurements to extract the transmission curve for this configuration were performed with a ^{74}Kr beam. As a result, the measured spectra are shown in figure 3.21. From this measurement, three converted transitions can be used for the transmission curve since the 853K belongs to an E0 transition and, consequently, there is no gamma line associated in the HPGe 1 spectrum.

A problem was found with the 728K transition. As can be seen in the HPGe 1 spectrum, the 728 keV gamma transition is observed in both, the ^{74}Kr beam and background measurements. This means that some counts in the 728 keV peak are coming from outside the measurement position. Probably, this radiation is coming from the tape which is stored in the white rollers located in the left side of the chamber in figure 3.1. This unwanted radiation could be measured in the background measurement and had to be subtracted from the ^{74}Kr beam measurement.

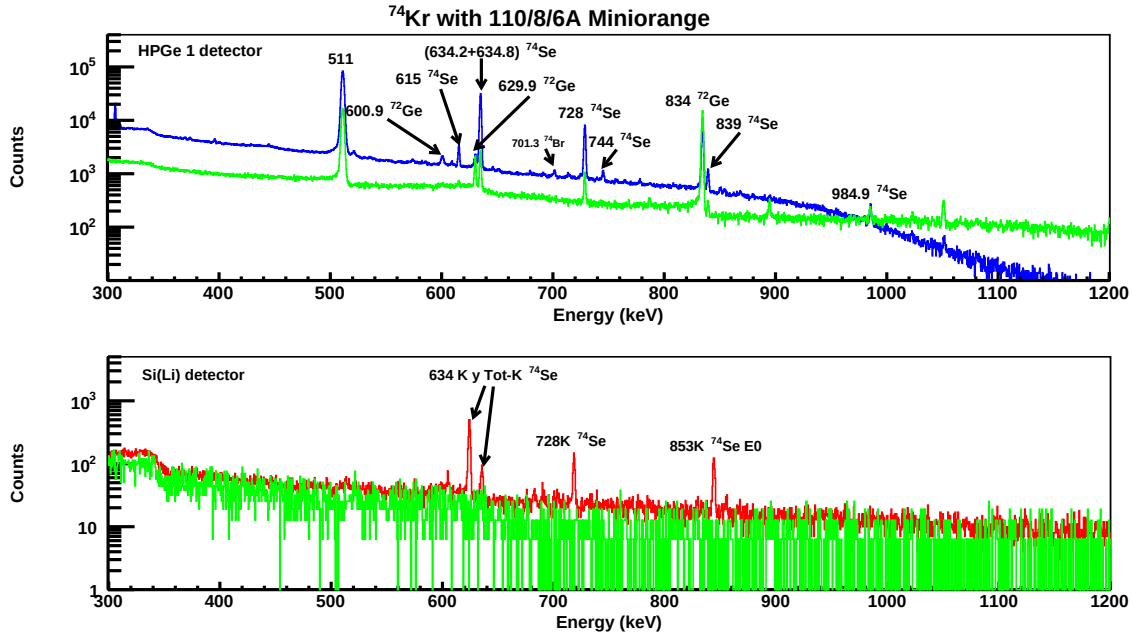

Figure 3.21: *Spectra taken with a ^{74}Kr beam on HPGe 1 (top spectrum) and Si(Li) (bottom spectrum) detectors when the 110/8/6A Miniorange configuration was used. In both spectra, the background spectra is overlaid in green in order to easily identify background contaminants. Background spectra are scaled in order to show the statistics corresponding to the same live time of the ^{74}Kr measurement. In the Si(Li) spectrum, the 634K, 634Tot-K and 728K transitions in ^{74}Se can be used in the determination of the transmission curve. One should notice that the 853K transition belongs to an E0 transition so there is no gamma transition associated and it is not possible to use it to obtain the transmission curve.*

Apart from the measurement with the internal source of ^{74}Kr beam, a measurement with an external ^{207}Bi source was performed with this Miniorange configuration.

In addition, in order to better describe the transmission curve in the whole effective energy range (400-1200 keV), it was necessary to add a couple of well-known transitions from the measurement with ^{72}Kr beam that, in principle, was carried out to obtain the conversion coefficients of transitions not previously known among the objectives of the present work. The 862K and 774.7K transitions in the de-excitation process of excited states in ^{72}Se fed by beta decay of ^{72}Br are both well-known E2 transitions, so the theoretical values of the conversion coefficients for these transitions (their multipolarity and energy) are calculated using the web tool [ANU].

The data included in table 3.28 are the transitions considered to obtain the transmission curve in figure 3.22. This set of data has been fitted to several curves in different energy ranges in order to better reproduce all the experimental data. Thus, the effective energy range from 200 up to 1200 keV has been divided in 4 ranges:

- **200 - 570 keV**: the fit function considered is equation 3.38 and the resulting values for the coefficients are given in table 3.24.

$$\tau_e(E) = \tau_0 + \frac{A}{\sigma \cdot \sqrt{\pi/2}} \times e^{-2\cdot[(E-C)/\sigma]^2} \tag{3.38}$$

Coefficient	Value
τ_0	5.0×10^{-3}
A	1711.76
σ	295.79
C	1504.63

Table 3.24: *Values of the coefficients of expression 3.38 obtained in the fit of the data in table 3.28 corresponding to the Miniorange configuration 110/8/6A in the energy range from 200 up to 570 keV.*

- **570 - 760 keV**: the fit function considered is a gaussian function, i.e. equation 3.38, with the value of the parameters shown in table:

Coefficient	Value
τ_0	0.0
A	8.40×10^{-2}
σ	70.39
C	684.02

Table 3.25: *Same as Table 3.24 for the energy range 570-760 keV*

- **760 - 850 keV**: the fit function considered is an exponential decay to reproduce the tendency observed in the data. It can be expressed as equation 3.39 with the value of the parameters given in table 3.26.

$$\tau_e(E) = \tau_0 + e^{a_0 + a_1 E} \tag{3.39}$$

Coefficient	Value
τ_0	0.0
a_0	2.81
a_1	-7.68 $\times 10^{-3}$

Table 3.26: *Same as Table 3.24 using the expression 3.39 for the energy range 760-850 keV*

- **850 - 1200 keV**: the fit function considered is an exponential plus constant (eq. 3.39) as well. The resulting values for the coefficients can be found in table 3.27.

Coefficient	Value
τ_0	5.0×10^{-3}
a_0	2.57
a_1	$-7.66 \cdot 10^{-3}$

Table 3.27: *Same as Table 3.24 using the expression 3.34 for the energy range 850-1200 keV*

Nucleus	E_γ (keV)	Transition	E_e (keV)	α	τ_e
^{207}Pb	569.7	K	481.69	0.0155(5)	0.0109(17)
^{207}Pb	569.7	L	553.84	0.00433(15)	0.018(3)
^{207}Pb	569.7	M	565.85	0.00109(5)	0.020(3)
^{74}Se	634.7	K	622.03	0.0012(1)	0.057(9)
^{74}Se	634.7	L	633.03	0.00015(1)	0.064(16)
^{74}Se	728.3	K	715.71	0.00083	0.076(12)
^{72}Se	774.7	K	762.07	0.000705	0.047(19)
^{72}Se	862	K	849.37	0.000537	0.024(4)
^{207}Pb	1063.6	K	975.65	0.097(2)	0.0130(19)
^{207}Pb	1063.6	L	1047.8	0.0247(14)	0.0092(15)
^{207}Pb	1063.6	M	1059.8	0.0060(4)	0.0086(15)

Table 3.28: *List of transitions used to obtain the transmission curve for the 110/8/6A configuration of the Miniorange spectrometer. The required conversion coefficients (α) for ^{207}Pb transitions (fed by ^{207}Bi beta decay) have been taken from [Mar93], while for the ^{72}Se 862K and 774.7K transitions, confirmed as E2 transitions, theoretical α have been used from [ANU]. For ^{74}Se transitions the values have been taken from [Sin06].*

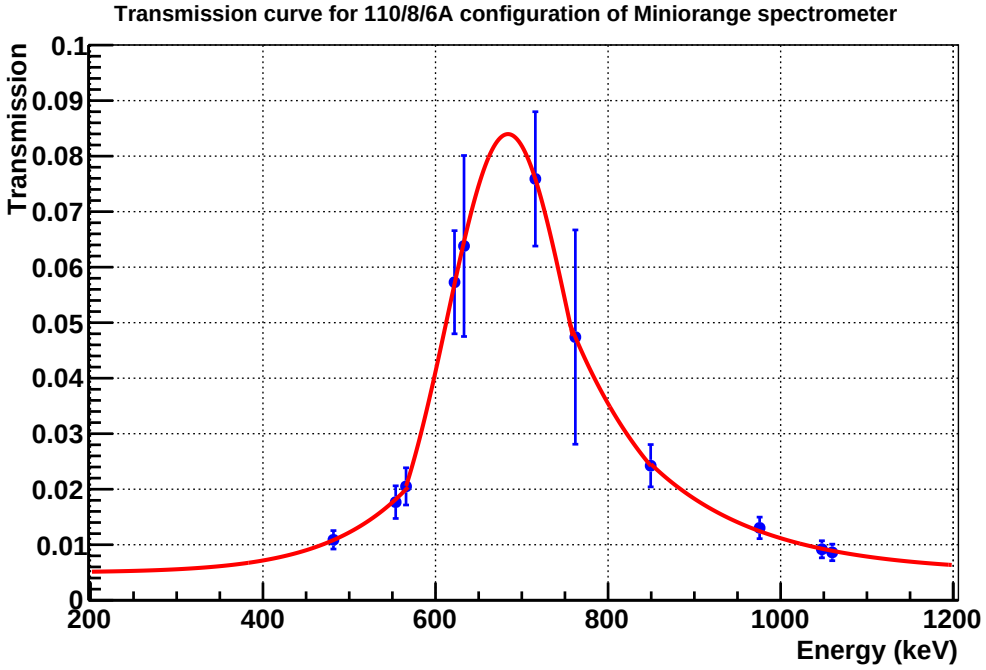

Figure 3.22: *Transmission curve of the 110/8/6A Miniorange configuration. As described in the text, transitions from ^{74}Se, ^{207}Pb and ^{72}Se are considered (see table 3.28). The red line is the result from the data fit with the curves 3.38-3.39 in four energy ranges and the resulting values for the parameters are given in tables 3.24-3.25-3.26-3.27.*

125/8/6A Miniorange

The fourth configuration used in the experiment was 125/8/6A. This configuration provides us with better electron efficiency for lower energies than the previous 110/8/6A. This fact can be observed in the comparison of spectra done with both configurations in figure 3.23 for the measurements with the ^{207}Bi source. It is remarkable the fact that the transmission

efficiency is higher for the configuration 125/8/6A in the energy range around 400-600 keV while it is lower for more energetic electron transitions than the 110/8/6A configuration. For example this is observed in the range 900-1100 keV just by checking the peak areas of electron transitions coming from the ^{207}Bi source: 569K, 569L and 569M associated to the 569 keV gamma transition and 1063K, 1063L and 1063M associated to the 1063 keV gamma transition in the de-excitation of ^{207}Pb.

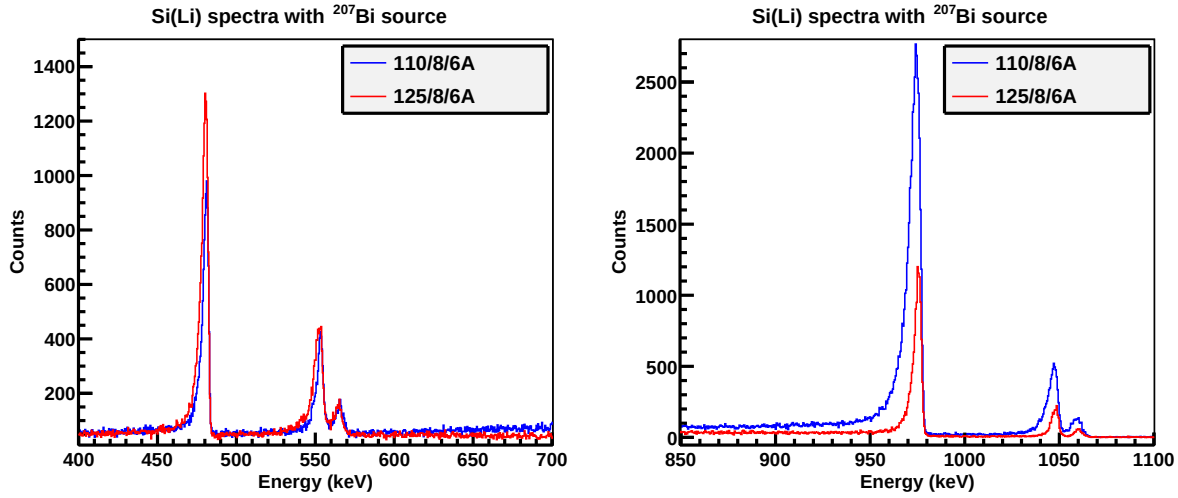

Figure 3.23: *Comparison of ^{207}Bi spectra taken with the Miniorange configurations 110/8/6A and 125/8/6A in two different energy ranges, one from 400 keV up to 700 keV (left side) and the other from 850 keV up to 1100 keV (right side), where the ^{207}Bi source has their electron transitions. The transmission efficiency of configuration 125/8/6A is higher for the energy range 400-700 keV and lower for 850-1100 keV than configuration 110/8/6A as can be seen in both figures where the areas of peaks 569K, 569L or 569M on the left side, and 1063K, 1063L and 1063M on the right side of the figure are plotted.*

Apart from the ^{207}Bi source, measurements with ^{74}Kr and ^{72}Kr beams were performed. The spectra corresponding to the measurement with ^{74}Kr as beam are shown in figure 3.24. The main transitions are indicated.

In the same way as in the previous configuration, some transitions in the decay chain of mass 72 beam were taken into account as they are well known E2 transitions. In this case only the 862K transition was considered as the transmission efficiency for these energies is lower than in the previous Miniorange configuration. The 774K transition is much less intense so it is not appreciable in this spectrum. Additionally, one transition from ^{74}Br de-excitation at 293 keV was used in order to extend the energy range to lower energies.

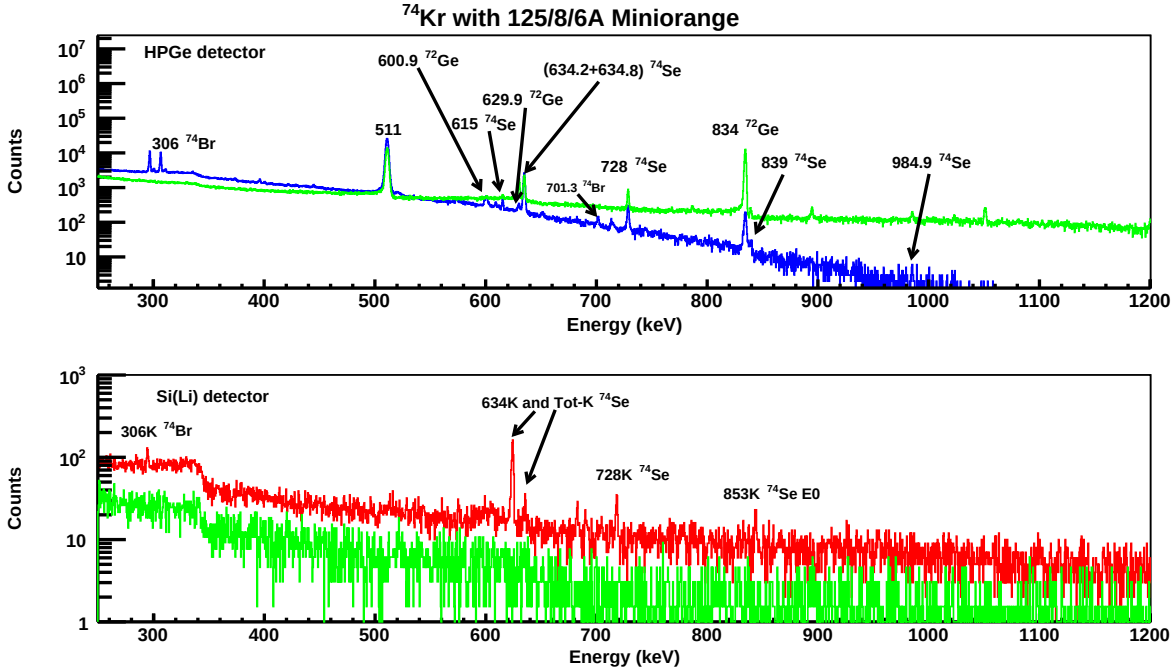

Figure 3.24: *Spectra taken with the Miniorange configuration 125/8/6A and ^{74}Kr as beam. In the upper part, the spectra from the HPGe detector measured with beam (blue) and without beam (green) are plotted in order to visually identify the peaks coming from the ^{74}Kr beam and the ones corresponding to the background radiation. Both spectra are normalized in order to be shown for the same live time of the measurements. In the lower part, the spectra from the Si(Li) detector with beam (red) and without beam (green) are illustrated. The peaks used to obtain the transmission curve are labeled and listed in table 3.32.*

In table 3.32 all the transitions used in the preparation of the transmission curve of this configuration are listed.

The data has been fitted to different models in three energy ranges.

- The first one is from **200 till 565 keV**, and the function used is a gaussian plus a constant (eq. 3.40). The values of the parameters are listed in table 3.29.

$$\tau_e(E) = \tau_0 + \frac{A}{\sigma \cdot \sqrt{\pi/2}} \times e^{-2\cdot[(E-C)/\sigma]^2} \tag{3.40}$$

Coefficient	Value
τ_0	5.0×10^{-3}
A	12.85
σ	97.56
C	514.45

Table 3.29: *Values of the coefficients of expression 3.40 obtained in the fit of the data in table 3.32 corresponding to the Miniorange configuration 125/8/6A in the energy range from 200 up to 565 keV.*

- The second region is from **565 up to 850 keV** and the model to be fitted to the data is a gaussian plus constant (eq. 3.40). The value of the fit parameters are shown in table 3.30.

Coefficient	Value
τ_0	5.0×10^{-3}
A	44.72
σ	238.59
C	330.33

Table 3.30: *Values of the coefficients of expression 3.40 obtained in the fit of the data in table 3.32 corresponding to the Miniorange configuration 125/8/6A in the energy range from 565 up to 850 keV.*

- Finally, the last energy region is from **850 up to 1100 keV** and the model function used to interpolate the data is exponential plus linear function 3.41. The value of the parameters is shown in table 3.31.

$$\tau_e(E) = a_0 + a_1 \cdot E + e^{(c_0 + c_1 \cdot E)} \tag{3.41}$$

Coefficient	Value
a_0	-1.53×10^{-2}
a_1	6.77×10^{-6}
c_0	-1.66
c_1	-2.55×10^{-3}

Table 3.31: *Values of the coefficients of expression 3.41 obtained in the fit of the data in table 3.32 corresponding to the Miniorange configuration 125/8/6A in the energy range from 850 up to 1100 keV.*

The graphical representation of the data, the fit functions used and the comparison of the transmission curves for the 110/8/6A and 125/8/6A configurations can be seen in figure 3.25. In this figure it can be noticed that the transmission with configuration 110/8/6A is better at higher energies than 125/8/6A as it was mentioned when the ^{207}Bi spectra from both configurations were compared in fig. 3.23.

Nucleus	E_γ (keV)	Transition	E_e (keV)	α	τ_e
^{74}Br	306	K	293	0.007	0.009(2)
^{207}Pb	569.7	K	481.69	0.0155(5)	0.054(6)
^{207}Pb	569.7	L	553.84	0.00433(15)	0.053(6)
^{207}Pb	569.7	M	565.85	0.00109(5)	0.051(6)
^{72}Se	862	K	849.37	0.000537	0.012(3)
^{207}Pb	1063.6	K	975.65	0.097(2)	0.0072(8)
^{207}Pb	1063.6	L	1047.8	0.0247(14)	0.0046(6)
^{207}Pb	1063.6	M	1059.8	0.0060(4)	0.0049(7)

Table 3.32: *Compilation of transitions used in the determination of 125/8/6A transmission curve. Conversion coefficients of ^{207}Pb transitions have been taken from [Mar93] while for the ^{72}Se 862K transition the theoretical conversion coefficient from [ANU] has been taken. For the ^{74}Br 306K transition, the value of conversion coefficient has been taken from [Sin06].*

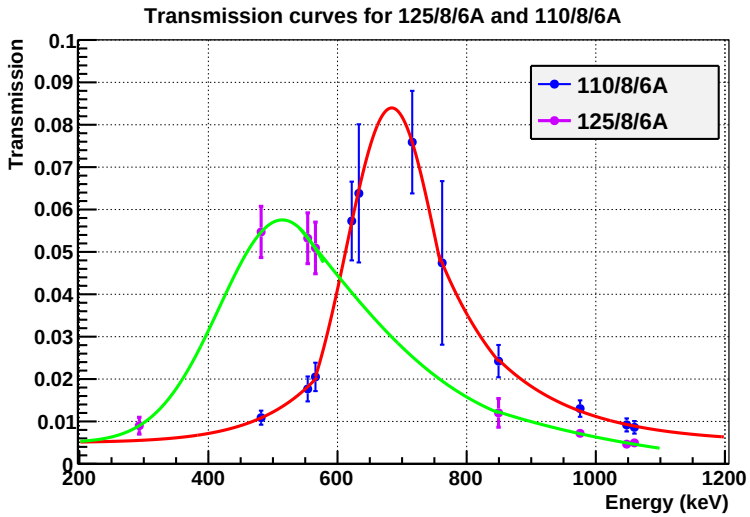

Figure 3.25: *Graphical representation of transmission curves for 110/8/6A and 125/8/6A Miniorange configurations. The experimental points of the 125/8/6A configuration correspond to the values in table 3.32 and for 110/8/6A in table 3.28. The green line is the result of the fitting procedure of the 125/8/6A Miniorange data points in 2 different energy ranges as it is described in the text. The ^{74}Kr transitions 634K and 728K have been rejected in the fitting procedure as they provide an overestimated transmission probably due to the large dead time (55-60 %) of that measurement.*
The transmission of the 125/8/6A Miniorange is higher at lower energies as the maximum transmission is provided at around 400-600 keV while for 110/8/6A is around 600 up to 900 keV.

3.3 Results

Once the characterization of the detectors, including efficiency and energy calibrations, is done, the analysis of the data of interest can be carried out.

The effective energy range of every configuration of the Miniorange spectrometer determines the energy range of study, so, at this point, it is good to have a look at the table 3.33 where the effective energy ranges are listed. The energy overlap of several configurations is useful to extract the conversion coefficients, the values obtained with different configurations will be compared in order to check the consistency of the results.

The energy ranges will be classified as **low energy region**, studied with configurations 125/8/3B and 85/8/4B, and **high energy region**, studied with configurations 110/8/6A and 125/8/6A.

The measurements to obtain the conversion coefficients shown in this section were done with a period of the tape movement of one super-cycle, which corresponds to 33.6 seconds. This was chosen in order to optimize the amount of ^{72}Kr decay radiation in comparison with its decay chain radiation, as ^{72}Br, ^{72}Se, etc..., decays. Other measurements with different cycling periods were performed but for different purposes than the study of the conversion coefficients.

In the table 3.33 are indicated the duration of the measurements with each magnets configuration as well as the deadtime of each measurement for the HPGe 1 and Si(Li) detectors. One can see that the deadtime is always larger for the HPGe 1 detector due to its higher counting rate in comparison with the one for the Si(Li) detector. The deadtime is different for each detector and, as for the conversion coefficients one is comparing peak areas of both detectors,

this is the reason why one should divide the peak areas by the corresponding live time of the detector.

D1/D2/NT	Effective energy range E(keV)	Measurement duration with ^{72}Kr (min)	Deadtime HPGe 1 / Si(Li) detectors with ^{72}Kr (%)	Beam used apart from ^{72}Kr
125/8/3B	20-170	240	26.5 / 20.5	^{76}Kr (calib)
85/8/4B	60-200	388	8.1 / 3.4	^{75}Kr (calib)
110/8/6A	400-1100	327	14.0 / 11.7	^{74}Kr (calib)
125/8/6A	300-1100	172	16.0 / 13.9	^{74}Kr (calib)

Table 3.33: *Configurations of the Miniorange magnets used in the IS370-A experiment. The effective electron energy range of each configuration is shown in the second column. The third and fourth columns give information on the measurement with ^{72}Kr as beam, while the third indicates the duration of each measurement the fourth gives the deadtime of the HPGe 1 and Si(Li) detectors in percentage. The beam used with each configuration of the magnets is given in the last column. Apart from the ^{72}Kr beam, other krypton isotopes were used to calibrate the different Miniorange configurations. The description of the Miniorange configurations and the meaning of D1, D2, N and T was done in section 3.1.2.1 and can be seen in figures 3.6 and 3.7. All the measurements to obtain the conversion coefficients were done with a timing period of one super-cycle of 33.6 seconds long.*

The conversion coefficients are obtained by dividing the intensity of electrons (I_e) by the intensity of gamma emission (I_γ):

$$\alpha = \frac{I_e}{I_\gamma} \tag{3.42}$$

As it was mentioned before, the intensity of every transition is defined as the peak area divided by the peak detection efficiency, that is gamma efficiency and electron transmission respectively. Further, one has to consider the live time of each detector, so one has to divide every intensity by the live time of the corresponding detector in order to take into account the differences in live times.

In summary, the equation that expresses the way of obtaining the conversion coefficients α is:

$$\alpha = \frac{A_e/(t_e \cdot \tau_e)}{A_\gamma/(t_\gamma \cdot \epsilon_\gamma)} = \frac{A_e \cdot \epsilon_\gamma \cdot t_\gamma}{A_\gamma \cdot t_e \cdot \tau_e} \tag{3.43}$$

The uncertainties of the experimental conversion coefficients have been estimated by using the propagation of deviations already mentioned in the previous subsection, and whose mathematical expression for a general physical quantity z which depends on other two quantities x and y is expressed as shown in equation 3.32.

For the current case of the conversion coefficients, whose dependence on other variables is given by expression 3.43, the variables whose uncertainty must be propagated are electron and gamma peak areas A_e and A_γ, gamma photo-peak efficiency $\epsilon(E_\gamma)$, the electron transmission τ_e and live time of the HPGe 1 and Si(Li) detectors t_γ and t_e respectively. The resulting expression to estimate the uncertainty is:

$$\Delta\alpha = \alpha\sqrt{\left(\frac{\Delta A_e}{A_e}\right)^2 + \left(\frac{\Delta\epsilon(E_\gamma)}{\epsilon(E_\gamma)}\right)^2 + \left(\frac{\Delta t_\gamma}{t_\gamma}\right)^2 + \left(\frac{\Delta A_\gamma}{A_\gamma}\right)^2 + \left(\frac{\Delta t_e}{t_e}\right)^2 + \left(\frac{\Delta\tau_e}{\tau_e}\right)^2} \tag{3.44}$$

The uncertainty coming from the peak areas is given when one fits the peaks to known models, that is gaussian for gamma peaks and the expression 3.10 for electron peaks, as it is

one parameter in the fitting procedure. The uncertainty in time, less than 1 per mile (1/1000) and it is insignificant in comparison with the rest of uncertainties involved. The uncertainty coming from efficiency, as it has already been explained, has been considered to be 10 % (for more details see subsection 3.2.2). Finally, the uncertainty from the transmission interpolated for a given electron energy has been estimated to be 20% as upper limit of the uncertainties of the experimental values. Those are shown in tables 3.18, 3.19, 3.28 and 3.32 which are smaller or around the chosen 20 % percentage.

The experimental values for the conversion coefficients will be presented in chapter 5 but now let us have a look at the spectra studied with every magnet configuration and comment some important features.

3.3.1 Low energy region: Miniorange 125/8/3B

The measurement performed with this magnets configuration was done for 4 hours as given in table 3.33 with a deadtime for the HPGe 1 detector of around 26 % and for the Si(Li) detector of 20 %. These values are quite high due to the high counting rate of this measurement, that was around 8 KHz in the HPGe 1 detector, 150 Hz in the Si(Li) but specially high for the other HPGe detector in the setup as it was 18 kHz. This problem was solved for the rest of magnets configuration and this is the reason why the larger deadtime is found for this configuration. Anyway, as in the analysis is taken into account the different deadtimes of each data channel associated to each detector, in principle, this problem has to be reduced.

As already mentioned above, the period of the tape movement for all the measurements leading to the extraction of the conversion coefficients was one super-cycle, that is 33.6 seconds.

In fig. 3.26 the measured spectra with 125/8/3B configuration are shown. HPGe 1 and Si(Li) detectors spectra are superimposed with their corresponding background measurements. The background spectra were scaled in order to correspond to a measurement of the same live time than the in-beam one.

It turns out that the only transitions of interest in these spectra are the **30.5Tot-K, 38.8K, 101.3K and 101.3Tot-K** in the de-excitation of ^{72}Br. The term Tot-K, as previously explained, mainly includes L and M components as the intensity of the transitios from different shells decreases quickly from one to the next shell.

The cases of 30.5Tot-K and 38.8K transitions are a little harder because of the presence of the indium X-rays. The energies of the indium X-rays are 24.0+24.2 keV and 27.2+27.8 keV and they are close to the electron energies for the electron transitions we are interested in. The 38.8K transition is located at 25.3 keV with its low-energy tail so is quite close to the first group of the indium X-rays and they cannot be resolved. Similar is the case of the 30.5Tot-K transition as it is located at 28.7 keV with its low-energy tail and the second group of peaks from indium X-rays is quite close and one has to subtract the X-rays contaminations.

For these reasons, one can only establish upper limits for both conversion coefficients as the intensity of the gamma radiation from the 30.5 and 38.8 keV transitions can be firmly measured but the electron intensities are mixed with some contamination of indium X-rays.

Also the conversion coefficient of 112K transition in the measurement with ^{76}Kr as beam could be extracted and it will be listed in the table of results in chapter 5.

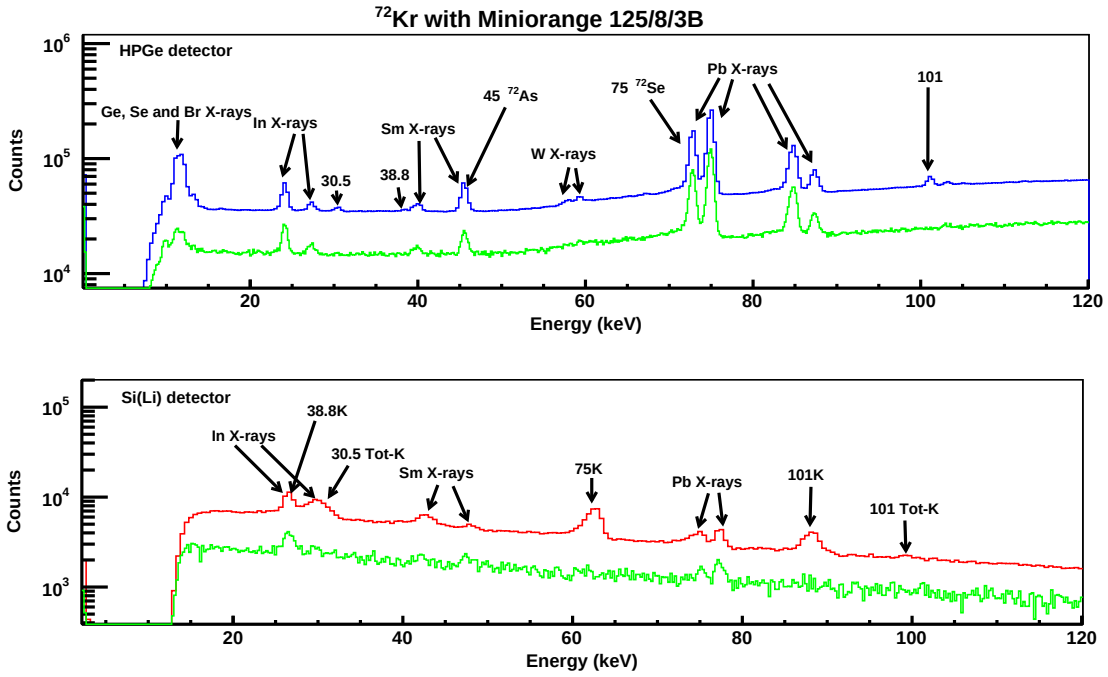

Figure 3.26: *Spectra acquired with a ^{72}Kr beam and the **125/8/3B Miniorange** spectrometer with the HPGe 1 detector (top-blue) and Si(Li) detector (bottom-red) during 37 and 40 minutes live time respectively. Shown in green, the spectra of the background measurement scaled to the same live time of the in-beam measurement in order to be able to identify possible background contaminations. Labels indicate the origin of each line and when only the energy is indicated, such as 101 keV or 30.5 keV, it belongs to the de-excitation of the decay daughter nucleus of interest, ^{72}Br.*

3.3.2 Low energy region: Miniorange 85/8/4B

The measurement with this magnets configuration lasted more than six hours as given in table 3.33. The deadtime for this measurement was reduced to the level of around 8 percent for the HPGe 1 detector and 3 percent for the Si(Li) detector as the other HPGe 2 detector was not included in the DAQ system for this measurement and the counting rates for these two detectors was around 3 KHz for the HPGe 1 and 150 Hz for the Si(Li) detector.

In the case of this configuration, labeled as 85/8/4B, the obtained spectra are shown in fig. 3.27. The corresponding background spectra are also shown in green after being scaled by the different live times of the in-beam and background measurements.

It can be observed that the following transitions in ^{72}Br can be examined: **101.3K, 101.3Tot-K, 124.4K, 124.4Tot-K, 147.2K, 162.7K, 162.7Tot-K and 178.5K**.

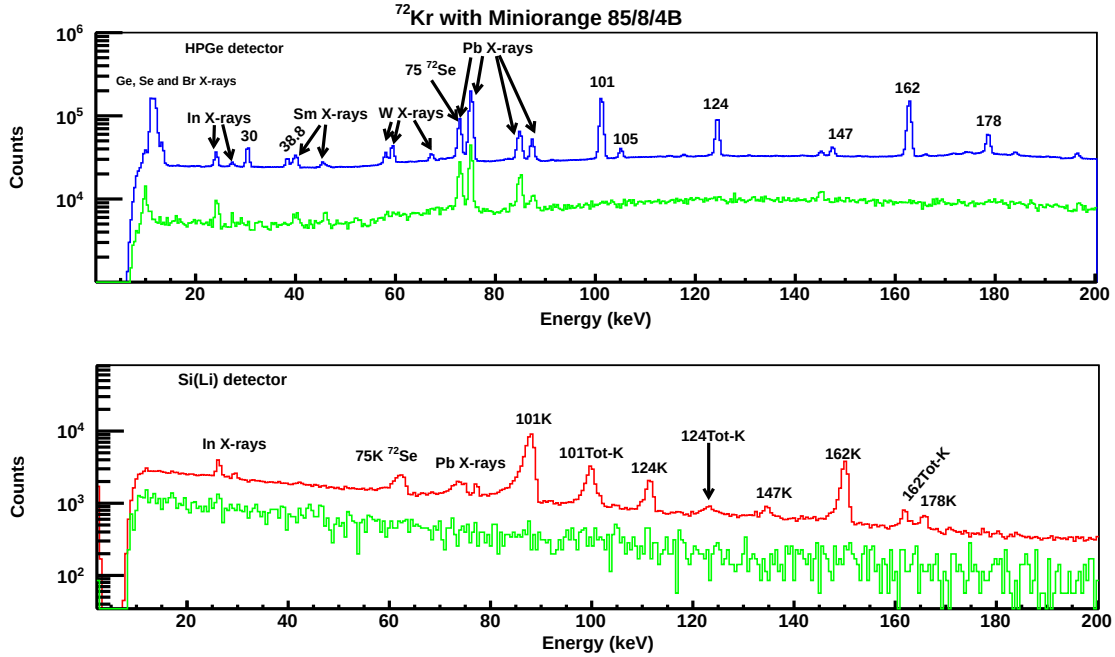

Figure 3.27: *Spectra acquired with a ^{72}Kr beam and the **125/8/4B Miniorange** spectrometer with the HPGe 1 detector (top-blue) and Si(Li) detector (bottom-red) during 357 and 375 minutes live time respectively. Shown in green the spectra from the background measurement in both detectors in order to identify possible contaminants. Background spectra have been scaled up to the same live time of the in-beam measurements. Labels indicate the origin of each line. Peaks where only the energy is indicated, such as 101 keV or 30.5 keV, belong to the de-excitation of the daughter nucleus of interest, ^{72}Br.*

3.3.3 High energy region: Miniorange 110/8/6A

This magnets configuration was used to study higher energy electron transitions for more than 5 hours as indicated in the table 3.33. The deadtime in this measurement was a little bit higher than in the previous case being 14 percent for the HPGe 1 detector and around 11 percent for the Si(Li) detector as the HPGe 2 detector was introduced in the DAQ. The counting rate for this measurement was kept around 3 kHz for the HPGe 1, 50 Hz for the Si(Li) and around 6 kHz for the HPGe 2 detector. Note as the deadtime of this measurement is quite lower than in the 125/8/3B case as the counting rate for the HPGe 2 detector was substantially reduced.

The spectra taken with this configuration are shown in fig. 3.28. As usual, in green are included the respective background spectra for contaminants identification scaled to the same live time. This background measurement shown corresponds to the background after the measurement with ^{74}Kr as beam measured just later than the ^{72}Kr measurement with this configuration. There was a background measurement immediately before than the measurement of interest but it was done removing magnets from position and the Si(Li) detector was not working as every time the vacuum chamber is opened the Si(Li) has to be kept aisled. This makes us to plot the other background file that is not exactly measured under the same conditions as a measurement with different mass was done in between.

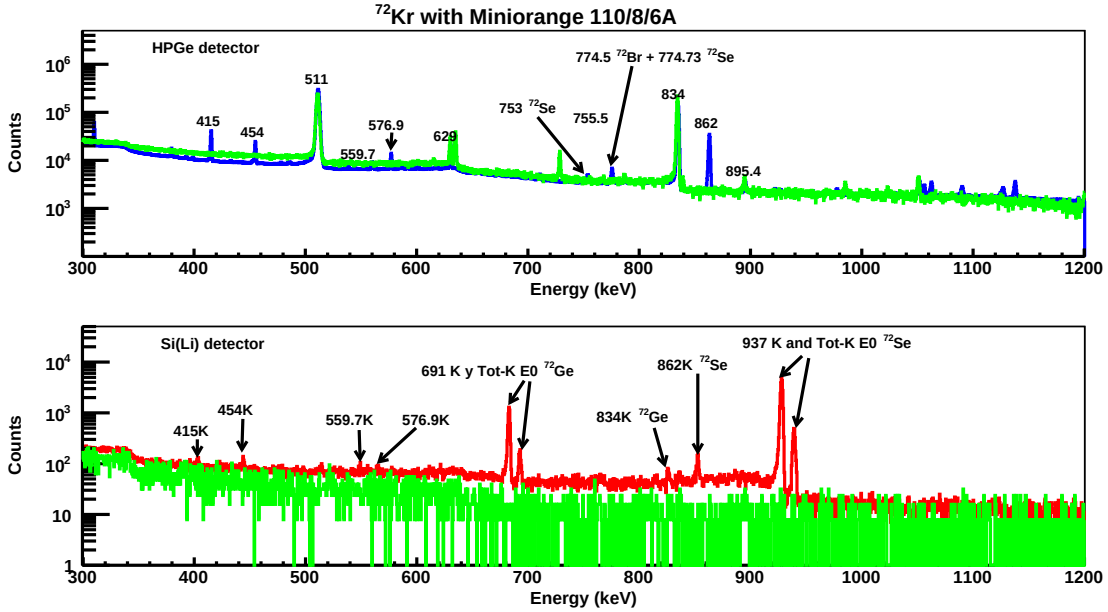

Figure 3.28: *Spectra acquired with a ^{72}Kr beam and the **110/8/6A Miniorange** spectrometer with the HPGe 1 detector (top-blue) and Si(Li) detector (bottom-red) during 281 and 289 minutes live time respectively. Shown in green the spectra from the background measurement in both detectors in order to identify possible background contaminations. Background spectra have been scaled to the same live time as the in-beam measurement except the Si(Li) that has been reduced a factor 0.3 in order to be able to clearly observe the in-beam spectrum. Labels indicate the origin of each line. Peaks where only the energy is indicated, such as 415 keV or 576.9 keV belong to the de-excitation of the daughter nucleus of interest, ^{72}Br, with the exception of the well known 511 peak seen in the HPGe 1 spectrum, which is coming from the annihilation of the positron emitted in the β^+ decay process.*

As can be seen, the conversion coefficients that can be extracted with this measurement are **(414.5+415.1)K, 454.7K, 559.7K and 576.9K** from the de-excitation of ^{72}Br.

Apart from these transitions, the K and Tot-K shell electrons corresponding to two E0 transitions, the 937-keV in ^{72}Se and 691-keV in ^{72}Ge, were found in the electron spectrum. The intensities for both transitions was studied and are discussed in section 5.1.5. Their intensity will be referred to the other two electron transitions observed in the spectrum belonging to the same level scheme, the 862K and 834K transitions corresponding to ^{72}Se and ^{72}Ge level schemes respectively.

It is good to remember as the 862K transition in ^{72}Se was used to determine the transmission curve of this configuration for being a well-known E2 transition. The 834K conversion coefficient cannot be extracted as the gamma radiation associated of 834 keV energy is present in the background measurement indicating that this radiation is reaching the HPGe 1 detector from other places than the measuring point as in the background measurement no beam was deposited in the tape.

3.3.4 High energy region: Miniorange 125/8/6A

The fourth configuration used is labelled as 125/8/6A and it was used with ^{72}Kr as beam for around a 3 hours-long measurement (see table 3.33. The deadtime is similar to the one for the previous configuration as the conditions were the same, being 16 % for the HPGe 1 detector and around 14 % for the Si(Li) detector. The counting rates of the three detectors included in

the DAQ system are approximately the same indicated in the previous configuration (4 kHz for HPGe 1, 50 Hz for Si(Li) and 8 kHz for HPGe 2).

The spectra corresponding to the measurement performed with the 125/8/6A configuration of the Miniorange spectrometer can be seen in fig. 3.29 together with the background spectra superimposed in green.

In the electron spectrum the following transitions belonging to the de-excitation of ^{72}Br can be identified: **309.9K, 392.7K, 398.4K, (414.5+415.1)K, 454.7K, 559.7K and 576.9K**.

Also the 691K and 691Tot-K transitions from the ^{72}Ge de-excitation on the one hand and 937K and 937Tot-K from the ^{72}Se de-excitation on the other hand, are present in the spectrum, as it was explained before, they are E0 transitions so there are no associated gamma transitions and the extraction of their conversion coefficients is not possible. The intensity of both E0 transitions is studied in section 5.1.5. Apart from these E0 electron transitions also one can see the 862K and 834K transitions which correspond to E2 transitions in the same nuclei, that is ^{72}Se and ^{72}Ge, and they will be used to refer the intensities of both E0 transitions.

The 862K transition in ^{72}Se was used to determine the transmission curve of this Miniorange configuration as in the case of the 110/8/6A configuration. The same reason explained in the measurement with the 110/8/6A configuration can be used to reject the possibility of extracting the conversion coefficient of the ^{72}Ge 834K transition.

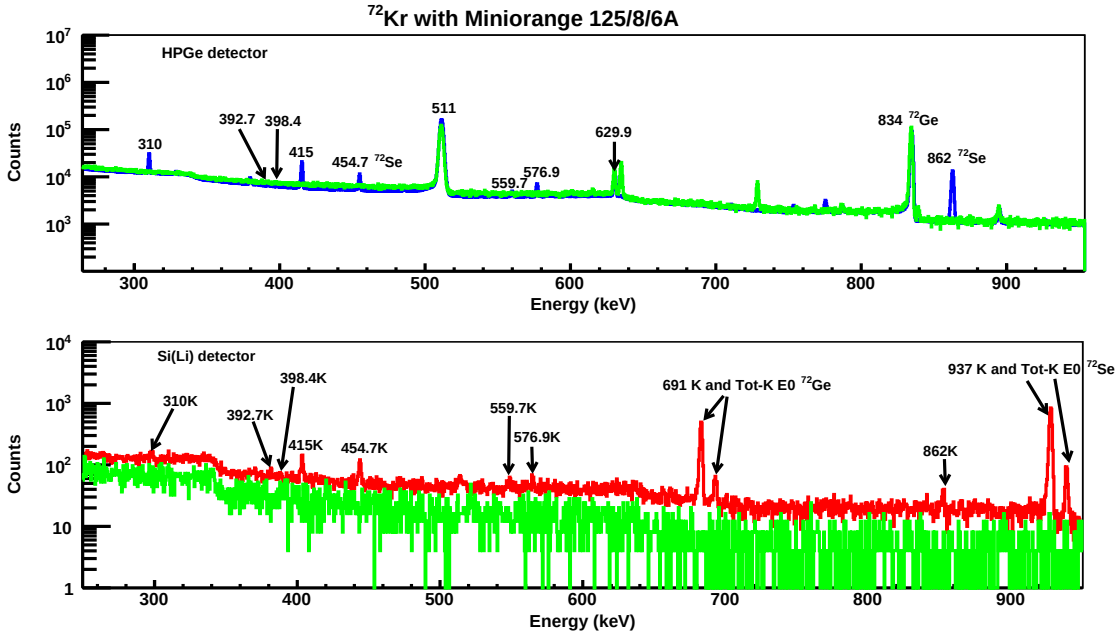

Figure 3.29: *Spectra acquired with a ^{72}Kr beam and the **125/8/6A Miniorange** spectrometer with the HPGe 1 detector (top-blue) and Si(Li) detector (bottom-red) during 144 and 147 minutes live time respectively. Shown in green the spectra from the background measurement in both detectors to identify possible contaminants. Labels indicate the origin of each line. Peaks where only the energy is indicated, such as 415 keV or 576.9 keV belong to the de-excitation of the daughter nucleus of interest, ^{72}Br, with the exception of the well known 511 peak seen in the HPGe 1 spectrum, which is coming from the annihilation of the positron emitted in the β^+ decay process.*

The values obtained in the analysis for the conversion coefficients in transitions belonging to the de-excitation of ^{72}Br (the 454.7K transition in ^{72}Se and 112K transition in ^{76}Br are included as well) are listed in table 3.34. The information to identify the electron transition

and the miniorange configuration used for every result are shown in columns 1, 2, 3 and 4. The values obtained for the conversion coefficient of every transition are listed in column 5. The theoretical values for the different multipolarities of a transition of the corresponding energy are shown in the following 5 columns (from 6^{th} to 10^{th}), in order to be compared with the experimental values and try to deduce the multipolarity of every transition. These theoretical values are obtained from [ANU]. The next column, 11^{th}, shows the dominant multipolarity that can be assigned for every transition in accordance with the experimental values of the conversion coefficient shown in the 5^{th} column and the comparison with the theoretical values which appear in the following five columns. In the 12^{th} column one can observe the value for the absolute value of the mixing ratio δ. The definition of this parameter and some explanations are included in the appendix A.

Before presenting the resulting values one can check the appendix B where the gamma intensities of the transitions identified in every measurement are listed and compared to the tabulated values in [Piq03], the current most detailed work on this decay.

Nucleus	Minio.	Transition	α(exp)	α(th) [ANU]					Dominant	| δ |	Previous ass.
				E1	M1	E2	M2	E3	Multipolarity•		
^{72}Br	3B	30.5(Tot-K)	**<5.9(1.4)**	0.321	0.397	21.47	20.16	1746	E1, ~~M1+E2~~, ~~E1+M2~~■	<0.74	(M1+E2)*
^{72}Br	3B	38.8K	**<18(7)**	1.202	1.479	20.48	35.11	274.9	M1+E2, M1, E2 or ~~E1~~■		(M1)*
^{72}Br	3B	101.3K	1.3(3)	0.072	0.098	0.718	0.987	5.863			α=1.145(21)*
^{72}Br	4B	101.3K	1.0(2)	0.072	0.098	0.718	0.987	5.863			
^{72}Br	Average	101.3K	**1.12(13)**	0.072	0.098	0.718	0.987	5.863	M2		M2*$^{\triangle}$
^{72}Br	3B	101.3(Tot-K)	0.14(7)	0.00907	0.01271	0.1202	0.1578	1.834			
^{72}Br	4B	101.3(Tot-K)	0.14(3)	0.00907	0.01271	0.1202	0.1578	1.834			α_K=1.4(3)
^{72}Br	Average	101.3(Tot-K)	**0.14(2)**	0.00907	0.01271	0.1202	0.1578	1.834			[Gri92]
^{72}Br	4B	124.28K	**0.069(17)**	0.039	0.056	0.34	0.478	2.424	M1(E2)	$0.22^{+0.12}_{-0.22}$	E2*
^{72}Br	4B	124.28(Tot-K)	**0.010(3)**	0.00492	0.00727	0.053	0.0733	0.623		$0.25^{+0.12}_{-0.25}$	
^{72}Br	4B	D147K	**0.036(12)**	0.02385	0.03578	0.1824	0.2654	1.163	M1 and M1, M1+E2 or E1°		M1*
^{72}Br	4B	162.2K	**0.053(12)**	0.018	0.028	0.128	0.19	0.763	M1+E2	0.57(20)	E2*
^{72}Br	4B	162.2(Tot-K)	**0.008(2)**	0.00222	0.00355	0.0186	0.028	0.1603		$0.65^{+0.25}_{-0.24}$	
^{72}Br	4B	178.5K	**0.028(8)**	0.01351	0.02158	0.08999	0.1377	0.5037	M1(E2)	$0.31^{+0.19}_{-0.31}$	E1*
^{72}Br	6A-125	310K	**0.0048(15)**	0.00279	0.005351	0.01254	0.02304	0.04879	M1, M1(E2)	$0^{+0.25}$	E2*
^{72}Br	6A-125	392.7K	**0.019(8)**	0.00148	0.00302	0.00566	0.01121	0.01900	E3 or E3(M2)		
^{72}Br	6A-125	398.4K	**0.011(7)**	0.001424	0.00292	0.005399	0.01074	0.01797	M2, E3 or M2(E3)		
^{72}Br	6A	D415K	0.0022(6)	0.00128	0.002649	0.004725	0.00951	0.01534			
^{72}Br	6A-125	D415K	0.0019(5)	0.00128	0.002649	0.004725	0.00951	0.01534			
^{72}Br	Average	D415K	**0.0020(3)**	0.00128	0.002649	0.004725	0.00951	0.01534	M1 or E1		
^{72}Br	6A	559.7K	0.0038(14)	6.10E-04	0.001325	0.001877	0.004024	0.005136			
^{72}Br	6A-125	559.7K	0.0041(17)	6.10E-04	0.001325	0.001877	0.004024	0.005136			
^{72}Br	Average	559.7K	**0.0040(8)**	6.10E-04	0.001325	0.001877	0.004024	0.005136	M2, M2(E3)		
^{72}Br	6A	576.9K	0.0014(5)	5.68E-04	0.001237	0.001718	0.003699	0.004625			
^{72}Br	6A-125	576.9K	0.0010(4)	5.68E-04	0.001237	0.001718	0.003699	0.004625			
^{72}Br	Average	576.9K	**0.0012(2)**	5.68E-04	0.001237	0.001718	0.003699	0.004625	M1, M1(E2)	$0.^{+0.78}$	
^{72}Se	6A	454.7K	0.0036(10)	0.0009388	0.001924	0.003289	0.006546	0.01017			
^{72}Se	6A-125	454.7K	0.0027(7)	0.0009388	0.001924	0.003289	0.006546	0.01017			
^{72}Se	Average	454.7K	**0.0031(4)**	0.0009388	0.001924	0.003289	0.006546	0.01017	E2, E2(M1)	$2.31^{+\infty}_{-1.21}$	
^{76}Br	3B	112K	**0.24(7)**	0.05368	0.07445	0.4974	0.6902	3.804	M1+E2	$0.81^{+0.33}_{-0.27}$	M1+E2‡ -0.3 $\geq \delta \geq$-2.4

Table 3.34: *Results obtained for the conversion coefficients of transitions in ^{72}Br, ^{72}Se and ^{76}Br from the IS370-A experiment. The comparison of experimental conversion coefficients shown in column 5 with the theoretical predictions in the following 5 columns provide us with the dominant multipolarity for each transition shown in column 11th. In the next column the module of the mixing ratio is shown for mixed transitions and in the last column the available up to date information can be seen.*

• *When several assignments are allowed, they are shown in order of decreasing probability.*

* *assignment made from intensity balance arguments in the work of I. Piqueras et al. [Piq03].*

$^{\triangle}$ *information from [Gar82].*

° *For the doublet, the assignment is given in order of increasing energy in the placement in the level scheme separated by "and".* ‡ *See references [Dö82],[Buc90], [Win90];*

■ *see text*

D415 notes the doublet 414.5 + 415.1 keV transition and D147 the doublet 147.2 keV.

4 Total Absorption Spectroscopy

Contents

Along this chapter the experimental setup, the data analysis procedure and the results obtained from the Total Absorption Spectroscopy measurement corresponding to the IS370 experiment will be presented. Firstly the main components of the experimental device will be described together with the calibrations of the detectors involved in this measurement. Later, the data analysis leading to obtain a reliable beta feeding distribution of the ^{72}Kr decay and the latter transformation into B(GT) will be explained in detail. Finally, the estimation of uncertainties in the B(GT) distribution obtained will be explained.

4.1 Experimental setup

The experimental setup of the IS370 experiment at ISOLDE (CERN) consisted of the following components:

- **Total Absorption Spectrometer (TAS detector)**: NaI(Tl) mono-crystal to fully absorb the gamma de-excitation cascades following the beta decay.
- **Ancillary detectors**: including a beta detector to detect electrons/positrons coming from the beta decay of the nuclides in the sample and a HPGe telescope composed by a planar and a coaxial detector to detect X-rays and γ radiation.
- **Tape transport system**: system to move the magnetic tape used to collect the sample in the measuring point and move it away once the measurement is performed every cycling period.
- **Shielding system**: made of four layers to reduce the background radiation reaching the NaI(Tl) crystal.

A general view of the whole experimental setup is shown in figure 4.1. Next, the main properties of each component in the setup are detailed.

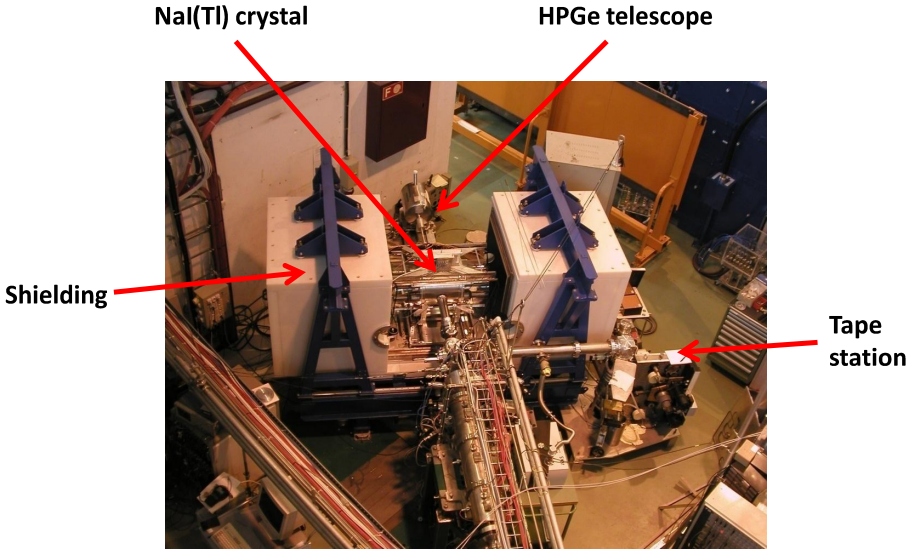

Figure 4.1: *General view of the experimental setup. The TAS detector is shown with the shielding opened. The ISOLDE beam line is shown from the bottom part of the picture to the center of the TAS detector. At the other side of the TAS detector, the germanium telescope can be seen. The details of all the components involved are explained in the text.*

4.1.1 Total Absorption Spectrometer (TAS)

The *"Lucrecia"* Total Absorption Spectrometer is a NaI(Tl) mono-crystal detector manufactured by *Saint-Gobain Crystals and Detectors* and installed at ISOLDE (CERN). It has cylindrical shape with 38 cm length and 38 cm base diameter. The detector has a transversal cylindrical

hole perpendicular to the symmetry axis of the cylinder of 7.5 cm of diameter. The purpose of this hole is twofold: it allows for the placement of ancillary detectors as well as to place the sample in the geometrical centre of the TAS detector. The solid angle coverage is, approximately, 97.8 $\%$ of 4π so it is close to the ideal full coverage.

A picture of the TAS detector is shown in figure 4.3 and a sketch of the experimental setup can be seen in figure 4.4.

The NaI(Tl) crystal is encapsulated in a 1.3 cm thick aluminium box with cylindrical shape to be protected from environmental humidity or mechanical strains. This layer is slightly thinner in the inside part of the transversal hole in order to avoid the suppression of γ radiation. A layer of 2 mm thickness of Al_2O_3 located in the inner side of the external aluminium case to improve the light reflection. The detector has 8 5-inch photo-multipliers tubes of type Electron Tubes 9792B, located 4 at each circular side of the cylindrical crystal in order to collect the scintillation light emitted by the crystal.

4.1.1.1 TAS calibrations

The energy calibration for the TAS detector was performed using the standard calibration sources with just 1 or 2 gamma transitions as if one uses a source with higher number of different radiations the spectrum gets complicated easily and the task of identifying every peak for the calibration turns to be almost impossible. For this purpose, measurements with the sources of ^{137}Cs, ^{60}Co and Co were performed and the equation of energy calibration for the *"Lucrecia"* TAS detector is found to be:

$$E(keV) = -0.103 \times 10^{-5} \cdot channel^2 + 2.179 \times channel - 17.423 \tag{4.1}$$

The efficiency of the TAS detector *"Lucrecia"* was already shown in figure 2.4 but here is reproduced again in figure 4.2. It is important to note that these efficiency curves come from GEANT4 simulations and they are not experimentally obtained but they can be considered as good approximation to the real efficiencies that one can found in experimental conditions. The detection efficiency refers to the ability of detecting the particles, no matters if full energy or a portion of the total energy is detected. On the other hand, the full-energy efficiency takes into consideration only events where the initial energy of the particle is fully deposited in the detector material.

As it is shown in the figure, the detection efficiency is quite high in the whole energy range shown, that is from 0 till 10 MeV, as is higher than 90 $\%$. The full-energy detection efficiency decreases as the energy of the radiation increases, however one has to take into account that in the de-excitation path of the fed excited levels usually a gamma cascade takes place where several gamma radiation of lower energy are emitted instead of only one gamma with the full high energy coming from the excitation energy of the initial level. This implies that one detects in most of the cases radiation with lower energy than 4 or 5 MeV where the full-energy efficiency is higher than 65 $\%$.

Another detail to remember is that as one follows the deconvolution method of the spectrum by means of the response function, in the analysis one not only takes into account those events with full-energy deposition but also those corresponding to the case of some energy "not detected" in the TAS. Therefore, this implies that the relevant efficiency of the TAS detector is not the full-energy detection efficiency but the total detection efficiency (in blue in Fig. 4.2).

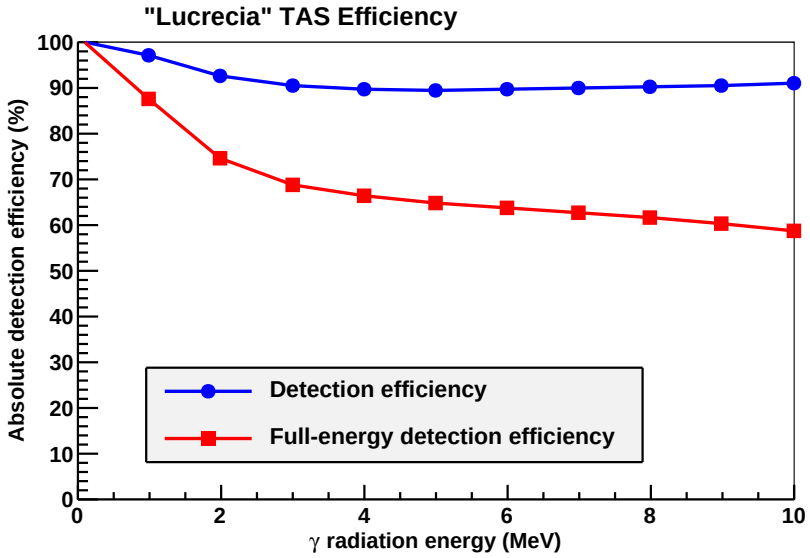

Figure 4.2: *Detection and full-energy deposition efficiency of "Lucrecia" Total Absorption Spectrometer obtained from simulations reproducing the experimental setup by using a GEANT4 code. As can be seen, the detection efficiency is higher than 90 percent in the whole energy range from 0 up to 10 MeV gamma radiation energy. The full-energy detection is lower, specially for relatively high energy, namely from 2 MeV on.*

Regarding the energy resolution of this detector, some experimental values are given in table 4.1. One can see that the resolution in keV are is worse than that corresponding to the HPGe detectors shown in table 4.3. This is the reason why the energy resolution of scintillators is usually expressed in terms of percentage (shown in last column of the table).

Radiation source	E_γ (keV)	TAS resolution FWHM(keV)	(%)
^{137}Cs	661.657(3)	56(12)	8.5(18)
^{60}Co	1173.228(3)	84(14)	7.2(12)
^{60}Co	1332.490(6)	86(17)	6.5(13)
^{60}Co	2505.718(9)	131(22)	5.2(9)

Table 4.1: *Energy resolution of Total Absorption gamma Spectrometer "Lucrecia" for several gamma transitions from the standard calibration source of ^{60}Co. It is important to note that the third transition is just the full cascade of gamma radiation following the beta decay of ^{60}Co that fed a level at 2505.765 keV and de-excites by emitting two gamma rays of energies 1173.228 and 1332.49 keV. This sum-peak is not usual to appear in HPGe detectors but for a TAS detector is the most likely possibility due to its high detection efficiency.*

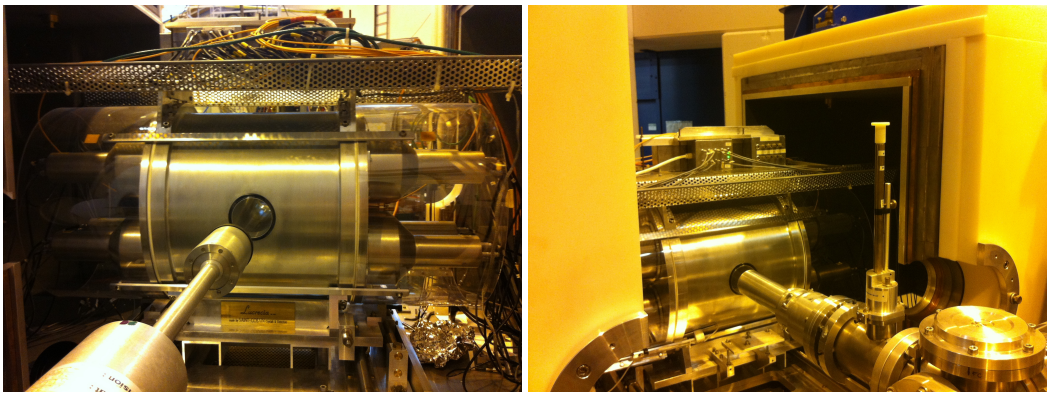

(a) (b)

Figure 4.3: *Pictures of the "Lucrecia" TAS detector installed at ISOLDE (CERN) (a) in upstream and (b) downstream directions. The transversal hole can be clearly seen in (a). The detector in the forefront of picture (a) is the HPGe telescope detector whose properties are explained in the text. There are 8 photo-multipliers located at both sides of the TAS detector that are visible in (a). The 4 layers of shielding materials can be seen in (b). In picture (b) the shielding surrounding the detector and that is composed by 4 different layers as explained in the text.*

4.1.2 Shielding system

The TAS detector has a high detection efficiency for gamma radiation so it is necessary to shield it from external radiation in order not to have a huge amount of background contamination. A shielding box made of 4 layers is surrounding the detector as can be seen in fig. 4.3(b) and 4.7. The layers are, from outside to inside:

- 10 cm **polyethylene**: for neutrons suppression,
- 5 cm **lead**: to reduce the amount of γ radiation,
- 2 cm **copper**: to absorb lead X-rays emitted by the previous layer
- 2 cm **aluminium**: to absorb copper X-rays from the previous layer.

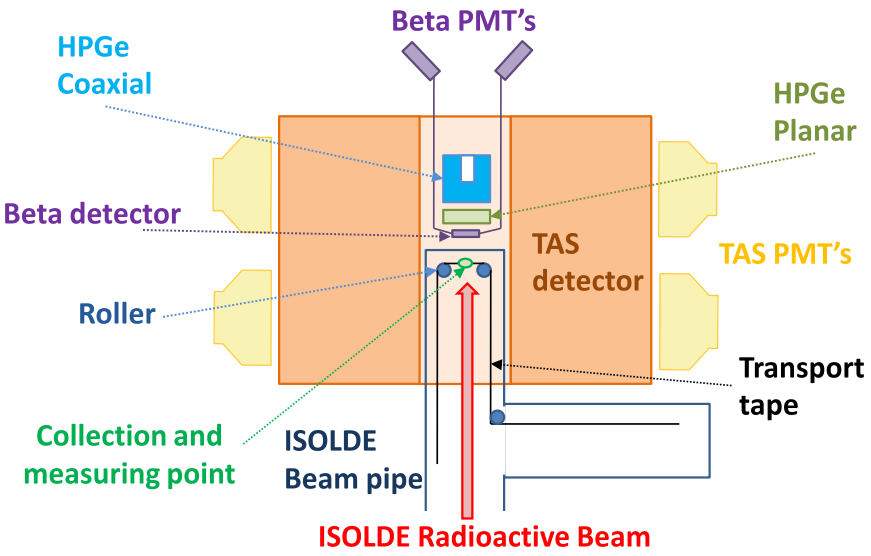

Figure 4.4: *Sketch of the TAS experimental setup. ISOLDE radioactive beam is collected in collection/measuring point. The NaI(Tl) mono-crystal is labelled as TAS. Despite looking like two NaI(Tl) crystals it is important to note that it is a single crystal. The scintillation light is collected in 8 photo-multipliers, 4 located at each side of the NaI(Tl) crystal. The beam is deposited and measured in the same position. The light from the beta detector is collected through two beta pmt's (named in the analysis as left and right). The germanium telescope (planar and coaxial detectors) is placed after the beta detector as indicated in the sketch. Other minor components as the transport tape, the rollers to guide the tape and the beam pipe are indicated. For further details see text.*

Apart from the TAS detector, the setup includes ancillary detectors that are described next.

4.1.3 HPGe telescope detector

Two HPGe detectors are placed in a telescope configuration. The front detector is a planar type of 1 cm thick and with 5 cm of diameter in order to measure the low-energy radiation coming from the source, especially X-rays. It was placed at 2.2 cm of the measurement (and collection) point so the solid angle covered by this detector was around 17 % by using the expression 3.2. The HPGe coaxial detector is 5 cm thick with 5 cm of diameter as well, and it was placed just behind the HPGe planar detector in order to measure higher-energy γ radiation.

The aim of these detectors is to identify the γ and X radiation coming from the sample with good resolution as in the TAS detector the resolution is not enough to distinguish individual lines. In particular, the main purpose of the planar detector is to tag the EC events as every EC event produces a characteristic X-ray. In this way one can select the EC component of the decay.

The frontal face of the HPGe telescope has a thin beryllium window in order not to absorb the low-energy radiation of interest to be measured with the planar germanium detector.

4.1.3.1 HPGe detectors calibrations

The energy calibrations of the HPGe Coaxial and Planar detectors were performed by the use of standard calibration sources, in particular ^{133}Ba, ^{152}Eu and ^{241}Am were used in our case.

The relation between channel number and energy for these detectors assuming a linear dependence is given by the expressions:

$$\text{HPGe Coaxial: } E(keV) = 0.5326(2) \times channel - 0.4(3)$$
$$\text{HPGe Planar: } E(keV) = 0.065159(8) \times channel + 0.14(3)$$

The deviation between the tabulated values for the energy of the reference γ-transitions and the values obtained with our calibration are given in Fig. 4.5(a) and 4.5(b).

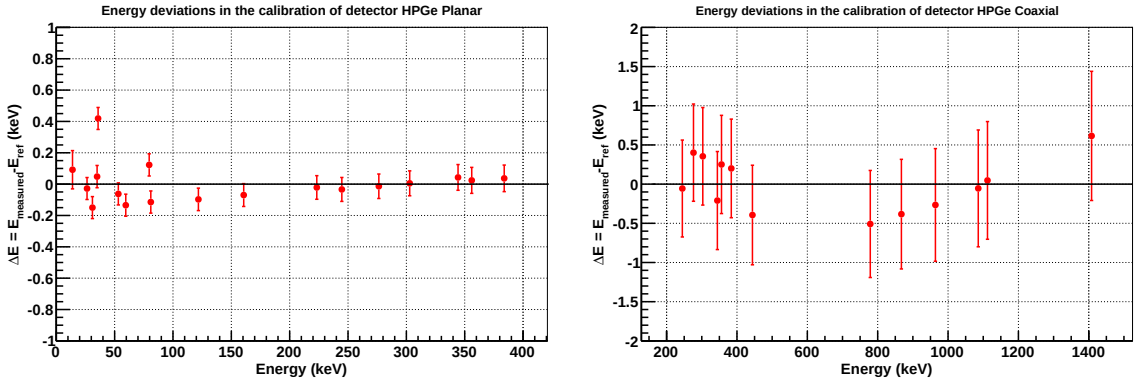

(a) (b)

Figure 4.5: *Energy difference between the γ-transition energies determined in this work and the reference values from [Sin06], [Far99], [Sin95] and [Mar93] for (a) HPGe Coaxial and (b) HPGe Planar detectors.*

The next step is to perform the efficiency calibrations for both detectors. The same sources were used in order to obtain the efficiency curves for both detectors, that is ^{133}Ba, ^{152}Eu and ^{241}Am.

The effective energy range for the HPGe planar detector is from around 20 keV up to 500 keV as it is shown in the figure 4.6. One should take into account that maybe it would be lower but due to the placement of the beta detector in between the source and the HPGe planar detector. In order to determine the efficiency calibration the Gallagher 3.20 and Jäckel 3.21 functions should be combined. The matching point between the two functions was found to be located at 101.5 keV.

For the HPGe coaxial detector the energy range is from around 100 keV up to 1500 keV so the Jäckel equation 3.21 is enough to describe its efficiency in the full range.

The resulting curves are compared in figure 4.6 while the found values for the fit parameters are given in tables 4.2(a) and 4.2(b) for the planar detector and 4.2(c) for the coaxial.

$$\varepsilon(E) = b_1 \times exp(b_2 E^{b_3})[1 - exp(b_4 E^{b_5})] \tag{3.20}$$

$$ln\ \varepsilon(E) = 2(a_1 + a_2x + a_3x^2) \cdot \frac{arctan[exp(a_4 + a_5x + a_6x^3)]}{\pi} - 25 \text{ where x=ln(E)} \qquad (3.21)$$

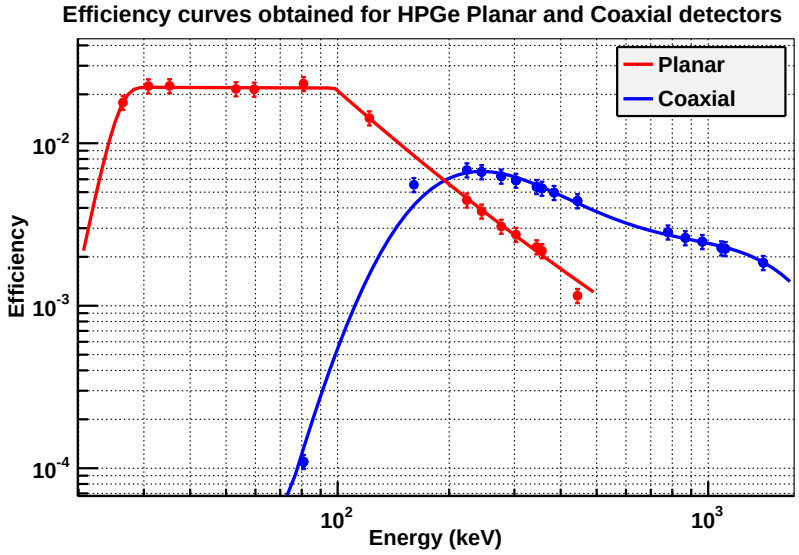

Figure 4.6: *Efficiency curves and data points obtained for both HPGe detectors in the TAS experiment, that is planar and coaxial. The energy ranges for every detector can be observed in the figure as it is established by the dramatic drop in the efficiency of every detector. The experimental data points plotted are coming from the standard gamma calibration sources as ^{133}Ba, ^{152}Eu and ^{241}Am.*

Table 4.2: *Parameter values for functions 3.20 and 3.21 used to fit the absolute efficiency points for HPGe coaxial and planar detectors.*

(a) Values of the Gallagher coefficients (eq. 3.20) from the efficiency calibration of HPGe planar detector

Parameter	Value
b_1	0.0067(5)
b_2	1.22(8)
b_3	-0.01(3)
b_4	-8(26)$\times 10^{-17}$
b_5	11.5(10)

(b) Values of the Jäckel coefficients (eq. 3.21) from the efficiency calibration of HPGe planar detector.

Parameter	Value
a_1	33.16(3)
a_2	-3.2181(10)
a_3	0.13189(11)
a_4	15127.1(14)
a_5	-670.6(14)
a_6	154.4(14)

(c) Values of the Jäckel coefficients (eq. 3.21) from the efficiency calibration of HPGe coaxial detector.

Parameter	Value
a_1	310(44)
a_2	-84(13)
a_3	6.4(10)
a_4	-7.71(13)
a_5	1.84(3)
a_6	-0.0148(3)

Referring the energy resolutions achieved with both HPGe detectors, some values are shown in table 4.3. The energy resolution of the Coaxial detector is a bit better in addition to the fact that it covers a larger energy range as it was already commented.

Radiation source	E_γ (keV)	HPGe Coaxial FWHM (keV)	HPGe Planar FWHM (keV)
^{241}Am	59.5412(1)	0.88(6)	1.03(14)
^{133}Ba	302.8510(6)	1.27(12)	1.24(14)
^{152}Eu	443.965(3)	1.43(10)	1.63(12)
^{152}Eu	778.9045(24)	1.62(8)	
^{152}Eu	964.079(18)	1.79(15)	
^{152}Eu	1112.074(4)	1.86(17)	
^{152}Eu	1408.011(4)	2.1(2)	

Table 4.3: *Energy resolution of HPGe Coaxial and Planar detectors for several gamma transitions coming from calibration sources such as ^{241}Am, ^{133}Ba and ^{152}Eu. The energy range for the Planar detector is up to 500 keV and this is why there is no resolution shown for higher energy gammas than the 443.965 keV one.*

4.1.4 β detector

The beta detector is a plastic scintillator of the type NE102 2 mm thick and with 3 cm of diameter. Its purpose is the detection of beta particles to extract the β component of the decay. The beta-TAS coincidence condition allows to extract the β^+ part of the decay in β^+/EC decays and the β^- decay. Thus, one gets rid of contaminants and obtains a clean TAS spectrum.

A system of light guides was incorporated in order to transport the scintillation light from the plastic detector located in the front part of the HPGe telescope. where the beta detector was placed, towards the photo-multipliers (two cylindrical tubes symmetrically placed with respect to the germanium telescope). In this case, two different photo-multipliers were used in order to collect as much light coming from the detector as possible.

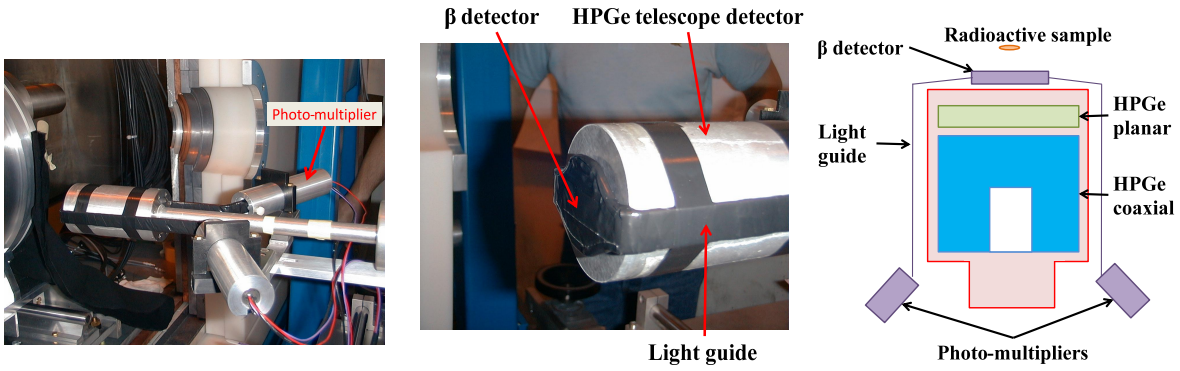

(a) (b) (c)

Figure 4.7: *Set-up of β detector plus HPGe telescope. (a) shows how the two photo-multipliers coupled to the β detector through the light guides and the four layers of the shielding system are visible as well. (b) shows a frontal view where one can see as the β detector is attached to the front part of the HPGe telescope. In (c) a scheme on how the beta detector is placed and coupled to the HPGe detector is shown.*

4.1.4.1 β detector calibrations

The calibration of the β detector is unnecessary at first sight but, at least the energy calibration will be needed in order to establish the energy range covered by the coincidence gate when imposing conditions with this detector.

The energy calibration of the β detector is determined roughly by the comparison of the experimental β-spectrum from the ^{60}Co source with the simulated spectrum for the same source with the GEANT4 code described in chapter 2. As explained in chapter 1, the $\beta^{+/-}$ particle spectrum in a $\beta^{+/-}$ decay is a continuous distribution as neutrino/antineutrino and $\beta^{+/-}$ particle share the available energy, see Fig. 1.2. Thus, one can use the energy of the maximum and the endpoint of the distribution as calibration points.

The result of this calibration for the signals coming from the two photo-multipliers coupled to the β detector is:

$$\text{Right PMT: E(keV)} = 0.225347 \times \text{channel} + 35.2592$$
$$\text{Left PMT: E(keV)} = 0.176677 \times \text{channel} + 58.2754$$

The absolute detection efficiency of this detector was simulated with GEANT4 and it is shown in figure 4.8 for two energy thresholds, 0 and 75 keV. This means that in one case all the detected particles were included while in the second case only when the deposited energy in the detector was larger than 75 keV where taken into account. Obviously, it decreases when increasing the energy threshold as those β particles that deposited from 0 up to 75 keV are not considered when the energy threshold is 75 keV.

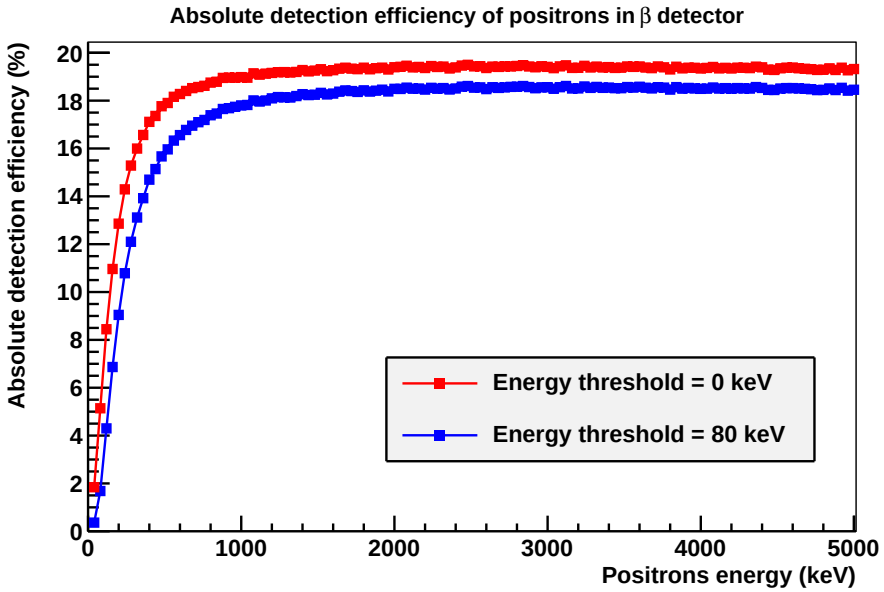

Figure 4.8: *Absolute detection efficiency of the β detector simulated using the GEANT4 simulation code. The red curve is the absolute detection efficiency assuming that the energy threshold of detection is 0 keV. The blue curve corresponds to the case that it is imposed a minimum energy deposited in the β detector of 75 keV which has been used in our analysis to get rid of the electronic noise that appears at low energies in the experimental spectra.*

4.1.5 Beam pipe

The vacuum pipe where the ISOLDE beam comes from has a special telescopic aluminium tube, with 68 mm diameter, that allows for the implantation right at the center of the TAS detector. It keeps a high vacuum level inside, around 10^{-6} mbar, and it ends in a 80 μm thick kapton window just in between the measuring point and the beta detector. In this

way the vacuum is kept and it permits to measure X-rays and low-energy gamma radiation emitted by the source. The beam pipe can be seen in the sketch of the setup, figure 4.4.

4.1.6 Tape transport system

It consists of a 55 μm thick aluminized mylar tape with a step motor system to drive the tape along a vacuum pipe perpendicular to the beam direction that can be seen on the right bottom side in figure 4.1. The motor moved the tape at a velocity of 1.3 m/s.

This component is very important in order to stop the sample in the measuring point, to accumulate it and to move it outside of the measuring point each cycle. This is done to remove the daughter activity and have a new sample in the measuring point every cycle.

4.1.7 Data acquisition system

The data acquisition system (usually abbreviated as DAQ) was based on a FERA-CAMAC system controlled by a VME processor working under Multi Instance Data Acquisition System (MIDAS) software.

The data from each detector (i.e. data channel) was saved in two independent ways:

- **Singles spectra**: data is stored via the HM413 ORTEC histogramming memory module connected to the CAMAC crate. Only direct histograms without any further information are saved in 8 kilobytes spectra (8192 channels).
- **List mode data** which includes the time information coming from all the data channels in an event-by-event basis.

The list mode data is based on the **trigger signal** which is the one that activates the acquisition of data by the data acquisition system (DAQ).

The list mode data can be understood as follows: once established what a trigger signal is, that is which signal fires the DAQ system, then one chooses how much the time coincidence window lasts, in this case was 2 μs. Then, every time a trigger signal is coming from one data channel (trigger provider) the information coming along this time window from all the data channel is stored as belonging to the same event. At the same time, a veto signal forbids the acquisition of any other trigger signal during the acquisition procedure.

The trigger signal of our experiment was elaborated as an OR logical output signal of the 8 TAS photomultipliers. This implies that one is saving the data when any radiation is detected by the TAS detector, which is, as it will be shown later, the most efficient detector in the setup.

For the data acquisition in list mode there are two electronics chains. On the one hand, the so-called **slow electronics** which aims to save the energy information of the input data channel. In our case one signal comes from each of the TAS Photomultipliers (PMT's), one signal for every beta detector when they were in coincidence between themselves, and the signals from the HPGe Coaxial and Planar. The first element of this circuit is the spectroscopic amplifier and then the signal is lead to the Analog to Digital Converter (ADC) whose output signal is stored in two ways singles and list-mode, as already mentioned.

The **fast electronics** has the aim of saving the time information of the signal from every data channel. Thus, a electronics chain composed by a Time Filter Amplifier (TFA), a Constant Fraction Discriminator (CFD) and a Gate and Delay Generator (GDG) and ADC was used before storing the data. Additionally, the time difference between the TAS PMT's signals and the one from HPGe coaxial, planar and beta detector was stored by using a Time to Amplitude

Converter (TAC). This module used as START signal the HPGe and beta detectors ones and as STOP the TAS PMT's signals.

4.1.7.1 Sorting of the data

The first step in the data-analysis procedure is to convert the data from the acquired files (raw data) to a readable and handy format. The analysis toolkit used is ROOT which is an object-oriented program and library developed at CERN written in C++ programming language. The raw data was transformed into ROOT trees, where the data is stored in an event-by-event basis collecting all the data channels corresponding for each event registered during the measurement.

Once the data have been organized in trees structure, an analysis code was prepared to read every tree and make projections of the data over the different data channels, such as TAS, HPGe coaxial, HPGe planar, β detector, etc... The data channels collected in the experiment were:

- **TAS(i):** where i=1,...,8. Every photo-multiplier of the TAS detector separately.
- **SumTAS.** The hardware addition of the signals coming from the 8 photo-multipliers of the TAS.
- **Beta Counter(j):** where j=1,2. Signals from the two different photo-multipliers coupled to the beta counter are collected in two data channels.
- **HPGe Coaxial.** energy signal of the HPGe coaxial detector.
- **HPGe Planar.** energy signal of the HPGe planar detector is registered. Note that this signal was derived through two different amplifiers to apply two different gains and cover two different energy ranges. So two data channels are associated to this detector.

In figure 4.9 some of the projections, that is SumTAS, HPGe coaxial and planar and the beta detector, are shown as example. They are shown already energy calibrated. Spectra were stored in 8192 channel spectra as 13-bits ADC were employed.

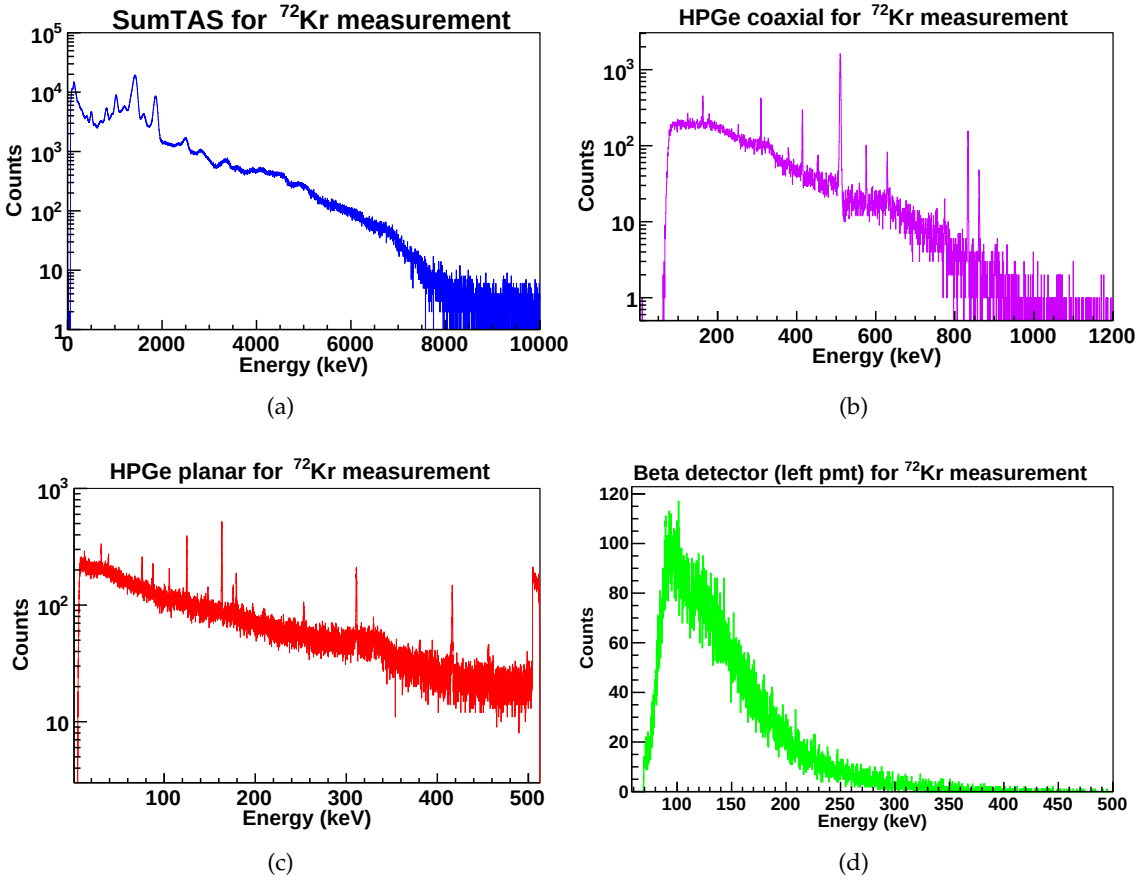

Figure 4.9: *Some projections from the raw data of the first measurement with ^{72}Kr beam as an example: (a) SumTAS spectrum: hardware addition of TAS photo-multipliers signals (b) HPGe coaxial spectrum (c) HPGe planar spectrum (d) Beta spectrum from one of the photo-multipliers coupled to the detector.*

4.2 Analysis

The decay of ^{72}Kr is a β^+/EC decay as it was mentioned. That means that the decay could take place via two different processes and the consequent total B(GT) distribution to be measured should have two contributions, that is EC and β^+ components.

The ratio between both components in the full Q_β window is shown in figure 4.10. The data has been taken from the tables in [Gov71] where log $f(\beta^+)$, log $f(\beta^+$+EC) and log $f(\mathrm{EC}/\beta^+)$ values can be obtained for every mass and excitation energy. In this figure is shown as from around 3 MeV of excitation energy on, the EC decay is dominant versus β^+ component up to the Q_{EC} = 5127(10) keV.

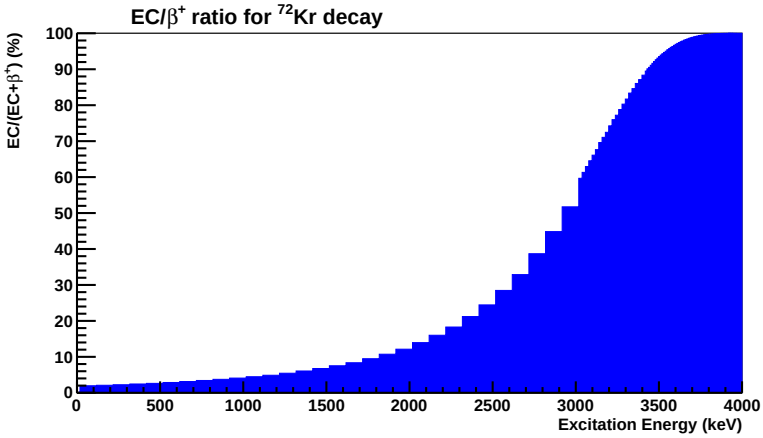

Figure 4.10: *Ratio EC/Total for the β^+/EC decay of ^{72}Kr obtained from tables in [Gov71]. This ratio is 100 % from 4000 keV up to the full Q_β as the β^+ decay has a energy threshold in 1022 keV, so for higher energies than Q_{EC}-1022 keV there is only the possibility of EC decay. This threshold for the ^{72}Kr is at 4105 keV as the Q_{EC}=5127(10) keV. As can be seen, from around 3 MeV of excitation energy in the daughter nucleus, is dominant the EC decay.*

4.2.1 Analysis of EC decay component

On the one hand, one would try to analyse the EC component of the decay. In order to do this, the first step would be to place an condition of coincidence in the HPGe planar detector with an detection of a characteristic X-ray of the daughter nucleus, ^{72}Br, which is emitted in every EC decay event.

This procedure has two problems in the case of ^{72}Kr decay. First, the energy of the most intense X-rays of ^{72}Br are 11.924 and 11.878 keV while for ^{72}Se are 11.222 and 11.182 keV and the energy resolution of the HPGe planar detector at these energies does not allow for resolving these transitions. So we are not able to separate the contributions from the EC decays of ^{72}Kr and ^{72}Br. Second, the ^{72}Br X-rays are also emitted when a conversion electron process which takes place in the de-excitation path of the excited level fed in the beta decay of ^{72}Kr. When there exists strongly converted transitions in the daughter, as in the decay of interest (see the conversion coefficients study in chapter 3), the selection of the EC component makes impossible as the resulting TAS X-ray gated spectrum would be a mixture of EC decay events and those β^+ decay events followed by a significantly converted de-excitation transition in the daughter.

Due to these reasons, we rejected the possibility of analysing the EC component of the decay and the total B(GT) distribution will be deduced from the β^+ component of the decay.

4.2.2 Analysis of β^+ decay component

In this section we will analyse the β^+ component of the decay, and from that, we will obtain the B(GT) distribution coming from the β^+ decay. As it is seen in figure 4.10, this component is dominating the low-energy part of the beta decay up to around 3 MeV and it finishes at Q_{β^+}=4105 keV obtained from:

$$Q_{\beta^+} = Q_{EC} - 1022\ keV = 5127\ keV - 1022\ keV = 4105\ keV \tag{4.2}$$

The spectra to be analysed is obtained from the projections of the ROOT trees that have been prepared for every file of data collection. Thus, for a given file one can obtain 14 spectra as has been indicated in the previous section 4.1.7.1.

In order to obtain the β^+ component one has to evaluate the data in an event-by-event basis imposing the condition that a β particle has been detected in the β detector and, then, store the value for the SumTAS signal. Basically, one imposes the coincidence condition between a β particle detection in the β detector, which is the coincidence of signals from both photo-multipliers of the β-detector, and any signal in the TAS detector. The condition of coincidence in both photo-multipliers of the beta detector guarantees that the signal is coming from the detection of a beta particle and the electronic noise of every individual photo-multiplier is eliminated.

The obtained **β-gated spectrum** includes contributions coming from β decay processes and no room background contamination is present. This condition guarantees that the registered events come from β decay events but not only from events of the decay of interest, in this case ^{72}Kr decay, but also events from the decay chain: ^{72}Br, ^{72}Se and ^{72}As would fulfill this condition. Figure 4.12 shows this decay chain starting in ^{72}Kr. As the tape station removes the sample from the measuring point every 15 seconds, the main contribution to the spectra should come from the ^{72}Kr decay but still contribution from the decay chain could appear.

Figure 4.11 shows a comparison between the SumTAS and β-gated spectra. The condition in the β detector was to obtain a detection with energy higher than 75 keV. As can be seen in the figure, the statistics of the β-gated spectrum is much smaller than the SumTAS spectrum. This is due mainly to three reasons: firstly, the contribution from the room background radiation is rejected in the β-gated spectrum and it appears in the SumTAS as it is not in coincidence with any β particle. Secondly, the β-gated spectrum is affected by the detection efficiency of the β detector, which can be observed in figure 4.8 with blue line for this case in which the energy threshold has been chosen to be 75 keV, and it is around 20 % except at smaller energies than 1 MeV where it decreases. This means that just this fact reduces five times the statistics with respect to the one from SumTAS spectrum. As a third reason, it is the fact that the EC decay events do not emit a beta particle and do emit the subsequent gamma radiation so they will contribute to the SumTAS spectrum and not to the β-gated one.

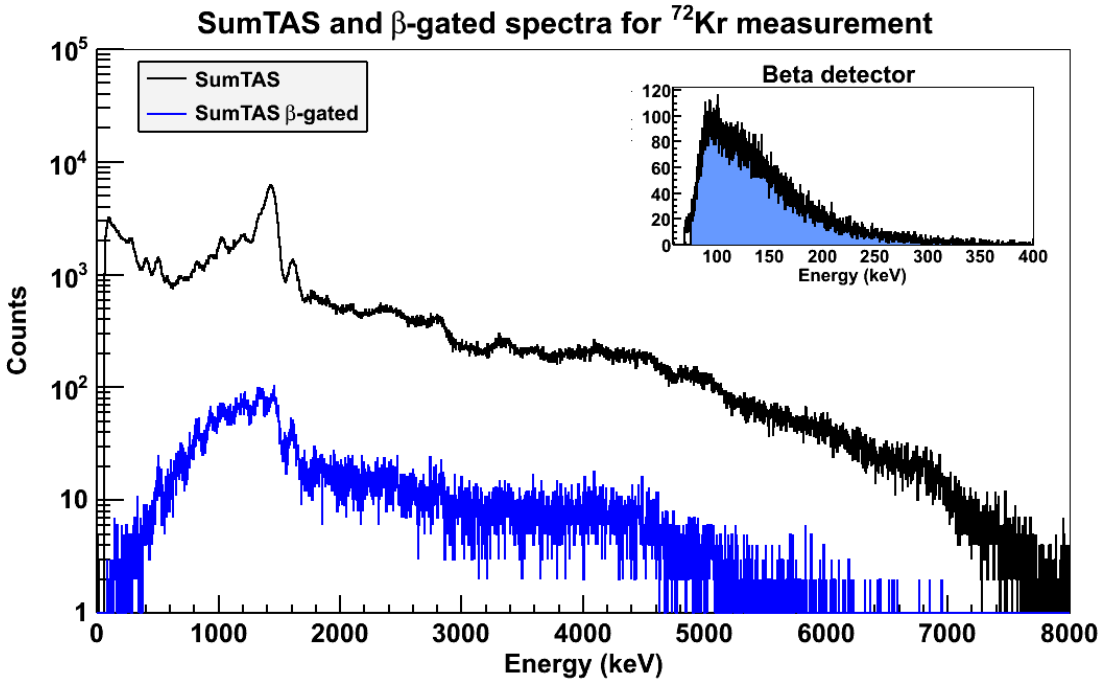

Figure 4.11: *Comparison of ^{72}Kr SumTAS and β-gated SumTAS spectra for a 75 min file as an example (file 1 in table 4.5. The inset figure at the upper right corner shows the beta detector spectrum used to establish the coincidence condition imposed on the TAS spectrum (black) to obtain the beta gated spectrum (blue). The statistics is reduced considerably due to 3 facts: the beta detection efficiency given in figure 4.8, the room background radiation and the EC decay-delayed γ radiation.*

4.2.2.1 Contaminants subtraction

The contaminants are the contributions to the experimental spectrum coming from different origin than the ^{72}Kr decay. Thus, in the current measurement, the main contaminant contributions could be the radiation from the decay chain (^{72}Br,^{72}Se,^{72}As, etc..., decays), room background and pile-up of electronic signals.

The most important contamination is the one from the **decay chain**, that is coming from the de-excitation radiation following the decay of the daughter, grand-daughter, etc... See the A=72 decay chain starting at ^{72}Kr in figure 4.12 and table 4.4. The main contribution will be the one of the ^{72}Br decay as the half-life of the next isotope in the chain, ^{72}Se, is quite long (8.4 days) in comparison with the duration of the measuring cycle periods (15 s for collection and measurement).

The **room background** contamination is negligible in the case of the β^+ gated spectrum as the condition of time coincidence with a positron detected in the β detector is required in the analysis.

The **pile-up contribution** depends on the counting rate of the measurement. Its influence in the measurement can be observed by looking to the TAS spectrum for energies beyond the largest Q_{EC} value of the decay chain. In case of being necessary the subtraction of this contamination, the procedure to remove the pileup contribution is explained in detail in Ref. [Can99b]. Basically it takes into account the shape of the TAS spectrum and the shape of the electronic signal coming from the TAS photo-multipliers.

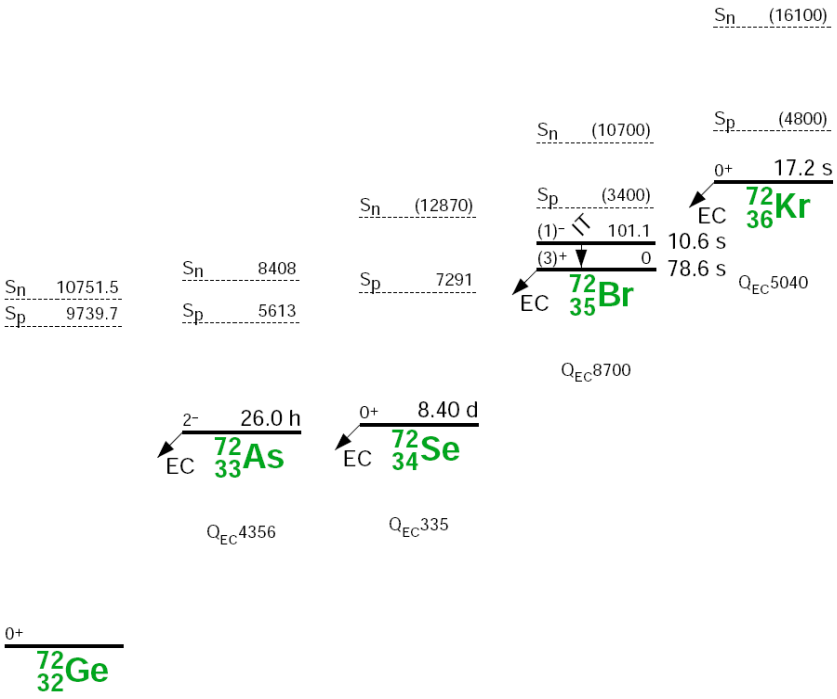

Figure 4.12: *^{72}Kr β^+/EC decay chain. For every decay it is shown the Q_{EC}, S_n, S_p and half life.Image taken from [Fir96]. More recent measurements of the ^{72}Kr and ^{72}Br masses [Rod04, Her11] gives a new Q_{EC} value for the ^{72}Kr decay of 5127(10) keV, as given in [Wan12b] and explained in sect. 1.3.3.*

Parent nucleus	$T_{1/2}$	Q_{EC} (keV)	Most intense γ lines (keV)
^{72}Kr	17.2 s	5127(10)	309.9, 415.1, 162.7, 576.9
^{72}Br	78.6 s	8799(7)	862.0, 1316.7, 454.7
^{72}Se	8.4 d	335	45.9
^{72}As	26 h	4356	833.99

Table 4.4: *A=72 mass decay chain starting at ^{72}Kr which is the beam in the current experiment. The decay of ^{72}Br, ^{72}Se and ^{72}As can be present in our spectra, specially the first of them as the half-life of ^{72}Se is quite large (8.4 days). . This is the new value for the ^{72}Kr decay Q_{EC} that has been recently determined [Wan12b] instead of the one shown in fig. 4.12 which corresponds to a previous compilation.*

A brief summary on how the measurements to study the β^+/EC decay of ^{72}Kr were performed is provided in table 4.5. The chronological order of the measurements is given and the relative amounts of each decaying nucleus is shown. This is estimated via the most intense gamma line in every decay seen in the HPGe spectra (coaxial or planar depending on the energy of the transition) while a coincidence condition with a signal from TAS detector is imposed via hardware. The gamma lines used are 415 keV in ^{72}Kr, 862 keV in ^{72}Br, 834 keV in ^{72}As, 286 keV for ^{75}Br and 360 keV in ^{73}Se. For ^{72}Kr files all the amounts are referred to the ^{72}Kr decay.

Note that the amount of ^{72}As is growing as time passes and this suggests the possibility of depositing the beam somewhere outside the tape. Otherwise, this amount should be approximately constant as new beam is being implanted every cycle. Another fact supporting this idea is that the amount of ^{72}Br decay is growing up to file number 4 and from this file on it decreases. This could tell us that the deposition of beam outside the transport tape had to stop at some point during file 4.

Another remarkable fact is that in the first 3 files devoted to measure ^{72}Kr decay, there is presence of ^{75}Br lines. This is due to the previous measurement with ^{75}Kr as beam. Probably, in the same way as in our measurement is likely that we implanted beam outside the transport tape, in the ^{75}Kr measurement happened the same and a small contamination of ^{75}Br decay is remaining when we started the ^{72}Kr measurement.

Several hints support the idea of the beam deposition outside the moving tape so from now this idea will be accepted and all these contributions has to be removed from the ^{72}Kr spectra to be able of extracting the good beta feeding distribution from the analysis of the spectra.

	Duration	Tape cycle	Relative amounts				
	(min)	Coll./Wait./Meas. (s)	^{72}Kr	^{72}Br	^{72}As	^{75}Br	^{73}Se
^{75}Kr measurement							
^{72}Kr file 1	75	15 / 0 / 15	100	8.1	0.0	7.1	0.0
^{72}Kr file 2	74	15 / 0 / 15	100	8.2	1.6	2.6	0.0
^{72}Kr file 3	47	15 / 0 / 15	100	11.1	2.5	1.3	0.0
^{72}Kr file 4	171	15 / 0 / 15	100	13.9	13.3	2.0	0.0
^{72}Kr file 5	60	15 / 0 / 15	100	10.8	28.6	0.0	0.0
^{72}Kr file 6	71	15 / 0 / 15	100	8.8	31.1	0.0	0.0
^{73}Kr measurement							
^{72}Br file	112	84 / 60 / 90	100	58.6	32.2	0.0	67.3
A=73 file	30		0.0	0.0	32.2	0.0	62.8

Table 4.5: *Chronological order of the measurements and amount of contaminants presents in each one. Amounts of each decay are estimated using the most intense gamma lines for each decay: 415 keV in ^{72}Kr, 862 keV in ^{72}Br, 834 keV in ^{72}As, 286 keV for ^{75}Br and 360 keV in ^{73}Se. Peak areas in the HPGe spectra (coaxial or planar depending on the energy of the transition) taken in coincidence with a signal in the TAS spectrum are divided by detector efficiency and gamma intensity per 100 parent decays. The coincidence condition guarantees the contribution to the TAS spectrum.*

The first contamination to be subtracted is the ^{72}Br decay radiation. For this purpose, a measurement with ^{72}Kr as beam and different time cycles than ^{72}Kr decay measurements in order to optimize the quantity of ^{72}Br in the measuring point was performed. For this measurement, the time cycles were 84 seconds collecting sample, 60 seconds waiting and then the measuring time lasted 90 seconds. This asymmetric cycle provided us with a higher ratio between the amount of ^{72}Br and ^{72}Kr as listed in table 4.5. The ratio ^{72}Br/^{72}Kr for this measurement is 58 % while for the ^{72}Kr measurements were around 8-10 %.

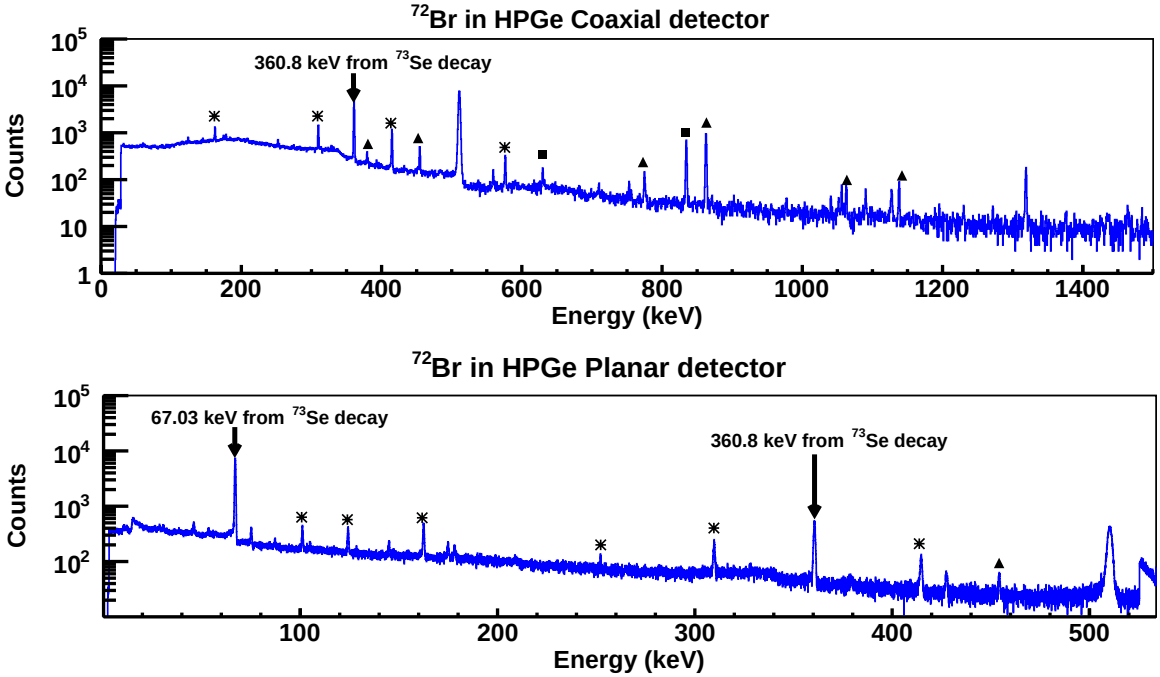

Figure 4.13: *HPGe spectra from Coaxial and Planar detectors for a file with time cycles optimized for ^{72}Br measurement. Peaks marked with an asterisk (*) are coming from ^{72}Kr decay while the ones marked with black triangles (▲) are from ^{72}Br decay. Contamination from the decay of ^{72}As decay was found and the lines at 630 and 834 keV are marked with black squares (■). Apart from the expected lines from the A=72 decay chain, there are some lines from the ^{73}Se decay as, for example, the 67.03 and 360.8 keV which are labelled with arrows. This is an indication that there is presence of A=73 radiation in the surrounding area of the sample from the previous measurements where the ^{73}Kr was used as beam.*

The ^{72}Br γ spectrum obtained with the cycle described above is shown in Fig. 4.13. It present γ lines coming from the ^{72}Kr decay (indicated with asterisk). We could also identify γ lines belonging to the ^{72}Br decay (market with triangles) and ^{72}As decay (identified with squares). Apart from those expected contributions, there are some lines belonging to the ^{73}Se decay, namely the 360.8 and 67.03 keV lines. The presence of ^{73}Se decay is not due to an impurity of the beam but rather a deposition of the previous measurement with ^{73}Kr beam in the surrounding area of the measuring point, somewhere outside of the transportation tape as, for example, the beam pipe, rollers to lead the tape along its path, etc...

The contribution of ^{73}Se decay has to be subtracted from the ^{72}Br decay spectrum before proceeding with the subtraction of the ^{72}Br decay contribution to the ^{72}Kr decay spectrum.

4.2.2.2 Subtraction of A=73 contamination from ^{72}Br spectrum

The beam used in the measurement previous to the ^{72}Br measurement, that is contaminating the spectrum, was ^{73}Kr. Having a look at the mass A=73 decay chain, shown in figure 4.14 and whose information is given in table 4.6, one notices that the half-lives of ^{73}Kr and ^{73}Br are relatively short, 27 seconds and 3.4 minutes respectively, as after few minutes almost no contribution from these decays would appear in the spectrum. However, the half-life of ^{73}Se is long enough to be present in the measurement of ^{72}Br as it is 7.15 hours with an isomer of 39.8 minutes.

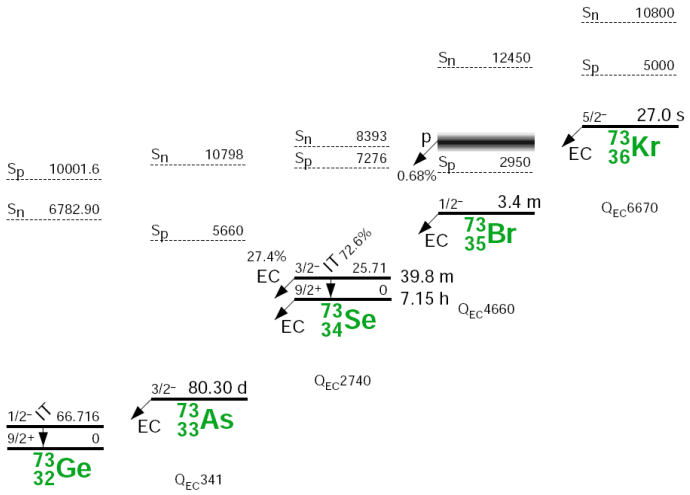

Figure 4.14: *^{73}Kr β^+/EC decay chain. For every decay it is shown the Q_{EC}, S_n, S_p and half life.Image taken from [Fir96].*

Parent nucleus	$T_{1/2}$	Q_{EC} (keV)	Most intense γ lines (keV)
^{73}Kr	27 s	6670	177.8, 62.5, 151.1, 473.6
^{73}Br	3.4 min	4660	65.0, 335.9, 699.8, 125.6, 400.9
^{73m}Se	39.8 min	2740.0+25.7*	β^+/EC: 67.03, 253.7, 84.0, 393.4, 401.5. IT: 25.7
^{73}Se	7.15 h	2740	360.8, 67.03
^{73}As	80.3 d	341	53.47

Table 4.6: *A=73 mass decay chain starting at ^{73}Kr which is the beam in the previous measurement to the one devoted to measured ^{72}Br decay. The decay of ^{73}Br, ^{73}Se, ^{73m}Se and ^{73}As could be present in our spectra, specially the decays of ^{73m}Se and ^{73}Se as the previous nuclei in the decay chain, ^{73}Kr and ^{73}Br, have relative short half-life so they have almost disappeared for our measurement and the ^{73}As decay has a quite long half-life so its contribution will be negligible.*

A measurement of mass A=73 was performed to subtract the contamination from the ^{72}Br spectrum. It was performed some hours after the ^{72}Br measurement. The procedure was to implant some ^{73}Kr beam on the tape, later close the beam gate to avoid any further beam position and then measuring without moving the transport tape. The measurement was 2 hours and 25 minutes long. In order to reproduce similar counting rates of ^{73}Se decay than the ones contaminating the ^{72}Br decay measurement just the last 30 minutes of this measurement has been chosen. This is due to the ^{72}Br decay measurement was started approximately 1 hour and 55 min later than the last ^{73}Kr beam deposition.

The spectrum measured by the TAS detector in this measurement of A=73 decays, imposing the coincidence with one signal in the β-detector is shown in figure 4.15. The Q-values of ^{73}Se and ^{72}As decays can explain the extend of the TAS spectrum as can be seen in figure 4.15. Another relevant fact that can be seen in this spectrum is the negligible amount of pile-up in this measurement as there are no counts at higher energies than the largest Q-value of the

contributing decays (see figure). This is in concordance with the fact that this measurement was kept at low counting rate (around 3 kHz in the TAS detector) as the waiting time was quite long after the irradiation period.

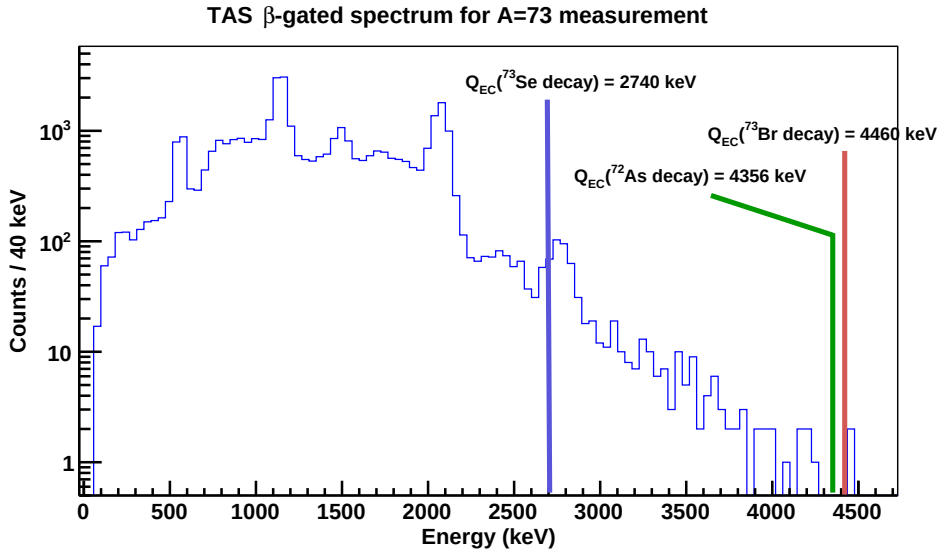

Figure 4.15: *Total Absorption Spectrometer spectrum for the A=73 measurement with the β-coincidence condition, also known as β-gated TAS spectrum. The Q-values of the contributing decays are indicated.*

The resulting HPGe spectra for this measurement is shown in figure 4.16. There are transitions from the ^{73}Se decay, namely the 67 and 360 keV transitions, and from the ^{72}As decay, the 630 and 834 keV transitions. These latter ones came from the contamination of the surrounding area of the measuring point done while measuring with mass A=72. The relative amounts was already included in table 4.5. This is done taking into account the absolute gamma intensities per 100 decays (I_γ) of each transition and the detector efficiencies.

The presence of ^{72}As decay in the A=73 spectrum is not a problem as the ^{72}As decay is also a contamination in the ^{72}Br file. However, one has to check that the relative amount of ^{72}As with respect to ^{73}Se decay is similar in A=73 and ^{72}Br files.

The relative amount of ^{72}As with respect to ^{73}Se in the A=73 and ^{72}Br measurements has been estimated by using the most intense gamma lines corresponding to each decay. For this purpose, the 360 keV transition in ^{73}Se decay and the 834 keV transition in ^{72}As have been chosen. In the case of the ^{72}Br file the amount of ^{72}As and ^{73}Se were referred to 100 % of ^{72}Kr decays. However, in the A=73 measurement the quantity of ^{73}Se has been referred to 32.2 % of ^{72}As in order to have the same normalization factor than in the ^{72}Br file. Thus, the amount of ^{73}Se decays in both spectra are similar, being 67.3 % in the ^{72}Br file and 62.8 % in the A=73 one as indicated in table 4.5. So one could state that both measurements are similar in terms of relative amounts of ^{73}Se and ^{72}As so if one subtracts the contamination of ^{73}Se at the same time it is subtracting the ^{72}As contamination along.

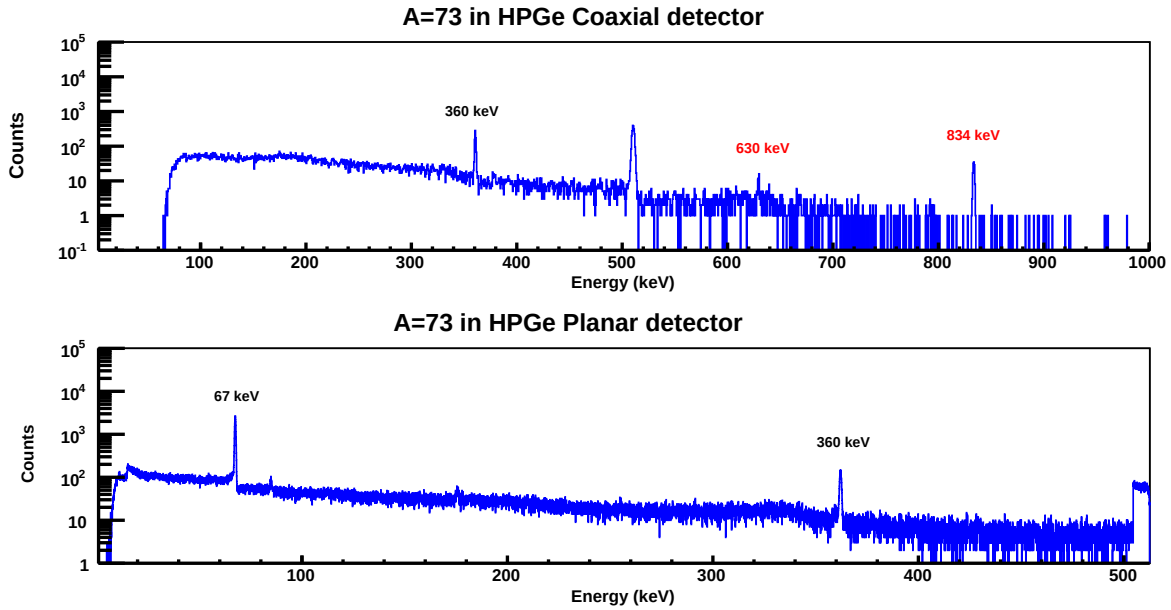

Figure 4.16: *HPGe spectra for the A=73 measurement. The upper spectrum corresponds to the HPGe coaxial detector and the lower one to the HPGe planar. In the planar detector only the 67 and 360 keV transitions belonging to the ^{73}Se decay are identified while in the coaxial spectrum also are found two transitions (630 and 834 keV) belonging to the ^{72}As decay, the ones labelled in red.*

Parent nucleus	E_γ (keV)	Peak area	Efficiency(coaxial)=ϵ_{coax}	I_γ(%)	N = $\frac{Area}{\epsilon_{coax} \times I_\gamma}$
^{73}Se	360	34872(198)	0.0053(5)	108	6.1(6)$\times 10^6$
^{72}Br	862	9078(100)	0.0026(3)	70	5.0(5)$\times 10^6$

Table 4.7: *Measurements performed on the spectrum belonging to the HPGe coaxial for the measurement of ^{72}Br beam which is contaminated with contribution from ^{73}Se decay. The efficiency of the detector is experimentally obtained as explained in section 4.1.3.1. I_γ is the absolute gamma intensity per 100 parent decays.*

The contribution of ^{73}Se decay is a contamination of the ^{72}Br spectrum and has to be removed from the ^{72}Br spectrum. For this purpose, the most intense gamma transitions following the ^{73}Se (360 keV) and ^{72}Br (862 keV) decays were used to obtain the amount of both decays in the spectrum. The obtained values can be seen in the table 4.7. Using this estimation of the amount of both decays, the subtraction factor has been estimated. However, looking at the clean spectrum we conclude that this factor is overestimated, as it completely remove the whole spectrum for energies below 2100 keV. We should reduce this factor in order to obtain a physically possible factor that we could consider as the "standard" value.

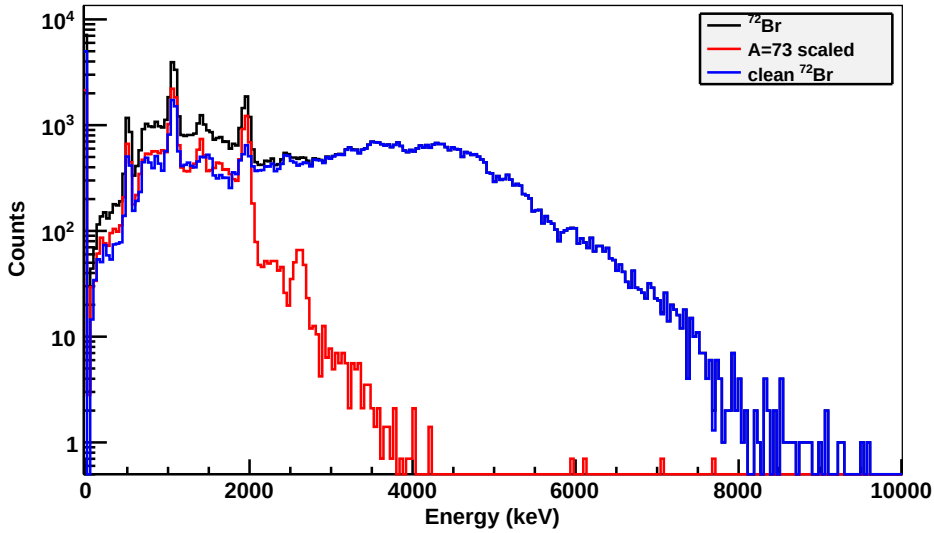

Figure 4.17: *Subtraction of A=73 contamination from the ^{72}Br spectrum. The subtraction factor is chosen by looking at the peak located at energy 1950 keV and the energy region around it, as described in the text. The peaks at 511 and 1022 keV are also important in the choice of this factor, as they are coming from the annihilation of the positrons emitted in the β^+ decay process. They are always visible when a β^+/EC decay is studied via a TAS measurement. In the ^{72}Br decay one expects to observe counts, at least, in both peaks, so the subtraction should keep visible both peaks.*

The figure 4.17 shows the "standard" subtraction factor that has been finally chosen. Standard here means that is the subtraction factor considered in the analysis. The reason for this choice is that if one looks at the prominent peak located at 1950 keV in the black spectrum (^{72}Br raw), the subtraction should remove this peak from the ^{72}Br spectrum as it belongs to the A=73 decay since it is present in the A=73 spectrum (red). The blue spectrum is the already subtracted one but as it can be seen, the peak has is removed. The reason is that the subtraction should provide a resulting spectrum with no big irregularities, and if one increases the factor a "hole" appears at the left part of the peak at 1950 keV. Other reason for not increasing the factor are the presence of 511 and 1022 keV peaks that are present in all the spectra (black, red an blue). They are coming from the annihilation of the positron emitted in the β^+ decay process that occurs for both, ^{72}Br and ^{73}Se decays. So the subtraction should keep these peaks as they should appear in the ^{72}Br clean spectrum. If one increases the factor these peaks also disappear.

As one sees, this subtraction is not very precise and for this reason one should include two other subtraction factors that provide us with a wide confidence interval in the value of the subtraction factor. Later, these subtractions will be used to estimate the uncertainty in the final results of the analysis.

The final subtractions considered are the ones shown in figure 4.18. They correspond to the following subtraction factors:

$$\text{Standard subtraction: } 0.274 \tag{4.3}$$

$$\text{Maximum subtraction: } 0.384 \tag{4.4}$$

$$\text{Minimum subtraction: } 0.164 \tag{4.5}$$

The criteria for the election of the maximum and minimum factors are:

- Maximum factor: the subtraction should not create a big step in the region around 2000 keV of the clean spectrum. This factor has been chosen that causes a step in this energy region as it is shown in the lower part of the fig. 4.18. This step is probably beyond the acceptable subtraction but it is just to be safe in the latter estimation of the uncertainties of the results. This subtraction cancels the peak at 1950 keV as well.

- Minimum factor: small enough to not reduce strongly the statistics in the low energy region of the spectrum, where the the A=73 spectrum contributes, but keeping the same shape of the spectrum.

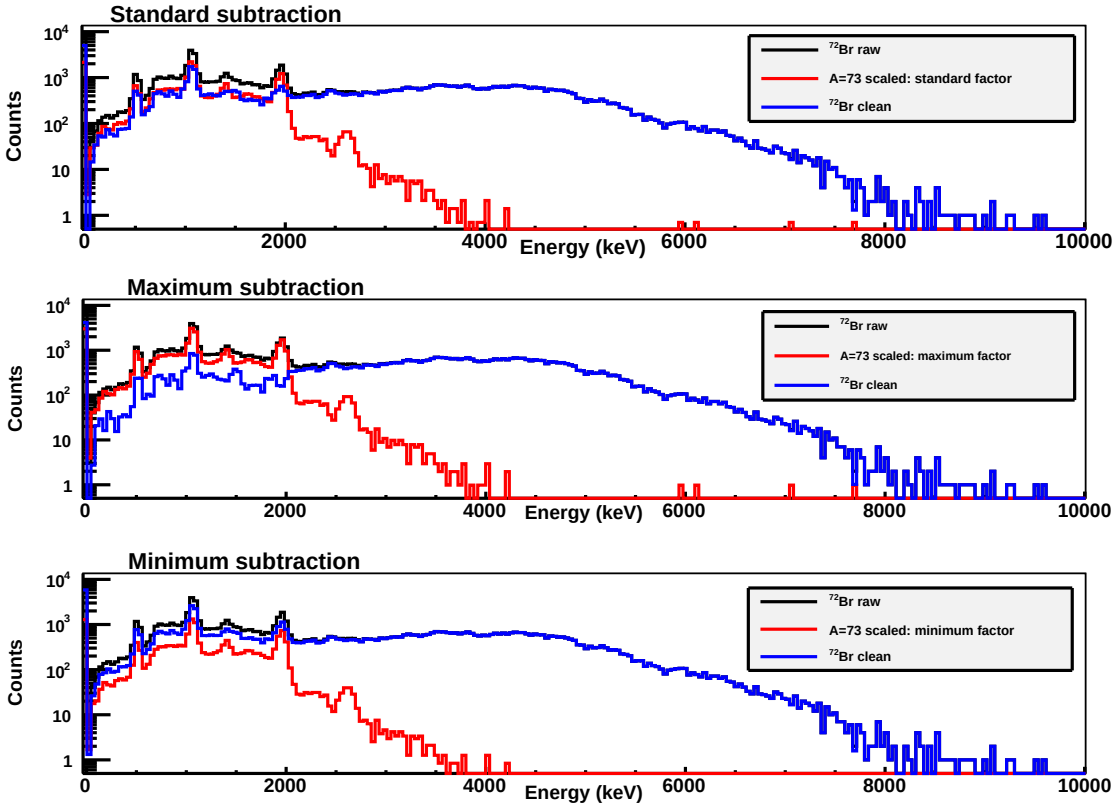

Figure 4.18: *Subtraction of A=73 contamination from the ^{72}Br spectrum. There are three different subtraction factors, given in eq. 4.3, the upper one is the standard subtraction factor, the middle one is the maximum factor and the bottom one shows the minimum subtraction.*

4.2.2.3 Subtraction of pile up contamination in the ^{72}Br spectrum

Once the ^{72}Br spectrum is clean from its A=73 contamination the next step in the procedure is to remove the pile up contribution. Figure 4.19 shows the ^{72}Br once the A=73 contribution has been subtracted. The Q_{EC} value of the ^{72}Br decay is 8799(7) keV and it is indicated in the spectrum. The statistics beyond the Q_{EC} value, where the pile up contribution should be clearly visible, is negligible. For this reason, this subtraction is not needed to be performed.

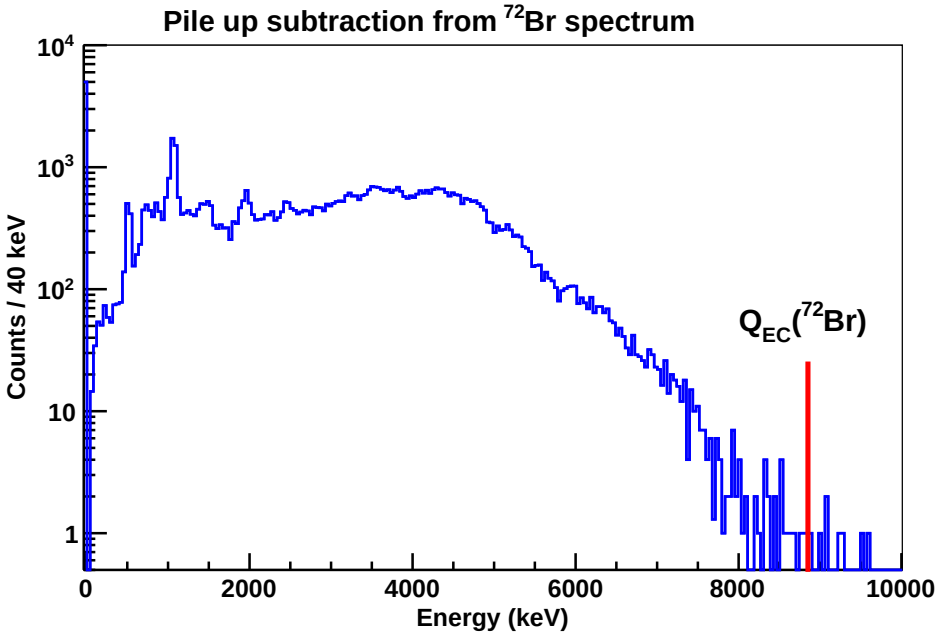

Figure 4.19: *Subtraction of pile up contribution from the ^{72}Br measurement. As can be seen, the statistics beyond the Q_{EC} (^{72}Br) is negligible. For this reason the subtraction of this contribution was finally rejected.*

4.2.2.4 Subtraction of ^{72}Br contamination from ^{72}Kr spectrum

Once the main contaminant spectrum, ^{72}Br decay, has been obtained as a clean spectrum from its own contamination, one can proceed to clean up the ^{72}Kr spectra from contaminants.

There were six different files taken with ^{72}Kr as beam in the data. The beta-gated TAS spectra are shown in figure 4.20 for the six files.

It is remarkable if one observes all the spectra carefully, there are some clear differences at low energies, mainly in the region around 1800 keV, where a peak is growing up as time passes. This peak is not appreciable for file 1, almost negligible for file 2 and is rising as one continues through files 3, 4, 5 and 6. This can indicate that some contaminant is growing as time passes due to a deposition of radiation not only in the tape but also in the surrounding area of the beam pipe such as the tubes, rollers, etc... and since this part is not movable with the cycles, this sample would decay following the decay chain.

In order to understand which contamination is the one growing a detailed study of the HPGe spectra has to be performed. The transitions found in these spectra belong to the following decays: ^{72}Kr, ^{72}Br, ^{72}Se and ^{72}As.

If one has a look carefully to the data in the table 4.5 is visible that the amount of ^{72}Br decays is similar in the 6 files taken for ^{72}Kr. Meanwhile, for the ^{72}As the amount is increasing from one file to the next one. This would suggest to consider for the analysis only the 3 first files of ^{72}Kr where the amount of ^{72}As is below 3 % as for the rest of files this amount is increasing up to 31.1 % in the last file.

The other contamination presents in some files is ^{75}Br decay radiation. This is due to the fact that just before the ^{72}Kr files, a measurement with ^{75}Kr as beam was performed and it seems that some beam was implanted in the area nearby the measuring position. In figure 4.22 the decay chain from ^{75}Kr is shown and the relevant information is given in table 4.8. The

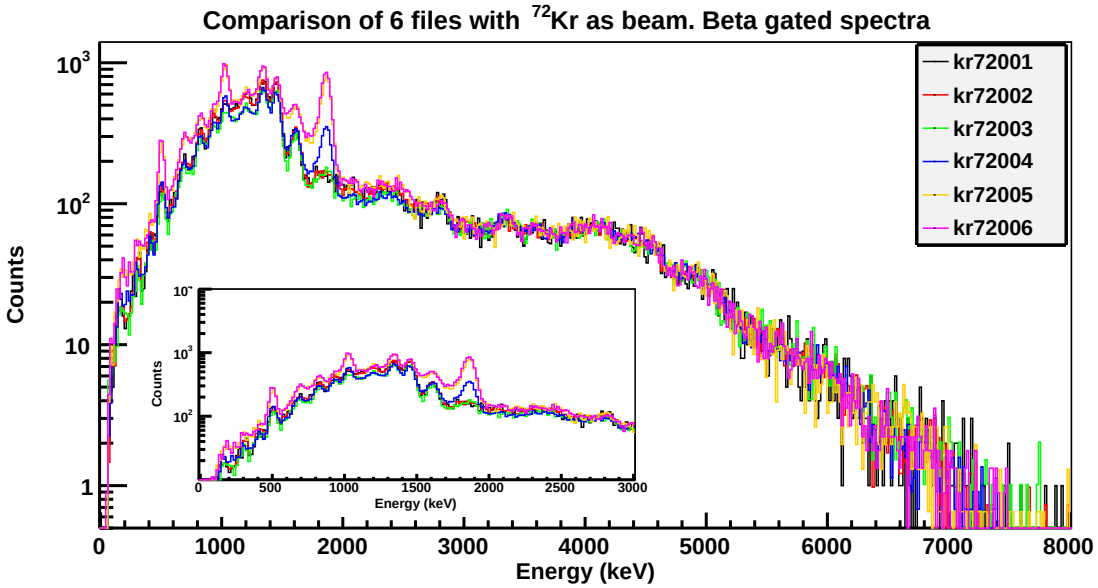

Figure 4.20: *Spectra corresponding to the β-gated TAS detector for the 6 different files collected with a ^{72}Kr beam and the time cycle of $t_{collection} = t_{measuring}$ =15 s, as given in table 4.5, in order to optimize the amount of ^{72}Kr in the sample. They have been scaled to the integral in the region from 4 to 7 MeV in order to better visualize the differences between the spectra. The inset shows the low energy region of the spectra to observe the differences in this region.*

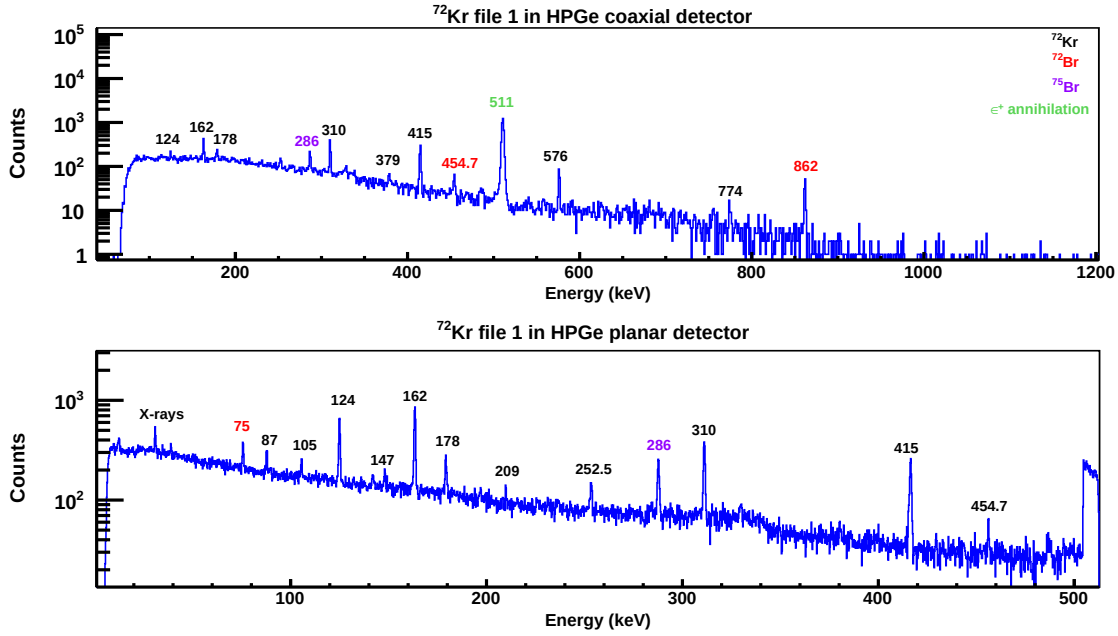

Figure 4.21: *HPGe spectra for the first file with ^{72}Kr beam and cycling periods optimized for the measurement of ^{72}Kr decay. There are contaminations from ^{72}Br and also ^{75}Br decay that was just measured before this file. A quantitative analysis of the contaminants presents in the 6 files for the ^{72}Kr decay measurements is shown in table 4.5*

half-life for ^{75}Kr is 4.3 minutes, this explains why it does not contribute to the measurement of ^{72}Kr. However, the half-life of ^{75}Br is 96.7 minutes so if ^{75}Kr contamination was implanted around the measuring position, the decay of ^{75}Br will contaminate the ^{72}Kr measurement as it does. Nevertheless, as can be seen in table 4.5 the amount of ^{75}Br decay measured during the ^{72}Kr study was very low, 7 % for the first file and decreasing for the second and third files up to 1 % in comparison with ^{72}Kr decays. The next descendant in the A=75 decay chain, ^{75}Se has a very long half-life of almost 120 days so its contribution is negligible and that is why its decay radiation is not seen in the HPGe spectra.

Summarizing, **the ^{72}Br content in the six files is quite stable** (varies in the range 8-13%), **the ^{72}As is increasing but is quite small for the first three files** while for ^{75}**Br decay is only appreciable for the first 4 files with a small contribution** (never larger than 7 % with respect to ^{72}Kr decays).

The subtraction of ^{75}Br is not easy to be done as the Q_{EC} is smaller than the corresponding to ^{72}Kr decay. Taking into account that this contribution is quantitative reduced and that last files of ^{72}Kr do not have this contribution, in principle the analysis will be done ignoring this contamination. If appreciable differences are found in the results from the 6 files we will take into consideration this contribution.

The contribution of ^{72}As is not very important for the first 3 files and for the other 3 one has to consider that when doing the ^{72}Br subtraction one is subtracting the ^{72}As contamination as well as in the ^{72}Br there is also the ^{72}As contamination.

For all these reasons, the analysis of the ^{72}Kr decay data will be performed for the 6 files individually and they will be compared afterwards to study if any significant influence from these contaminants shows up. Furthermore, we will use the deviations in the results from these 6 measurements to estimate the uncertainty in the determination of the feeding distribution.

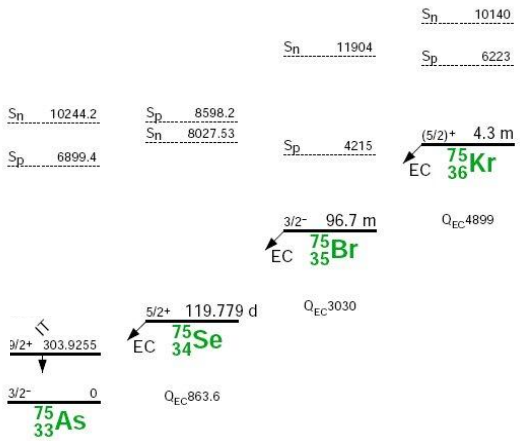

Figure 4.22: *^{75}Kr β^+/EC decay chain. For every decay it is shown the Q_{EC}, S_n, S_p and half life. Image taken from [Fir96].*

Parent nucleus	$T_{1/2}$	Q_{EC} (keV)	Most intense γ lines (keV)
^{75}Kr	4.3 min	4899	132.5, 154.5, 153.2
^{75}Br	96.7 min	3030	286.5, 141.19, 427.79
^{75}Se	119.779 d	863.6	264.66, 136.0, 279.54

Table 4.8: *A=75 mass decay chain starting at ^{75}Kr which is the beam used in the measurement previous to the ^{72}Kr measurement in the current experiment. The decays of ^{75}Br and ^{75}Se can be present in our spectra, specially the first of them as the half-life of ^{75}Se is very large (119.779 days) and its contribution is almost negligible.*

The Q_{EC} of ^{72}Br decay is 8799(7) keV [Abr10], larger than the value for the ^{72}Kr decay, 5127 keV. The normalization factor between both spectra in order to subtract the ^{72}Br decay contribution is obtained using the energy range beyond 5127 keV where no contribution from the ^{72}Kr decay is expected to appear. The case for the file 1 of the ^{72}Kr measurement is shown in figure 4.23 as an example.

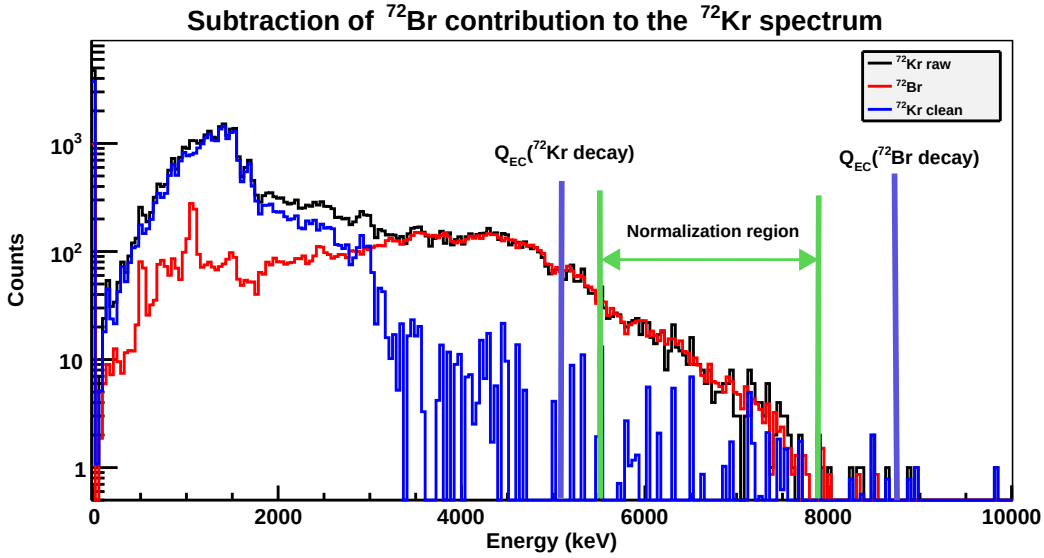

Figure 4.23: *Subtraction of ^{72}Br decay contribution to the file 1 of ^{72}Kr spectrum. The normalization region has been selected in the energy region from the Q_{EC} of ^{72}Kr decay and the one corresponding to the ^{72}Br decay as labelled in the plot. This energy region is supposed to have only contribution from the ^{72}Br decay as it lies beyond the ^{72}Kr Q_{EC} value.*

One effect not desirable occurs for energies higher than 3200 keV where as the statistics is quite low there are quite big fluctuations in the bin contents from one bin to the neighbouring one. This happens due to the subtraction of ^{72}Br contamination, as one can see in figure 4.23 from the energy of 4000 keV on one is basically subtracting almost all the counts as both spectra have the same shape. So small differences between both spectra due to statistical fluctuations in the measurements are the explanation of these fluctuations and discontinuities appearing in the ^{72}Kr clean spectrum.

In order to estimate the uncertainty coming from the subtraction of this contaminant, three different subtraction factors of ^{72}Br contribution to the ^{72}Kr spectrum are considered. The

underlying idea of choosing three factors is to estimate the systematic uncertainties inherent to the contaminants subtractions.

Therefore, one has three subtraction factors for the subtraction of A=73 contribution to the ^{72}Br spectrum and other three factors for the subtraction of ^{72}Br contribution to the ^{72}Kr spectrum. In this way, one ends up with 9 possible analysis corresponding to 9 different subtraction factors (3×3) for each ^{72}Kr file. These 9 analysis will help us to estimate the uncertainty in the final β-feeding distribution.

The three subtractions of ^{72}Br contribution to the ^{72}Kr spectrum file 1 are shown in figure 4.24 as an example. The standard subtraction factor comes from the normalization between both spectra calculated as given in figure 4.23. There, the energy region from 5535 up to 8100 keV was used to calculate it. The minimum and maximum subtraction factor has been finally chosen to be a 10 $\%$ larger and lower than the standard one. The choice of these factors is based in the fact of the standard subtraction factor lets the clean spectrum to have statistics up to the Q_{EC} value of the ^{72}Kr decay (5127 keV) and the 10% to establish upper and lower extremes in the subtraction to be large enough to allow for counts up to 6 MeV in the lower subtraction (without any possible physical meaning as further than the Q_{EC} no statistics can show up) and the upper to show a dramatic decrease in statistics at 3.5 MeV (quite below the Q_{EC}) as shown in fig. 4.24. For sure the range of values of the factor could be lower than 10%, probably with 3 or 5 $\%$ would be enough but is safer in the estimation of the uncertainty to established it in 10%.

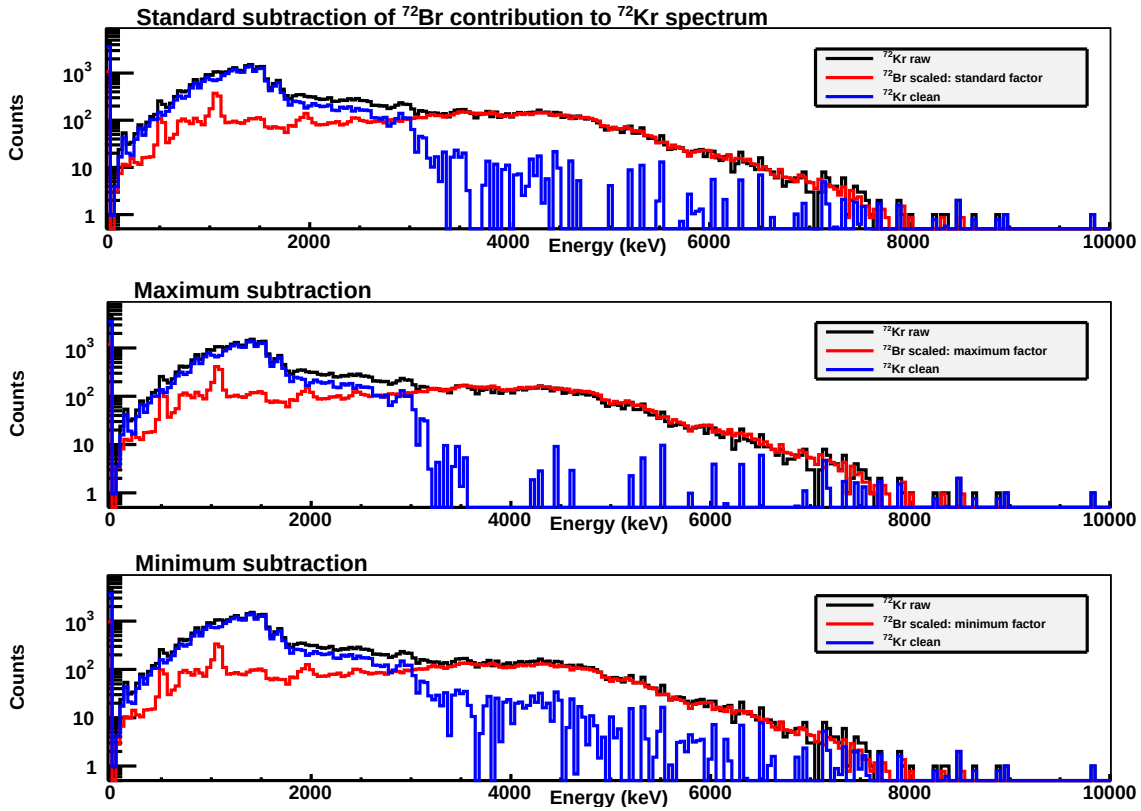

Figure 4.24: *Subtraction of ^{72}Br decay contribution to the ^{72}Kr spectrum corresponding to file 1 (75 min long as given in table 4.5). The standard subtraction (upper) is obtained by normalizing in the energy region indicated in fig. 4.23 while the minimum and maximum factors are deduced as 10% variations on the standard one to safely estimate the uncertainty in the analysis from this subtraction. Minimum factor allows for statistics further than Q_{EC}(^{72}Kr decay)=5127 keV (physically not allowed) and the maximum suppresses strongly the spectrum at 3.5 MeV, quite below the Q_{EC} of the decay of interest.*

The resulting subtraction factors are given in table 4.9. The factors of subtraction of A=73 from ^{72}Br are given in the first row while in the lower part of the table the set of subtraction factors of ^{72}Br contribution from every ^{72}Kr file are listed.

Subtraction of A=73 contamination			
	Maximum	Standard	Minimum
	0.384	0.274	0.164
Subtraction of ^{72}Br contamination			
File	Maximum	Standard	Minimum
1	0.237683	0.216075	0.194468
2	0.996879	0.906254	0.815629
3	0.491674	0.446976	0.402278
4	0.987511	0.897737	0.807963
5	0.339348	0.308499	0.277649
6	0.533311	0.484829	0.436346

Table 4.9: *Subtraction factors used in the analysis of the ^{72}Kr measurements. The subtraction factors of A=73 contribution to the ^{72}Br are the same for the analysis of the 6 files of ^{72}Kr while the factors given for the subtraction of ^{72}Br from ^{72}Kr files are different for each and are given their corresponding values in the last 6 rows.*

An important issue referring the standard subtraction is shown in figure 4.25. Once the subtraction of the ^{72}Br contribution has been done from the ^{72}Kr spectra, the spectrum shows oscillations around zero counts from a certain energy level. These oscillations have their origin in statistical fluctuations of the measurements and the subtractions but they really do not belong to real data coming from the response of the detector to feeding at a certain level. Additionally, they cause big amounts of total feeding at higher excitation energies when the analysis algorithm tries to reproduce the shape of the spectrum at these energies since when transforming the $beta^+$ feeding into total (β^++EC) feedings they are increased enormously as the EC/β^+ ratio is large in this energy window close to the Q_{β^+}. Due to this, we do not rely on the spectrum beyond an energy threshold where starts these fluctuations.

For these reasons an upper limit in the analysis has been chosen to be located at 3640 keV as shown in fig. 4.25 for the file 1 as example. The rest of files shows the same behaviour and the position of this limit is similar for the 6 files. In addition to this upper limit, another action has been used in the analysis. As it was already explained in E. Nácher Ph.D. thesis [Ná04a], the analysis has been carrying out without doing the subtraction and including the contaminants in the algorithm. This improve the results for the region where low statistics is obtained after the subtractions and that are caused by them. To do this, the equation 4.6 transforms in the algorithm to eq. 4.7.

$$d_i = \sum_j R_{ij} f_j \tag{4.6}$$

$$d_i = \sum_j R_{ij} f_j + k_1 \times (^{72}Bractivity) + k_2 \times (pileup) \tag{4.7}$$

where k_1 and k_2 are the subtraction factors found for ^{72}Br decay radiation and pile up contributions respectively.

In terms of excitation energy in ^{72}Br, since we are dealing with β^+-gated spectra, the gamma excitation energies are displaced at higher energies since the energy coming from the annihilation of the positron emitted in the β^+ decay is added. The annihilation process contributes with two gamma rays of 511 keV which could add an extra 1022 keV energy to the

detected gamma de-excitation process of the daughter nucleus. Therefore, the highest level in the scheme of ^{72}Br which could contributes with counts in the experimental spectrum up to this upper limit, 3640 keV, is the one located 1022 keV below as one can observe in the response of the TAS detector to feeding at a level located at 3 MeV excitation energy shown in fig. 2.11(b). The maximum of the response in that example, is located at around 4 MeV, approximately 1022 keV beyond than 3 MeV. Thus, the upper limit of 3640 keV in our TAS spectra corresponds to an excitation energy in ^{72}Br of 2620 keV and all our resulting feedings will be obtained up to this energy threshold.

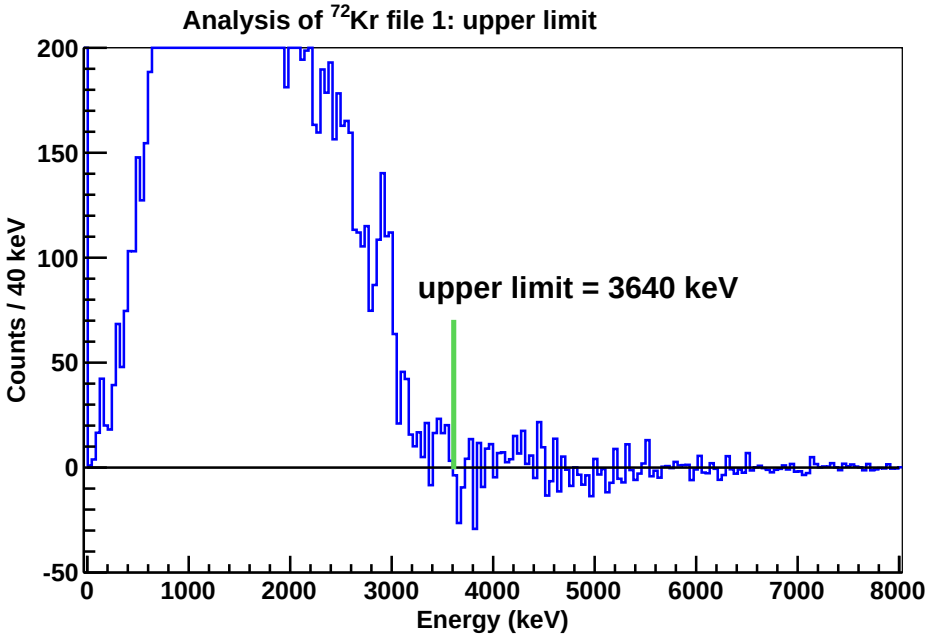

Figure 4.25: *^{72}Kr clean spectrum for file 1, as example. The upper limit chosen in the analysis for the energy spectrum is shown. The reason for this choice is mainly that from this energy on the energy spectrum shows oscillations around zero counts giving negative statistics in some bins and few positive counts in others.*

The subtraction of pile up from the ^{72}Kr measurement has been rejected as the normalization of this contribution should be performed at higher energies than the Q_{EC} value of the decay of ^{72}Kr, which is 5127(10) keV, and in this energy region the spectrum shows no counts. This tell us that the contribution of pile up is negligible and the uncertainty due to not perform this subtraction will be well below the error bars chosen from the systematic uncertainty that will be presented later.

4.2.2.5 Response Matrix

As it was already explained in chapter 2, in order to perform the analysis of the TAS data one needs the Response Matrix of the detector to the decay of interest. In this case, the decay of interest is the β^+ decay of ^{72}Kr. For c the case of the β-gated analysis one has to apply the same conditions in the simulations than in the experimental data, that is, the condition of coincidence with beta particles detected in the plastic scintillator detector. When one imposes this condition, the absolute efficiency of the beta detector can be deduced via simulations and the result is shown in figure 4.8. It is roughly around 20 percent for positron energies higher

than 1 MeV and it drops as the energy decreases. The red line indicates the case in which no threshold is imposed for the positron energy and the blue is the result of considering only events in which the positron deposits more than 75 keV energy in the beta detector. Logically the total efficiency decreases in 1-2 % but not dramatically.

Following the steps detailed in [Can99a] and explained in chapter 2, one ends up with the response matrix of the decay.

4.3 Results

Once we have calculated the response matrix of the TAS detector to the decay and the ^{72}Kr-decay raw spectrum and ^{72}Br-decay clean spectrum with the corresponding subtraction factor is ready, one can perform the bayesian analysis of the data as detailed in [Tai07a] and explained in chapter 2.

The results of the analysis will give, mainly, two sets of information. On the one hand, the beta feeding distribution in the full Q_β window and, on the other hand, the reconstructed ^{72}Kr spectrum obtained as the convolution of the beta feeding distribution obtained as a result of the analysis with the response matrix of the detector to the decay of interest. The former is the important result that will be used to obtain the final B(GT) distribution while the latter provide a cross-check of the reliability of the result.

The comparison between the ^{72}Kr raw spectrum (including contaminants) and the reconstructed spectrum is shown in figure 4.26 for the analysis performed with the file number 1 of the ^{72}Kr measurement. From now on, the spectra coming from the file 1 of the ^{72}Kr measurement will be shown in the figures as an example since the procedure is the same for the six files of ^{72}Kr measurement. As one can observe, the relative deviations shown in the lower panel are quite low as it does not get larger than 30-40 % in the full spectra except for the 2 or 3 lower bins where the low statistics allows for larger relative deviations.

If one would subtract the contaminants from the raw spectrum shown in fig. 4.26, the result is the spectrum shown in the figure 4.27 in red, where the reconstructed spectrum from the convolution of the feeding distribution found with the response matrix to the decay is also plotted in blue. There, one can see that the spectra only reach the upper limit imposed in energy at 3640 keV indicated in fig. 4.25. It is important to note that the most interesting comparison is the one with clean spectra as the contribution of the contaminations can hide the real differences between the experimental and the reconstructed spectra of interest shown in figure 4.27.

There is good agreement between both spectra (experimental and reconstructed) as one can see that the relative deviation is only significant where the statistics of the spectra is low, less than 10 counts per bin, namely in the first 300 keV and from 3300 keV on.

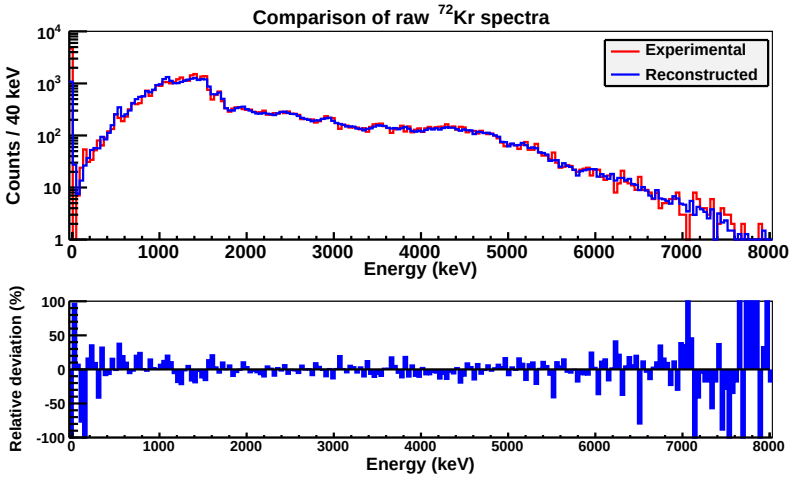

Figure 4.26: *Comparison of experimental TAS and reconstructed raw spectra (including contributions from contaminants) for the ^{72}Kr measurement (file 1 as example). This analysis was performed imposing an upper limit at E=3640 keV.*

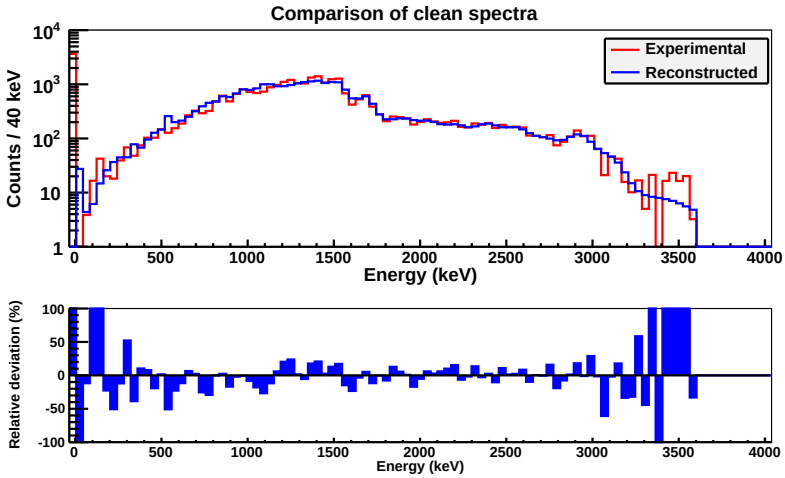

Figure 4.27: *Comparison of experimental and reconstructed clean spectra for the ^{72}Kr measurement (file 1 as example). The analysis was done with an upper limit at E=3640 keV. Note as the spectra (reconstructed and experimental) end at this energy level as from this energy on there is zero counts in every bin.*

This leads us to perform the analysis up to this energy limit of 3640 keV and the result for the reconstructed spectrum and its comparison with the experimental one for raw and clean ^{72}Kr spectra are shown in figures 4.26 and 4.27.

One can notice that the deviations of the reconstructed spectrum from the experimental spectrum in the case of raw spectra are quite limited in general, see fig. 4.27. The reproduction of the experimental clean spectrum in fig. 4.27 is quite nice except for the first 300 keV and the last part of the spectrum, where bigger deviations are found since the statistics is quite low: below 20 counts per bin. Both fluctuations, in the lower and last part of the spectrum, will be considered in the final uncertainty by means of the wide uncertainty chosen for the subtraction factors. Thus, quite different subtraction factors will provide us with spectra with

quite different behaviour in these regions where low statistics is present. Because of this, the final uncertainties will be bigger in these regions as we will see in chapter 5.

The resulting ^{72}Kr β^+ feeding distribution from this latter analysis is shown in figure 4.28. Remember that the result is up to an excitation energy of E=2620 keV as already explained. The feeding distribution is represented in percentage when normalized to total β^+ feeding probability is 100 %. It is important to note that this feeding distribution is the direct result of the TAS analysis for the β^+ part of the ^{72}Kr decay. The next steps in the data processing are devoted to extract the B(GT) distribution which is the quantity one can compare with theoretical predictions from different approaches as it was presented in chapter 1.

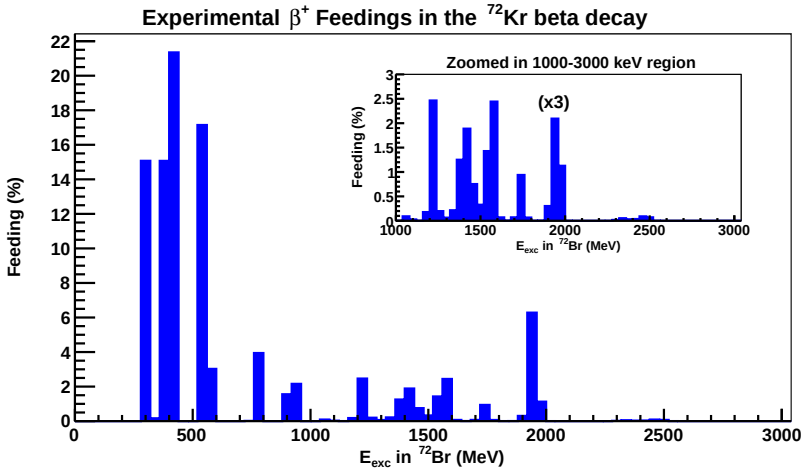

Figure 4.28: *β^+ feeding distribution shown up to the Q_{β^+}=4105 keV window obtained from the analysis with an upper limit in the TAS spectrum of 3640 keV in the energy for the measurement of ^{72}Kr file 1. The feedings are found up to 2620 keV for the reasons given in the text. The comparison of reconstructed spectrum with the experimental one is shown in fig. 4.26 and 4.27. The bin labelled with "(x3)" in the inset has its statistics reduced a factor 3.*

5 Results

Contents

5.1 Results from the Conversion Electron Spectroscopy study

In the following, the results from the experiment described in chapter 3 are presented.

5.1.1 Results on conversion coefficients

The results on the conversion coefficients for transitions in ^{72}Br were presented in chapter 3 and are collected in table 3.34. A more visual way of representing these results is given in figures 5.1 and 5.3 for K-shell conversion coefficients and 5.2 for Total-K-shell conversion coefficients.

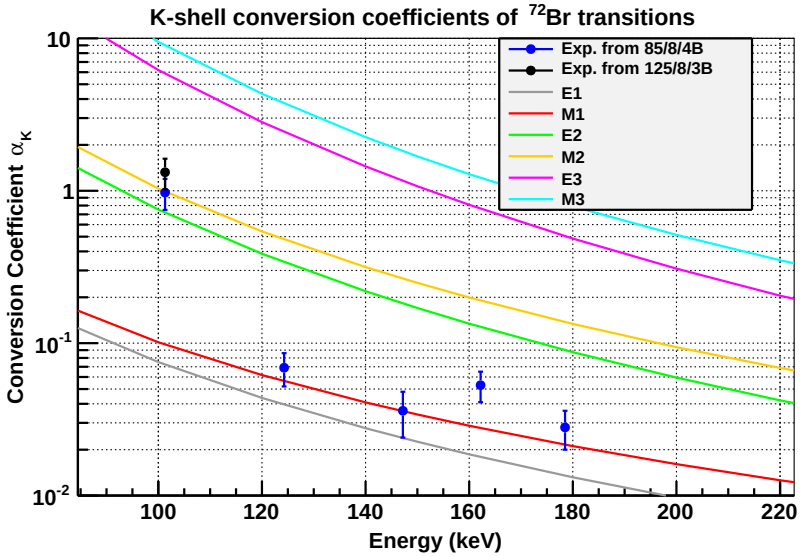

Figure 5.1: *Experimental conversion coefficients for K-shell transitions obtained in the low energy range with the miniorange configurations 85/8/4B and 125/8/3B. The comparison with the theoretical predictions from [ANU] is presented for the different multipolarities.*

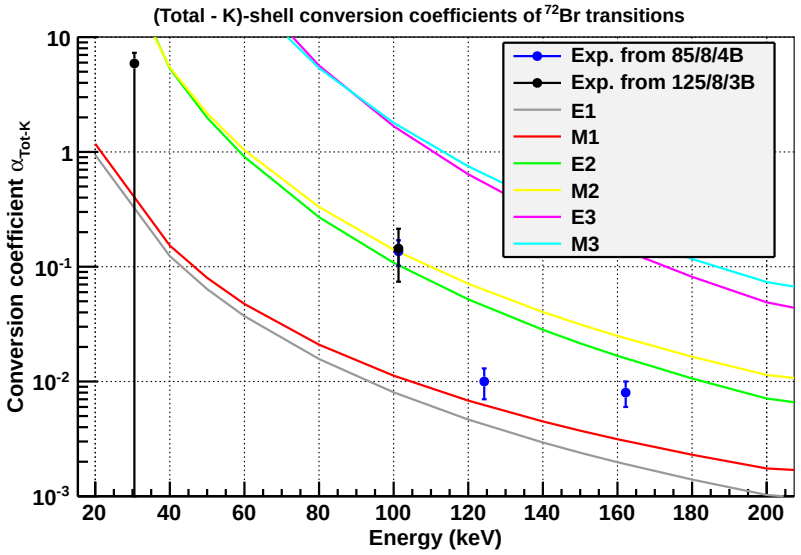

Figure 5.2: *Experimental conversion coefficients for (Total-K)-shell transitions obtained in the low energy range with the miniorange configuration 85/8/4B. The comparison with the theoretical predictions from [ANU] is presented for the different multipolarities.*

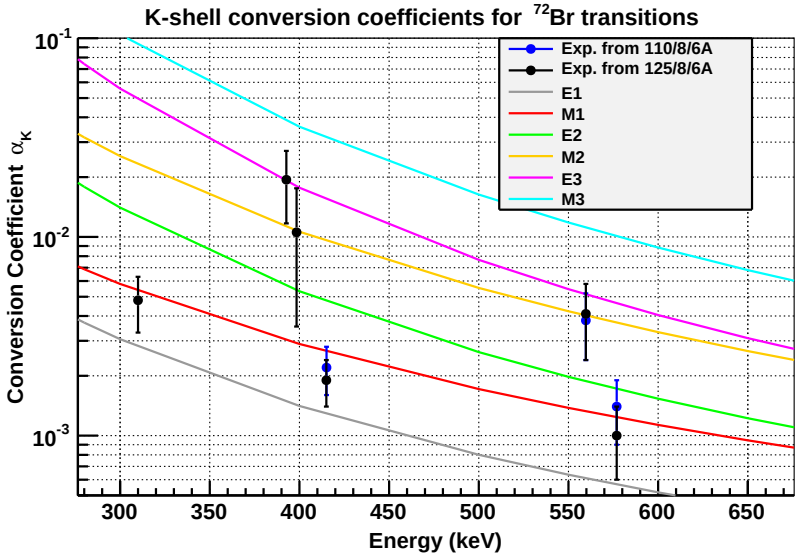

Figure 5.3: *Experimental conversion coefficients for K-shell transitions obtained in the high energy range with the miniorange configurations 110/8/6A and 125/8/6A. The comparison with the theoretical predictions from [ANU] is presented for the different multipolarities.*

Now, the multipolarity of transitions whose conversion coefficients have been determined are discussed.

5.1.2 Transition multipolarities

The conclusions on the transition multipolarities and spin and parity of the states involved in the transitions whose conversion coefficients have been studied are presented next. They are extracted from the results shown in table 3.34 and figures 5.1- 5.2-5.3, and they are based on the properties of the multipole radiation given in section 1.1.2.1.

30.5-keV transition

An upper limit for the value of the conversion coefficient was found to be:

$$\alpha_{Tot-K} < 5.9 \pm 1.4 \tag{5.1}$$

The theoretical values for this coefficient are: 0.321 (E1), 0.397 (M1), 21.47 (E2) and 20.16 (M2). The comparison suggests the following possibilities for the character of the transition:

- mixed M1+E2
- pure M1
- E1+M2
- pure E1

taking into account that M1 only can be mixed with E2 as they both conserve the parity between initial and final states and E1 can only be mixed with M2 from parity change restrictions as described in section 1.1.2.1.

The Weisskopf estimate [Wei51] for a transition of 30.5 keV and in a nucleus with A=72 provides us with the following ratios of the transition probabilities λ for the different multipolarities:

$\lambda(E1)$:	$\lambda(M1)$:	$\lambda(E2)$:	$\lambda(M2)$
1 :	3.2×10^{-2} :	1.18×10^{-2} :	3.26×10^{-4}

As one can see the most likely multipolarity for the transition is E1 and is compatible with the experimental result as this is an upper limit for the conversion coefficient. Nevertheless, if one takes the value of the experimental coefficient and compare it with the theoretical prediction for the (Tot-K) conversion coefficient a certain amount of mixing with the M2 multipolarity is required. The multipolarity E1 cannot mix with M1 and E2 as they conserve parity while E1 does not. However the relative intensity of M2 with respect to the one for E1 is very small as they differ in four orders of magnitude. This almost rejects the possibility of a mixed E1+M2 multipolarity for the 30.5 keV transition and only an E1 multipolarity is allowed.

The other possibility of being a mixed M1+E2 transition is possible as well, despite being less probable, since both multipolarities (M1 and E2) are similarly probable (both in the order of 10^{-2}) and they could mix. However, as it will be shown later when discussing the spin of states in section 5.1.3, by parity change arguments between initial and final states, a change of parity is required and this rejects the possibility of being M1+E2.

$$| \delta | < 0.74 \tag{5.2}$$

The previous assignment from intensity balance arguments in [Piq03], was to be a mixed transition M1+E2. On the contrary, we have found it to be E1.

38.8-keV transition

An estimation of the upper limit for the value of the conversion coefficient of K-shell for the 38.8-keV transition was found as:

$$\alpha_K < 18 \pm 7 \tag{5.3}$$

The theoretical values for this coefficient are: 1.202 (E1), 1.479 (M1) and 20.48 (E2). The comparison does not firmly establish the multipolarity as it allows for an E2, M1 or even E1 characters. It only rules out M2, E3 and higher orders. This is the first experimental determination of this conversion coefficient.

The possibility of being E1 is rejected based on parity conservation arguments used in the discussion of the spin of the levels that is included in next section. This is due to the parity has to be conserved between initial and final states and E1 requires parity change.

The conclusion is that the multipolarity of this transition should be M1+E2, notation that includes the possibility of being E2 or M1 pure transition.

101.3-keV transition

The conversion coefficients of this transition were found to be:

$$\begin{aligned} \text{125/8/3B spectrometer: } \alpha_K &= 1.3 \pm 0.3 \\ \text{85/8/4B miniorange: } \alpha_K &= 1.0 \pm 0.2 \\ \textbf{Weighted average value: } \alpha_K &= 1.12 \pm 0.13 \end{aligned} \tag{5.4}$$

$$\begin{aligned} \text{125/8/3B spectrometer: } \alpha_{Tot-K} &= 0.14 \pm 0.07 \\ \text{85/8/4B miniorange: } \alpha_{Tot-K} &= 0.14 \pm 0.03 \\ \textbf{Weighted average value: } \alpha_{Tot-K} &= 0.14 \pm 0.02 \end{aligned} \tag{5.5}$$

The final values for the α_K and α_{Tot-K} shown in eq. 5.4 and 5.5 are calculated as the weighted average by their uncertainties of the values from the two spectrometer configurations as both agree within the error bars. The theoretical values for the α_K coefficient are: 0.718 (E2), 0.987 (M2) and 5.863 (E3) while for the α_{Tot-K}: 0.1202 (E2), 0.1578 (M2) and 1.834 (E3). All these values support the assignment of the M2 multipolarity which is in good agreement with the results in previous works, see [Piq03] and [Gar82].

124.4-keV transition

The values of conversion coefficients obtained for this transition are:

$$\begin{aligned} \alpha_K &= 0.069 \pm 0.017 \\ \alpha_{Tot-K} &= 0.010 \pm 0.003 \end{aligned}$$

The theoretical values for these coefficients are: α_K = 0.056 (M1) and 0.34 (E2), and for α_{Tot-K}=0.00727 (M1) and 0.053 (E2). The comparison suggests the transition to be an M1(E2) with similar mixing ratios of $\mid \delta \mid = 0.22^{+0.12}_{-0.22}$ and $\mid \delta \mid = 0.25^{+0.12}_{-0.25}$ respectively. So the conclusion is that it could be a pure M1 transition but as some mixing with E2 cannot be ruled out, the assignment must be M1(E2) meaning dominantly M1.

147.2-keV double transition

The conversion coefficient obtained for this double transition is:

$$\alpha_K = 0.036 \pm 0.012 \tag{5.6}$$

The theoretical values for this coefficient are: 0.02385 for E1, 0.003578 for M1 and 0.1824 for E2. In this case, the conversion coefficient agrees completely with the value for an M1 transition. Despite of this, the error bar also allows for a pure E1 multipolarity or even a small amount of mixture with E2, being M1(E2).

As it can be seen in the level scheme in figure 5.9, there are two different transitions with this energy, 147.2 keV, that cannot be discriminated in this experiment. The lower one in excitation energy is connecting the 310 keV and the 162.7 keV levels and has to be a pure M1

transition (or mixed M1+E2) as these two levels are well-known 1^+ states. Also, the work from [Piq03] suggested this transition to be M1 pure based on intensity balance arguments.

On the other hand, the 147.2 keV transition connecting the 545.7 keV level and the 398.5 keV level can be either an E1 or an M1 transition, as there is no available knowledge on the spin-parity of these two levels, only a hint on the 398.5 keV level to be a 2^+ state based on intensity balance arguments from [Piq03]. The most certain possibility is to be an M1 transition as the value of the compound coefficient is really coincident with the one corresponding to an M1 transition but as the error bar also allows for a value closer to the one for an E1 transition one cannot firmly reject the option of the 147.2 keV transition of being an E1.

The absolute intensities for both transition taken from [Piq03], which are compatible with ours in all the transitions measured as shown in appendix B, are 3.52(32) and 0.60(23) $\%$ respectively so the one connecting the 310-keV and 162.7-keV levels is the dominant (around 6 times higher) in terms of transition intensity. This most probably indicates that the most intense one could be assigned firmly as M1 leaving the less intense one. connecting the levels 545.7-keV and 398.5-keV levels to be either E1 or M1+E2 or even a pure M1.

162.7-keV transition

The results for the coefficients of this transition are:

$$\begin{aligned} \alpha_K &= 0.053 \pm 0.012 \\ \alpha_{Tot-K} &= 0.008 \pm 0.002 \end{aligned} \tag{5.7}$$

The theoretical values for α_K coefficient are 0.028 for M1 and 0.128 for E2 while for the α_{Tot-K} coefficient are 0.00355 (M1) and 0.0186 (E2). Both values suggest the transition to be an M1+E2 mixed transition with values for the mixing ratio of $\mid \delta \mid = 0.57 \pm 0.20$ and $\mid \delta \mid = 0.65^{+0.25}_{-0.24}$ respectively. These results obtained for the K and (Tot - K) coefficients agree with this assignment and give similar mixing ratio values. The proposed multipolarity for this transition in [Piq03] was E2 based on intensity balance arguments but, as the δ value is quite consistent from both coefficients, K and $Tot - K$, and both indicate the M1+E2 character our assignment should be this.

178.5-keV transition

For this transition the measured coefficient is

$$\alpha_K = 0.028 \pm 0.008 \tag{5.8}$$

The theoretical values in this case are 0.02158 for M1 and 0.08999 for E2. Therefore, the multipolarity is obtained to be M1(E2). The experimental conversion coefficient is far closer to the M1 theoretical value but a mixed transition cannot be ruled out. The mixing ratio obtained is $\mid \delta \mid = 0.31^{+0.19}_{-0.31}$.

This transition was established as E1 in the work of I. Piqueras et al. [Piq03] based on intensity balance arguments but this possibility is not compatible with the experimental conversion coefficient obtained in the current study.

It is connecting the level at 310 keV with the one at 131.8 keV. The parity of the final level must be positive as the initial state is positive and the multipolarity of the transition does

not allow for a change in parity following the selection rules for gamma de-excitation given in section 1.1.2.1.

In addition, in the work of I. Piqueras et al. [Piq03] the existence of a gamma transition of 177.2 keV is suggested whose α_T=0.0248 is estimated from intensity balance arguments. In the current experiment, the transition at 177.2 keV has not been seen and, in principle, as the energy resolution of the HPGe 1 detector at this energy should be smaller than 1 keV as indicated in table 3.1, it should be possible to discriminate both transitions. So this work rejects the existence of the 177.2 keV transition or its intensity is so low that it does not influence the result on the conversion coefficient of 178.5K transition for being low the gamma intensity and the suggested conversion coefficient, α of the 177.2-keV transition.

310-keV transition

The value of the conversion coefficient is

$$\alpha_K = 0.0048 \pm 0.0015 \tag{5.9}$$

The theoretical predictions for this coefficient are 0.00279 (E1), 0.005351 (M1) and 0.01254 (E2). The experimental value is quite close to the theoretical value corresponding to an M1 but one cannot reject the possibility of small amount of mixing with E2 multipolarity cannot be ruled out from the error bar of the coefficient. The value of the coefficient with error bars is not compatible with the theoretical value for an E1 transition. Therefore, the result is dominantly M1 that it is usually expressed as M1(E2).

392.7-keV transition

The value of the conversion coefficient is

$$\alpha_K = 0.019 \pm 0.008 \tag{5.10}$$

While the theoretical one for M2 is 0.01121 and for E3 is 0.01900. The experimental value is exactly the theoretical value for an E3 transition but, as it could mix with M2 multipolarity and the error bars allow for this, a certain amount of mixing cannot be rejected. The good agreement with the E3 multipolarity can be graphically seen in the figure 5.3. As a conclusion, the assignment is E3 or E3(M2).

398.4-keV transition

The value of the conversion coefficient is

$$\alpha_K = 0.011 \pm 0.007 \tag{5.11}$$

And the predicted value for an M2 transition of this energy in this nucleus is 0.01074 in the case of M2 and 0.01797 if it was an E3. The experimental value is almost identical to the theoretical value for an M2 transition but, as the error bar also allows for a mixture with E3 multipolarity or even pure M2 these possibilities cannot be ruled out. Therefore, the possibilities of multipolarity for this transition are, in order of decreasing probability, M2, M2(E3) or even E3.

Transition	Possibility 1	Possibility 2	Possibility 3	Possibility 4
414.5K	E1	M1	E1	M1
415.1K	E1	E1	M1	M1
Expected α_K(doublet)	0.001282	0.00173	0.00220	0.002652
Experimental α_K(doublet)	0.0020(3)			

Table 5.1: *Available possibilities in the assignment of the multipolarity of the transitions involved in the 414.5+415.1 doublet transition and their expected values for the conversion coefficient of the compound transition.*

414.5-keV and 415.1-keV transitions

Here, a double transition that cannot be experimentally resolved in the electron spectrum is treated. The conversion coefficient was found to be

$$\begin{gathered}\text{110/8/6A configuration: } \alpha_K = 0.0022 \pm 0.0006 \\ \text{125/8/6A configuration: } \alpha_K = 0.0019 \pm 0.0005 \\ \\ \textbf{Weighted average: } \alpha_K = 0.0020 \pm 0.0003\end{gathered} \tag{5.12}$$

The theoretical values for this coefficient are 0.00128 if they were both E1 and 0.002649 if they both were M1. The value from 110/8/6A configuration is quite close to the one corresponding to an M1 transition but it does not rule out the possibility of one of the transitions to be an E1.

The intensity of both transitions in the work of Piqueras et al. [Piq03], whose gamma intensities are compatible with the ones of this work as shown in appendix B, is 41(4)% for the 414.5 keV transition and 84(5) % for the 415.1 keV transition. This means that the 415.1 keV transition is roughly twice as much intense as the other so, in the case of having different multipolarities (E1 and M1), the value of the compound conversion coefficient should be closer to the value corresponding to the multipolarity of the 415.1 keV transition for being more intense.

Let us consider all the possibilities taking into account the relative intensity of both transitions for their multipolarity and the subsequent value for the compound conversion coefficient, see table 5.1. As can be seen in the table, the final experimental value for this conversion coefficient allows us for two different possibilities for the assignment, either the 414.5 keV transition to be an M1 and the 415.1 keV transition an E1 or the 414.5 keV transition to be an E1 and the 415.1 keV transition to be an M1.

Despite the compound coefficient has a reduced error bar that is not compatible with the possibility of both transitions to be M1, if one looks at the two individual experimental values found for every miniorange configuration, their error bars are larger, allowing for this possibility that cannot be fully rejected. Furthermore, this latter option is the most likely, as it will be shown later, from parity arguments, as both transitions should keep the parity between initial and final states, rejecting the possibility of one of them being E1.

Due to these reasons, the suggested multipolarity for both transitions is being an M1.

559.7-keV transition

The resulting conversion coefficient is:

$$\begin{aligned} &\text{110/8/6A configuration: } \alpha_K = 0.0038 \pm 0.0014 \\ &\text{125/8/6A configuration: } \alpha_K = 0.0041 \pm 0.0017 \\ &\\ &\textbf{Weighted average value: } \alpha_K = 0.0040 \pm 0.0008 \end{aligned} \tag{5.13}$$

While the theoretical predictions for this transitions are 0.004024 (M2) and 0.005136 (E3). The experimental conversion coefficients obtained are very close to the theoretical value for an M2 transition in both cases but it cannot be concluded that this is its character as the error bar allows for an assignment of mixture with E3 or even a pure E3. In order of decreasing probability the possible assignment would be: M2, M2(E3) or even E3.

576.9-keV transition

The values of the conversion coefficient 576.9K obtained from 110/8/6A and 125/8/6A configurations are

$$\begin{aligned} &\text{110/8/6A configuration: } \alpha_K = 0.0014 \pm 0.0005 \\ &\text{125/8/6A configuration: } \alpha_K = 0.0010 \pm 0.0004 \\ &\\ &\textbf{Weighted average value: } \alpha_K = 0.0012 \pm 0.0002 \end{aligned}$$

The theoretical values for this transition are 0.001237 if it was an M1 or 0.001718 for E2 multipolarity. The final value is almost equal to the corresponding to a pure M1 transition. However, a certain mixing with E2 cannot be rejected as the error bars allows for a mixing ratio of up to 0.78. The possibility of being an E1 can be ruled out as the measurement with the spectrometer 110/8/6A, including its error bars, is quite far from the theoretical value for E1 and the other measurement with the Miniorange 125/8/6A despite the error bars get quite close to the value for E1 it does not allows for this value.

As a conclusion, the assignment is dominantly M1 but with E2 mixing, so M1(E2).

Apart from the conversion coefficients of ^{72}Br de-excitation transitions other two transitions were studied. These are the 454.7-keV in ^{72}Se and the 112-keV transition in ^{76}Br.

454.7-keV transition in ^{72}Se

This transition links the states at 1316.78 keV and 862 keV of excitation energy in ^{72}Se as suggested in [Col74] through gamma-gamma coincidence arguments with the 862-keV transition de-exciting the 862-keV level. Other works support this placement of the transition [Dor70]. The spin and parity of these levels is well-known to be 2^+ for both from several independent studies. The 862-keV level is reported to be directly fed in the beta decay of ^{72}Br with an intensity of 23.2 % in [Col74] and it is also seen in [Nol70, Lie70], which suggests the state to be 2^+. The 1316.78-keV level was reported to be 2^+ based on the gamma angular distributions

in [LK77], and on the decay characteristics of the transition in [Col74] in agreement with the work in [Nol70].

The conversion coefficient of this transition was found to be:

$$\begin{gathered}110/8/6\text{A spectrometer: } \alpha_K = 0.0036 \pm 0.0010 \\ 125/8/6\text{A spectrometer: } \alpha_K = 0.0027 \pm 0.0007 \\ \\ \textbf{Weighted average value: } \alpha_K = 0.0031 \pm 0.0004\end{gathered} \tag{5.14}$$

while the theoretical values are 0.001924 (M1) and 0.003289 (E2). The measured conversion coefficient is found to correspond to a pure E2 or dominantly E2, that is E2(M1). This result is compatible with the location of the transition as it conserves the parity from initial to final state and the spin difference should be smaller or equal to 2. In case of being a mixed transition it mixing ratio could be $\mid \delta \mid = 2.31^{+\infty}_{-1.21}$. The possibility of being M2 is rejected as the value of the coefficient is far enough from the M2 theoretical value and it does not keep the parity between initial and final states and the location of the transition does not allow it. This rules out the possibility of been an M2 so the assignment from this study is an E2 or a small mixing with M1 as allowed for the error bar.

112-keV transition in ^{76}Br

Finally, this transition belonging to the deexcitation of ^{76}Br was previously assigned to be a mixed M1+E2 with a mixing ratio of $-0.3 \geq \delta \geq -2.4$ in works performed by Döring et al. [Dö82], Buccino et al. [Buc90] and Winchell et al. [Win90] via in-beam γ-ray spectroscopy studies of products coming from fusion-evaporation reactions ending up in ^{76}Br. It is connecting a 6^+ state at 357 keV with a 5^+ state at 245 keV.

The obtained conversion coefficient is:

$$\alpha_K = 0.24 \pm 0.07 \tag{5.15}$$

The theoretical value for a transition of this energy in bromine are 0.07445 (M1) and 0.4974 (E2). The result from this work support the previous assignment of a mixture M1+E2 transition. The value for the module of the mixing ratio is found to be $0.81^{+0.33}_{-0.27}$ which is compatible with previous estimations as it has been mentioned.

5.1.3 Spin of states

Following the selection rules for the gamma de-excitation process given in section 1.1.2.1, the spin and parity of the involved states in the studied transitions will be discussed below.

Ground state

The spin of the ground state of ^{72}Br has been debated between 1^+ [Sch73, Piq03] and 3^+ [Col74] as explained in section 1.3.2.1. The gamma intensities of our work are similar to the ones reported by I. Piqueras et al. in [Piq03]. In this work, they proposed three levels, i.e.

310.0-keV, 415.2-keV and 577.0-keV, to be clearly fed directly in the beta decay of ^{72}Kr. They found 16.42, 15.79 and 13.06 % beta feedings, respectively, to these levels. This gives log(ft) values for these states of 4.83, 4.79 and 4.78. These values are below 5.0 and, recalling the fig. 1.3, the systematics of log(ft) values shown that forbidden transitions with log(ft) below 5.0 have not been found. Because of this, we can assume that these three are allowed transitions, $0^+ \rightarrow 1^+$. From this, one can assumed that these three levels are 1^+.

The multipolarities of the transitions connecting these 3 levels with the ground state have been determined from the conversion coefficient study and the situation is shown in fig. 5.4. They were found to be M1 and probably the 576.9 keV transition could have a certain amount of mixing with E2 character. Based on these multipolarities the allowed possibilities for the ground state spin-parity are $(0,1,2)^+$.

The previous knowledge on the ground state spin was controversial since some studies proposed it to be 1^+ refs. [Sch73, Piq03] and other 3^+ [Col74]. Our result is compatible with the 1^+ possibility but rejects the 3^+ option.

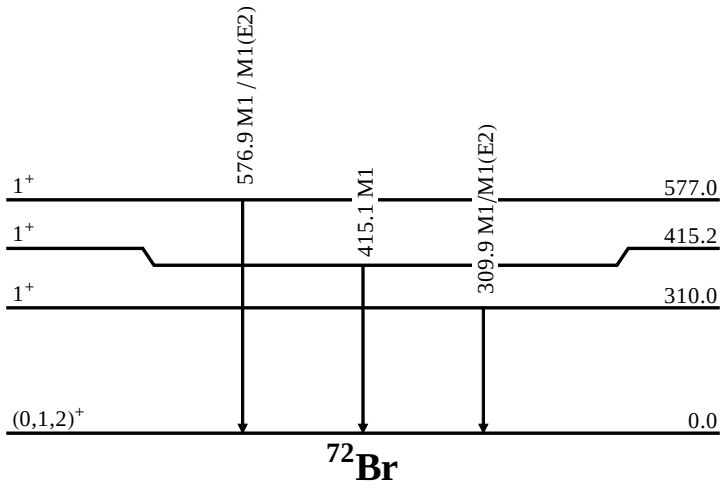

Figure 5.4: *Levels and transitions involved in the discussion of the spin-parity assignment of the ground state.*

The 310.0-131.8-101.3-0 keV group of states

The 310.0-keV, 131.8-keV, 101.3-keV and ground states are connected through the 178.5-keV, 30.5-keV and 101.3-keV transitions. The multipolarities of these transitions were found to be M1(E2), E1 and M2 respectively. The information is shown in fig. 5.5.

The 310-keV level is assumed to be 1^+ as mentioned in the discussion of the ground state spin-parity. The 178.5 keV transition is an M1(E2) which allows the 131.8-keV state to be either 0^+, 1^+ or 2^+. The spin-parity of this state at 131.8 keV was suggested in [Piq03] to be an (2^-) based on intensity balance arguments.

The ground state has been deduced that could be $(0,1,2)^+$ and the 101-keV transition has been found to have M2 multipolarity. This allows the 101.3-keV state to be $(2,3,4)^-$. However, the multipolarity found for the 30.5-keV transition, E1, rejects the possibilities of the 101.3-keV state to be 4^- and the 131-keV state to be 0^+.

The spin-parity of the initial state at 100.76 keV of excitation energy was proposed to be (3^-) in previous works, see last review of Nuclear Data Sheets on this mass A=72 by Abriola et al [Abr10] for further details. This spin was assigned based on the spin assignment for the

ground state that was 1^+ or 3^+ as previously proposed in refs. [Sch73, Piq03] and [Col74] respectively.

The possible assignments for this group of states stays as shown in fig. 5.5.

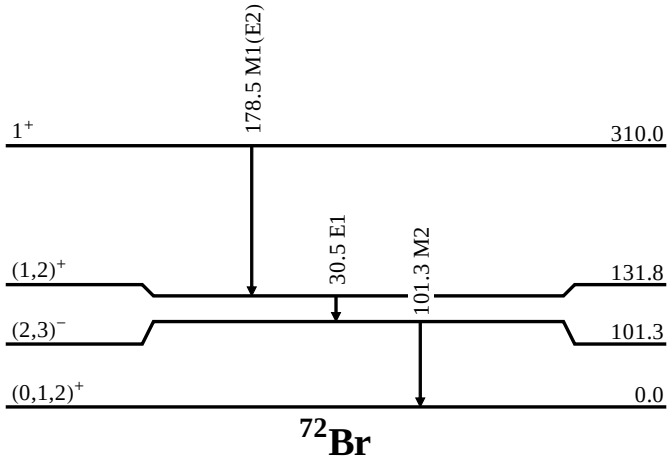

Figure 5.5: *Levels and transitions involved in the discussion of the spin-parity assignments of the 310.0-131.8-101.3-0 keV group of states.*

The 310.0-162.8-124.4-0 keV group of states

These transitions are linked through the 147.2-keV, 38.8-keV and 124.4-keV and 162.7-keV transitions. The 310.0-keV state is assumed to be 1^+ from the log(ft) value given in [Piq03] and ground state is obtained to be $(0,1,2)^+$ based on this assumption.

Since the 147.2-keV transition has been determined to be M1, the possible spins of the 162.8-keV state are $(0,1,2)^+$. This result is compatible with the possibilities allowed from the assignment of M1+E2 multipolarity for the 162.7-keV transition connecting with the ground state and rejects the also allowed of 3^+.

The M1(E2) character found for the 124.4-keV transition gives the possibilities for the spin of the 124.4-keV state $(0,1,2,3)^+$. The 38.8-keV transition, found to be M1+E2, connecting the 162.8-keV and 124.4-keV states is compatible with the spin-parity assignments given previously for both states. The spin of the 124.4-keV state was previously reported to be a 1^+ based on log(ft) values, see refs. [Dav73, Sch73].

Fig. 5.6 shows these levels and the transitions involved.

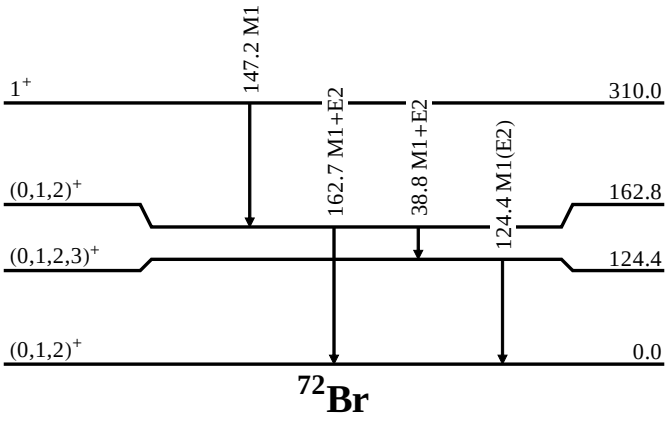

Figure 5.6: *Levels and transitions involved in the discussion of the spin-parity assignments of the 310.0-162.8-124.4-0 keV group of states.*

The 545.7-398.5-392.8-0 group of states

The 392.7-keV transition has been determined to be either E3 or E3(M2) and as it ends at the ground state, which could have $(0,1,2)^+$, the possible spins for the 392.8-keV level are $(0,1,2,3,4)^-$.

The 398.4-keV transition has been determined to be either M2, M2(E3) or even E3, and as it ends up at the ground state, which could have $(0,1,2)^+$, the possible spins for the 398.5-keV state are $(0,1,2,3,4)^-$. Based on this assignment, as the 147.2-keV transition starting at the 545.7-keV level was found to be M1, M1+E2 or even E1 but very unlikely from the conversion coefficient measured, the possible spins for the 545.7-keV level are $(0,1,2,3,4,5)^-$. The 398.5-keV level is suggested to be an (2^+) in the ref. [Piq03] based on intensity balance arguments.

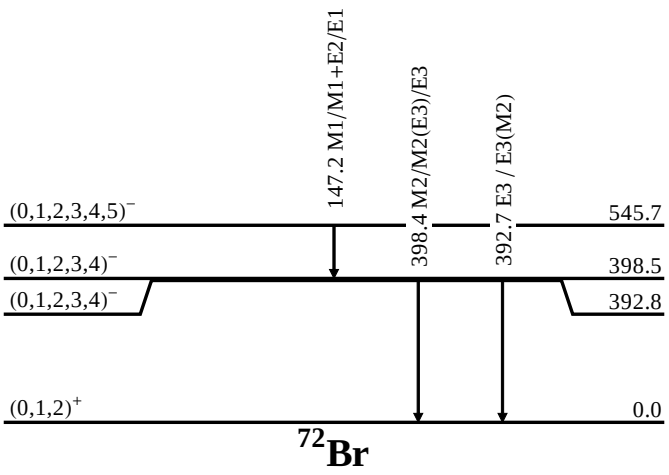

Figure 5.7: *Levels and transitions involved in the discussion of the spin-parity assignments of the 545.7-398.5-392.8-0 keV group of states.*

The 722.2-577.0-162.8-0 group of states

The 559.7-keV transition connects the 722.2-keV level with the 162.8-keV state. The possible spins for the 162.8-keV state has been found to be $(0,1,2)^+$. Since the multipolarity of the 559.7-keV transition was determined to be M2 or M2(E3), a change in parity between the linked levels is expected as selection rules given in section 1.1.2.1 determine. The final level, 162.8-keV state, was previously determined to be $(0,1,2)^+$, so the possible spins for the 722.2-keV state are $(0,1,2,3,4)^-$.

The 414.5-keV transition, which is studied together with the 415.1-keV transition forming a double transition, was finally established to be an M1 transition which is in agreement with the spin and parity of the connected levels as can be seen in fig. 5.8. The 577.0-keV levels is a well-known 1^+ state as it is directly beta fed via an allowed beta decay transition, and the final level, the 162.8-keV state, has been previously determine to be $(0,1,2)^+$ and these possibilities are exactly the same allowed from the M1 multipolarity of the 414.5-keV transition as it starts at a 1^+ state. The possibility of the transition 414.5-keV being E1 is finally rejected as this multipolarity implies the change in parity and between the linked levels with this transition no change is expected.

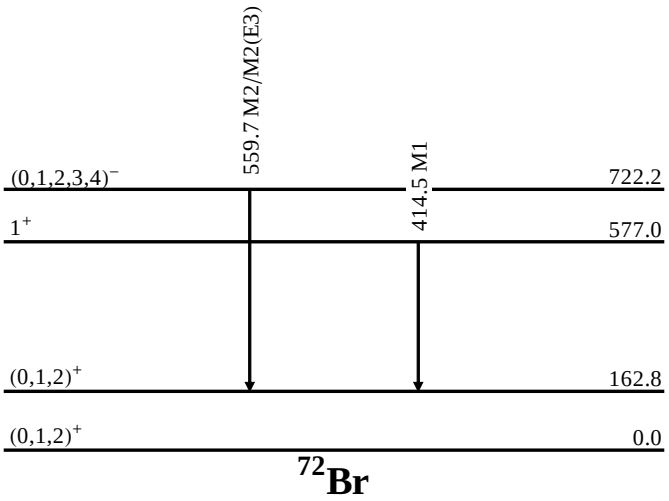

Figure 5.8: *Levels and transitions involved in the discussion of the spin-parity assignments of the 722.2-577.0-162.8-0 keV group of states.*

5.1.4 Level scheme of ^{72}Br

The level scheme of the nucleus ^{72}Br deduced from the current study on the conversion coefficients is shown in fig. 5.9. This is the result of putting together all the previously discussed transition multipolarities and levels spin-parities.

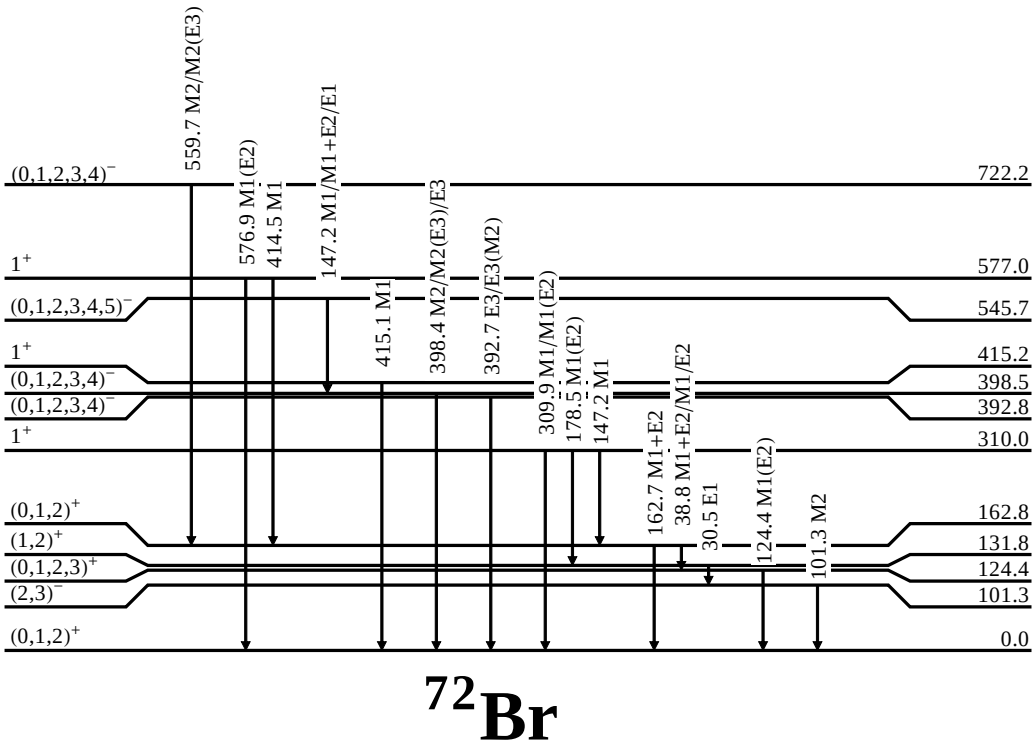

Figure 5.9: *Low energy region of the level scheme of ^{72}Br obtained through the conversion coefficients study done in this work. The multipolarity of 15 transitions has been obtained and the spin-parity of the ground state is limited to be an $(0,1,2)^+$ rejecting the previously proposed value of 3^+ [Col74]. Furthermore, other spin-parity of excited levels has been deduced through this study whose reasoning can be review in the text.*

These results are very important for the analysis of the TAS data as explained in section 2.2.2. All the conclusions derived from the TAS measurement and data analysis rely therefore on the results given in this section.

5.1.5 Intensity of E0 transitions

Transitions in ^{72}Se such as 862K, 937K and 937Tot-K and also 834K, 691K and 691Tot-K in ^{72}Ge can be seen in the Si(Li) spectrum. The 937 transitions in ^{72}Se and 691 transitions in ^{72}Ge are E0 transitions so it means that their corresponding gamma lines in the HPGe 1 are not observed as this multipolarity has the selection rule of having forbidden the gamma emission. This implies that their conversion coefficients cannot be extracted. Nevertheless, their relative intensities to the 862K and 834K transitions can be deduced from this study.

For the case of the ^{72}Se transitions, 937K and 937Tot-K, their intensities are compared to the 862K electron (K-shell electron of E2 transition) transition. The latter one is a well-known E2 transition, so the gamma intensity is deduced from the theoretical conversion coefficient obtained from [ANU] and the relative intensity is given in table 5.2. Also the results obtained for 691K and 691Tot-K transitions from ^{72}Ge level scheme are given in table 5.2 and their intensities are referred to the 834K transition, which is also the K-shell electron for an E2 transition.

Two relative intensities are reported for E0 transitions. One, the intensity with respect to the electron intensity of the K-shell electrons of the E2 transition, called 862K in ^{72}Se and 834K in ^{72}Ge, which is given in the 7^{th} column in table 5.2 and, the other, the intensity referred to the gamma intensity of the E2 transition, I_γ(E2), shown in the 8^{th} column in table 5.2, which is obtained from the electron peak intensity and dividing it by the theoretical conversion coefficient for K-shell obtained from Ref. [ANU]. Thus, as the I_γ(E2) is tabulated, one can compare the intensities of E0 transitions with the resulting values from previous works.

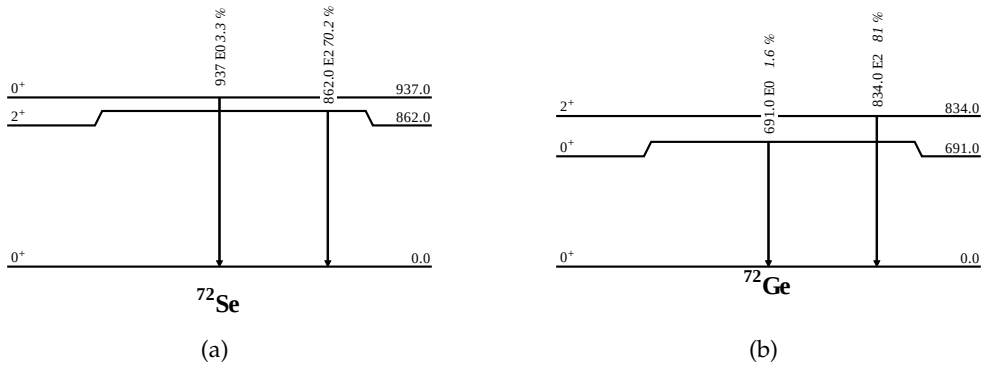

Figure 5.10: *(a) Level scheme of ^{72}Se showing only the transitions involved in the discussion of the E0 intensities. The intensities are given from [Col74, Ham74] (b) Same as (a) for the ^{72}Ge with intensities taken from [Cam68, Res71].*

As shown in table 5.2, the resulting values for the intensities of the 937 keV E0 transition in ^{72}Se are compatible within the error bars and also to the previously known intensity. They are 3.9(11) and 2.6(13) % whose weighted average provide a final value of **3.2(4)** and the previously known value from [Col74] and [Ham74] is 3.3(17). Also the $I_{ce}(Tot-K)/I_{ce}(K)$ ratios for the E0 transition where obtained with both miniorange configurations obtaining similar values whose weighted average value is 0.10(3).

In the case of the E0 transition in ^{72}Ge only the value corresponding for the 110/8/6A configuration was obtained since the 834K electron transition was not observed with the 125/8/6A configuration due to its lower transmission at this energy. With both configurations the $I_{ce}(Tot-K)/I_{ce}(K)$ ratios for the E0 transition are similar, 0.10(3) and 0.12(3), which average gives a final value for this ratio of 0.11(3). There were no possibility of referring the reported intensity of the E0 transition to the I_γ of the E2 as the gamma peak for the E2 transition was observed in the background measurement as can be seen in green in Fig. 3.29.

Miniorange configuration	Nucleus	Transition	Electron energy (keV)	Peak area / τ_e	I_{CE}(K)/I_{CE}(Tot-K)	I(E0)/I_{ce}(E2)* (%)	$I_{\gamma+ce}$** (%)	$I_{\gamma+ce}$ ref.*** (%)
110/8/6A	^{72}Se	862K	849.3	$1.5(3) \times 10^4$		100**	70.2	70.2
	^{72}Se	937K	924.3	$1.4(3) \times 10^6$		$9(3) \times 10^3$	3.5(10)	
	^{72}Se	937Tot-K	935.3	$1.5(3) \times 10^5$		$1.0(2) \times 10^3$	0.38(9)	
110/8/6A	^{72}Se	937		$1.5(5) \times 10^6$	**0.11(3)**		**3.9(11)**	3.3(17)
125/8/6A	^{72}Se	862K	849.3	$6.5(20) \times 10^3$		100**	70.2	70.2
	^{72}Se	937K	924.3	$4.1(8) \times 10^5$		$6(2) \times 10^3$	2.4(10)	
	^{72}Se	937Tot-K	935.3	$3.7(8) \times 10^4$		570(130)	0.21(5)	
125/8/6A	^{72}Se	937		$4.5(9) \times 10^5$	**0.09(3)**		**2.6(13)**	3.3(17)
Average	^{72}Se	937			**0.10(3)**		**3.2(4)**	3.3(17)
110/8/6A	^{72}Ge	834K	822.9	$4.8(11) \times 10^3$		100**	81(2)	81(2)
	^{72}Ge	691K	679.9	$6.1(12) \times 10^4$		1300(400)	0.51(17)	
	^{72}Ge	691Tot-K	689.6	$7.1(15) \times 10^3$		150(30)	0.060(13)	
110/8/6A	^{72}Ge	691		$7(2) \times 10^4$	**0.12(3)**		**0.57(19)**	1.6(3)
125/8/6A	^{72}Ge	834K	822.9	0■		100**	81(2)	81(2)
	^{72}Ge	691K	679.9	$6.2(12) \times 10^4$				
	^{72}Ge	691Tot-K	689.6	$6.0(15) \times 10^3$				
125/8/6A	^{72}Ge	691		$7(2) \times 10^4$	**0.10(3)**			
Average	^{72}Ge	691			**0.11(3)**		**0.57(19)**	1.6(3)

Table 5.2: *Intensity of E0 transitions, 937 keV in ^{72}Se and 691 keV in ^{72}Ge, studied via its conversion electrons intensity. The first four columns identify the transition as well as the measurement leading to the ratio peak areas/τ_e indicated in the 5^{th} column. The ratio of intensities of K-shell and Tot-K shell electrons in reported in the 6^{th} column. The relative intensity of each transition with respect to the E2 transition are given in the 7^{th} and to the E2 gamma intensity in the 8^{th}. The last column just shows the tabulated values for comparison. Two grey rows show the average values for each E0 transition obtained from both miniorange configurations used.*
**Intensity of E0 transition referred to the one for K-shell conversion electron of the E2 transition (862K for ^{72}Se and 834K for ^{72}Ge).*
***absolute intensity per 100 decays assuming the intensity of the E2 transition given in 8^{th} column. Gamma intensities of E2 transitions are estimated by dividing CE intensity by the corresponding theoretical α_K for E2 multipolarity obtained from [ANU].*
****from [Col74] and [Ham74] for 937 keV transition and from [Cam68] and [Res71] for the 691 keV transition.*
■ *No 834K transition was observed in electron spectrum and, therefore, no relative intensities for E0 transitions could be extracted. Only I_{ce}(Tot-K)/I_{ce}(K) ratio was obtained in this case.*

5.2 Results from Total Absorption Spectroscopy

Recalling the β^+ feeding distribution of the ^{72}Kr decay obtained in the chapter 4 from the beta gated analysis of TAS data that is shown in fig. C.5.

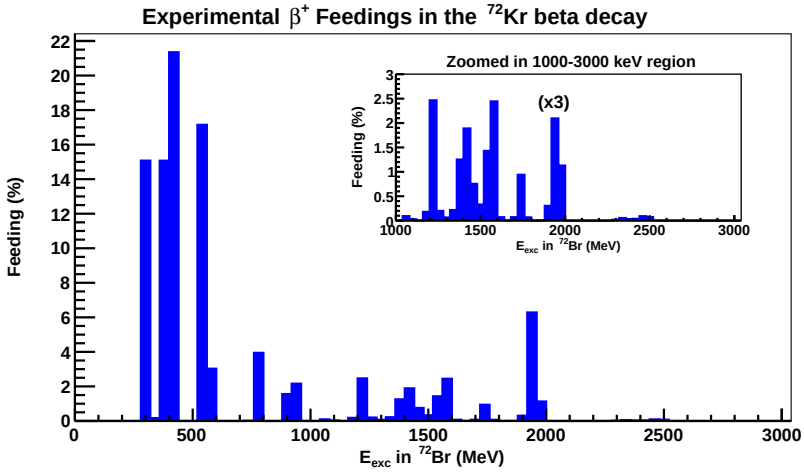

Figure 5.11: *β^+ feeding distribution shown up to the Q_{β^+}=4105 keV window obtained from the analysis with an upper limit in the TAS spectrum of 3640 keV in the energy for the measurement of ^{72}Kr file 1. The feedings are found up to 2620 keV for the reasons given in the text. The comparison of reconstructed spectrum with the experimental one is shown in figs. 4.26 and 4.27. The bin labelled with "(x3)" in the inset has its statistics reduced a factor 3.*

In order to get the B(GT) distribution one needs as input information the total (β^+ + EC) feeding distribution and not only the β^+ feeding distribution as is the currently available information. So one has to deduce from the experimental data the total feeding distribution, meaning the EC plus the β^+ components. In this analysis (β-gated) one obtains only the β^+ component so one has to deduce the total feeding distribution from the β^+ feeding.

To this purpose we use the ratio EC vs. β^+ tabulated in the form $logf(EC/\beta^+)$ in [Gov71]. The ratio $EC/(EC+\beta^+)$ for ^{72}Kr decay was already shown in figure 4.10. Thus, one has to convolute the obtained β^+ feeding distribution, F, (shown in fig. C.5) with this theoretically estimated ratio for each energy E, according to the formula:

$$I_{EC+\beta^+}(E) = I_{EC}(E) + I_{\beta^+}(E) = I_{\beta^+}(E) \times (1 + \frac{EC}{\beta^+}) \tag{5.16}$$

In this way one obtains the total feeding distribution of the β^+/EC decay of ^{72}Kr shown in figure 5.12. If one looks at the figure one sees that this transformation enhances the feedings to levels located at high excitation energy in ^{72}Br. Note that the total feeding distribution shown in the figure is not normalized to 100 % in contrast with the beta feeding. The following step would be to normalize before continuing the procedure but here it is shown without normalization in order to clearly see the effect of this transformation.

We can clearly appreciate an enhancement on the feeding located at high excitation energies, therefore, when one normalizes the total feeding, this causes a decrease in the feeding at lower energies.

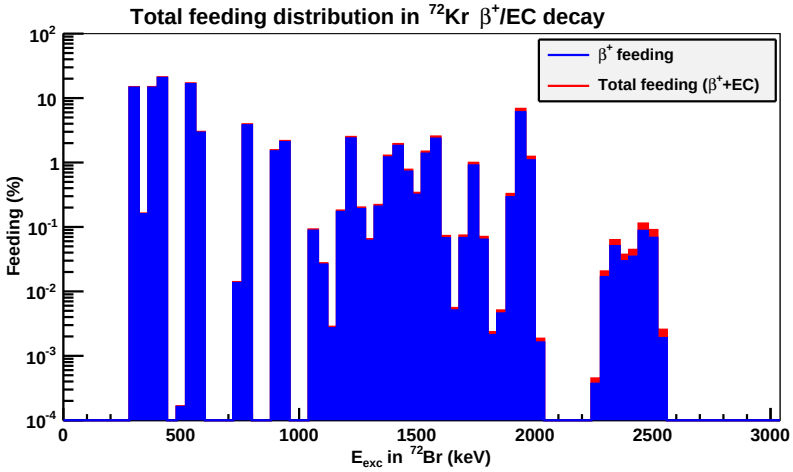

Figure 5.12: *Beta and total feeding distributions up to an excitation energy of 2618 keV in ^{72}Br, as the upper limit was established in the analysis to 3640 keV and one has to subtract the 1022 keV energy coming from the annihilation of the positron of the β^+ decay. It can be observed the effect of enhancing the total feedings at high excitation energies when deducing the (EC+β^+) feeding from β^+ feeding. The EC/β^+ ratio enhances the feeding located at high excitation energies. The normalization of the total feeding reduces the feeding located at low excitation energies.*

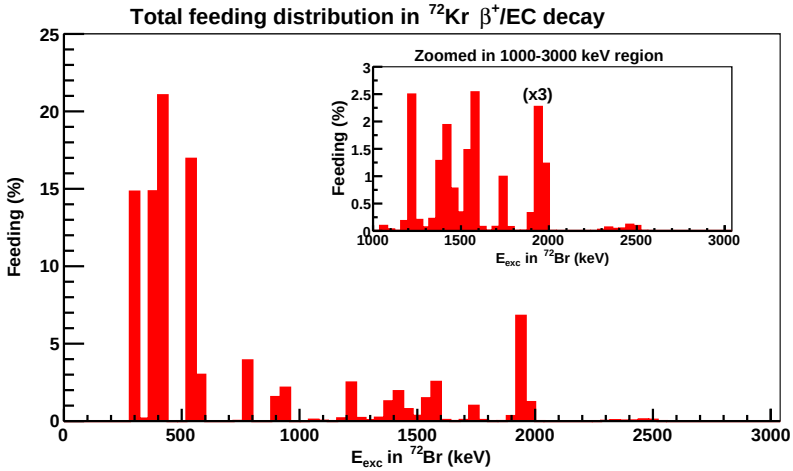

Figure 5.13: *Total feeding distribution in the ^{72}Kr decay obtained from the analysis of the file 1 of our measurement. It is measured up to an excitation energy in ^{72}Br of 2618 keV, where the upper limit was established in the analysis. The bin labelled with "(x3)" in the inset indicates that the statistics of this bin has been reduced a factor 3.*

As defined in chapter 1, the reduced transition probability of a Gamow-Teller transition, the only ones allowed among the intense β-transitions in ^{72}Kr decay, is:

$$B(GT) = K'\left(\frac{g_v}{g_a}\right)^2 \frac{I_\beta(E)}{fT_{1/2}} = K\left(\frac{g_v}{g_a}\right)^2 \frac{1}{ft_{1/2}} \tag{5.17}$$

Usually, when dealing with large Q_β values that allow feeding to regions with high-level density it is more convenient to use the strength function S_β that mathematically can be

expressed as:

$$S_\beta(E_x) = \frac{1}{K'} \cdot \left(\frac{g_a}{g_v}\right)^2 \sum_{E_f \in \Delta E} \frac{1}{\Delta E} B(GT)_{(i \to f)} \tag{5.18}$$

in terms of the known constants K' and g_a/g_v whose values are given in equations 1.33 and 1.34. Including the definition of the reduced transition probability $B(GT)$ from eq. 5.17:

$$S_\beta(E_x) = \frac{\sum_{E_f \in \Delta E} \frac{I_\beta(E_f)}{\Delta E}}{f \cdot T_{1/2}} \tag{5.19}$$

where E_x is the center value of the energy corresponding to a bin whose width is ΔE. This expression considers the feeding in energy intervals ΔE to take into account the very fragmented feeding distribution to high level density regions that are usually located at high excitation energies (E_f) in the daughter nucleus. This is useful because in the analysis of the TAS data one performs the analysis dividing the excitation energy spectra in energy bins, in this case, of 40 keV width and one obtain the feeding distribution with this segmentation.

The average value of the B(GT) in the bin corresponding to the energy interval ($E_x - \Delta E/2, E_x + \Delta E/2$) can be obtained afterwards by doing the transformation:

$$\overline{B(GT)(E_x)} = K' \left(\frac{g_a}{g_v}\right)^2 \cdot S_\beta(E_x) \tag{5.20}$$

The result of performing this operation on the total feeding distribution obtained in the analysis is shown in figure 5.14 shown in bins of 40 keV width.

A usual way of representing the B(GT) distribution is via its accumulated sum along the Q_β window. This way is especially interesting when one is interested in comparing with theoretical models. This is due to the theoretical levels are not placed at the exact same energies than the experimental ones and a accumulated distribution displays the general trend not paying much attention to small displacements in energy with respect to theoretical levels. The accumulated B(GT) distribution obtained of the analysis is shown in figure 5.15.

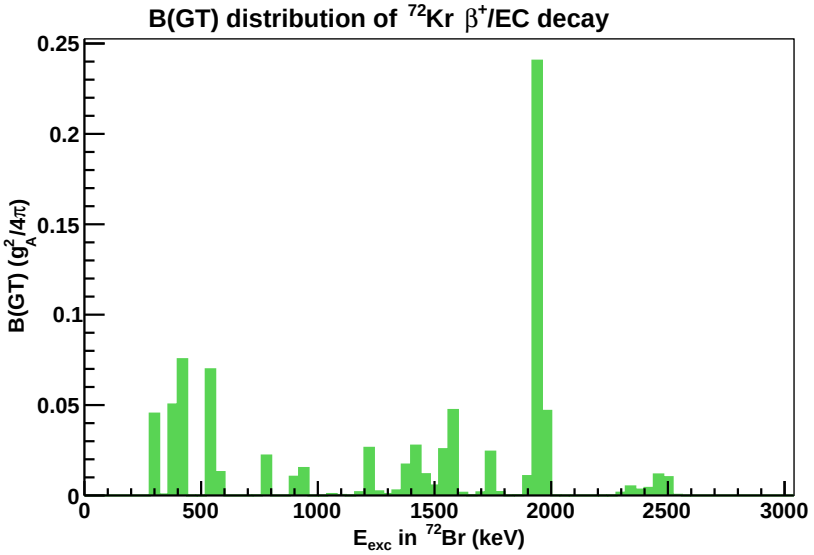

Figure 5.14: *B(GT) distribution obtained from the β^+ analysis of the file 1 of the study of the ^{72}Kr β^+/EC decay. Note that this analysis ends at 2618 keV and therefore no B(GT) can be obtained at higher energies than this level.*

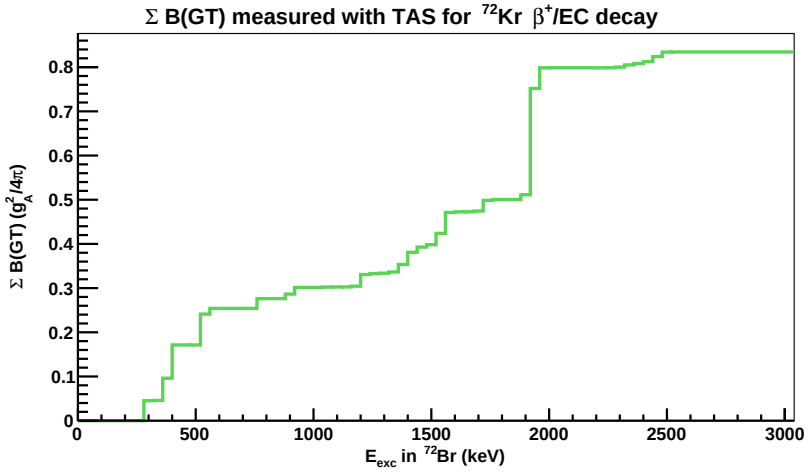

Figure 5.15: *Accumulated B(GT) distribution obtained from the β^+ analysis of the data corresponding to the file 1 of the study of the ^{72}Kr EC/β^+ decay.*

The procedure explained up to this moment can be repeated for the six different files measured for ^{72}Kr and one can take the average of them as the final B(GT) distribution. Also, if one remembers the points discussed before on the contaminations present in the ^{72}Kr measurements summarized in table 4.5, they were ^{75}Br, ^{72}As and ^{72}Br. The contribution from descendants and contaminants were changing from one file to other as time passes. The ^{75}Br contribution decreased and the ^{72}As contamination increased, a good estimation of their influence in the feeding and B(GT) distributions can be obtained from the careful analysis of the six files and then by comparing the provided results and see if any differences emerge from them.

The results for the accumulated B(GT) for the six files are shown in figure 5.16. As one can see, the accumulated B(GT) distributions are quite similar in the energy range used in the

analysis, i.e. from 0 till 2618 keV of excitation energy in ^{72}Br. As expected, the behaviour is similar giving consistency to the method. Due to this similar behaviour, one can average the six results and take this average distribution as the final experimental one.

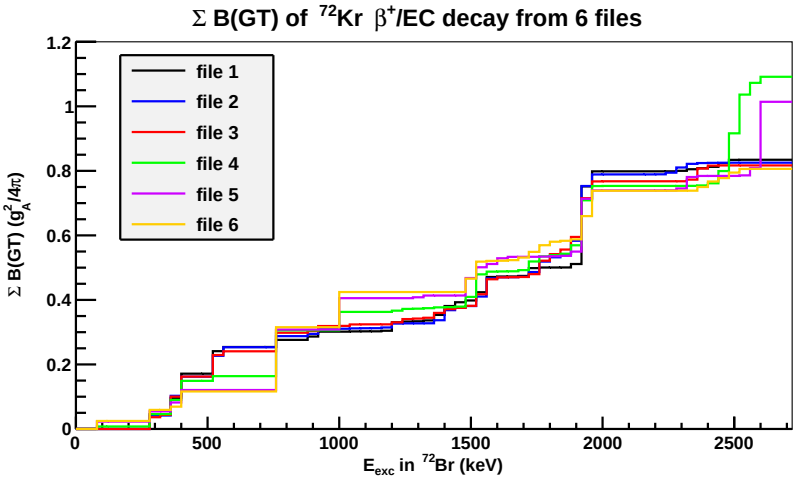

Figure 5.16: *Accumulated B(GT) distribution obtained from the β^+ analysis of the six files measured for the study of ^{72}Kr EC/β^+ decay. As can be observed, there are no huge differences in the six accumulated B(GT) distributions up to 2618 keV where the upper limit of the analysis was set.*

5.2.1 Uncertainties

The results shown up to this point correspond to the analysis of the first file of the measurement of ^{72}Kr. In this analysis we have used the subtraction factor obtained for the A=73 contamination present in the ^{72}Br spectrum. Then the clean ^{72}Br spectrum is subtracted from the ^{72}Kr.

The experimental result should include an uncertainty region that provide us the degree of confidence of the beta feeding and B(GT) distributions. The uncertainty is the maximum difference on the value of these quantities compatible with these measurements.

In order to estimate the uncertainty of this measurement one has two main components:

- **Systematic uncertainties:** the dominant contribution to the systematic errors is coming from the subtraction of contaminants. Thus, in every subtraction of contributions to the spectrum from different origins than the decay of interest, an upper and lower limits for the value of the subtraction factor were chosen This interval gives an estimation of the systematic uncertainties associated to this measurement.

- **Statistical uncertainties:** this kind of errors are usually estimated by measuring repeatedly the same quantity. In this study, as it was already mentioned, six different measurements were performed. They will help us to estimate the statistical errors. Another source of statistical uncertainties is the covariance between different bins but this was checked and finally ruled out for being negligible in comparison with the other.

5.2.1.1 Systematic uncertainty

In the procedure of analysis, two subtractions were performed with significant loss of statistics, namely the subtraction of A=73 contamination from the ^{72}Br spectrum and, later, the subtraction of the ^{72}Br spectrum from the file ^{72}Kr.

For each of these subtractions, 3 different subtraction factors were chosen. They are given in table 4.9. In this way, one finds 9 possible combinations of subtraction factors if one combines maximum, standard and minimum subtraction factors for both subtractions. The way of proceeding will be to perform the same analysis already explained for file 1, with the standard factors in both contamination subtractions, but now nine different analysis with all the possibilities of the combination of factors.

By doing this, one ends up with 9 different β feeding distribution and B(GT) distributions from which one can extract the maximum and minimum values of the $\Sigma B(GT)$ at each 40 keV width bins in the energy range of the analysis among those nine analysis. If one performs this procedure on the file 1 the result is the one shown in figure 5.17 where the shaded region indicates the maximum and minimum values for the accumulated B(GT) obtained from the nine analysis performed on the file 1 of the ^{72}Kr measurement.

As can be seen in the figure, the uncertainty only is significantly large from 2400 keV and only diverges in the last energy region, for energies higher than 2500 keV.

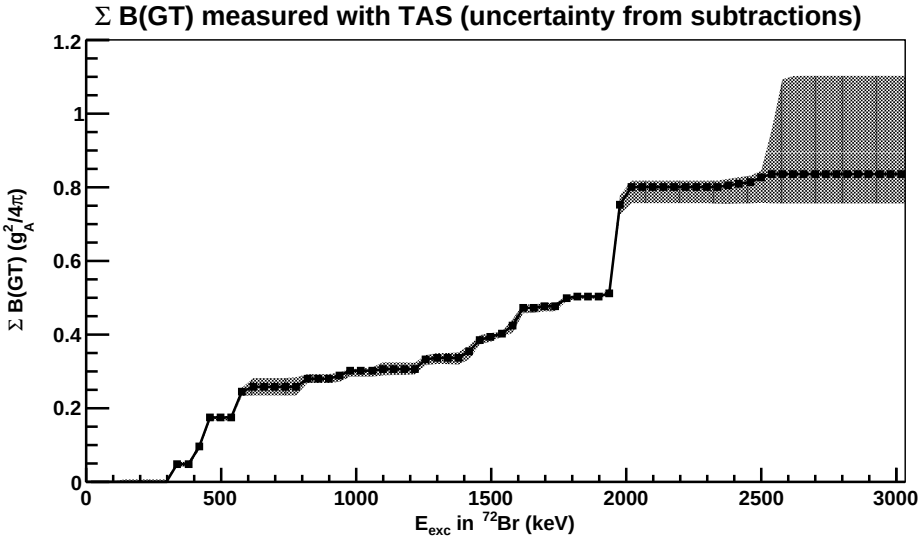

Figure 5.17: *Accumulated B(GT) distribution for the β^+/EC decay of ^{72}Kr obtained from the analysis with standard subtraction factors for file number 1. The shaded region is an attempt to quantify the uncertainty but in this case only the systematic uncertainties are included as this shaded region is limited by the maximum and minimum values of the Σ B(GT) obtained in the 9 analysis for each bin of 40 keV width in which the energy region was divided.*

5.2.1.2 Statistical uncertainty

The analysis performed for the six different files taken with the conditions to measure the ^{72}Kr decay were considered and the corresponding B(GT) distributions were averaged in order to obtain the final distribution.

To estimate the statistical uncertainties associated to this study the procedure to was to calculate the standard deviation of the accumulated B(GT) of the six files. In figure 5.18 the result of the averaging procedure is shown for the results obtained of the six independent analysis of the six files measured favouring the study of the ^{72}Kr decay. The green lines are placed to show the maximum and minimum values for the accumulated B(GT) at each energy obtained from the six analysis. The shaded region is an attempt to quantify the statistical uncertainty by calculating the standard deviation of the mean which is defined as the standard deviation divided by the squared root of the number of measurements. The way in which the uncertainty was obtained is given by the usual expression:

$$(\Delta B(GT))_{stat} = \frac{\sqrt{\frac{\sum_{i=1}^{n}(m_i-\bar{m})^2}{(n-1)}}}{\sqrt{n}} = \sqrt{\frac{\sum_{i=1}^{n}(m_i-\bar{m})^2}{n\cdot(n-1)}} \tag{5.21}$$

where ΔB is the standard deviation of the mean value, n is the number of measurements (in this case is $n = 6$), m_i are the bin content of the file i and $\bar{m}$ is the mean value of the $n = 6$ files m_i.

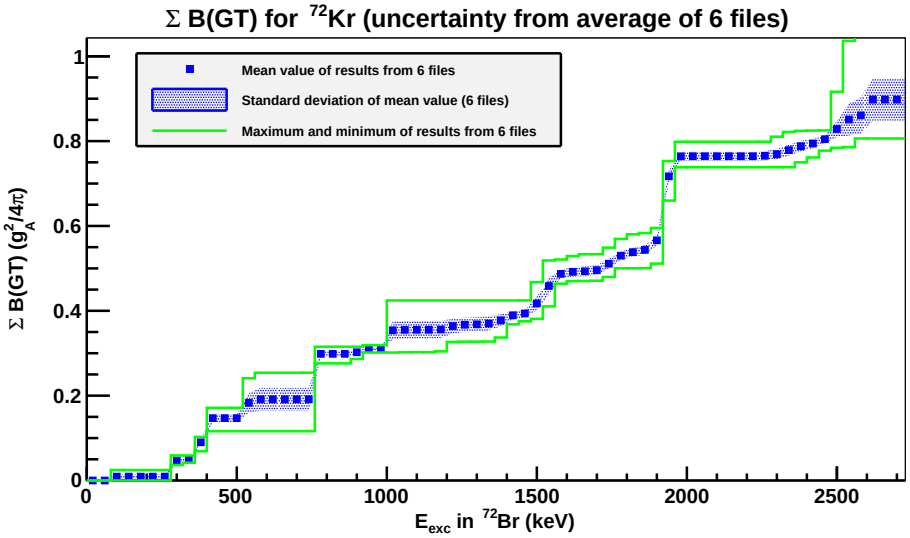

Figure 5.18: *Accumulated B(GT) distribution obtained as the mean value of the result from the six files of the measurement of ^{72}Kr decay. The shaded region shows the uncertainty coming from the standard deviation of the results from the six files (statistical uncertainty). The green lines indicates the maximum and minimum values for each bin of the six analysis performed. As expected, the standard deviation shows lower uncertainty that considering the maximum and minimum values.*

One important aspect to take into consideration is the fact that the previous estimation of the systematic uncertainty was done for one file (file 1) as an example but now one can improve this estimation as one has the uncertainty coming from subtractions for the six measured files.

Now, instead of taking the maximum and minimum values of the accumulated B(GT) for each bin, one can calculate the deviations from the mean value (this mean value is the average shown of the six results of the different files) and then reduce this difference by the square root of the number of measurements performed, six in this case, in order to account for the reduction of the uncertainties due to the fact of performing several measurements of the same quantity.

The comparison of systematic and statistical uncertainties for the analysis is shown in figure 5.19. As it is clearly shown, systematic is larger than statistical uncertainty. The statistical uncertainties is minimum in comparison with the systematic one despite the changeable room background contribution to the TAS spectra. The systematic uncertainty grows enormously while approaching to the Q_EC value as small variations of statistics there means a big change in B(GT) because of the small value of the Fermi function f and the big value of the EC/β^+ value which increases the feeding found at these energies. This is in concordance with the safely large difference between subtraction factors considered (10%). This was justified before due to the bigger uncertainty in the analysis is the subtraction of the contribution of contaminants and one has to be safe by choosing extreme values of the factors wide enough to account for the possible errors introduced in the analysis from this origin.

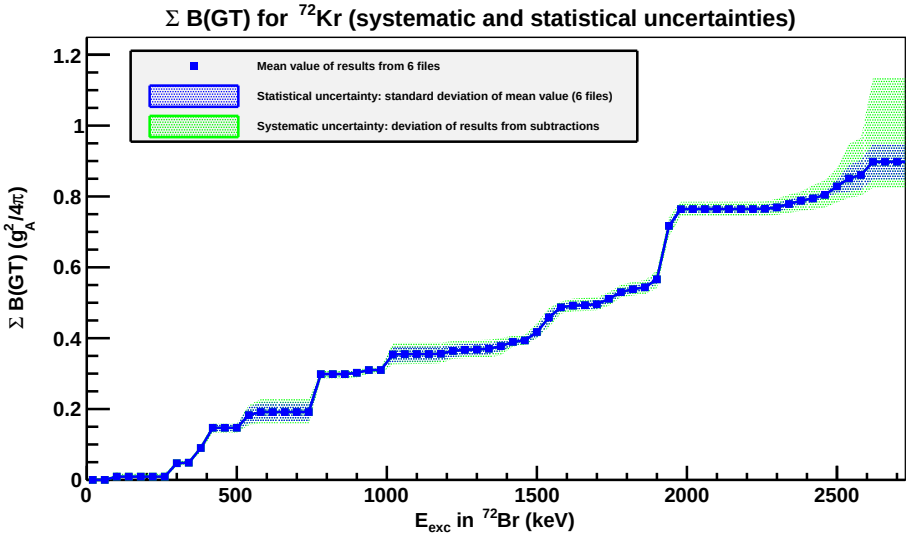

Figure 5.19: *Accumulated B(GT) distribution obtained from the TAS analysis for the β^+/EC decay of ^{72}Kr decay and the experimental uncertainties considered in the analysis. The statistical uncertainty is shown as the blue shaded region being the standard deviation of the mean value of the results from the analysis of the six files measured to study ^{72}Kr. The systematic uncertainty has been obtained, as described in the text, by the deviation of the maximum and minimum values of the results considering the different subtraction factors from the mean value of the six analysis and is shown in the plot with the green shaded region.*

Once the systematic and statistical uncertainties have been estimated one should add them in order to obtain a global uncertainty. The way in which this addition will be performed is by making use of the expression 5.22.

$$\Delta B(GT) = \sqrt{(\Delta B(GT)_{syst})^2 + (\Delta B(GT)_{stat})^2} \tag{5.22}$$

The result of this propagation of uncertainties ends up with the final estimation of the uncertainty in the determination of the experimental distribution of the accumulated B(GT) shown in figure 5.20. This experimental accumulated B(GT) distribution will be compared with several theoretical models in the chapter 5 where conclusions from this comparison will be extracted and a detailed discussion of this results will be addressed.

The values obtained for the accumulated B(GT) are listed in table 5.3 up to the maximum energy in the data analysis, that is 2618 keV. The value of the energy given in the table is the

corresponding to the end of the bin which is 40-keV width, so the analysis ended at 2640 keV. For example, bin number 1 corresponds to the energy interval from 0 up to 40 keV and the energy given in the table would be 40 keV indicating that the accumulated B(GT) listed is the one found in the analysis summed up to 40 keV.

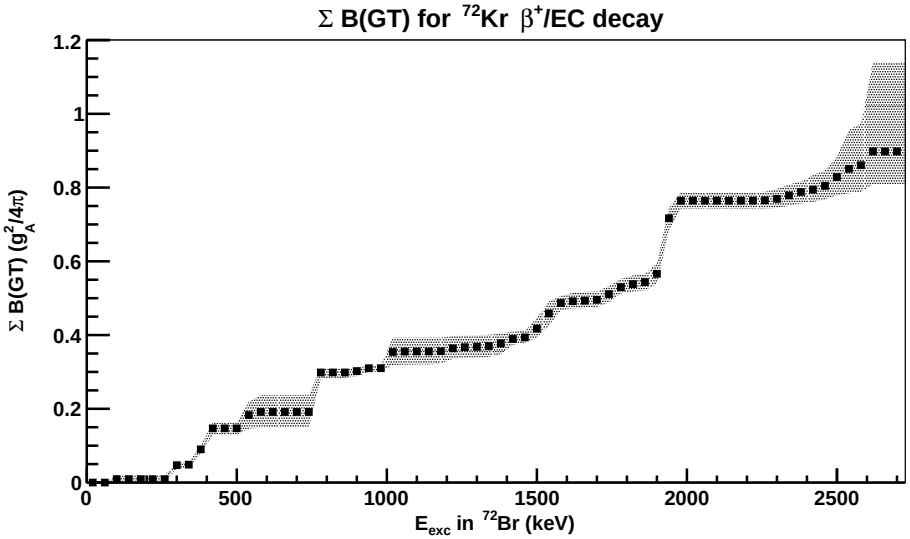

Figure 5.20: *Accumulated B(GT) distribution for the β^+/EC decay of ^{72}Kr obtained from this analysis of the β^+ decay component via TAS spectroscopy. The uncertainty region shown is estimated from systematic and statistical origin as described in the text.*

5.2.2 Sensitivity to the knowledge on the daughter level scheme

5.2.2.1 Modifications of the known part

The analysis presented up to now has been performed by using the information on the level scheme coming from the most exhaustive beta decay study of ^{72}Kr included in the work of I. Piqueras [Piq03]. An upper limit for the known part of the level scheme has been imposed at the level of 1 MeV of excitation energy in the daughter nucleus. The information from this work is listed in table 2.1 given in the chapter 2.

Now, the question that could arise to an experimentalist is how a different limit in the known part of the level scheme, for example change it up to 2 MeV, would influence the results obtained from the analysis in terms of the accumulated B(GT) distribution.

The procedure previously described was followed in order to obtain the accumulated B(GT) distribution for this decay by using a different level scheme in the preparation of the response matrix of the detector to the ^{72}Kr decay.

Three cases were studied:

- Level scheme from I. Piqueras work [Piq03] with an upper limit of the known part at 1 MeV (analysis already explained).

- Level scheme from I. Piqueras work [Piq03] but increasing the upper limit of the known part up to 2 MeV.

E_{exc} in ^{72}Br (keV)	Accumulated B(GT) $(g_A^2/4\pi)$	E_{exc} in ^{72}Br (keV)	Accumulated B(GT) $(g_A^2/4\pi)$	E_{exc} in ^{72}Br (keV)	Accumulated B(GT) $(g_A^2/4\pi)$
40	$0\ ^{+0}_{-0}$	920	$0.302\ ^{+0.010}_{-0.014}$	1800	$0.530\ ^{+0.020}_{-0.017}$
80	$0\ ^{+0}_{-0}$	960	$0.310\ ^{+0.007}_{-0.011}$	1840	$0.54\ ^{+0.02}_{-0.02}$
120	$0.009\ ^{+0.010}_{-0.006}$	1000	$0.310\ ^{+0.007}_{-0.011}$	1880	$0.54\ ^{+0.02}_{-0.02}$
160	$0.009\ ^{+0.010}_{-0.006}$	1040	$0.35\ ^{+0.04}_{-0.03}$	1920	$0.57\ ^{+0.03}_{-0.03}$
200	$0.009\ ^{+0.010}_{-0.006}$	1080	$0.35\ ^{+0.04}_{-0.03}$	1960	$0.72\ ^{+0.03}_{-0.03}$
240	$0.009\ ^{+0.010}_{-0.006}$	1120	$0.35\ ^{+0.04}_{-0.03}$	2000	$0.76\ ^{+0.02}_{-0.02}$
280	$0.009\ ^{+0.010}_{-0.006}$	1160	$0.35\ ^{+0.04}_{-0.03}$	2040	$0.76\ ^{+0.02}_{-0.02}$
320	$0.047\ ^{+0.008}_{-0.009}$	1200	$0.36\ ^{+0.04}_{-0.03}$	2080	$0.76\ ^{+0.02}_{-0.02}$
360	$0.048\ ^{+0.007}_{-0.006}$	1240	$0.36\ ^{+0.03}_{-0.03}$	2120	$0.76\ ^{+0.02}_{-0.02}$
400	$0.090\ ^{+0.010}_{-0.011}$	1280	$0.37\ ^{+0.03}_{-0.03}$	2160	$0.76\ ^{+0.02}_{-0.02}$
440	$0.147\ ^{+0.015}_{-0.017}$	1320	$0.37\ ^{+0.03}_{-0.03}$	2200	$0.76\ ^{+0.02}_{-0.02}$
480	$0.147\ ^{+0.015}_{-0.017}$	1360	$0.37\ ^{+0.03}_{-0.03}$	2240	$0.76\ ^{+0.02}_{-0.02}$
520	$0.147\ ^{+0.015}_{-0.017}$	1400	$0.38\ ^{+0.03}_{-0.03}$	2280	$0.76\ ^{+0.02}_{-0.02}$
560	$0.18\ ^{+0.04}_{-0.04}$	1440	$0.389\ ^{+0.020}_{-0.016}$	2320	$0.77\ ^{+0.03}_{-0.02}$
600	$0.19\ ^{+0.05}_{-0.04}$	1480	$0.394\ ^{+0.020}_{-0.014}$	2360	$0.78\ ^{+0.03}_{-0.03}$
640	$0.19\ ^{+0.05}_{-0.04}$	1520	$0.42\ ^{+0.03}_{-0.02}$	2400	$0.79\ ^{+0.03}_{-0.03}$
680	$0.19\ ^{+0.05}_{-0.04}$	1560	$0.46\ ^{+0.03}_{-0.03}$	2440	$0.79\ ^{+0.04}_{-0.03}$
720	$0.19\ ^{+0.05}_{-0.04}$	1600	$0.487\ ^{+0.019}_{-0.020}$	2480	$0.80\ ^{+0.04}_{-0.04}$
760	$0.19\ ^{+0.05}_{-0.04}$	1640	$0.49\ ^{+0.02}_{-0.02}$	2520	$0.83\ ^{+0.05}_{-0.05}$
800	$0.299\ ^{+0.012}_{-0.015}$	1680	$0.49\ ^{+0.02}_{-0.02}$	2560	$0.85\ ^{+0.11}_{-0.07}$
840	$0.299\ ^{+0.012}_{-0.015}$	1720	$0.50\ ^{+0.02}_{-0.02}$	2600	$0.86\ ^{+0.11}_{-0.07}$
880	$0.299\ ^{+0.012}_{-0.015}$	1760	$0.51\ ^{+0.02}_{-0.02}$	2640	$0.90\ ^{+0.24}_{-0.09}$

Table 5.3: *Accumulated B(GT) distribution obtained in the analysis of this work. The excitation energy in ^{72}Br corresponds to the end of bin energy from the analysis, that is the first bin accumulates the B(GT) found in the energy interval from 0 up to 40 keV and is indicated here corresponding to an energy of 40 keV. Remember that the bin width was chosen as 40 keV. The graphical representation of this set of data is shown in fig. 5.20.*

- Randomly modified the previous level scheme by modifying the spin-parities of the levels reported in I. Piqueras work, that are in most of cases 1^+, to spin-parities 2^+, 3^+ and 1^-.

The results from these three possibilities are compared in the figure 5.21. The result using the Piqueras level scheme up to 1 MeV as known part of the level scheme is displayed with the final uncertainties (shaded region). As it is shown, the differences in the distributions are quite small, the general trend is very similar for all the level schemes and all the results agree with the chosen errorbars in the analysis.

This supports the reliability of the results of this analysis as for this measurement a very precise and complete knowledge of the ^{72}Br level scheme does not strongly influence the experimental accumulated B(GT) distributions.

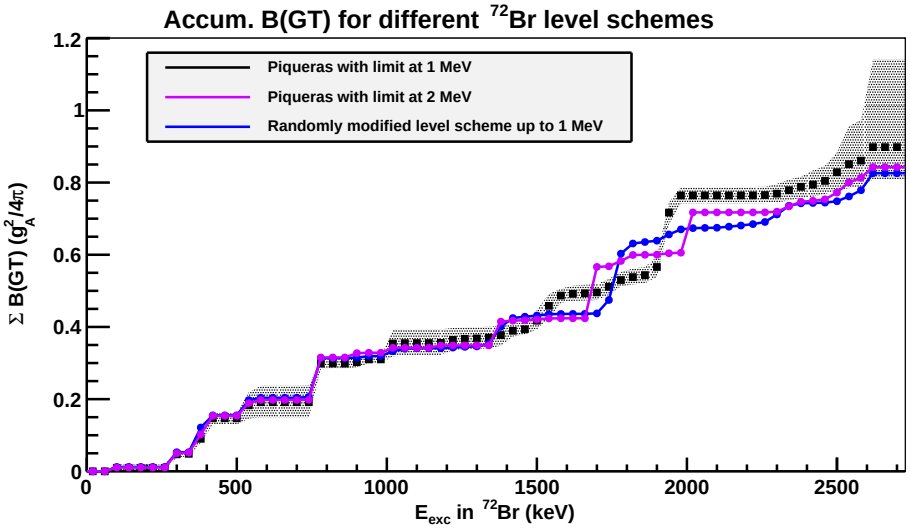

Figure 5.21: *Accumulated B(GT) distributions obtained from the β^+ analysis of the ^{72}Kr β^+/EC decay using three different sets of information on the ^{72}Br level scheme: in black is taking the information from [Piq03] up to excitation energy of 1 MeV as known part, the violet one shows the result using the same set of information but taking up to 2 MeV as known part of the level scheme and the blue line was obtained using the same information on the level scheme but modifying the spin-parities of the levels randomly to 2^+, 3^+ and 1^- spin-parities. The information from [Piq03] is listed in table 2.1.*

Another test that was performed consists of using as known part of the level scheme a theoretical level scheme of ^{72}Br obtained from the QRPA calculations of P. Sarriguren described in chapter 1 and in Refs. [Sar99, Sar01, Sar09]. The considered level scheme was the one that these calculations provide for an oblate deformation of the ground state of both, ^{72}Kr and ^{72}Br as several experimental works on the deformation of ^{72}Kr ground state suggest this deformation.

Again, two upper limits for the known part of the theoretical level scheme were chosen, at 1 MeV of excitation energy and at 2 MeV. The comparison of these analysis with the one obtained from the experimental level scheme of Piqueras et al. in [Piq03] are shown in fig. 5.22. No huge differences were found between them being compatible. The one obtained from the theoretical level scheme up to 1 MeV of excitation energy differs more than the one up to 2 MeV but the difference is acceptable as it is of the same order than uncertainties that can be observed in fig. 5.20.

Note that accumulated B(GT) distribution in fig. 5.22 corresponds to the result of analysis on file 1 only and not the average of all the files.

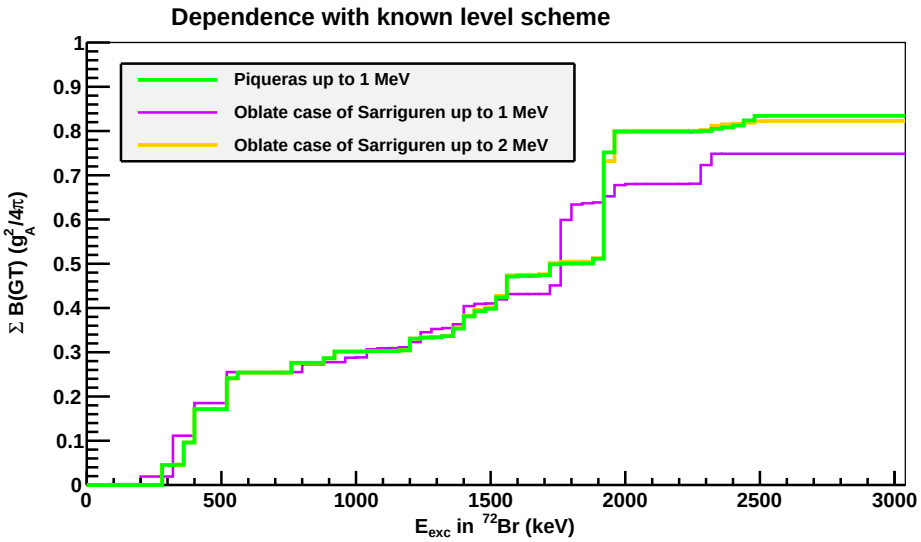

Figure 5.22: *Comparison of accumulated B(GT) distributions obtained using three different known parts of the ^{72}Br level schemes. The first one is the one from the work of Piqueras et al. [Piq03] up to 1 MeV as known part, the second is the theoretically obtained from QRPA calculations of P. Sarriguren described in [Sar99, Sar01, Sar09] considering the ground state of ^{72}Kr to be oblate deformed and the known part of the level scheme up to 1 MeV and the third is the same as the previous but the known part was considered up to 2 MeV.*

5.2.2.2 Modifications of the unknown part

In order to check the sensitivity of the analysis to the level scheme in the daughter nucleus in the unknown part of the level scheme we will modify the value of the level density parameters that were determined in the chapter 2. The equation where both parameters were included is 2.11 and the found values were:

$$a = 10.697, \Delta = -0.839 \text{ MeV} \tag{5.23}$$

Both are modified a 20% over their value and the result is the one shown in fig. 5.23. No appreciable differences were found between these analysis so the result taken is reliable from the level density parameters point of view.

Note that accumulated B(GT) distribution in fig. 5.23 corresponds to the result of analysis on file 1 only and not the average of all the files.

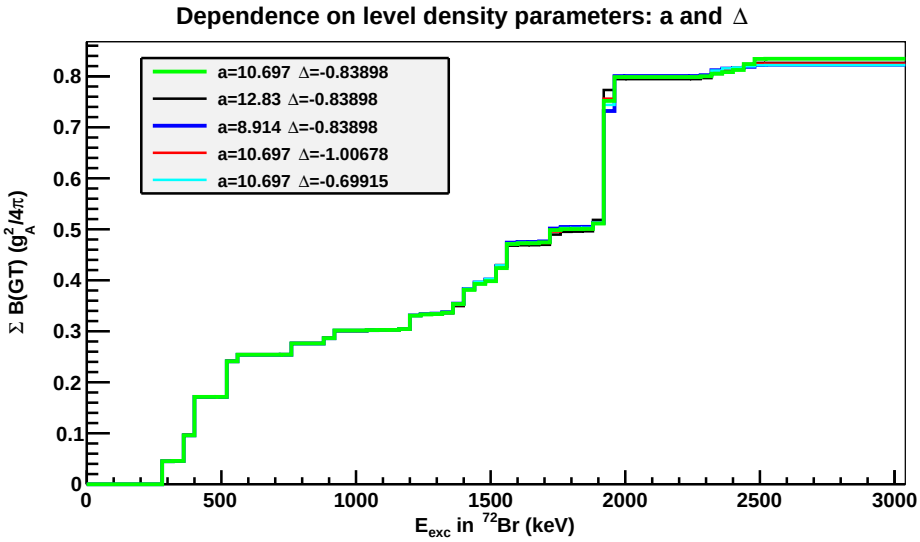

Figure 5.23: *Accumulated B(GT) distributions obtained from the β^+ analysis of the file 1 only of ^{72}Kr β^+/EC decay using level schemes built in the unknown part with different values of the level density parameters a and Δ from 2.11 whose values were found to be 2.12. Both parameters have been modified $\pm 20\%$ to check its influence. Almost no dependence in these parameters was found as shown in the figure.*

5.2.3 Reproduction of gamma intensities in the ^{72}Br level scheme

Another consistency check of the results is to calculate the gamma intensities of the transitions involved in the de-excitation of the daughter nucleus, ^{72}Br, resulting from the beta feedings distribution obtained in the analysis of the TAS data.

Thus, if one starts from the upper bin in the level scheme of the daughter nucleus making the intensity balance:

$$\sum I_i(in) = \sum I_i(out) \tag{5.24}$$

of incoming and outgoing intensities for each bin i, where incoming intensity are the beta feeding and the gamma intensity from upper levels connected with the one of interest, i. One can calculate the gamma intensity of every transition as the multiplication of the outgoing intensity and the branching ratio of de-excitation in the starting level of the transition:

$$I_\gamma(i,j) = BR(i,j) \times I_i(out) \tag{5.25}$$

where i and j are the starting and ending level of the transition and I_i is the total de-excitation intensity of the level.

One establishes a reference transition to refer the intensities to, that in our case was chosen the 310 keV for being the most intense one. Then, the intensity of the rest of transitions can be compared with the tabulated values from [Piq03].

To this purpose one has to choose a final set of beta feedings that one can consider as final distribution. Therefore, as we have 6 different beta feeding distributions, coming each of them from the 6 analysis performed over the different ^{72}Kr files, the average of these 6 distributions is done. The results is given in fig. 5.24. The error bars are obtained as the variance from the

mean value calculated as:

$$\Delta\bar{f} = \frac{\sqrt{\frac{\sum_j (f_j - \bar{f})^2}{5}}}{6} \tag{5.26}$$

where $\bar{f}$ is the mean value of the feedings, f_j is the feeding for the file j, 5 is the number of measurements minus 1, that is $n-1$ to calculate the standard deviation, and 6 is the number of measurements, n.

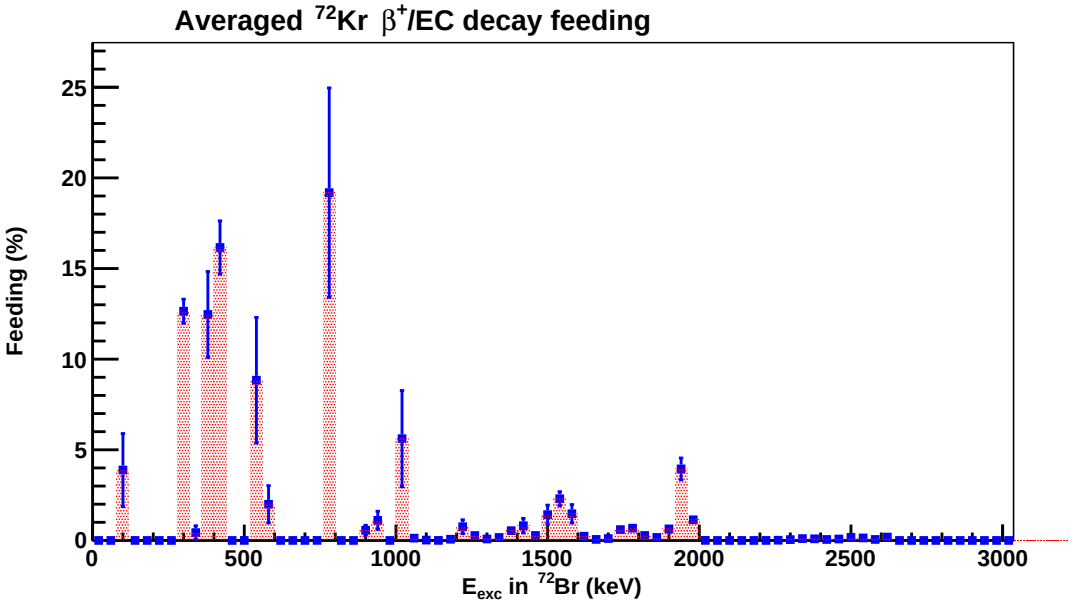

Figure 5.24: *Beta feeding distribution of the ^{72}Kr decay obtained as the average of the feeding distribution from the 6 independent analysis performed with the 6 files of measurements to study the ^{72}Kr decay with free conditions in the feeding distribution.*

E_{exc} in ^{72}Br (keV)	β^+/EC-feeding (%)	E_{exc} in ^{72}Br (keV)	β^+/EC-feeding (%)	E_{exc} in ^{72}Br (keV)	β^+/EC-feeding (%)
20	0(0)	900	0.56 (0.75)	1780	0.68(0.82)
60	0(0)	940	1.1 (1.1)	1820	0.27(0.52)
100	4(2)	980	0 (0)	1860	0.17(0.41)
140	0.001(0.032)	1020	5.6 (2.4)	1900	0.6(0.8)
180	0.000001(0.001)	1060	0.13 (0.36)	1940	3.9(2.0)
220	0(0)	1100	0.018 (0.13)	1980	1.1(1.1)
260	0(0)	1140	0.0026 (0.051)	2020	0.004(0.063)
300	12.6(3.6)	1180	0.067 (0.26)	2060	0(0.0021)
340	0.43(0.66)	1220	0.76 (0.87)	2100	0(0)
380	12.5(3.5)	1260	0.27 (0.52)	2140	0(0)
420	16.2(4.0)	1300	0.08 (0.29)	2180	0(0)
460	0(0)	1340	0.16 (0.40)	2220	0.0008(0.0280)
500	0.0016(0.04)	1380	0.54 (0.73)	2260	0.011(0.110)
540	8.84(3.00)	1420	0.8 (0.9)	2300	0.05(0.21)
580	2.0(1.4)	1460	0.27 (0.52)	2340	0.10(0.32)
620	0(0)	1500	1.42 (1.20)	2380	0.09(0.30)
660	0(0)	1540	2.3 (1.5)	2420	0.05(0.23)
700	0(0)	1580	1.5 (1.2)	2460	0.08(0.28)
740	0.0026(0.051)	1620	0.24 (0.48)	2500	0.17(0.41)
780	19.2(4.4)	1660	0.06 (0.24)	2540	0.14(0.37)
820	0(0)	1700	0.11 (0.32)	2580	0.06(0.24)
860	0(0)	1740	0.60 (0.77)	2620	0.19(0.43)

Table 5.4: *Average β-feeding distribution obtained in the analysis of this work. The excitation energy in ^{72}Br corresponds to the bin center energy from the analysis. Remember that the bin width was chosen as 40 keV. The graphical representation of this set of data is shown in fig. 5.24.*

If one takes the feeding distribution listed in table 5.4 the result obtained for the most intense gamma lines in the de-excitation of ^{72}Br are the ones given in table 5.5. The results from this analysis is the one listed in column 4 of the table. The values of the gamma intensities does not match very well with the values reported by I. Piqueras et al. in [Piq03].

Due to this, another analysis with some restrictions on the possible feeding intensities to some bins (levels) was performed. The conditions imposed to the analysis were:

- Feeding 0.7 % to bin 3, which includes the 101.3-keV level.
- Feeding 5.0 % to bin 5, including the 162.8-keV level.
- Feeding 22.6 % to bin 8, which includes the 310.0-keV and 313.8-keV levels.
- Feeding 25.15 % to bin 11, which includes the 415.2-keV level.
- Feeding 19.84 % to bin 15, including the 575.9-keV and 577.0-keV levels.

Starting bin (number)	Levels included in bin (keV)	I_γ(ref.) (%) [Piq03]	I_γ (%) this work	I_γ (%) restricted
3	101.3	2.4(3)	14.98	8.30
4	124.4, 131.8	4.9(5) + 0.0	7.03	3.99
5	162.8	10.8(10)	3.65	10.12
8	310.0, 313.8	15.7(5) + 0.567(22) = 16.3(5)*	16.3*	16.3*
10	379.3, 392.7, 398.5	0.82(16)+0.59(3)+0.57(3) = 1.98(17)	6.89	2.12
11	415.2	13.2(9)	11.47	13.34
15	575.9, 577.0	1.15(13)+6.3(3)=7.45(11)	0.79	6.37

Table 5.5: *List of gamma intensities obtained for the most intense gamma lines in the decay scheme of ^{72}Kr. As shown, the values from this work with all the feedings free does not fairly reproduce the transition intensities. However, the analysis performed with some restrictions on the feeding distribution gives a nice reproduction of the experimental values obtained from the high resolution measurement from [Piq03].*

The resulting gamma intensities from this restricted analysis are shown in the last column of table 5.5. As shown, the reproduction of experimental gamma intensities is quite good in comparison with the previous results (column 4). The comparison between this restricted feeding distribution with the obtained previously with the free analysis is shown in fig. 5.26. The distributions are visibly different. However, the differences between both B(GT) distributions from both analysis are not so remarked and are quite similar as can be seen in fig. 5.27. The total accumulated B(GT) values up to the maximum energy of the analysis, which is 2620 keV, is similar:

$$\sum B(GT)_{free} = 0.90^{+0.24}_{-0.09}(g_A^2/4\pi) \tag{5.27}$$

$$\sum B(GT)_{restricted} = 0.99^{+0.28}_{-0.12}(g_A^2/4\pi) \tag{5.28}$$

$$\tag{5.29}$$

The B(GT) provided is very similar but the reproduction of the experimental spectra is quite worse in the restricted analysis than in the free analysis as shown in fig. 5.25 for the analysis of file 1. The χ^2/ndf value for the restricted analysis is worse than in the free analysis as shown in eq. 5.30, where ndf is the number of degrees of freedom in the analysis chosen to be 225 channels, beyond the upper limit of the analysis, 3640 keV which corresponds to channel 92 in the experimental spectrum. The differences between experimental and reconstructed spectra are bigger than in the free analysis and for the rest of the files is much worse than in this case.

$$\sum \left(\chi^2/ndf\right)_{free} = 4231/225 \tag{5.30}$$

$$\sum \left(\chi^2/ndf\right)_{restricted} = 4533/225 \tag{5.31}$$

$$\tag{5.32}$$

All these comparisons lead us to conclude that the best analysis is the one with free conditions on the feedings as it better reproduces the experimental spectra. Despite it is true that the feeding distributions obtained with the two types of analysis (free and restricted) are remarkably different, see fig. 5.26, their corresponding accumulated B(GT) distributions are

quite similar, see fig. 5.27. As the experimental results that we are going to compare with models is the accumulated B(GT), the feeding distribution is not important for being so different and we prefer to stress the prevalence of the fair reproduction of experimental spectra over the reproduction of gamma intensities.

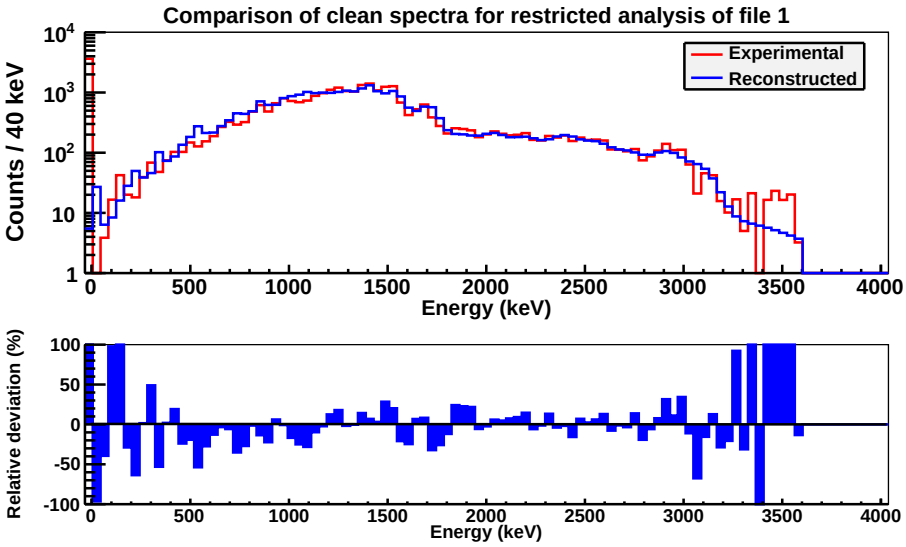

Figure 5.25: *Comparison of experimental (red) and reconstructed (blue) TAS spectra for the ^{72}Kr measurement of file 1. The reconstructed is the result of the analysis done using the restrictions on the feedings mentioned in the text.*

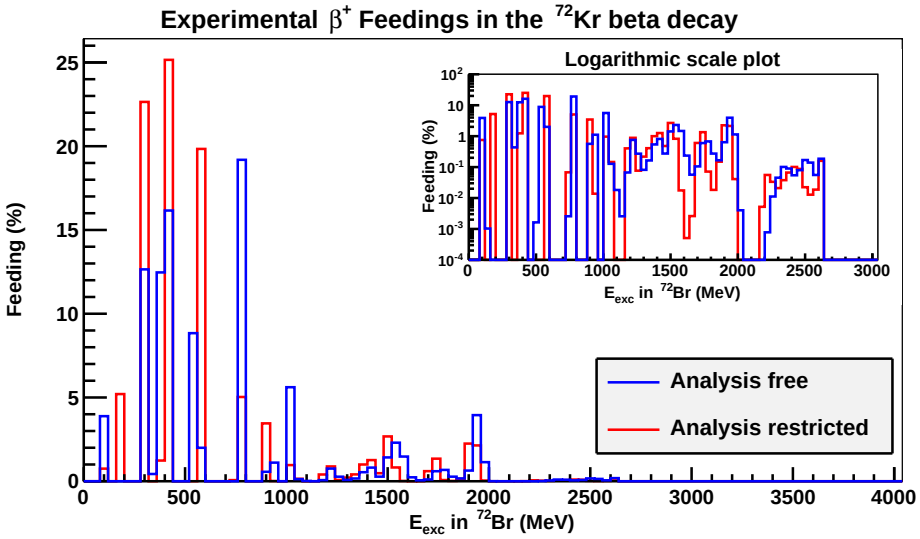

Figure 5.26: *Comparison of β-feeding distributions obtained from the analysis with all the feedings free (blue) and restricted (red). The inset shows a logarithmic scale comparison to better appreciate the differences.*

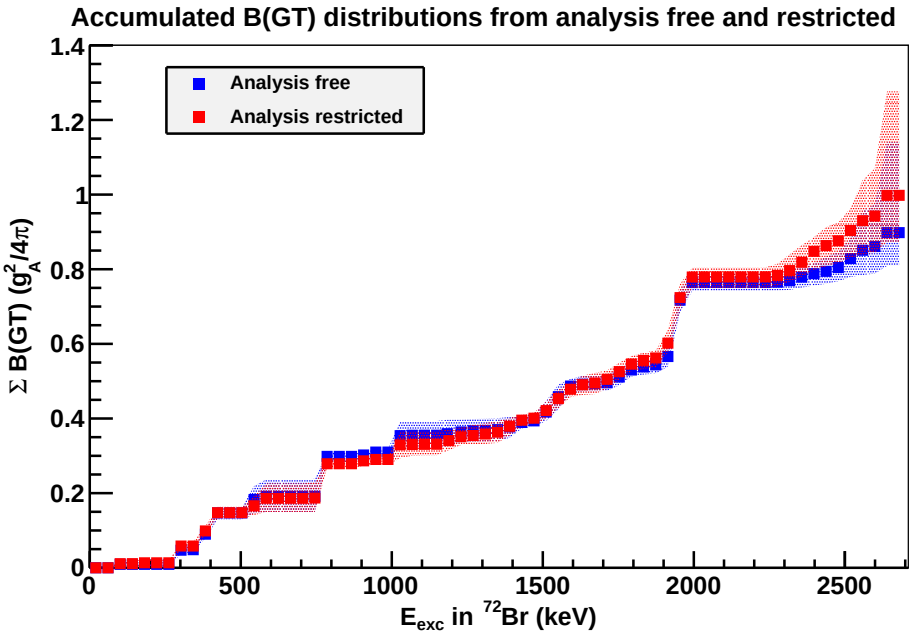

Figure 5.27: *Comparison of accumulated B(GT) distributions obtained from the analysis with all the feedings free (blue) and with some of them restricted (red). The trend of both results is similar and the value of the total B(GT) accumulated up to 2640 keV are similar in both analysis:* $B(GT)_{free} = 0.90^{+0.24}_{-0.09}(g_A^2/4\pi)$ *and* $\sum B(GT)_{restricted} = 0.99^{+0.28}_{-0.12}(g_A^2/4\pi)$

5.2.4 Comparison with theoretical predictions

One of the main goals of the present study was to compare the experimental B(GT) distribution, which is shown in fig. 5.20, with the theoretical predictions for the oblate and prolate case from [Sar09]. This could provide us with information on the deformation of the ground state of ^{72}Kr. Fig. 5.28 shows this comparison. The experimental results fairly reproduces the predicted distribution for an oblate deformation of the ground state of ^{72}Kr which supports the theoretical predictions and previous experimental works explained in chapter 1.

Recalling the work of Bouchez and collaborators, [Bou03], they found a mixing amplitude for the ground state of 10% with the first 0^+ state which is supposed to be of prolate deformation. One could estimate the predictions from [Sar09] for this mixing amplitude in a non formally correct way but visually estimative (to guide the eye), simply by calculating a mixing of 90% of the B(GT) predicted for the oblate deformation and 10% of the predicted for prolate deformation and add them. The result is the plot shown in fig. 5.29. The green line shows the prediction for the mixed ground state deformation. One can observe as the experimental accumulated B(GT) distribution is nicely compatible with both predictions, for the oblate deformation of the ^{72}Kr ground state or with a mixing of the oblate ground state the prolate first 0^+ state at 671(2) keV of excitation energy.

Therefore, from this comparison of accumulated B(GT) we can infer that the **deformation of the ground state of ^{72}Kr is dominantly oblate**.

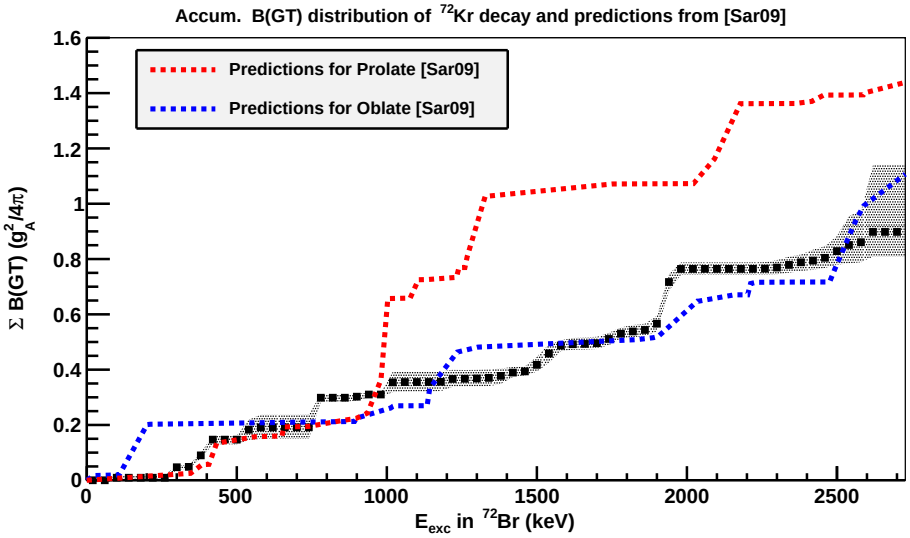

Figure 5.28: *Comparison of experimental accumulated B(GT) distribution for the β^+/EC decay of ^{72}Kr with theoretical predictions from [Sar09] for oblate (blue) and prolate (red) deformations of the ground state of the parent nucleus. The experimental results fits fairly well with the theoretical predictions for the oblate case as expected from information from previous theoretical and experimental works, see chapter 1.*

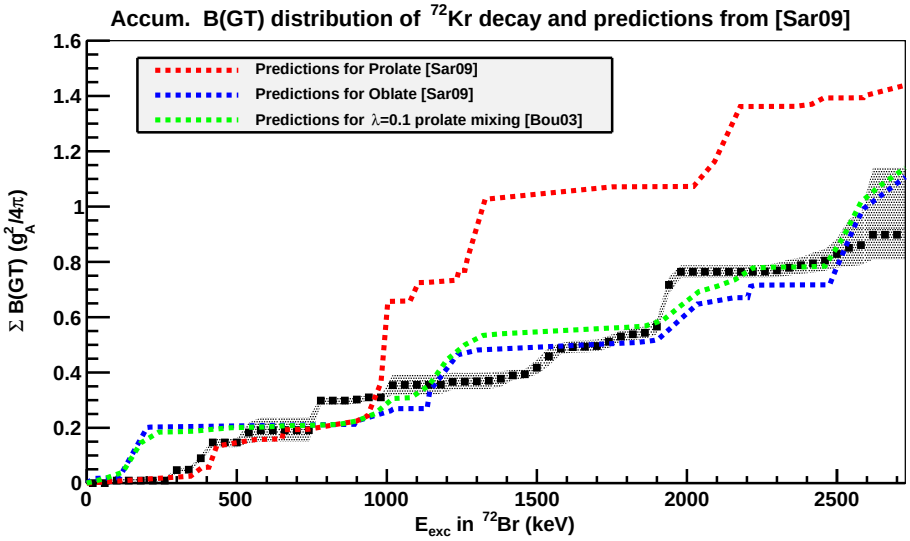

Figure 5.29: *Same as fig. 5.28 but adding the predicted distribution of accumulated B(GT) corresponding to a mixing amplitude of the ground state of 10% with the prolate deformed first excited state, 0^+ state at 671(2) keV of excitation energy, in green as suggested in [Bou03].*

As mentioned in chapter 1, there exists other type of calculations that we can use to compare our experimental B(GT) with. In the work of Petrovici et al. [Pet11] a accumulated B(GT) distribution was published in comparison with the experimental results from the high resolution spectroscopy measurement of Piqueras, as shown in fig. 1.19. The comparison of our results with these predictions is shown in figure 5.30. As can be seen, they underestimate the

total B(GT) found in the present work as they were reasonably similar to the B(GT) distribution reported in [Piq03] that is shown in the next section.

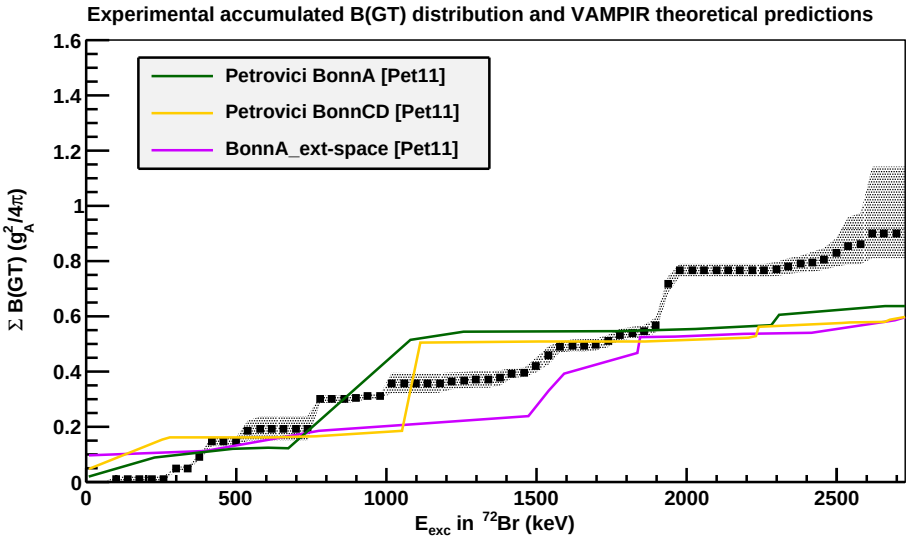

Figure 5.30: *Comparison of experimental accumulated B(GT) distribution for the β^+/EC decay of ^{72}Kr with theoretical predictions from [Pet11] calculated with three different conditions: interaction Bonn A, interaction Bonn CD and interaction Bonn A and using an extended model space as described in section 1.2.3.2. The experimental results fits fairly well with the theoretical predictions for the oblate case as expected from previous information from theoretical and experimental works, see chapter 1.*

5.2.5 Comparison with High Resolution Spectroscopy results

The comparison of the resulting accumulated B(GT) distribution with the one obtained in the Piqueras et al. work [Piq03] is performed and the result is shown in fig. 5.31. The *Pandemonium* effect exhibits in the accumulated B(GT) distribution as the distribution obtained from High Resolution Spectroscopy in [Piq03] overestimates the B(GT) at low excitation energies and it underestimates it at high excitation energies. However, the result from Piqueras agrees fairly well with our distribution up to an excitation energy of approximately 1500 keV and in their work they concluded that they observed all the 1^+ states in the ^{72}Br level scheme up to an excitation energy of 1173.3 keV by comparing with theoretical level densities, see [Piq03].

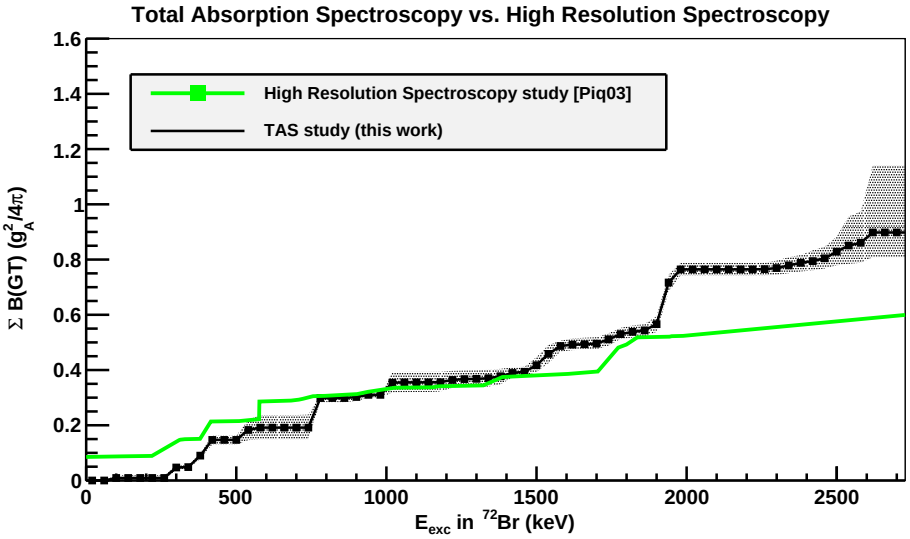

Figure 5.31: *Comparison of experimental accumulated B(GT) distribution for the β^+/EC decay of ^{72}Kr with theoretical predictions from [Pet11] calculated with three different conditions: interaction Bonn A, interaction Bonn CD and interaction Bonn A and using an extended model space as described in section 1.2.3.2. The experimental results fits fairly well with the theoretical predictions for the oblate case as expected from previous information from theoretical and experimental works, see chapter 1.*

5.3 Summary of results

5.3.1 Conversion electrons spectroscopy

The following results have been obtained in the study of conversion coefficients presented here:

- 14 experimental conversion coefficients for low-energy transitions in ^{72}Br not previously known have been measured: 101.3K, 101.3(Tot-K), 124.4K, 124.4(Tot-K), 147.2K doublet, 162.7K, 162.7(Tot-K), 178.5K, 309.9K, 392.7K, 398.4K, doublet (414.5+415.1)K, 559.7K and 576.9K. Additionally, an upper limit for the values of the conversion coefficients of 30.5Tot-K and 38.8K transitions has been established.

- The **spin-parity of the ground state of ^{72}Br can be** assigned with three possible values **(0,1,2)**$^+$. Previous works supported two possibilities, being and 1^+ and 3^+. Works performed by Piqueras et al. [Piq03] and Schmeing et al. [Sch73] assigned an spin-parity of 1^+ based on a direct ground state beta feeding of 34 % and 53.6 % from ^{72}Kr decay, respectively. On the other hand, the study of Collins et al. [Col74] where they assigned a 3^+ based on the direct feeding of 2^+ and 4^+ states in ^{72}Se via the beta decay of ^{72}Br. The feeding that they report is 23.2 % and 20 % to the 2^+ levels at 862 and 1316.7 keV respectively and 5 % to the 4^+ state at 1636.8 keV of excitation energy. The current work rules out the 3^+ keeping the possibility of 1^+ as well as it allows for other two possible values: 0^+ and 2^+.

- The multipolarity of 9 transitions in ^{72}Br have been established: 30.5-keV being an E1, 101.3-keV being an M2, 124.4-keV being an M1(E2), the 147.2-keV transition linking the

310.0-keV and 162.8-keV states to be an M1, 162.7-keV being an M1+E2, 178.5-keV being an M1(E2), 576.9-keV being an M1(E2) transition and the 414.5+415.1 keV doublet where individual transitions have been found to be both of M1 multipolarity.

- The multipolarity of 6 transitions have not been firmly determined but they have been restricted: 38.8-keV could be M1+E2, pure M1 or pure E2, the 147.2-keV transition linking the 545.7-keV and 398.5-keV states to be an M1/M1+E2/E1, 309.9-keV being an M1/M1(E2), 392.7-keV could be an E3 or E3(M2), 398.4-keV could be M2 or M2(E3) and 559.7-keV being an M2/M2(E3).
- The conversion coefficients of the 454.7-keV transition in ^{72}Se and 112-keV transition in ^{76}Br have been measured and their multipolarity have been deduced to be an E2 or E2(M1) for the 454.7-keV transition and M1+E2 the 112-keV one.
- The intensity of two E0 transitions, the 937 keV in ^{72}Se and the 691 keV in ^{72}Ge have been measured and compared to the strongest E2 transition in both de-excitation schemes.

5.3.2 Total Absorption Spectroscopy

The Total Absorption Spectroscopy measurement has provided the following pieces of information:

- the β^+ feeding distribution from the ^{72}Kr beta decay has been determined and the total (β^+/EC) feeding distribution has been deduced from the latter up to an excitation energy of 2640 keV.
- the accumulated B(GT) distribution of the ^{72}Kr β^+/EC decay has been determined up to an excitation energy of 2640 keV. The uncertainty of the distribution includes systematic and statistical components that have been estimated during the analysis.
- the comparison of the accumulated B(GT) distribution with the theoretical predictions from [Sar09] suggest a dominantly oblate deformation for the ^{72}Kr ground state.
- the total amount of B(GT) found up to an excitation energy of 2640 keV has been determined to be: $\sum B(GT)_{free} = 0.90^{+0.24}_{-0.09}$ in units of $(g_A^2/4\pi)$ following the convention given by [BM98].

6 Discussion

6.1 ^{72}Br ground state spin

The spin and parity of the ground state of ^{72}Br was previously debated. On the one hand, 1^+ was suggested as a consequence of a strong beta feeding found to the ground state, 54 % in [Sch73] and 35 % in [Piq03]. These transitions give log(ft) values of 4.5 and 4.66 respectively, indicating strongly the allowed character of the transitions since forbidden start at log(ft)=5 as shown in fig. 1.3. It was understood as allowed 0^+ to 1^+ transition since Fermi decay was not allowed by isospin selection rules, as already explained in section 1.1.1.2. On the other hand, 3^+ was proposed as a result of the beta feeding to 2^+ (23.2 % to the first excited state and 20% to the second) and one 4^+ state (5 % to the 1636.8-keV level) in the decay of ^{72}Br ground state to ^{72}Se [Col74]. These transitions have log(ft) values of 6.7 for the transitions reaching the 2^+ states and 7.1 for the one feeding the 4^+. These log(ft) values could suggest from the systematics in fig. 1.3 two options, either being allowed $\Delta J = 0, 1$ with $\Delta\pi$= no, which is the most probable, or forbidden $\Delta J = 0, 1$ with $\Delta\pi$= yes. The first type is the one linking with the levels in ^{72}Se as no change in parity happens. As 2^+ and 4^+ states are fed, the spin should be 3^+ following the selection rules of allowed Gamow-Teller transitions indicated in table 1.1.

From the present study of conversion coefficients three options for the spin-parity of the ground state of ^{72}Br are allowed, 0^+, 1^+ or 2^+. The Total Absorption Spectroscopy study did not found any feeding to the ground state of ^{72}Br which could indicate that the possibility of being 1^+ is, at least, doubtful.

However, the analysis of the TAS data is not a very conclusive tool when looking at specific feeding to the ground state. If one checks the response of the TAS to feeding to the ground state, shown in blue in fig. 6.1 and feeding to bin 3, which only contains the 101.3-keV isomeric state, in green in the plot, they are almost identical. They only differ slightly in the peak at around 0.5 MeV where the response to ground state feeding can be appreciated behind the response to feeding at bin 3. This is due to the fact that an enormous conversion coefficient was introduced in the analysis on account for two facts: the experimental conversion coefficient of the 101.3-keV transition obtained as a result of the study of chapter 3 (α(101.3)=α_K(101.3)+α_{Tot-K}(101.3)), and another term to reproduce the low probability of detecting the 101.3-keV transition due to the long half-life of the level ($T_{1/2}$=10.6(3) s [Abr10]) in comparison with the length of the coincidence window (2 μs) of the data acquisition system. Apart from that, the response to feeding at a level in bin 8, includes 310.0-keV and 313.8-keV

states, shown in red, despite it is quite different from the others, shows certain probability of contributing to the same channels in the spectra shown as maximum probability in the others responses. This means that a non-negligible part of the feeding to these levels (ground and isomeric states) is masked with all the other feedings. The algorithm is not able to distinguish them and it could locate feeding to other bins instead of to the ground state. For these reasons the TAS analysis is not very sensitive to the feeding to the ground state and one has to rely on the results with caution.

Despite of that, if one relies on the results from the analysis of the TAS data, a feeding of 4(2)% to the 101.3-keV state and no feeding to the ground state. One could assume that this amount of feeding could be located in both levels. However, the multipolarity of the transition connecting these levels, the 101.3-keV transition, was determined to be M2 in the conversion coefficient study. This indicates that a change in parity is required between these two levels and suggests that the feeding is entirely located at one of the levels.

The 4(2) % obtained feeding, if populating the ground state, would provide a log(ft) value of 5.64(22) not been firmly conclusive on the ground state spin since it allows for being a first forbidden transition as well, as can be seen in fig. 1.3. The allowed transition would feed a 1^+ state (since the Fermi transition 0^+ to 0^+ is forbidden from the isospin selection rules, see table 1.1) but a first forbidden could feed a negative-parity state that could be 0^- or 1^-. As obtained from the conversion coefficient study, the possible values were 0^+, 1^+ or 2^+, the possibilities with negative parity are ruled out and it seems to indicate that the most likely possibility for the **ground state spin would be 1^+ with the assumption of the 4(2)% feeding totally located at the ground state**. If such is the case, the **spin parity for the isomeric state would be 3^-** as previously proposed based on the M2 multipolarity of the 101.3-keV connecting with the ground state.

The same argument but considering that the 4(2)% feeding is located at the isomeric state would provide the same possible spins for the isomeric state than the ones mentioned for the ground state due to the parallel situation with a log(ft) value of 5.59(22) in this case. It would provide the following possible spins for the isomeric state: 0^+ (which would be forbidden as the Fermi transitions are) and 1^+ if the transition to the isomeric would be allowed or 0^- and 1^- if it would be first forbidden. The possibility of being 1^+ would require the ground state to be 3^- from the M2 multipolarity of the 101.3-keV transition, which is not any of the possibilities allowed by the conversion coefficient study. The possibility of being 0^- requires the ground state to be 2^+ and the other option, being a 1^- would indicate the ground state to be 3^+, which is also out of the possibilities extracted from the conversion coefficients study. As a conclusion, if the **feeding is located at the isomeric state**, the only possible **spin for the ground state would be 2^+ and for the isomeric state 0^-**. This possibility is quite unlikely since it corresponds to a forbidden transition to the isomeric state and the log(ft) value is more probable to correspond to an allowed transition.

All together gives as a conclusion that the most likely spin for the ^{72}Br ground state would be 1^+, since the log(ft) is more likely to correspond to an allowed transition, or 2^+, a less likely possibility, while rejecting the 0^+ option from isospin selection rules.

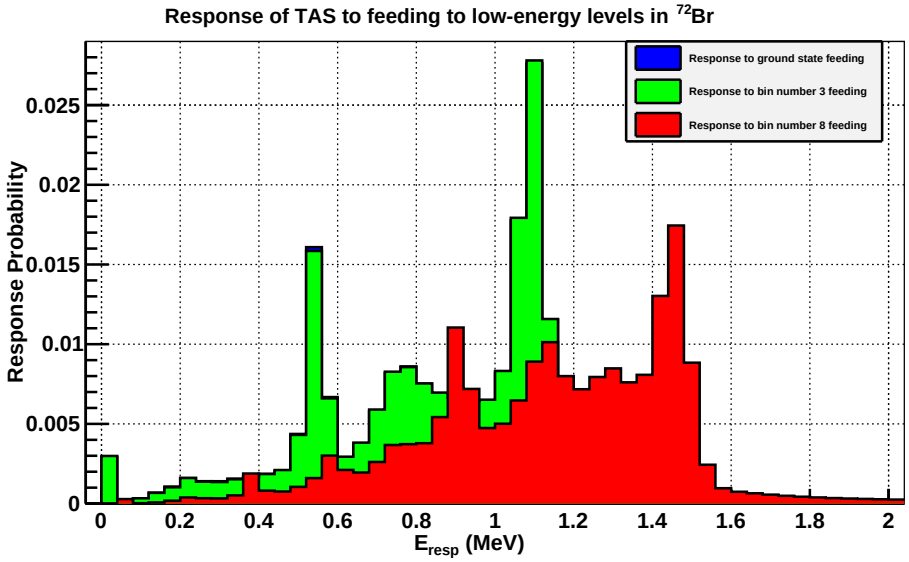

Figure 6.1: *Comparison of Total Absorption Spectrometer responses to feeding at low lying levels in ^{72}Br. The response probability distribution for feeding to the ground state (blue) and to the bin 3, which only contains the 101.3-keV isomeric state (red), are almost identical. They only differ a tiny amount in the peak at 0.5 MeV, where the blue spectrum can be appreciated behind the green one. The response to feeding at bin 8, including 310.0-keV and 313.8-keV states, is also shown in green and it is quite different from the previous ones.*

The calculations that reproduce fairly well the accumulated B(GT) distribution shown in fig. 5.28 can be used to discuss the spin of the ground state of ^{72}Br as well. However, this argument has to be taken carefully, as this calculation is not fully reliable to look at excitation energy of levels, levels spin and parities and this type of information for being a mean field calculation instead a shell model. But as a suggestion they can be used. For the case of oblate deformation, the calculations provide that the ground state could be either 0^+ or 1^+ as both states are located at exactly the same excitation energy. The Gallagher-Moszkowski Rules for coupling of angular momenta [Gal58] favour the ground state to be 1^+. One conclusive idea from these calculations is that they seem to rule out the possibility of 2^+ as the first 2^+ state is located at more than 400 keV above these states, and that both possibilities, 0^+ and 1^+ are more likely with slight preference for 1^+.

6.2 Deformation of ^{72}Kr

The importance of the deformation of ^{72}Kr was already mentioned in chapter 1. It is a rare case where coexisting oblate ground state and low-lying prolate deformed excited states are predicted [Mö09] and experimental information support this idea [Bou03, Cle11]. However, no experimental evidence for the oblate deformation of the ground state has been reported yet. The work by A. Gade et al. [Gad05, Gad06] reported a value for the deformation parameter which agrees with theoretical calculations predicting oblate deformation for the ground state. Despite of this achievement, no direct observation of the sign of this deformation has been reported yet.

This study through Total Absorption Spectroscopy offers an experimental way of finding out information on the sign of the deformation of the ground states, which is a difficult quan-

tity to be experimentally determined. Despite being a model-dependent study, it provides us with a reliable accumulated B(GT) distribution that can be compared with theoretical predictions. These predictions have shown quite different behaviours for different deformations of the ground state of the parent nucleus. In this case, a dominantly oblate deformation for the ^{72}Kr was determined. As seen in fig. 5.29, the accumulated B(GT) distribution found in this study is quite similar to the predictions for both, a pure oblate deformation of the ground state and with the distribution shown in green in that comparison to guide the eye that would correspond to a mixing ratio of 0.1 with the prolate low-lying 0^+ state at 671(2) keV of excitation energy as proposed in [Bou03].

These calculations are obtained by using the QRPA formalism including the SLy4 skyrme type force as given in [Sar09]. The absolute energy minimum is calculated to happen at a deformation parameter of β_2=-0.1759. The approximate picture of the ^{72}Kr ground state with this deformation parameter is shown in fig. 6.2. This quadrupole deformation parameter is sensitively lower than the proposed by W. Nazarewicz calculations in [Naz85], β_2=-0.31, or the P. Möller et al. predictions in [Mö95] where β_2=-0.349 was reported. However, the value from more recent theoretical predictions from P. Möller and colleagues in [Mö09] suggested a lower value of ε_2=0.28 which is approximately β_2=0.22, a value closer to the predictions of QRPA calculations.

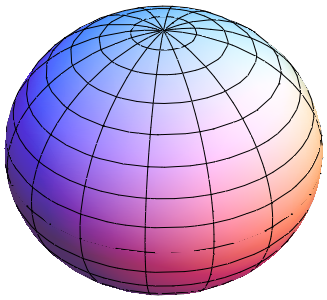

Figure 6.2: *Nuclear shape of ^{72}Kr ground state calculated for a quadrupole deformation parameter of β_2=-0.1759 as reported by P. Sarriguren [Sar09]. This value corresponds to the oblate deformed local minimum obtained using the SLy4 force whose theoretical accumulated B(GT) associated matches with the experimentally obtained as shown in fig. 5.28.*

The experimental work of A. Gade et al. [Gad05] reports a B(E2; $0_1^+ \rightarrow 2_1^+$)=4997(647) e^2fm^4 which suggests a deformation parameter β_2=0.330(21). This value has to be taken carefully as an erratum publication of the latter paper [Gad06] was published indicating a possible source of additional systematic error in that measurement due to a possible contamination of the beam with ^{72}Kr in form of its 0^+ isomer state.

Another technique that allows to study the deformation of nuclei is by means of the orientation effect, which could provide information to help to determine the sign of the spectroscopic quadrupole moment of the excited states. This method has been used in a recently performed experiment, IS478 [SBNS], carried out at ISOLDE (CERN). I was also involved in

the data-taking of the experiment and the data is currently under analysis. The experiment is expected to provide information on the sign of the quadrupole moment of the first 2^+ state, which is fed by Coulomb excitation of ^{72}Kr isotopes. The accelerated ^{72}Kr at REX-ISOLDE post-accelerator of ISOLDE up to E≈3.1 MeV/u impinged a 2 mg/cm^2 ^{104}Pd target producing the excitation of ^{72}Kr ground state up to the first 2^+ state located at 710 keV of excitation energy. These two states (ground and first 2^+ states) belong to the ground state band which is considered to be mainly oblate [Naz85, Mö95, Mö09, Cle11]. This method will provide the sign of the quadrupole moment of the 2_1^+ state and will report the sign of the deformation of the ^{72}Kr ground state in a non-model dependent manner.

6.3 Microscopic configuration of ^{72}Kr ground state

The self-consistent Hartree-Fock QRPA calculations presented in chapter 1 whose predicted B(GT) distribution for the ^{72}Kr beta decay has been compared to the experimentally found in this work. The comparison has shown good agreement for the oblate deformed case of the ^{72}Kr ground state. These calculations includes several ingredients complicating the microscopic scenario as pairing correlations in BCS approximation for like nucleons (pp and nn)and later solving the Quasi-particle Random Phase Approximation (QRPA) equations.

However, one can have a look at the single particle levels obtained as the solution of the Hartree-Fock equation before facing these complications to have an idea of the microscopic picture of ^{72}Kr in its ground state. Thus, table 6.1 gives the single particle levels and their occupations for neutrons and protons for the calculation performed for the oblate case of ^{72}Kr. Fig. 6.3 shows the same data plotted with the Fermi levels for neutrons and protons indicated. They are located at -13.274 MeV for neutrons and at -2.6483 MeV for protons. All these data is courtesy of P. Sarriguren.

After these occupation probabilities are obtained for every shell, the residual interactions are added to the calculation and the QRPA equations are solved, the situation gets more complex at microscopic level. As an example, the feeding to the ^{72}Br ground state is predicted and understood as the transformation of a neutron in the 5^{th} $1/2^-$ shell in the table 6.1, which is the level located at approximately the Fermi level of neutrons shown in fig. 6.3, to the same shell in protons (5^th $1/2^-$ shell).

	Neutrons		Protons	
Single particle Level	$E_{s.p.}$ (MeV)	Occupation probability	$E_{s.p.}$ (MeV)	Occupation probability
$1/2^+$	-54.7224	0.999673	-42.2986	0.999643
$3/2^-$	-44.3298	0.999418	-32.5103	0.999370
$1/2^-$	-43.5724	0.999388	-31.7640	0.999338
$1/2^-$	-40.3961	0.999237	-28.6373	0.999169
$5/2^+$	-33.4882	0.998629	-22.1576	0.998529
$3/2^+$	-32.2599	0.998447	-20.9474	0.998329
$1/2^+$	-31.7624	0.998362	-20.4110	0.998227
$3/2^+$	-28.2127	0.997498	-16.9998	0.997291
$1/2^+$	-28.0891	0.997457	-16.7756	0.997205
$1/2^+$	-24.3248	0.995456	-13.1189	0.994947
$7/2^-$	-22.5778	0.993625	-11.6704	0.993230
$5/2^-$	-21.2268	0.991336	-10.3477	0.990773
$3/2^-$	-20.4991	0.989560	-9.60183	0.988758
$1/2^-$	-20.0518	0.988187	-9.15291	0.987213
$3/2^-$	-16.4736	0.952714	-5.62786	0.946601
$5/2^-$	-15.4697	0.912840	-4.76390	0.907883
$1/2^-$	-15.2990	0.901762	-4.51787	0.889996
$1/2^-$	-13.1817	0.469196	-2.48904	0.447226
$3/2^-$	-12.6845	0.317035	-2.06412	0.318561
$9/2^+$	-11.7998	0.149493	-1.26985	0.161685
$7/2^+$	-10.4606	0.0587839	0.0295639	0.0637764
$5/2^+$	-9.62257	0.0374989	0.858808	0.0402840
$1/2^-$	-9.58472	0.0368160	0.916081	0.0391466
$3/2^+$	-9.02510	0.0285152	1.44767	0.0304938
$1/2^+$	-8.71255	0.0250197	1.75496	0.0267090
$5/2^+$	-5.99461	0.0102881	4.25220	0.0114104
$1/2^+$	-4.63693	0.00737349	5.43998	0.00838273
$3/2^+$	-4.26534	0.00678985	5.80361	0.00769314
$7/2^+$	-3.24903	0.00550447	6.89540	0.00606368
$3/2^+$	-2.66891	0.00492737	7.29763	0.00559118
$1/2^+$	-2.11032	0.00445303	7.79820	0.00507612
$11/2^-$	-1.28806	0.00386986	8.81843	0.00422393
$5/2^+$	-1.16203	0.00379065	8.85976	0.00419402
$9/2^-$	-0.0345380	0.00317840	10.0136	0.00347206
$1/2^+$	0.325397	0.00301388	10.0440	0.00345561
$7/2^-$	0.876936	0.00278545	10.7273	0.00311478
$3/2^+$	0.889718	0.00278047	10.8093	0.00307728
$5/2^-$	1.48868	0.00256112	11.3463	0.00284761
$3/2^-$	1.92044	0.00241868	11.6241	0.00273876
$1/2^-$	2.12801	0.00235438	11.7834	0.00267909
$1/2^+$	2.72232	0.00218381	12.2387	0.00251896
$7/2^-$	3.48395	0.00199098	12.6671	0.00238098
$3/2^-$	4.20579	0.00183083	12.8149	0.00233602

Table 6.1: *Single particle levels for neutrons and protons obtained via the constrained deformed Hartree-Fock calculation used in [Sar09] and whose B(GT) distribution matches fairly well with the one experimentally determined in this work. The occupation of each level is indicated. The Fermi level for neutrons is obtained at E_n=-13.274 MeV while for protons is located at E_p=-2.3483 MeV. These data is courtesy of P. Sarriguren and is plotted in fig. 6.3.*

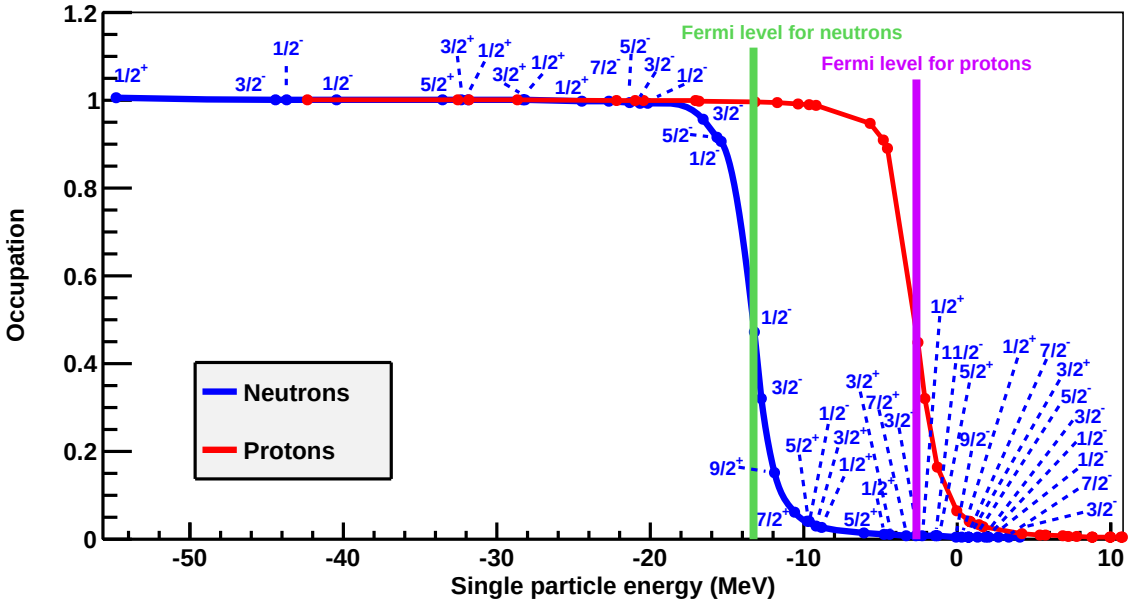

Figure 6.3: *Occupation of single particle levels as given by P. Sarriguren from the theoretical calculations reported in [Sar09] for an oblate deformation of the ^{72}Kr ground state. The data plotted is the one given in table 6.1 for both, neutrons and protons. Only neutrons single particle levels are indicated to not complicated the plot. The order of single particle levels for protons is the same as the given for neutrons. The Fermi levels for neutrons and protons are indicated. Data represented here and listed in table 6.1 is courtesy of P. Sarriguren.*

7 Conclusions

^{72}Kr is an N=Z nucleus located in the mass region A≈70-80 where strong shape transitions occurs and the shape coexistence phenomenon happens. Additionally, it participates in the rp-process with a role of waiting point slowing down the process as the next nucleus in the proton capture chain is unbound. All these reasons make the study of this nucleus very attractive for the experimentalist.

The β^+/EC decay of ^{72}Kr has been investigated through two complementary experiments at the ISOLDE facility, in the accelerator complex of CERN. On the one hand, the low-spin structure of the daughter nucleus, ^{72}Br, has been revisited through conversion electron spectroscopy where the conversion coefficients of the low-energy transitions has been determined. These coefficients allow for the determination of the transition multipolarities by comparison with theoretical predictions. As a consequence, the spin and parity of the low-lying levels in ^{72}Br has been discussed and either defined or restricted to certain values fulfilling the selection rules of gamma de-excitation. Additionally, the intensity of two E0 transitions were measured in comparison with the strongest E2 transition in the de-excitation schemes of ^{72}Se and ^{72}Ge.

On the other hand, the Total Absorption Spectroscopy technique was used in order to measure the beta feeding distribution in the decay of interest. This study was encouraged by the possibility to deduce information on the shape of the ground state of the parent nucleus of the decay by comparing the experimental B(GT) distribution with theoretical predictions. QRPA calculations were already employed to compare with neighbouring nuclei providing successful results, as ^{76}Sr, ^{74}Kr or ^{78}Sr and have been used in this work as well. The β^+ component of the β decay of ^{72}Kr was studied and the β^+ feeding distribution determined in a 40-keV bin width basis. From this, the total feeding distribution, meaning the β^+ plus EC feeding distributions, was determined by using the tabulated EC/β^+ ratio and then the B(GT) was calculated in a accumulated way. The comparison with the theoretical predictions suggests the ground state of ^{72}Kr to be dominantly oblate as previously predicted.

The main results which have been extracted from this work are the following:

- 14 experimental conversion coefficients for low-energy transitions in ^{72}Br not previously known have been measured: 101.3K, 101.3(Tot-K), 124.4K, 124.4(Tot-K), 147.2K doublet, 162.7K, 162.7(Tot-K), 178.5K, 309.9K, 392.7K, 398.4K, doublet (414.5+415.1)K, 559.7K and 576.9K. Additionally, an upper limit for the values of the conversion coefficients of 30.5Tot-K and 38.8K transitions has been established.

- The **spin-parity of the ground state of ^{72}Br have been restricted to** three possible values **(0,1,2)$^+$**. The most likely but not exclusive, spin-parity according to our discussion would be 1^+.

  The current work rules out the previously suggested value of 3^+.

- The multipolarity of 9 transitions in ^{72}Br have been established: 30.5-keV being an E1, 101.3-keV being an M2, 124.4-keV being an M1(E2), the 147.2-keV transition linking the 310.0-keV and 162.8-keV states to be an M1, 162.7-keV being an M1+E2, 178.5-keV being an M1(E2), 576.9-keV being an M1(E2) transition and the 414.5+415.1 keV doublet where individual transitions have been found to be both of M1 multipolarity.

- The multipolarity of 6 transitions have not been firmly determined but they have been restricted: 38.8-keV could be M1+E2, pure M1 or pure E2, the 147.2-keV transition linking the 545.7-keV and 398.5-keV states to be an M1/M1+E2/E1, 309.9-keV being an M1/M1(E2), 392.7-keV could be an E3 or E3(M2), 398.4-keV could be M2 or M2(E3) and 559.7-keV being an M2/M2(E3).

- The conversion coefficients of the 454.7-keV transition in ^{72}Se and 112-keV transition in ^{76}Br have been measured and their multipolarity have been deduced to be an E2 or E2(M1) for the 454.7-keV transition and M1+E2 the 112-keV one.

- The intensity of two E0 transitions, the 937 keV in ^{72}Se and the 691 keV in ^{72}Ge have been measured and compared to the strongest E2 transition in both de-excitation schemes.

- The β^+ feeding distribution from the ^{72}Kr beta decay has been determined and the total (β^+/EC) feeding distribution has been deduced from the latter up to an excitation energy of 2640 keV.

- The accumulated B(GT) distribution of the ^{72}Kr β^+/EC decay has been determined up to an excitation energy of 2640 keV. The uncertainty of the distribution includes systematic and statistical components that have been estimated during the analysis.

- The comparison of the accumulated B(GT) distribution with the theoretical predictions suggest a dominantly oblate deformation for the ^{72}Kr ground state.

- the total amount of B(GT) found up to an excitation energy of 2640 keV has been determined to be: $\sum B(GT)_{free} = 0.90^{+0.24}_{-0.09}$ in units of $(g_A^2/4\pi)$.

Appendices

Appendix A: Mixing ratio δ

For a given γ transition, the selection rules can allow several multipolar components, when the allowed component of lower order is of electric character, this one prevails over the rest. But in the opposite case, when the allowed component of lower order is magnetic both components can compete in terms of transition probability. One defines the mixing ratio δ as the ratio of absolute gamma transition amplitudes of both components. A more practical parameter is the squared of the mixing ratio δ^2, which is the ratio between both gamma transition probabilities that mathematically is expressed as follows:

$$\delta(X\lambda/X'\lambda')^2 = \frac{I_\gamma^{X\lambda}}{I_\gamma^{X'\lambda'}} \tag{A.1}$$

where X can be E (electric) or M (magnetic) and λ is the order of the multipolarity. Thus, Xλ and X$'\lambda'$ name both components.

The following expression for the total gamma intensity, I_γ, is fullfilled:

$$I_\gamma = I_\gamma^{X\lambda} + I_\gamma^{X'\lambda'} \tag{A.2}$$

where $0 \leq \delta^2 \leq \infty$.

For a practical case, when Xλ=M1 and X$'\lambda'$=E2 one can extract both transition intensities through the expression:

$$I_\gamma^{M1} = \frac{1}{1+\delta^2} I_\gamma \tag{A.3}$$

$$I_\gamma^{E2} = \frac{\delta^2}{1+\delta^2} I_\gamma \tag{A.4}$$

The total transition intensity, I_T, when the conversion electron process is relevant, can be expressed as:

$$I_T = I_\gamma^{M1}(1+\alpha_T^{M1}) + I_\gamma^{E2}(1+\alpha_T^{E2}) = I_\gamma \frac{1}{1+\delta^2}(1+\alpha_T^{M1}) + I_\gamma \frac{\delta^2}{1+\delta^2}(1+\alpha_T^{E2}) =$$
$$I_\gamma(1 + \frac{1}{1+\delta^2}\alpha_T^{M1} + \frac{\delta^2}{1+\delta^2}\alpha_T^{E2}) = I_\gamma(1+\alpha_T)$$

where has been defined:

$$\alpha_T = \frac{1}{1+\delta^2}\alpha_T^{M1} + \frac{\delta^2}{1+\delta^2}\alpha_T^{E2} \tag{A.5}$$

One can try to work out the value of δ^2:

$$\delta^2 = \frac{\alpha_T - \alpha_T^{M1}}{\alpha_T^{E2} - \alpha_T} \tag{A.6}$$

or equivalently for a given shell component of the coefficient, for example K:

$$\delta^2 = \frac{\alpha_K - \alpha_K^{M1}}{\alpha_K^{E2} - \alpha_K} \tag{A.7}$$

The expression A.7 will be useful to obtain the values of δ given in the table of results 3.34 of the chapter 3 as from that work one obtains the experimental values of the conversion coefficients α_K or α_{Tot-K} and the theoretical values for the multipolarities is extracted from ref. [ANU].

Appendix B: Gamma transition intensities

In the next tables the experimental intensities for the gamma transitions in the de-excitation of the daughter nucleus, ^{72}Br are given for the measurement of the IS370-A experiment, devoted to study the conversion coefficients of low-energy transitions. They are compared to the intensities from the β-decay study of the ^{72}Kr performed in Ref. [Piq03] and the difference between them is shown in the last column.

The intensities from this work are fairly compatible with the reported values in Ref. [Piq03]. The bigger deviations are found for:

- the 101.3 keV transition, which is an isomer decay whose observed intensity depends on the measuring cycle,

- the high energy transitions ($E_\gamma > 1000$ keV), where the efficiency calibration was not so reliable as at lower energies and these deviations could be due to this.

- doublet transitions with transitions from different decays, e.g. 379.8, 560.1 and 775.7 keV transitions from ^{72}Br and ^{72}Se de-excitations, where the amount of intensity coming from the de-excitation of the other nucleus than ^{72}Br are not added as it depends on the cycling periods of collection and measurement.

	Experimental values		Reference values [Piq03]		
Nuclide	E_γ (keV)	$I_\gamma(^{72}Br)$	E_γ (keV)	I_γ ^{72}Br (%)	ΔI_γ (%)
^{72}Br	30.4387 (3)	0.89	30.5(5)	0.12 (12)	0.77
^{72}Br	38.3959 (7)	0.34	38.8(2)	0.47 (11)	-0.13
Pb X-rays + ^{72}Br	87.3538 (3)	1.13	87.3 + 87.2(5)	0.83 (12)	0.30
^{72}Br	101.236 (1)	7.04	101.3(3)	2.4 (3)	4.64
^{72}Br	105.118 (7)	0.48	105.3(1)	0.49 (4)	-0.01
^{72}Br	124.409 (1)	3.57	124.4(2)	4.9 (5)	-1.33
^{72}Br	147.475 (8)	0.64	147.2(1)	0.64 (9)	0.00
^{72}Br	162.788 (1)	9.00	162.7(1)	10.8 (10)	-1.80
^{72}Br	178.607 (3)	2.18	178.5(5)	2.52 (21)	-0.34
^{72}Br	196.446 (14)	0.46	196.2(5)	0.36 (12)	0.10
^{72}Br	209.054 (11)	0.65	208.9(3)	0.66 (5)	-0.01
^{72}Br	230.493 (13)	0.60	230.1(3)	0.37 (3)	0.23
^{72}Br	235.815 (16)	0.47	235.5(4)	0.51 (4)	-0.04
^{72}Br	252.659 (4)	2.40	252.4(2)	2.43 (10)	-0.03
^{72}Br	255.207 (42)	0.20	254.9(5)	0.193 (15)	0.00
^{72}Br	266.031 (20)	0.50	265.7(2)	0.086 (22)	0.41
^{72}Br	274.601 (46)	0.17	274.2(3)	0.19 (12)	-0.02
^{72}Br	283.781 (13)	0.77	283.4(4)	0.74 (3)	0.03
^{72}Br	310.323 (1)	15.70	309.9(1)	15.7 (5)	0.00
^{72}Br	314.251 (18)	0.59	313.8(3)	0.567 (22)	0.03
^{72}Br	328.885 (10)	1.23	328.4(2)	1.19 (5)	0.04
^{72}Br+^{72}Se	379.845 (5)	4.07	379.3(5)	0.84 (16)	3.23
^{72}Br	381.366 (23)	0.40	380.8(2)	0.61 (3)	-0.21
^{72}Br	393.197 (23)	0.55	392.7(2)	0.59 (3)	-0.04
^{72}Br	399.004 (21)	0.61	398.4(2)	0.57 (3)	0.04
^{72}Br	414.827 (142)	3.21	414.5(5)	6.4 (6)	-3.19
^{72}Br	415.558 (18)	16.24	415.1(2)	13.2 (9)	3.04
^{72}Br	453.238 (50)	1.37	452.3(3)	0.73 (3)	0.64
^{72}Br	485.949 (38)	0.84	485.9(5)	0.443 (17)	0.40
^{72}Br+^{72}Se	560.14 (10)	3.50	559.7(4) + 559.3(3)	0.473 (22)	3.02
^{72}Br	577.283 (4)	7.25	576.9(4)	6.3 (3)	0.95
^{72}Br+^{72}Ge	630.745 (21)	1.04	629.8(5) + 629.92(5)	0.133 (9)	0.91
^{72}Br?	756.709 (24)	0.96	755.5(4)	1.15 (8)	-0.19
^{72}Br+^{72}Se	775.726 (5)	7.78	774.5(8)+774.8(3)	0.079 (16)	7.70
^{72}Br	902.814 (45)	0.60	901.9(5)	0.74 (8)	-0.14
^{72}Br?	956.082 (43)	0.90	954.6(5)	0.15 (3)	0.75
^{72}Br?	977.827 (25)	1.88	976.6(5)	0.69 (3)	1.19
^{72}Br?	1056.29 (10)	3.17	1058.0(5)	0.3 (4)	2.87

Table B.1: *List of gamma transitions identified to belong to the ^{72}Kr decay scheme in the measurement with the miniorange configuration 85/8/4B used to obtained the conversion coefficients. The gamma intensities are calculated and referred to the most intense one, the 415.1 keV transition. The intensities are compared to the reference values in Ref. [Abr10] which come from the work of I. Piqueras et al. [Piq03].*

	Experimental values		Reference values [Piq03]		
Nuclide	E_γ (keV)	$I_\gamma(^{72}Br)$	E_γ (keV)	I_γ ^{72}Br (%)	ΔI_γ (%)
^{72}Br	30.474 (23)	0.86	30.5(5)	0.12 (12)	0.74
^{72}Br	38.485 (49)	0.36	38.8(2)	0.47 (11)	-0.11
Pb X-rays + ^{72}Br	87.326 (4)	9.39	87.3 + 87.2(5)	0.83 (12)	8.56
^{72}Br	101.149 (7)	3.52	101.3(3)	2.40 (3)	1.12
^{72}Br	124.301 (10)	3.29	124.4(2)	4.90 (5)	-1.61
^{72}Br	162.637 (5)	8.44	162.7(1)	10.80 (10)	-2.36
^{72}Br	178.436 (22)	2.39	178.5(5)	2.52 (21)	-0.13
^{72}Br	252.195 (14)	5.88	252.4(2)	2.43 (10)	3.45
^{72}Br	310.007 (5)	15.70	309.9(1)	15.70 (5)	0.00
^{72}Br	328.445 (78)	1.81	328.4(2)	1.19 (5)	0.62
^{72}Br+^{72}Se	379.497 (46)	1.75	379.3(5)	0.84 (16)	0.91
^{72}Br	415.073 (6)	18.16	414.5(5) + 415.1(2)	19.40 (15)	-1.24
^{72}Br	451.941 (14)	8.39	452.3(3)	0.73 (3)	7.66
^{72}Br+^{72}Se	559.215 (1)	165.69	559.7(4) + 559.3(3)	0.47 (22)	165.21
^{72}Br	576.785 (85)	6.82	576.9(4)	6.30 (3)	0.52
^{72}Br	575.502 (240)	2.16	575.8(4)	1.15 (13)	1.01
^{72}Br+^{72}Ge	630.137 (6)	29.21	629.8(5) + 629.92(5)	0.13 (9)	29.08
^{72}Br	681.644 (90)	1.85	682.5(5)	0.31 (22)	1.53
^{72}Br	755.594 (119)	1.00	755.5(4)	1.15 (8)	-0.15
^{72}Br+^{72}Se	774.947 (42)	3.19	774.5(8)+774.8(3)	0.08 (16)	3.11
^{72}Br	901.423 (95)	1.06	901.9(5)	0.74 (8)	0.32
^{72}Br	976.984 (143)	0.74	976.6(5)	0.69 (3)	0.05
^{72}Br	1029.923 (82)	3.52	1029.0(2)	0.20 (11)	3.32
^{72}Br	1050.921 (32)	6.59	1049.9(6)	0.57 (4)	6.02

Table B.2: *List of gamma transitions identified to belong to the ^{72}Kr decay scheme in the measurement with the miniorange configuration 125/8/3B used to obtained the conversion coefficients. The gamma intensities are calculated and referred to the most intense one, the 415.1 keV transition. The intensities are compared to the reference values in Ref. [Abr10] which come from the work of I. Piqueras et al. [Piq03].*

	Experimental values		Reference values [Piq03]		
Nuclide	E_γ (keV)	$I_\gamma(^{72}Br)$	E_γ (keV)	I_γ ^{72}Br (%)	ΔI_γ (%)
^{72}Br	30.443 (6)	0.97	30.5(5)	0.12 (12)	0.85
^{72}Br	38.413 (15)	0.37	38.8(2)	0.47 (11)	-0.10
Pb X-rays + ^{72}Br	87.393 (4)	2.53	87.3 + 87.2(5)	0.83 (12)	1.70
^{72}Br	101.242 (2)	4.99	101.3(3)	2.4 (3)	2.59
^{72}Br	105.132 (17)	0.46	105.3(1)	0.49 (4)	-0.03
^{72}Br	124.404 (3)	3.61	124.4(2)	4.9 (5)	-1.29
^{72}Br	147.451 (17)	0.61	147.2(1)	0.64 (9)	-0.03
^{72}Br	162.780 (2)	9.04	162.7(1)	10.8 (10)	-1.76
^{72}Br	178.581 (7)	2.19	178.5(5)	2.52 (21)	-0.33
^{72}Br	196.452 (33)	0.46	196.2(5)	0.36 (12)	0.10
^{72}Br	209.035 (23)	0.57	208.9(3)	0.66 (5)	-0.09
^{72}Br	230.420 (40)	0.62	230.1(3)	0.37 (3)	0.25
^{72}Br	235.759 (49)	0.46	235.5(4)	0.51 (4)	-0.05
^{72}Br	252.613 (8)	2.50	252.4(2)	2.43 (10)	0.07
^{72}Br	266.045 (56)	0.68	265.7(2)	0.086 (22)	0.60
^{72}Br	283.751 (28)	0.69	283.4(4)	0.74 (3)	-0.05
^{72}Br	310.259 (2)	15.70	309.9(1)	15.7 (5)	0.00
^{72}Br	314.138 (36)	0.65	313.8(3)	0.567 (22)	0.08
^{72}Br	328.807 (21)	1.19	328.4(2)	1.19 (5)	0.00
^{72}Br+^{72}Se	379.745 (12)	3.25	379.3(5)	0.84 (16)	2.41
^{72}Br	381.238 (52)	0.47	380.8(2)	0.61 (3)	-0.14
^{72}Br	393.071 (39)	0.49	392.7(2)	0.59 (3)	-0.10
^{72}Br	398.868 (43)	0.64	398.4(2)	0.57 (3)	0.07
^{72}Br	415.486 (17)	14.05	415.1(2)	13.2 (9)	0.85
^{72}Br	414.989 (166)	5.63	414.5(5)	6.4 (6)	-0.77
^{72}Br	453.001 (105)	1.22	452.3(3)	0.73 (3)	0.49
^{72}Br	485.756 (83)	0.83	485.9(5)	0.443 (17)	0.39
^{72}Br+^{72}Se	559.994 (16)	2.52	559.7(4) + 559.3(3)	0.473 (22)	2.05
^{72}Br	577.149 (7)	7.26	576.9(4)	6.3 (3)	0.96
^{72}Br+^{72}Ge	630.630 (4)	15.82	629.8(5) + 629.92(5)	0.133 (9)	15.69
^{72}Br	756.535 (45)	1.08	755.5(4)	1.15 (8)	-0.07
^{72}Br+^{72}Se	775.612 (11)	5.57	774.5(8)+774.8(3)	0.079 (16)	5.50
^{72}Br	902.592 (87)	0.70	901.9(5)	0.74 (8)	-0.04
^{72}Br	977.685 (51)	1.62	976.6(5)	0.69 (3)	0.93

Table B.3: *List of gamma transitions identified to belong to the ^{72}Kr decay scheme in the measurement with the miniorange configuration 110/8/6A used to obtained the conversion coefficients. The gamma intensities are calculated and referred to the most intense one, the 415.1 keV transition. The intensities are compared to the reference values in Ref. [Abr10] which come from the work of I. Piqueras et al. [Piq03].*

	Experimental values		Reference values [Piq03]		
Nuclide	E_γ (keV)	$I_\gamma(^{72}Br)$	E_γ (keV)	I_γ ^{72}Br (%)	ΔI_γ (%)
^{72}Br	30.443 (6)	0.84	30.5(5)	0.12 (12)	0.72
^{72}Br	38.360 (22)	0.32	38.8(2)	0.47 (11)	-0.15
Pb X-rays + ^{72}Br	87.382 (5)	3.16	87.3 + 87.2(5)	0.83 (12)	2.33
^{72}Br	101.214 (3)	4.24	101.3(3)	2.4 (3)	1.84
^{72}Br	105.106 (30)	0.45	105.3(1)	0.49 (4)	-0.04
^{72}Br	124.379 (5)	3.53	124.4(2)	4.9 (5)	-1.37
^{72}Br	147.443 (27)	0.60	147.2(1)	0.64 (9)	-0.04
^{72}Br	162.734 (3)	8.80	162.7(1)	10.8 (10)	-2.00
^{72}Br	178.551 (12)	2.11	178.5(5)	2.52 (21)	-0.41
^{72}Br	196.409 (48)	0.53	196.2(5)	0.36 (12)	0.17
^{72}Br	208.963 (31)	0.61	208.9(3)	0.66 (5)	-0.05
^{72}Br	230.389 (59)	0.52	230.1(3)	0.37 (3)	0.15
^{72}Br	235.842 (66)	0.75	235.5(4)	0.51 (4)	0.24
^{72}Br	252.539 (13)	2.36	252.4(2)	2.43 (10)	-0.07
^{72}Br	265.997 (90)	0.62	265.7(2)	0.086 (22)	0.53
^{72}Br	283.643 (53)	0.69	283.4(4)	0.74 (3)	-0.05
^{72}Br	310.192 (3)	15.70	309.9(1)	15.7 (5)	0.00
^{72}Br	314.139 (67)	0.58	313.8(3)	0.567 (22)	0.01
^{72}Br	328.711 (34)	1.25	328.4(2)	1.19 (5)	0.06
^{72}Br+^{72}Se	379.626 (23)	2.83	379.3(5)	0.84 (16)	1.99
^{72}Br	381.109 (115)	0.44	380.8(2)	0.61 (3)	-0.17
^{72}Br	393.063 (67)	0.50	392.7(2)	0.59 (3)	-0.09
^{72}Br	398.723 (64)	0.69	398.4(2)	0.57 (3)	0.12
^{72}Br	414.952 (183)	6.53	414.5(5)	6.4 (6)	0.13
^{72}Br	415.411 (31)	12.49	415.1(2)	13.2 (9)	-0.71
^{72}Br	452.770 (69)	0.66	452.3(3)	0.73 (3)	-0.07
^{72}Br	485.656 (116)	1.07	485.9(5)	0.443 (17)	0.63
^{72}Br+^{72}Se	559.910 (31)	2.24	559.7(4) + 559.3(3)	0.473 (22)	1.77
^{72}Br	577.036 (11)	7.02	576.9(4)	6.3 (3)	0.72
^{72}Br+^{72}Ge	630.493 (5)	21.58	629.8(5) + 629.92(5)	0.133 (9)	21.45
^{72}Br	756.201 (66)	1.15	755.5(4)	1.15 (8)	0.00
^{72}Br+^{72}Se	775.424 (20)	4.41	774.5(8)+774.8(3)	0.079 (16)	4.33
^{72}Br	902.373 (119)	0.70	901.9(5)	0.74 (8)	-0.04
^{72}Br	955.545 (175)	0.81	954.6(5)	0.15 (3)	0.66
^{72}Br	977.453 (91)	1.23	976.6(5)	0.69 (3)	0.54

Table B.4: *List of gamma transitions identified to belong to the ^{72}Kr decay scheme in the measurement with the miniorange configuration 125/8/6A used to obtained the conversion coefficients. The gamma intensities are calculated and referred to the most intense one, the 415.1 keV transition. The intensities are compared to the reference values in Ref. [Abr10] which come from the work of I. Piqueras et al. [Piq03].*

C

Appendix C: Summary

The study here presented is devoted to the study of the deformation shown by the ^{72}Kr in the ground state by means of beta decay studies.

C.1 Introduction

Previous studies in the same mass region than ^{72}Kr of the nuclide chart were carried out to determine the deformation of ^{76}Sr [Ná04b], ^{74}Kr [Poi04] and ^{78}Sr [Pé13]. They provided successful information on the deformation of these nuclei as shown in fig. D.1 for the case of ^{76}Sr as an example.

This work pretends to employ the same technique in the determination of the deformation of the N=Z nucleus ^{72}Kr, nucleus of remarkable importance in both, the nuclear structure domain and in astrophysical scenarios. From the nuclear structure point of view, ^{72}Kr is relevant for being located in a mass region where strong shape transitions are predicted and shape coexistence phenomenon occurs [Mö95, Ham74, Var87]. The latter consists of the presence of states with different deformations, prolate-spherical-oblate, of the nucleus at close excitation energies. This phenomenon was predicted to occur in ^{72}Kr as shown in fig. D.2 which has been taken from [Mö09]. Additionally, ^{72}Kr is interesting as well because is one of the rare cases where oblate deformed ground state is predicted with low-lying prolate deformed excited states. Thus, the existence of oblate deformed nuclei in their ground state in Nature is uncommon and the experimental confirmation of this deformation for the ^{72}Kr ground state would be of essential interest. Other kind of studies could provide a value for the quadrupole deformation parameter β_2 as, for example did the work of A. Gade [Gad05, Gad06] where a value of $|\beta_2|$=0.33 was provided but no information on the sign of this deformation could be determined through this method.

From the nuclear astrophysics point of view, ^{72}Kr is interesting for participating in the rp-process, which is the mechanism leading to the X-ray bursts and takes place in hydrogen-rich environments of accreting compact objects, typically neutron stars, which are fed from a binary companion, typically a red giant. The rp-process consists of the fast capture of protons up to the following nucleus in the proton capture path is unbound, the process slows down. At that point, the process reaches a so-called waiting point of the process and the competition between proton capture and beta decay arises. This is the case of ^{72}Kr and the properties of their beta decay are important in astrophysical network calculations.

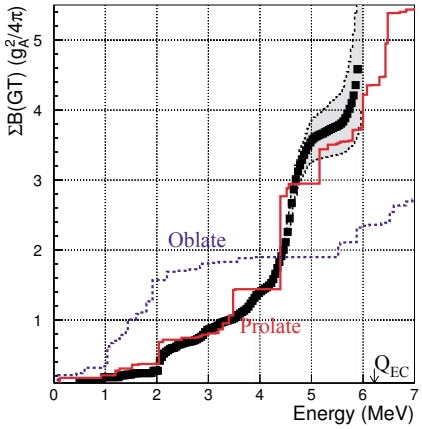

Figure C.1: *Comparison of experimental accumulated B(GT) distribution with theoretical predictions from [Sar01] for oblate (blue line) and prolate (red line) deformation of the ^{76}Sr ground state [Ná04b]. The experimental B(GT) distribution is fairly similar to the predicted for oblate case so this suggests the ground state of ^{76}Sr to be oblate.*

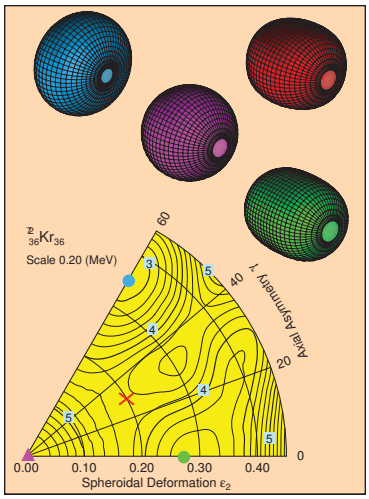

Figure C.2: *Potential energy surfaces for ^{72}Kr with respect to ε_2 and γ parameters obtained from a macroscopic-microscopic calculation [Mö09]. Equipotential lines are distanced 0.2 MeV. The numbers indicate the energy in MeV corresponding to the line on top of which they are placed. Several energy minima, indicated with blue, green, red and violet markers, are found corresponding to different shapes, blue, greeen, red and violet shapes shown in the upper part of the plot. This is a sign of shape coexistence when these minima are close in excitation energy as in this case.*

C.2 Objectives

One of the main purposes of the present work is to extract information on the deformation of ^{72}Kr in its ground state. The experimental way to do this is to determine the feeding distribution in the β^+/EC decay of ^{72}Kr, to transform it into B(GT) and then compare it with theoretical predictions for prolate and oblate deformations of ^{72}Kr from [Sar09].

Another objective is to study the low-spin levels in ^{72}Br fed in the ^{72}Kr β^+/EC decay. Specially important is to measure the conversion coefficients of low-energy transitions as they are important for the analysis of the data which could provide information on the ^{72}Kr deformation, but also they help to determine important information of the decay scheme as transition multipolarities and levels spin-parities. This is important to better know the level scheme of ^{72}Br since some quantities were previously debated as, for example, the ground state spin-parity [Sch73, Piq03, Col74].

C.3 Experiments

Two complementary experiments were carried out at ISOLDE facility (CERN) in order to study the β^+/EC decay of ^{72}Kr into ^{72}Br, the IS370 and its addendum IS370-A.

On the one hand, the IS370 experiment makes use of the Total Absorption Spectroscopy (TAS) technique in order to determine the beta feeding distribution to the excited states in the daughter nucleus, ^{72}Br. This technique uses a large scintillator detector, usually known as TAS detector, which covers as close to 4π solid angle as possible around the source, to detect all the subsequent de-excitation radiation emitted by the source following the beta decay. Thus, the beta feeding is determined through the measurement of the full de-excitation cascade from the directly fed level to the ground state. This beta feeding leads to obtain the B(GT) distribution that will be compared to theoretical predictions from [Sar09]. Apart from the almost 4π scintillator, a plastic scintillator for β-particle detection and a HPGe telescope detector composed by one planar plus one coaxial types detector for γ radiation detection are included in the experimental setup. Their purpose is to select the decay components (β^+/ β^- and EC decays) and to identify the radioactive source composition.

On the other hand, the IS370-A experiment was performed mainly to determine the conversion coefficients of the low-energy transitions in the de-excitation of fed levels in ^{72}Br through the β^+/EC decay of ^{72}Kr. The de-excitation transitions in ^{72}Br have a competition between gamma emission and internal conversion whose relative intensity is quantified through the conversion coefficients, α=I$_e$/I$_\gamma$. The experimental setup includes a miniorange spectrometer to measure the intensity of the electron transitions coming from the internal conversion de-excitation and a HPGe detector to determine the intensity of the corresponding gamma transitions. The miniorange includes a set of permanent magnets with a central piece of tungsten and a Si(Li) cooled detector. The central piece prevents the gamma radiation to reach the Si(Li) detector while the magnets focus the electrons towards the Si(Li) detector. The experimental conversion coefficients, α, are then determined as the ratio between both intensities: α=I$_e$/I$_\gamma$.

C.4 Data analysis

Since the results from the analysis of the data taken in the IS370-A experiment (conversion coefficients) are included in the analysis of IS370 experiment (TAS measurement), we will begin with the description of the analysis of the conversion electron spectroscopy study done in the IS370-A experiment. Later, the analysis of the Total Absorption Spectroscopy data corresponding to the IS370 experiment will be described.

C.4.1 Conversion electron spectroscopy

The analysis of the data taken in IS370-A experiment includes the calibration of the HPGe and Si(Li) detectors in energy and efficiency. The calibrations of the HPGe detector are performed using standard γ calibration sources of ^{133}Ba, ^{152}Eu and ^{241}Am. The Si(Li) detector is calibrated using a standard electron source of ^{207}Bi and performing internal calibrations with beams of ^{74,75,76}Kr isotopes. The efficiency calibration of the miniorange spectrometer is usually called transmission curve due to the predominance of the factor coming from the transmission of electrons towards the Si(Li) detector over its intrinsic efficiency. These transmission curves are obtained using transitions with well-known conversion coefficients. Several sets of magnets and different detector-magnets distances are used to cover a wider energy range in the study. Table C.1 shows a summary of the configurations used and the duration of each measurement.

D1/D2/NT	Effective energy range E(keV)	Measurement duration with ^{72}Kr (min)	Beam used apart from ^{72}Kr
125/8/3B	20-170	240	^{76}Kr (calib)
85/8/4B	60-200	388	^{75}Kr (calib)
110/8/6A	400-1100	327	^{74}Kr (calib)
125/8/6A	300-1100	172	^{74}Kr (calib)

Table C.1: *Configurations of the Miniorange magnets used in the IS370-A experiment. The effective electron energy range of each configuration is shown in the second column. The third column indicates the duration of each measurement with ^{72}Kr as beam. The beam used with each configuration of the magnets is given in the last column. Apart from the ^{72}Kr beam, other Kr isotopes were used to calibrate the different Miniorange configurations.*

Once the calibrations are performed, the analysis is straightforward by calculating the conversion coefficients using the expression:

$$\alpha = \frac{I_e}{I_\gamma} = \frac{A_e/(t_e \cdot \tau_e)}{A_\gamma/(t_\gamma \cdot \varepsilon_\gamma)} = \frac{A_e \cdot \varepsilon_\gamma \cdot t_\gamma}{A_\gamma \cdot t_e \cdot \tau_e} \tag{C.1}$$

where I_e and I_γ are the electron and gamma intensities respectively, A_e and A_γ are the peak areas corresponding to the electron and gamma peaks, t_e and t_γ are the live times of Si(Li) and HPGe detectors and τ_e and ε_γ are the electron and gamma efficiencies, respectively. The live times are included to correct the peak areas by the difference in dead time between the HPGe and Si(Li) detectors.

C.4.2 Total Absorption Spectroscopy

The TAS data analysis can be performed for the total decay, which includes the β^+ and electron capture components, where we would perform the analysis without any coincidence restriction with the ancillary detectors, or by separating both components of the decay by requiring a coincidence condition with a β-particle in the plastic scintillator or with an X-ray in the HPGe detectors. In our case, a problem consisting in a variation of the background radiation was present and the spectra of the total analysis which includes this contribution and has to be subtracted, had to be ruled out. The analysis of the EC component had to be ruled out as well due to two main reasons: first, that the X-rays from bromine could not be resolved from the ones from selenium as they are distanced 0.6 keV, below the energy resolution of the HPGe planar detector (the one covering the lower energy range), and second, every time that a conversion electron is emitted in the de-excitation of the daughter nucleus, an X-ray is emitted so, even if we would be able to separate them from the selenium X-rays, we would have a mixture of bromine X-rays coming from the EC decay and from the internal conversion processes. As a result of this, the analysis performed in this study will be the one corresponding to the β^+ decay component and both, the total feeding distribution and the B(GT) will be deduced from the β^+ component.

The data analysis of the TAS experiment is a complex procedure due to the high detection efficiency of the TAS detector. This makes that contributions from different origins than the decay of interest are present in the spectrum. Due to this, an exhaustive subtraction procedure to get rid of these contributions, so-called contaminations, was carried out. The β^+/EC decay of the daughter nucleus, ^{72}Br, was the main contamination in the spectrum to be subtracted. In order to perform this subtraction, another independent measurement was dedicated to measure the ^{72}Br decay. An additional complication was the fact that the HPGe spectra of the latter measurement showed contamination from the decay of isotopes corresponding to the A=73 mass, that was measured just before the ^{72}Br measurement. This implies that the subtraction of A=73 decay radiation from the ^{72}Br measurement has to be performed and another measurement was devoted to measure the A=73 decay.

Once the ^{72}Br spectrum is cleaned from A=73 contamination, the subtraction of ^{72}Br contamination from the experimental ^{72}Kr spectrum is done as shown in fig. C.3. The ^{72}Br spectrum is normalized to the ^{72}Kr one by integrating them in the energy region where no counts are expected to appear from the ^{72}Kr decay, that is beyond the Q_{EC} value of ^{72}Kr decay. This can be done since the ^{72}Kr decay has a lower Q_{EC} value, 5129(10) keV, than ^{72}Br, 8799(7) keV.

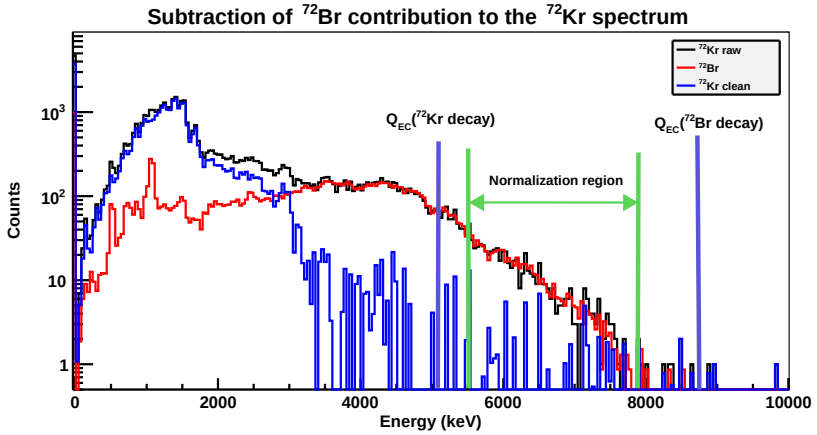

Figure C.3: *Subtraction of ^{72}Br decay contribution to the file 1 of ^{72}Kr spectrum. The normalization region has been selected in the energy region from the Q_{EC} of ^{72}Kr decay and the one corresponding to the ^{72}Br decay as labelled in the plot. This energy region is supposed to have only contribution from the ^{72}Br decay as it lies beyond the ^{72}Kr Q_{EC} value.*

The analysis is done without performing the subtraction of contaminants to avoid the undesirable effect caused by regions with low and negative statistics due to the subtractions. The statistical fluctuations of the measurements make that the subtractions cause negative counts in some channels of the spectrum and positive in others as can be shown in fig. C.4. This has the consequence that the analysis provides unreal feeding located in these regions since the algorithm of the analysis only treats bins with positive statistics. In addition to this, and also to avoid this effect, an energy threshold was chosen as upper limit in the analysis at 3640 keV, as shown in fig. C.4. This energy threshold in the spectrum corresponds to an excitation energy in ^{72}Br approximately of 2618 keV due to the 1022 keV additional energy coming from the annihilation process of the positron emitted in the β^+ decay. Thus, the feeding distribution will be obtained only up to this energy level of 2618 keV.

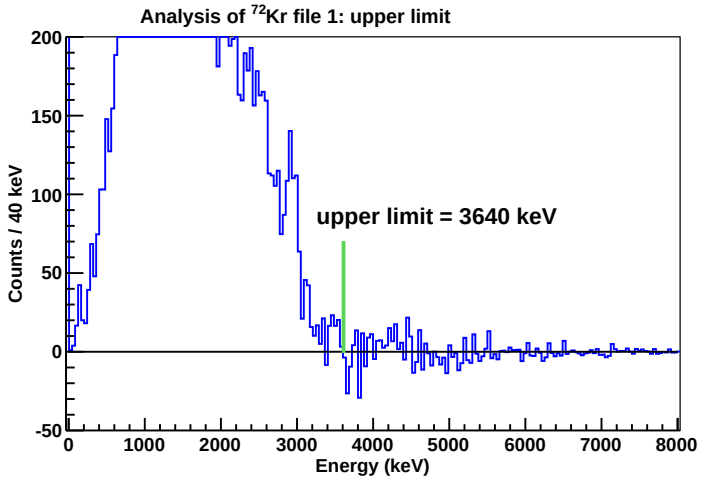

Figure C.4: *^{72}Kr clean spectrum for file 1, as example. The upper limit chosen in the analysis for the energy spectrum is shown. The reason for this choice is mainly that from this energy on the energy spectrum shows oscillations around zero counts giving negative statistics in some bins and few positive counts in others.*

The data analysis consists of the procedure to extract the feeding distribution f_j, for every j bin, from the experimental data d_i, in every i channel of the spectrum, knowing that they are related by means of the expression C.2.

$$d_i = \sum_j R_{ij} f_j \tag{C.2}$$

where R_{ij} is the response matrix of the TAS detector to the decay of interest. This matrix includes two main ingredients, first, the information on the level scheme of the daughter nucleus and second, the response of the TAS detector to the radiation emitted in the decay of interest. In this case, the knowledge on the ^{72}Br level scheme is taken from the high resolution spectroscopy work [Piq03] up to an excitation energy of 1 MeV and it is completed with the conversion coefficients resulting from the analysis of the IS370-A experiment. From 1 MeV up to the Q_{EC} statistical models were used for both, level excitation energies and de-excitation branching ratios following the procedure described in [Tai07b]. The response of the TAS detector to the radiation emitted in the decay is calculated by using a Monte Carlo simulation code developed using the GEANT4 package [GEA]. This code was checked by comparing the simulated and experimental spectra of several radioactive sources. The way of obtaining the feeding distributions requires the inversion of the response matrix from the latter equation. This cannot be generally done for not being a regular matrix and the Expectation-Maximization algorithm is used to deduce the beta feeding distribution as described in [Tai07a].

In the present analysis, as the subtractions were not performed before the analysis, they were included in the analysis by transforming the eq. C.2 into eq. D.2.

$$d_i = \sum_j R_{ij} f_j + k_1 \times (^{72}\text{Br activity}) + k_2 \times (\text{pile up}) \tag{C.3}$$

where k_1 and k_2 are the subtraction factors found for ^{72}Br decay radiation and pile up contributions respectively. Note that the analysis is done by using a binned experimental spectrum d_i of 40-keV bin and the same bin width for the feedings f_j in the ^{72}Br level scheme.

The subtraction of pile up was finally rejected, k_2=0, since the choice of upper limit in the analysis means that no statistics is considered as real contributions from the ^{72}Kr decay beyond the upper limit located at 3640 keV. This value is below the Q_{EC} value of ^{72}Kr decay, 5127(10) keV, and we know that the pile up should appear beyond this energy. This indicates that the pile up is not affecting our measurement or that its contribution is negligible.

The direct result of the analysis of the first measurement of ^{72}Kr (file 1) is the β^+ feeding distribution shown in fig. C.5 which is shown as an example. This quantity is transformed into total feeding distribution by multiplying by the EC/β^+ ratio obtained from [Gov71].

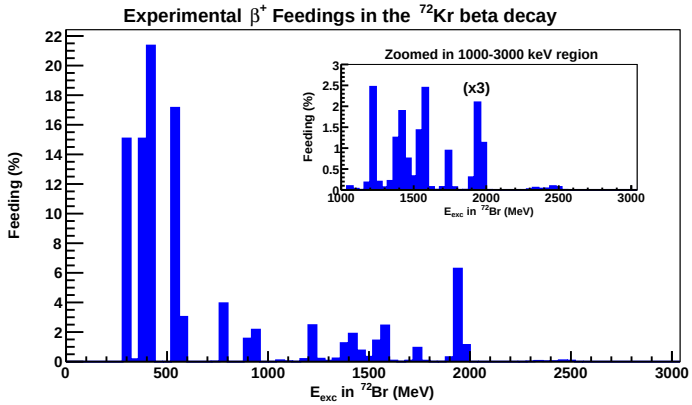

Figure C.5: *β^+ feeding distribution shown up to the Q_{β^+}=4105 keV window obtained from the analysis with an upper limit in the TAS spectrum of 3640 keV in the energy for the measurement of ^{72}Kr file 1. The feedings are found up to 2620 keV for the reasons given in the text. The bin labelled with "(x3)" in the inset has the statistics reduced a factor 3.*

Later, the $B(GT)$ is determined in bins of ΔE =40 keV width from the feeding distribution by means of the expression:

$$B(GT)(E_x) = K' \left(\frac{g_a}{g_v}\right)^2 \cdot \frac{\sum_{E_x \in \Delta E} \frac{I_\beta(E_x)}{\Delta E}}{f \cdot T_{1/2}} \tag{C.4}$$

where the $B(GT)$ in the bin corresponding to the energy interval $(E_x - \Delta E/2, E_x + \Delta E/2)$ is obtained. Later, the B(GT) is determined in accumulated way, meaning that the value at each energy corresponds to the B(GT) from 0 keV up to the energy considered. This is done to better compare with theoretical predictions due to the different placement of the levels in theoretical calculations and experimental measurements.

Six independent measurements were performed to study the ^{72}Kr decay. They have been independently analysed and the resulting B(GT) distribution averaged to determine the final distribution.

The uncertainty over the final B(GT) distribution has been determined having two terms:

1. Statistical uncertainty: the deviations from the mean value at every bin of the individual B(GT) distributions has been determine with respect to the averaged B(GT) distribution, as six independent measurements were carried out.

2. Systematic uncertainty: 9 analysis were performed for every ^{72}Kr file taken into account the 9 different sets of subtraction factors (3×3) since 3 subtraction factors were chosen to remove A=73 contamination from ^{72}Br spectrum and other 3 factors to subtract the ^{72}Br contribution from the ^{72}Kr spectrum. The maximum and minimum of the accumulated B(GT) for every bin of the results of the 9 analysis were considered as the systematic uncertainty.

The total uncertainty was then calculated as:

$$\Delta B(GT) = \sqrt{(\Delta B(GT)_{syst})^2 + (\Delta B(GT)_{stat})^2} \tag{C.5}$$

The final result including the uncertainty for the accumulated B(GT) distribution is shown in fig. C.6.

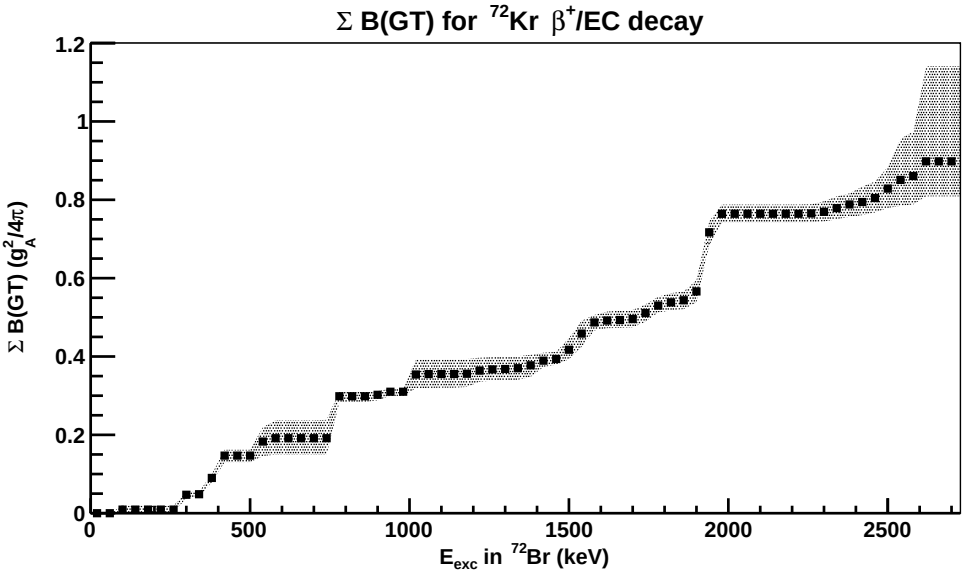

Figure C.6: *Accumulated B(GT) distribution for the β^+/EC decay of ^{72}Kr obtained from this analysis of the β^+ decay component via TAS spectroscopy. The uncertainty region shown is estimated from systematic and statistical origin as described in the text.*

The resulting accumulated B(GT) distribution has been compared with the result of using different level schemes of the ^{72}Br: the one used in the analysis taken from [Piq03] but considering its information up to an upper energy threshold located at 2 MeV instead of 1 MeV as previously considered, a randomly modified level scheme in the known part, modifying the parameters of the statistical models used for the unknown part of the level scheme, using theoretical level schemes provided by P. Sarriguren from its calculations using the QRPA approach for the oblate case with 1 and 2 MeV as upper energy thresholds for the known part of the schemes. These comparisons confirm the reliability of the accumulated B(GT) distribution obtained from our analysis.

The reproduction of gamma intensities of the most intense transitions was done by imposing some conditions in the analysis which make worse the reproduction of the experimental TAS spectrum. The result of this parallel analysis reproducing the gamma intensity, called *restricted*, is very similar to the considered as good analysis, known as *free*, as can be seen in fig. C.7. We maintain as good result for the B(GT) distribution the one that better reproduces the experimental spectrum as this is our real experimental data. Since these two different analysis provide very similar accumulated B(GT) distributions, the reliability of the result is increased by this comparison.

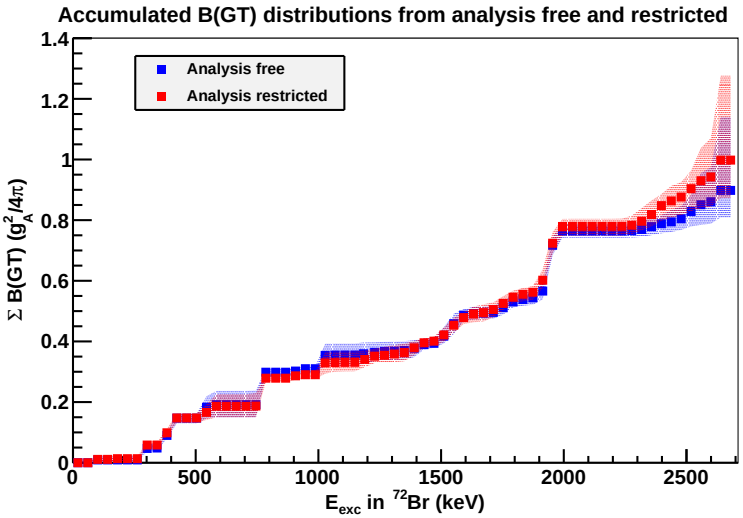

Figure C.7: *Comparison of accumulated B(GT) distributions obtained from the analysis with all the feedings free (blue) and with some of them restricted (red). The trend of both results is similar and the value of the total B(GT) accumulated up to 2640 keV are similar in both analysis:* $B(GT)_{free} = 0.90^{+0.24}_{-0.09}(g_A^2/4\pi)$ *and* $\sum B(GT)_{restricted} = 0.99^{+0.28}_{-0.12}(g_A^2/4\pi)$

C.5 Results

The main results of the present study can be summarized as follows.

C.5.1 Conversion electron spectroscopy experiment

The analysis of the data corresponding to the IS370-A experiment provided the values for the conversion coefficients shown in figs. C.8, C.9 and C.10.

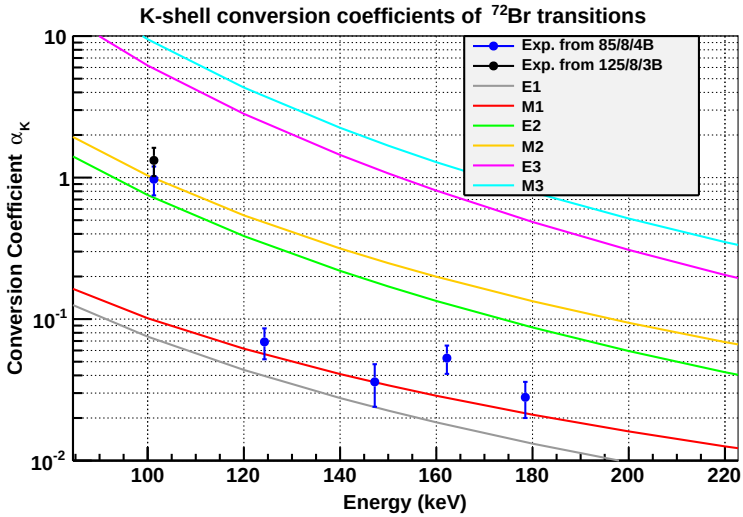

Figure C.8: *Experimental conversion coefficients for K-shell transitions obtained in the low energy range with the miniorange configurations 85/8/4B and 125/8/3B. The comparison with the theoretical predictions from [ANU] is presented for the different multipolarities.*

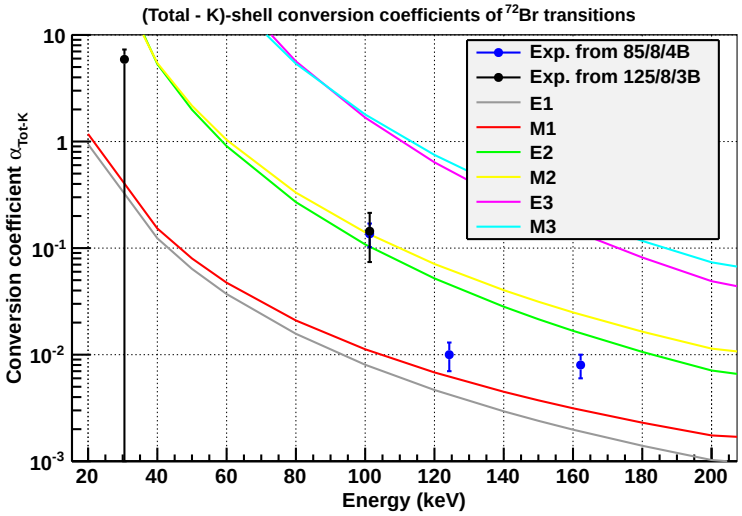

Figure C.9: *Experimental conversion coefficients for (Total-K)-shell transitions obtained in the low energy range with the miniorange configuration 85/8/4B. The comparison with the theoretical predictions from [ANU] is presented for the different multipolarities.*

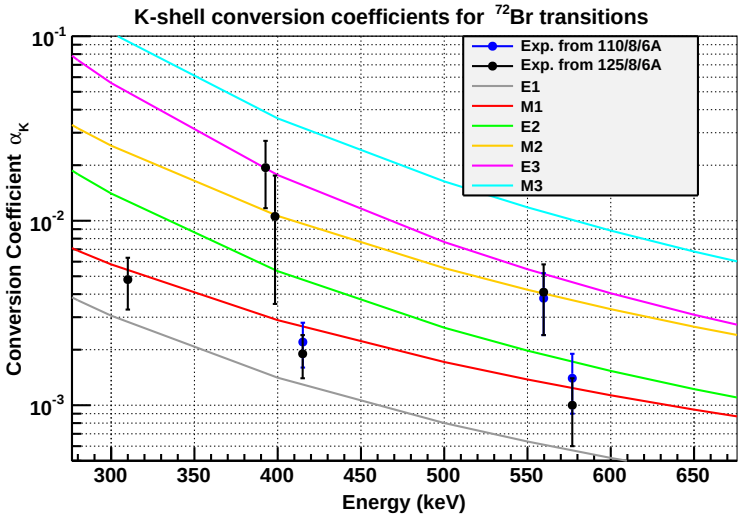

Figure C.10: *Experimental conversion coefficients for K-shell transitions obtained in the high energy range with the miniorange configurations 110/8/6A and 125/8/6A. The comparison with the theoretical predictions from [ANU] is presented for the different multipolarities.*

The results obtained from this experiment can be summarized as follows:

- 14 experimental conversion coefficients for low-energy transitions in ^{72}Br not previously known have been measured: 101.3K, 101.3(Tot-K), 124.4K, 124.4(Tot-K), 147.2K doublet, 162.7K, 162.7(Tot-K), 178.5K, 309.9K, 392.7K, 398.4K, doublet (414.5+415.1)K, 559.7K and 576.9K. Additionally, an upper limit for the values of the conversion coefficients of 30.5Tot-K and 38.8K transitions has been established.

- The **spin-parity of the ground state of ^{72}Br can be** assigned with three possible values **(0,1,2)**$^+$. Previous works supported two possibilities, being and 1^+ and 3^+. Works performed by Piqueras et al. [Piq03] and Schmeing et al. [Sch73] assigned an spin-parity of 1^+ based on a direct ground state beta feeding of 34 % and 53.6 % from ^{72}Kr decay, respectively. On the other hand, the study of Collins et al. [Col74] where they assigned a 3^+ based on the direct feeding of 2^+ and 4^+ states in ^{72}Se via the beta decay of the ground state of ^{72}Br. The feeding that they report is 23.2 % and 20 % to the 2^+ levels at 862 and 1316.7 keV respectively and 5 % to the 4^+ state at 1636.8 keV of excitation energy. The current work rules out the 3^+ keeping the possibility of 1^+ as well as it allows for other two possible values: 0^+ and 2^+.

- The multipolarity of 9 transitions in ^{72}Br have been established: 30.5-keV being an E1, 101.3-keV being an M2, 124.4-keV being an M1(E2), the 147.2-keV transition linking the 310.0-keV and 162.8-keV states to be an M1, 162.7-keV being an M1+E2, 178.5-keV being an M1(E2), 576.9-keV being an M1(E2) transition and the 414.5+415.1 keV doublet where individual transitions have been found to be both of M1 multipolarity.

- The multipolarity of 6 transitions have not been firmly determined but they have been restricted: 38.8-keV could be M1+E2, pure M1 or pure E2, the 147.2-keV transition linking the 545.7-keV and 398.5-keV states to be an M1/M1+E2/E1, 309.9-keV being an M1/M1(E2), 392.7-keV could be an E3 or E3(M2), 398.4-keV could be M2 or M2(E3) and 559.7-keV being an M2/M2(E3).

- The conversion coefficients of the 454.7-keV transition in ^{72}Se and 112-keV transition in ^{76}Br have been measured and their multipolarity have been deduced to be an E2 or E2(M1) for the 454.7-keV transition and M1+E2 the 112-keV one.

- The intensity of two E0 transitions, the 937 keV in ^{72}Se and the 691 keV in ^{72}Ge have been measured and compared to the strongest E2 transition in both de-excitation schemes.

C.5.2 Total Absorption Spectroscopy experiment

The Total Absorption Spectroscopy measurement has provided the following results:

- the β^+ feeding distribution from the ^{72}Kr beta decay has been determined and the total (β^+/EC) feeding distribution has been deduced from the latter up to an excitation energy of 2640 keV.

- the accumulated B(GT) distribution of the ^{72}Kr β^+/EC decay has been determined up to an excitation energy of 2640 keV. The uncertainty of the distribution includes systematic and statistical components that have been estimated during the analysis.

- the comparison of the accumulated B(GT) distribution with the theoretical predictions from [Sar09] suggest a dominantly oblate deformation for the ^{72}Kr ground state.

- the total amount of B(GT) found up to an excitation energy of 2640 keV has been determined to be: $\sum B(GT)_{free} = 0.90^{+0.24}_{-0.09}$ in units of $(g_A^2/4\pi)$ following the convention given by [BM98].

C.6 Conclusions

The comparison of the experimental B(GT) distribution with the theoretical predictions from P. Sarriguren [Sar09] for the oblate (blue), prolate (red) and a dominantly oblate (green), mixed with 10% prolate deformation of ^{72}Kr, is shown in fig. C.11. The mixing ratio of 10% with the 671(2) keV 0^+ state considered as prolate deformed was suggested in [Bou03]. The mixing ratio is considered in an approximate but not strictly proper way since the mixing ratio of the accumulated B(GT) distributions of oblate and prolate distributions have been weighted by the mixing ratios in every bin and no modifications were performed in the formalism. However, it guides the eye to have an idea if the experimental distribution is compatible with this mixing ratio.

The result fits fairly well with the predictions for the oblate case (blue) and also for the predominantly oblate mixed state (green). The prediction for oblate corresponds to a minimum located at a value for the quadrupole deformation parameter β_2=-0.1759 whose approximate shape is shown in fig. C.12.

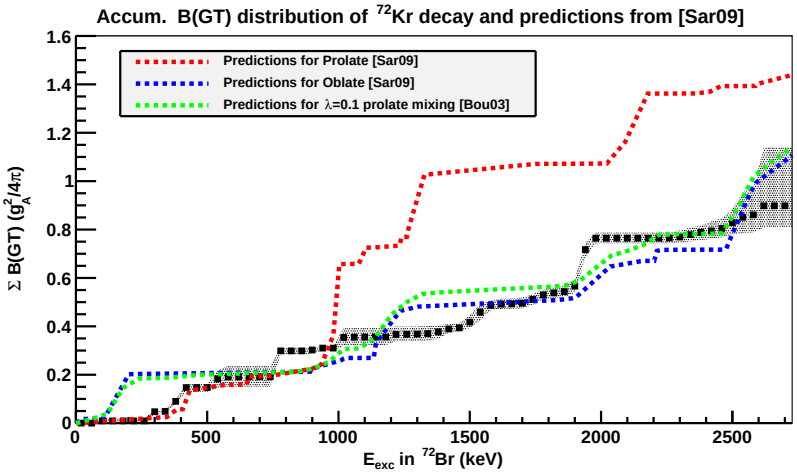

Figure C.11: *Comparison of experimental accumulated B(GT) distribution for the β^+/EC decay of ^{72}Kr with theoretical predictions from [Sar09] for oblate (blue), prolate (red) and dominantly oblate (green) deformations of the ground state of the parent nucleus. The mixing ratio used to roughly estimate the prediction for the dominantly oblate case is the suggested value in [Bou03] of λ=0.1 (mixing of 10% with the prolate first excited state at 671(2) keV. The experimental results fits fairly well with the theoretical predictions for the oblate and mixed cases as expected from information from previous theoretical and experimental works.*

The level scheme of ^{72}Br has been enriched with the experimental conversion coefficients studied as well as the discussion on transition multipolarities and levels spin improve the knowledge on the ^{72}Br level scheme. However, the spin and parity of the ^{72}Br ground state, that was previously debated [Sch73, Piq03, Col74], cannot firmly established but only some possible values are proposed based on the conversion coefficient study, the TAS measurement and the theoretical calculations from P. Sarriguren that fit fairly well with the experimental B(GT) distribution.

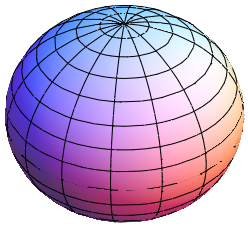

Figure C.12: *Nuclear shape of ^{72}Kr ground state calculated for a quadrupole deformation parameter of β_2=-0.1759 as reported by P. Sarriguren [Sar09]. This value corresponds to the oblate deformed local minimum obtained using the SLy4 force whose theoretical accumulated B(GT) associated matches with the experimentally obtained as shown in fig. C.11.*

Appendix D: Resumen en castellano

El estudio que se presenta está dedicado al estudio de la deformación que el núcleo ^{72}Kr muestra en su estado fundamental a través de estudios de desintegración beta.

D.1 Introducción

Estudios previos en la misma región de masas que ^{72}Kr de la tabla de núclidos fueron realizados para determinar la deformación de ^{76}Sr [Ná04b], ^{74}Kr [Poi04] y ^{78}Sr [Pé13]. Proporcionaron información satisfactoria sobre la deformación de esos núcleos como se muestra, por ejemplo, en la fig. D.1 para el caso de ^{76}Sr.

Este trabajo pretende emplear la misma técnica experimental para determinar la deformación del núcleo con N=Z ^{72}Kr. Este núcleo es de gran importancia en estructura nuclear y en astrofísica nuclear. Desde el punto de vista de estructura nuclear, es importante por estar localizado en una región de masas donde fuertes transiciones de forma se predicen teóricamente y el fenómeno de coexistencia de forma ha sido ya observado [Mö95, Ham74, Var87]. Éste último consiste en la presencia de estados del núcleo con diferente deformación cuadrupolar, prolada, esférica u oblada, a energías de excitación relativamente cercanas. Este fenómeno fue predicho que occuriría en nuestro núcleo de interés, ^{72}Kr, como se puede observar en la figura D.2 que aparece en [Mö09]. Por otro lado, este núcleo es interesante también porque constituye uno de los extraños casos donde se predice un estado fundamental oblado y estados excitados prolados a energías de excitación relativamente bajas. Esto es importante sobre todo porque núcleos con deformación oblada en el estado fundamental son bastante escasos en la naturaleza y la confirmación experimental de este tipo de forma para el estado fundamental de ^{72}Kr sería de un gran interés. Otro tipo de estudios pueden proporcionar un valor para el parámetro de deformación cuadrupolar β_2 como hicieron A. Gade y sus colaboradores en [Gad05, Gad06] donde obtuvieron un valor del módulo de dicho parámetro $|\beta_2|$=0.33, que, aunque coincide con la cantidad de deformación predicha para una deformación oblada, no puede concluir firmemente que la deformación sea de este tipo ya que el signo de la misma no puede extraerse a través de ese método.

Desde el punto de vista de astrofísica nuclear, ^{72}Kr es interesante porque participa en el proceso de captura rápida de protones (proceso rp), conocido como *rp-process*. Este proceso es el mecanismo que conduce hacia las explosiones de rayos X que tienen lugar en medios ricos en hidrógeno de objetos compactos acrecientes, típicamente estrellas de neutrones, que

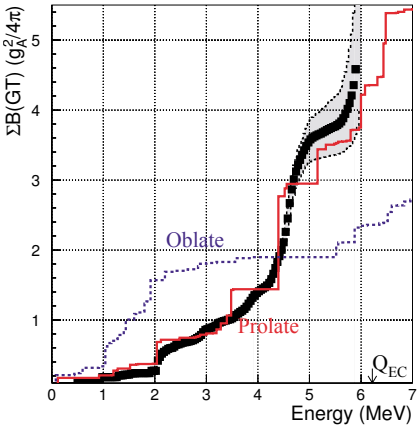

Figure D.1: *Comparación de la distribución experimental de B(GT) acumulada con predicciones teóricas [Sar01] para deformación oblada (línea azul) y prolada (línea roja) del estado fundamental de ^{76}Sr [Ná04b]. La distribución experimental de B(GT) acumulada es similar a la predicción para el caso oblado lo cual sugiere este tipo de deformación para el estado fundamental de ^{76}Sr.*

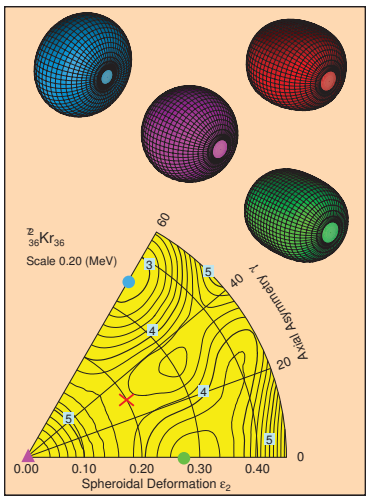

Figure D.2: *Superficies de energía potencial para ^{72}Kr con respecto a los parámetros de deformación ε_2 y γ obtenidos de cálculos macroscópicos-microscópicos realizados en [Mö09]. Las líneas equipotenciales están distanciadas 0.2 MeV. Los números indican la energía en MeV de la línea sobre la que aparecen. Varios mínimos de energía se encuentran para este caso, indicados con marcadores azul, verde, rojo y violeta, que se corresponden con las formas del núcleo representadas en la parte superior de la figura en los mismos colores que los marcadores a que corresponden. Esta variedad de deformaciones para mínimos locales que se encuentran próximos en energía constituye lo que se denomina coexistencia de formas.*

son alimentados desde un compañero binario, que típicamente suele ser una estrella gigante roja. El proceso rp consiste en la captura rápida de protones hasta que el siguiente núcleo en dicho proceso sea no ligado, entonces el proceso se frena. En estos puntos el proceso alcanza lo que se conoce como puntos de espera, o *waiting points* en inglés, del proceso y la competición entre los procesos de captura rápida de protones y la desintegración beta surge. Este es el caso del núcleo ^{72}Kr y las propiedades de su desintegración beta son importantes en cálculos astrofísicos.

D.2 Objetivos

Uno de los principales propósitos del presente trabajo es extraer información sobre la deformación de ^{72}Kr en su estado fundamental. La forma experimental de hacerlo es mediante la comparación de la distribución experimental de B(GT), determinado a partir de la distribución de alimentación beta en la desintegración β^+/CE de ^{72}Kr, con predicciones teóricas para deformaciones oblada y prolada del núcleo de interés, ^{72}Kr, tomadas de [Sar09].

Otro objetivo es estudiar los niveles de bajo espín en el núcleo ^{72}Br que son alimentados a través de la desintegración β^+/CE de ^{72}Kr. Especialmente relevante es la medida de los coeficientes de conversión de las transiciones de baja energía porque son importantes para el análisis de los datos tomados en el experimento que intenta obtener informacion de la forma de ^{72}Kr, pero también ayudarán a determinar importante información del esquema de desexcitación como puede ser la multipolaridad de transiciones y espín-paridad de los niveles. Esta información es importante para conocer mejor el esquema de niveles de ^{72}Br puesto que algunas magnitudes fueron previamente debatidas como, por ejemplo, el espín y paridad del estado fundamental [Sch73, Piq03, Col74].

D.3 Experimentos

Dos experimentos complementarios fueron realizados en la instalación ISOLDE (CERN) para estudiar la desintegración beta de ^{72}Kr en ^{72}Br, el IS370 y su *addendum* el IS370-A.

Por una parte, el experimento IS370 empleaba la técnica de Espectroscopía de Absorción Total, conocida por sus siglas en inglés TAS, para determinar la distribución de alimentación beta de estados excitados en el núcleo hijo, ^{72}Br. Esta técnica usa un detector centelleador grande, que usualmente se conoce como detector TAS, el cual cubre un ángulo sólido tan cercano a 4π como sea posible entorno a la fuente radioactiva, para detectar toda la radiación de desexcitación que se emite a continuación de la desintegración beta en la fuente radioactiva. Así, la alimentación beta a los niveles es determinada a través de la medida de la cascada completa de desexcitación a partir del nivel directamente alimentado hasta alcanzar el estado fundamental. Esta alimentación beta conduce a obtener la distribución de B(GT) que será comparada con las predicciones teóricas de [Sar09]. Además del detector TAS, un centelleador plástico para la detección de partículas beta y un telescopio de detectores de HPGe compuesto por uno de tipo planar y otro de tipo coaxial para la detección de radiación gamma son incluidos en el montaje. Su función es poder seleccionar las componentes de la desintegración: β^+, β^- o captura electrónica y para la identificación de la composición de la fuente radioactiva.

Por otro lado, el experimento IS370-A fue realizado para determinar los coeficientes de conversión de las transiciones de baja energía en la desexcitación de los niveles alimentados en ^{72}Br a través de la desintegración β^+/CE de ^{72}Kr. Las transiciones de desexcitación de ^{72}Br

presentan la competición entre la emisión gamma y la conversión interna cuya intensidad relativa es expresada a través de los coeficientes de conversión α=I_e/I_γ. El montaje experimental incluye un espectrómetro *miniorange* para medir la intensidad de las transiciones de electrones procedentes de la conversión interna de desexcitación y un detector de HPGe para determinar la intensidad de la correspondiente transición gamma. El espectrómetro *miniorange* incluye unos imanes permanentes con una pieza central de tungsteno y un detector refrigerado de Si(Li). La pieza central evita que la radiación gamma alcance el detector de Si(Li) mientras que los imanes actúan como lente electromagnética focalizando los electrones hacia el detector de Si(Li). Los coeficientes de conversión experimentales, α, son obtenidos como el cociente de ambas intensidades: α=I_e/I_γ.

D.4 Análisis de datos

Puesto que los resultados del análisis de los datos tomados en el experimento IS370-A (coeficientes de conversión) son incluidos en el análisis del experimento IS3702 (medida TAS), comenzaremos con la descripción del análisis correspondiente al estudio de espectroscopía de electrones de conversión. A continuación, el análisis de los datos tomados en la medida TAS será descrito.

D.4.1 Espectroscopía de electrones de conversión

El análisis de los datos tomados en el experimento IS370-A incluye la calibración de los detectores de HPGe y Si(Li) en energía y eficiencia. Las calibraciones del detector de HPGe fueron realizadas usando fuentes gamma de calibración convencionales de ^{133}Ba, ^{152}Eu and ^{241}Am. El detector de Si(Li) por su parte, fue calibrado empleando la fuente de calibración de ^{207}Bi y haciendo medidas de calibración interna con haces de los isótopos ^{74,75,76}Kr. La calibración en eficiencia del espectrómetro *miniorange* es conocida como curva de transmisión debido a que el factor dominante en la eficiencia es la transmision de los electrones hacia el detector por delante de la eficiencia intrínseca del detector. Estas curvas de transmisión se obtienen usando transiciones con coeficientes de conversión conocidos. Varios conjuntos de imanes y diferentes distancias detector-imanes son empleadas para cubrir un rango energético más amplio en el estudio. La tabla D.1 muestra un resumen de las configuraciones empleadas y la duración de las medidas realizadas con cada configuración.

D1/D2/NT	Rango energético efectivo E(keV)	Duración medida con ^{72}Kr (min)	Haz empleado además de ^{72}Kr
125/8/3B	20-170	240	^{76}Kr (calib)
85/8/4B	60-200	388	^{75}Kr (calib)
110/8/6A	400-1100	327	^{74}Kr (calib)
125/8/6A	300-1100	172	^{74}Kr (calib)

Table D.1: *Configuraciones de imanes y distancias del espectrómetro miniorange empleadas en el experimento IS370-A. La primera columna indica la configuración del espectrometro usando la etiqueta D1/D2/NT en donde D1 es la distancia desde un origen arbitrario hasta la posición del detector, D2 es la distancia desde la fuente radioactiva hasta los imanes y NT indica el número de imanes N y el tipo T de los mismos. El rango efectivo de energías de electrones de cada configuración es indicado en la segunda columna. La tercera columna da la duración de la medida con haz de ^{72}Kr. La última columna indica qué haz fue empleado con cada configuración dele espectrómetro ya que medidas con otros isótopos de Kriptón como ^{74,75,76}Kr fueron empleadas para las calibraciones de las diferentes configuraciones del miniorange.*

Una vez que las calibraciones están listas, el análisis de los datos es directo para obtener los coeficientes de conversión a partir de la expresión:

$$\alpha = \frac{I_e}{I_\gamma} = \frac{A_e/(t_e \cdot \tau_e)}{A_\gamma/(t_\gamma \cdot \varepsilon_\gamma)} = \frac{A_e \cdot \varepsilon_\gamma \cdot t_\gamma}{A_\gamma \cdot t_e \cdot \tau_e} \tag{D.1}$$

donde I_e e I_γ son las intensidades de electrones y radiación gamma respectivamente, A_e y A_γ son las áreas de los picos de electrones y radiación gamma, t_e y t_γ son los tiempos activos (*live times*) de los detectores de Si(Li) y HPGe en la medida y τ_e y ε_γ son las eficiencias del detector de electrones y de radiación gamma, respectivamente. Los tiempos activos (*live times*) son incluidos para corregir por la diferencia en tiempo muerto de los detectores de HPGe y Si(Li).

D.4.2 Espectroscopía de Absorción Total

El análisis TAS puede realizarse bien de la desintegración completa incluyendo las componentes β^+ y captura electrónica que se realizaría sin requerir ninguna coincidencia con detectores auxiliares o bien separando ambas componentes imponiendo la condición de coincidencia con una partícula β en el centelleador plástico o con un rayo X en los detectores de HPGe. En nuestro caso hubo un problema de variación de la radiación de fondo y el análisis conjunto, que incluye dicha radiación y debe ser sustraída para afrontar el análisis, tuvo que ser desestimado. Por otra parte, la componente de captura electrónica tampoco pudo ser estudiada debido a dos efectos, por un lado los rayos X de bromo y selenio, ambos presentes en los espectros, están demasiado próximos en energía (ΔE=0.6 keV) para ser diferenciados en nuestro detector HPGe planar (el de más bajo rango energético), y, por otro, cada vez que un electrón de conversión es emitido en la desexcitación del núcleo hijo, también se emite un rayo X por lo que, aunque pudiésemos separar los rayos X de bromo de los de selenio, tendríamos mezclados los procedentes de la componente de captura electrónica con aquellos procedentes de la desexcitación por conversión interna. Por todo esto, el análisis que se ha realizado es el que comprende la componente β^+ de la desintegración y tanto la distribución de alimentación total β^++CE como la de B(GT) serán obtenidos a partir de la componente β^+.

El análisis de los datos del experimento TAS es un procedimiento complejo debido a la alta eficiencia de detección del detector TAS. Esto causa que aparezcan en el espectro contribuciones procedentes de diferentes orígenes a la desintegración de interés. Por ello, un procedimiento cuidadoso de sustracción de estas contribuciones, normalmente denominadas contaminaciones, es realizado. La radiación procedente de la desintegración β^+/CE del núcleo hijo, ^{72}Br, es la principal contaminación presente en el espectro que debe ser sustraída. Para realizar esta sustracción, otra medida independiente fue dedicada a medir la desintegración de ^{72}Br. Sin embargo, una complicación adicional fue encontrada al observar el espectro de los detectores de HPGe correspondientes a esta medida. Radiación proveniente de la desintegración de la cadena radioactiva de masa A=73, que fue medida justo antes de la medida de ^{72}Br, fue encontrada en dichos espectros y, por lo tanto, otra medida de la desintegración de la masa A=73 fue realizada para poder sustraer su contribución al espectro de ^{72}Br.

Una vez que fue obtenido el espectro de ^{72}Br limpio de contaminación de la masa A=73, la sustracción de la contaminación de ^{72}Br del espectro de ^{72}Kr es realizada como se muestra en la figura D.3. El espectro de ^{72}Br se normaliza al de ^{72}Kr integrando ambos espectros en la región de energía por encima del valor Q_{CE} de la desintegración de ^{72}Kr, en donde no se espera que haya cuentas procedentes de la desintegración de ^{72}Kr. Esto es factible puesto que el valor Q_{CE} de la desintegración de ^{72}Kr, 5129(10) keV, es menor que el correspondiente a la desintegración de ^{72}Br, 8799(7) keV.

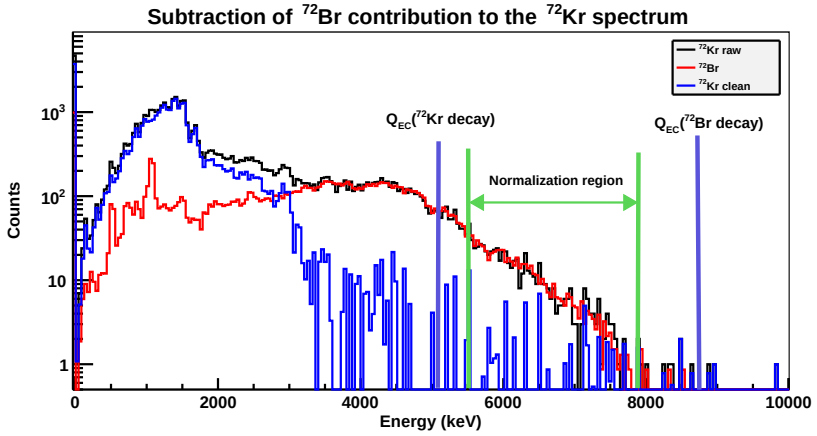

Figure D.3: *Sustracción de la contribución de la desintegración de ^{72}Br al espectro de la medida del fichero 1 de la desintegración de ^{72}Kr. La región considerada para la normalización se muestra indicada y es elegida entre los valores Q_{CE} de la desintegraciones de ^{72}Kr y ^{72}Br. En esta región energética se espera encontrar únicamente contribución procedente de la desintegración de ^{72}Br.*

El análisis es realizado sin hacer las sustracciones previamente para evitar efectos indeseables causados por regiones con baja estadística e incluso negativa, debido a las sustracciones. Las fluctuaciones estadísticas de las medidas hacen que las sustracciones dejen un número de cuentas negativo en algunos canales del espectro y positivos en otros como se muestra en la figura D.4. Esto tiene la consecuencia de que el análisis ubica alimentación beta irreal en esas regiones puesto que el algoritmo únicamente puede tratar canales con estadística positiva. Además de esto, y también para evitar este efecto, un umbral de energía fue elegido en el análisis en forma de límite superior en energía localizado a 3460 keV como se muestra en la figura D.4. Este umbral corresponde a una energía de excitación en ^{72}Br aproximada de

2618 keV debido a la energía adicional de 1022 keV procedente de la aniquilación del positron emitido en la desintegración β^+. Por ello, la distribución de alimentación beta será obtenida sólo hasta esta energía de excitación de 2618 keV.

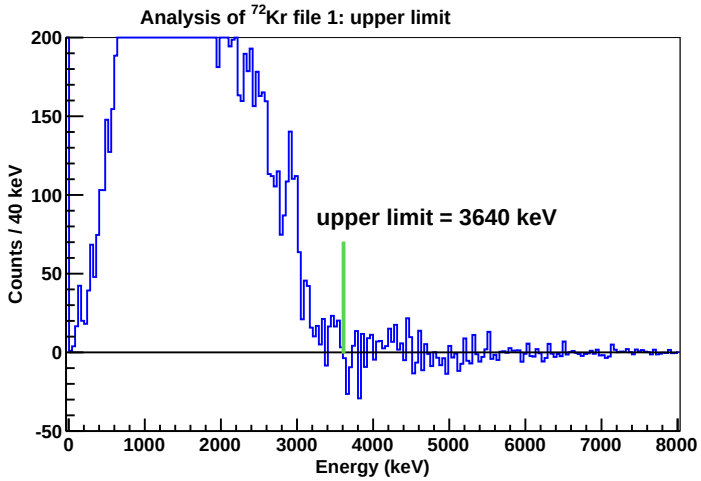

Figure D.4: *Espectro correspondiente a la medida del fichero 1 de la desintegración de ^{72}Kr una vez han sido ya sustraídas las contaminaciones, a modo de ejemplo. El límite superior en energía que es elegido en el análisis para el espectro energético se indica. La razón principal para esta elección es que a partir de esta energía el espectro muestra oscilaciones alrededor de número de cuentas cero alternando entre canales con estadística negativa y positiva.*

El análisis de datos consiste en el procedimiento para extraer la distribución de alimentación beta para cada bin j, f_j, a partir de los datos experimentales d_i, en cada canal i del espectro, conociendo que estas magnitudes están relacionadas por medio de la expresión D.2.

$$d_i = \sum_j R_{ij} f_j \tag{D.2}$$

en donde R_{ij} es la matriz de respuesta del detector TAS a la desintegración de interés. Esta matriz contiene dos ingredientes principales, por un lado la información sobre el esquema de niveles del núcleo hijo y, por otro, la respuesta del detector TAS a la radiación emitida en la desintegración de interés. En nuestro caso, el conocimiento del esquema de niveles de ^{72}Br se toma del trabajo de espectroscopía de alta resolución de I. Piqueras y colaboradores [Piq03] hasta una energía de excitación de 1 MeV y esta información es completada con los coeficientes de conversión obtenidos en el análisis del experimento IS370-A. A partir de 1 MeV de energía de excitación y hasta el valor Q_{CE} de la desintegración de ^{72}Kr se emplean modelos estadísticos para ubicar los niveles excitados y las razones de ramificación en la desexcitación de los mismos siguiendo el procedimiento que se describe detalladamente en [Tai07b]. La respuesta del detector TAS a la radiación emitida en la desintegración es calculada mediante un código de simulación Monte Carlo empleando el paquete GEANT4 [GEA]. Este código es revisado comparando los espectros simulados y experimentales de varias fuentes radiactivas. La forma de obtener la distribución de alimentación beta requiere de la inversión de la matrix de respuesta R_{ij} de la ecuación D.2. Esto no es posible realizarlo siempre porque dicha matrix no es siempre regular y, por ello, el algoritmo de Expectación-Maximización es empleado como se describe en [Tai07a].

En el presente análisis, puesto que las sustracciones no fueron realizadas antes de abordar el análisis, las contaminaciones fueron incluidas en el analisis transformando la ecuación D.2 en la D.3.

$$d_i = \sum_j R_{ij} f_j + k_1 \times (^{72}\text{Br activity}) + k_2 \times (\text{pile up}) \tag{D.3}$$

en donde k_1 y k_2 son los factores de sustracción encontrados para las contribuciones de la radiación de la desintegración de ^{72}Br y apilamiento de señales (*pile up*) respectivamente. Es importante recordar que el análisis se realiza empleando un espectro experimental dividido en canales de 40 keV de anchura y que el esquema de niveles de ^{72}Br también es dividido en divisiones del mismo ancho para obtener la alimentación beta en cada división j, f_j.

La sustracción de apilamiento de señales electrónicas, *pile up*, fue finalmente desestimada: k_2=0, porque la elección del límite superior en energía para el análisis implica que se considera que no existen cuentas reales en el espectro por encima de dicho límite. Thus, puesto que este valor está por debajo del valor Q_{CE} de la desintegración de ^{72}Kr, 5127(10) keV, y sabemos que los efectos de apilamiento de señales deberían ser visibles por encima de dicho umbral, consideramos que el efecto de apilamiento no está afectando a nuestra medida o que su contribución es mínima y podemos despreciarla.

El resultado directo de nuestro análisis de la medida del fichero 1 para la desintegración de ^{72}Kr es la distribución de alimentación β^+ mostrada en la figura D.5 que se muestra a modo de ejemplo. Esta magnitud es transformada en alimentación total (β^++CE) multiplicando por el cociente CE/β^+ que se puede obtener de [Gov71].

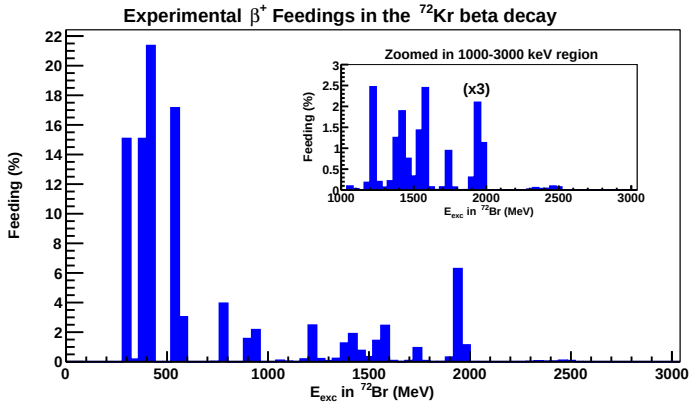

Figure D.5: *Distribución de alimentación β^+ mostrado en la ventana energética hasta el valor $_{\beta^+}$=4105 keV obtenida a partir del análisis del espectro TAS, con condición de coincidencia con el detector β, imponiendo un límite superior en el análisis a una energía de 3640 keV en la medida del fichero 1 para la desintegración de ^{72}Kr. Las alimentaciones son encontradas hasta una energía de excitación de 2620 keV por las razones expuestas en el texto. El canal del gráfico insertado que está etiquedato con "(x3)" tiene su estadística reducida un factor 3 para que pudiese ser visto por completo en el gráfico.*

A continuación, la intensidad reducida de la transiciones Gamow-Teller, $B(GT)$, es obtenida en divisiones de ancho ΔE =40 keV a partir de la distribución de alimentación beta por medio de la expresión:

$$B(GT)(E_x) = K' \left(\frac{g_a}{g_v}\right)^2 \cdot \frac{\sum_{E_x \in \Delta E} \frac{I_\beta(E_x)}{\Delta E}}{f \cdot T_{1/2}} \tag{D.4}$$

donde se obtiene la $B(GT)$ correspondiente al intervalo de energías $(E_x - \Delta E/2, E_x + \Delta E/2)$. Posteriormente, se determina el $B(GT)$ de forma acumulada, esto es, que el valor del $B(GT)$ en cada división corresponde a la integral de la magnitud $B(GT)$ desde cero hasta la energía de excitación correspondiente a esa división. Esto se hace así para poder realizar una comparativa mejor con las predicciones teóricas debido a que la ubicación de los niveles en los cálculos teóricos no se corresponde con la ubicación de los mismos que se determina experimentalmente.

Seis medidas independientes fueron realizadas para estudiar la desintegración de ^{72}Kr. Han sido analizadas independientemente y las distribuciones de B(GT) han sido promedidas para obtener el resultado final.

La incertidumbre experimental sobre la distribución final de B(GT) ha sido determinada a través de dos términos:

1. Incertidumbre estadística: las desviaciones del valor medio en cada división de la distribución de $B(GT)$ se ha determinado con respecto a la distribución de $B(GT)$ promedio para las 6 medidas realizadas.

2. Incertidumbre sistemática: fueron realizados 9 análisis para cada fichero de ^{72}Kr considerando 9 conjuntos diferentes de factores de sustracción de contaminantes, 3 en cada una de las dos sustracciones: masa A=73 del espectro de ^{72}Br y ^{72}Br del espectro de ^{72}Kr. Por tanto, tendremos 3×3 sustracciones diferentes. El máximo y mínimo de $B(GT)$ acumulado para cada división de los 9 análisis realizados para cada fichero fueron considerados como la incertidumbre estadística.

A partir de estas componentes, la incertidumbre total fue calculada como:

$$\Delta B(GT) = \sqrt{(\Delta B(GT)_{syst})^2 + (\Delta B(GT)_{stat})^2} \tag{D.5}$$

El resultado final incluyendo la incertidumbre final para la distribución acumulada de $B(GT)$ se muestra en la figura D.6.

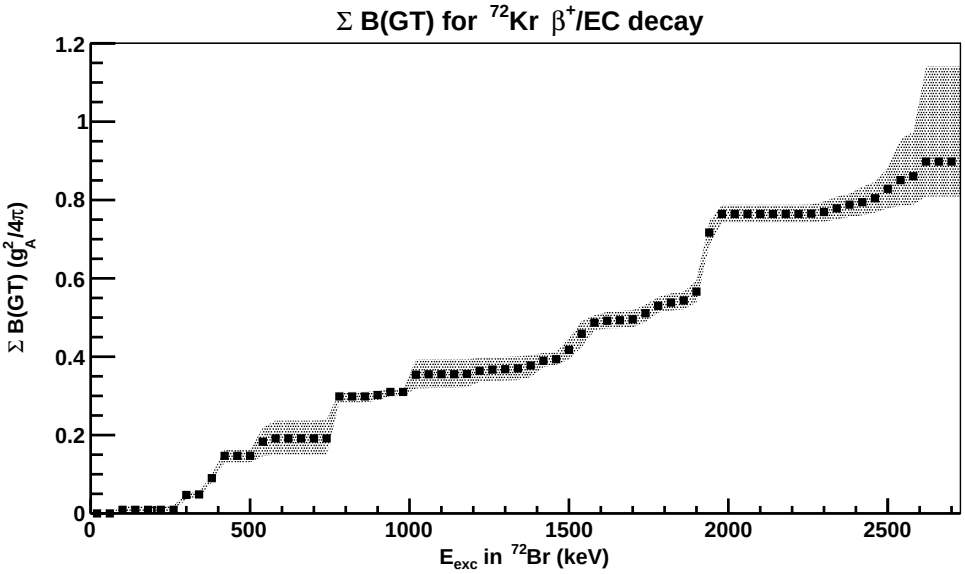

Figure D.6: *Distribución de $B(GT)$ acumulada para la desintegración β^+/CE de ^{72}Kr obtenida del presente analisis de la componente β^+ a través de Espectrospía de Absorción Total (TAS). La región de incertidumbre mostrada es estimada a partir de origen estadístico y sistemático como se describe en el texto.*

La distribución de B(GT) acumulado resultante ha sido comparada con el resultado obtenido empleando diferentes conjuntos de información para el esquema de niveles de ^{72}Br: por un lado, se ha comparado con los resultados empleando la información que aparece en [Piq03] hasta una energía de excitación de 2 MeV en lugar de sólo 1 MeV como se hizo en el análisis realizado previamente, y con un esquema de niveles modificando aleatoriamente el espin y paridad de los niveles y las razones de ramificación de cada nivel. También se ha comparado el resultado con el que se obtiene de modificar los parámetros de los modelos estadísticos para la densidad de niveles y empleando el esquema de niveles teórico obtenido de los cálculos de P. Sarriguren para el caso oblado hasta 1 MeV y 2 MeV de excitación para la parte conocida del esquema de niveles. Todas estas comparaciones indican la fiabilidad de la distribución de B(GT) acumulado obtenido de nuestro análisis.

La reproducción de las intensidades de desexcitación gamma de las transiciones más intensas ha sido realizado imponiendo algunas condiciones en el análisis que provocan una peor reproducción del espectro experimental del espectro del detector TAS. El resultado de este análisis paralelo, que se ha etiquetado como "restricted" por imponer restricciones en la alimentación beta a ciertos niveles, el cual reproduce razonablemente bien las intensidades de las transiciones gamma, es muy parecido al resultado obtenido por el análisis que se considera como "bueno", que es el obtenido sin imponer ninguna restricción, se etiqueta como "free" y que mejor reproduce el espectro del detector TAS, como se puede observar en la figura D.7. El valor para el $B(GT)$ acumulado hasta una energía de excitación de 2640 keV ha sido encontrado ser de:

$$\sum B(GT)_{free} = 0.90^{+0.24}_{-0.09}(g_A^2/4\pi) \tag{D.6}$$

$$\sum B(GT)_{restricted} = 0.99^{+0.28}_{-0.12}(g_A^2/4\pi) \tag{D.7}$$

y, como se puede observar, el resultado es bastante similar en ambos casos.

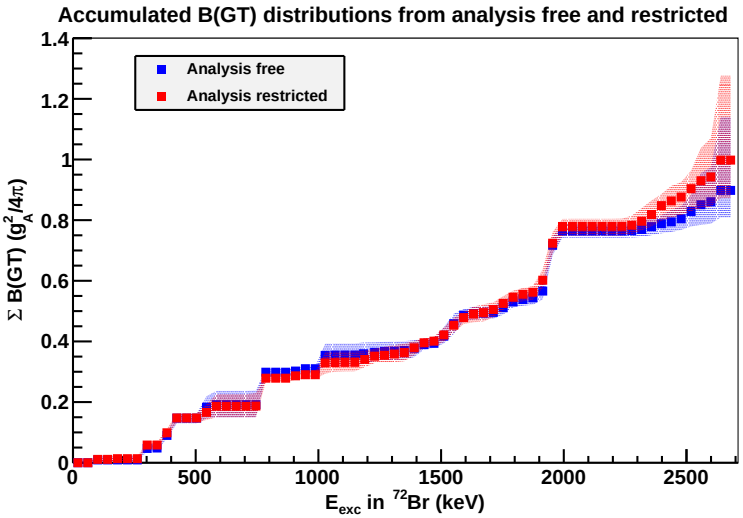

Figure D.7: *Comparación de las distribuciones de $B(GT)$ acumuladas obtenidas del análisis sin restricciones sobre las alimentaciones beta (azul) y con algunas restricciones impuestas (rojo). La tendencia de ambas distribuciones es parecida y el valor del $B(GT)$ acumulado hasta 2640 keV es similar para ambos análisis: $B(GT)_{free} = 0.90^{+0.24}_{-0.09}(g_A^2/4\pi)$ y $\sum B(GT)_{restricted} = 0.99^{+0.28}_{-0.12}(g_A^2/4\pi)$*

Mantenemos el análisis sin restricciones como el definitivo porque, a pesar de reproducir peor las intensidades gamma de las transiciones más intensas, reproduce mejor el espectro experimental del detector TAS, que constituye nuestro conjunto de datos experimentales. Puesto que estas dos distribuciones no difieren demasiado, suministrando resultados muy parecidos, la fiabilidad del resultado se ve incrementada.

D.5 Resultados

Los resultados principales del presente estudio puede ser resumidos como sigue.

D.5.1 Experimento de espectroscopía de electrones de conversión

El análisis de los datos correspondientes al experimento IS370-A proporcionó los valores de los coeficientes de conversión que se muestran en las figuras D.8, D.9 and D.10.

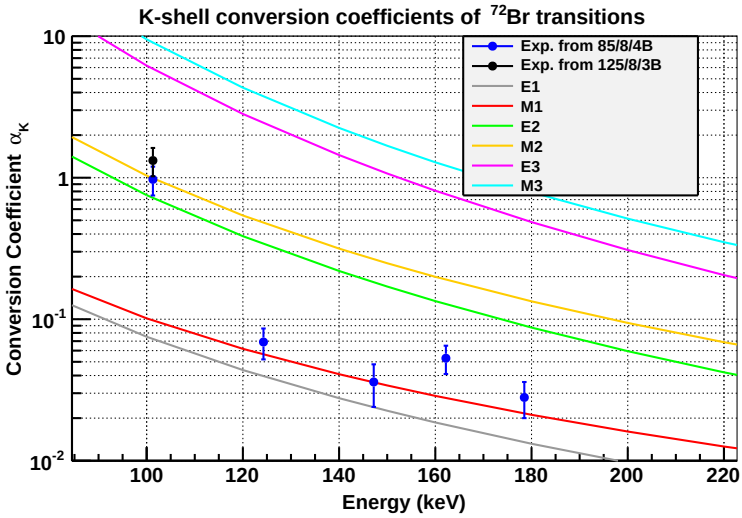

Figure D.8: *Coeficientes de conversión experimentales para transiciones de electrones de capa K obtenidas con las configuraciones 85/8/4B y 125/8/3B del espectrómetro de electrones. La comparación se hace con las predicciones teóricas tomadas de Ref. [ANU] para las diferentes multipolaridades.*

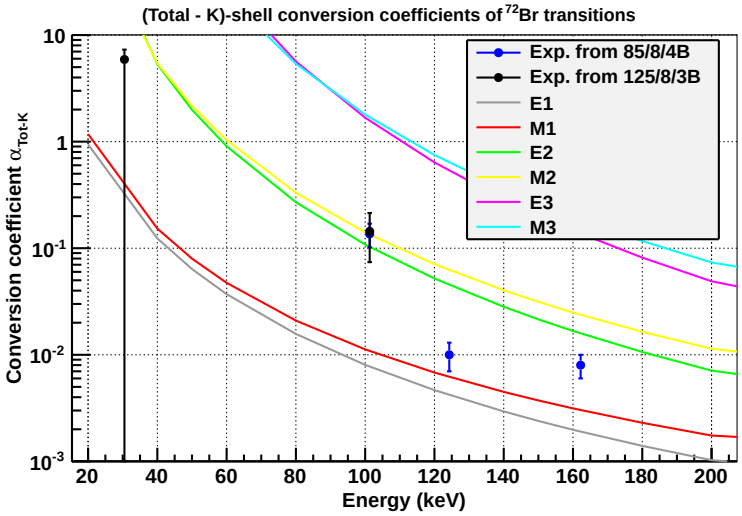

Figure D.9: *Coeficientes de conversión experimentales para transiciones de electrones de capas (Total-K) obtenidos con la configuración 85/8/4B del espectrómetro miniorange. La comparación se hace con las predicciones teóricas tomadas de Ref. [ANU] para las diferentes multipolaridades.*

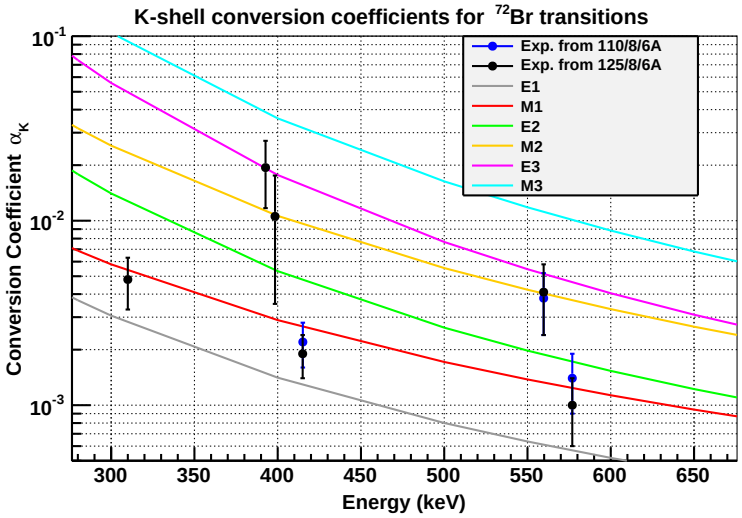

Figure D.10: *Coeficientes de conversión experimentales para transiciones de electrones de capa K obtenidos con las configuraciones 110/8/6A y 125/8/6A del espectrómetro de electrones. La comparación se hace con las predicciones teóricas tomadas de Ref. [ANU] para las diferentes multipolaridades.*

Los resultados obtenidos a través de este experimento pueden resumirse en los siguientes puntos:

- 14 coeficientes de conversión desconocidos previamente han sido determinados experimentalmente para transiciones de baja energía en ^{72}Br 101.3K, 101.3(Tot-K), 124.4K, 124.4(Tot-K), la doble transición 147.2K, 162.7K, 162.7(Tot-K), 178.5K, 309.9K, 392.7K, 398.4K, la doble transición (414.5+415.1)K, 559.7K y 576.9K. Además, un límite superior para el valor de los coefficientes de conversión de las transiciones 30.5Tot-K and 38.8K ha sido establecido.

- **El espín y paridad del estado fundamental de ^{72}Br** queda restringido a 3 posibles valores **(0,1,2)**$^{+}$. Trabajos anteriores apoyaron dos posibilidades 1^{+} y 3^{+}. Los trabajos de Piqueras *et al.* [Piq03] y Schmeing *et al.* [Sch73] asignaron 1^{+} en base a una alimentación beta directa al estado fundamental de ^{72}Br de 34 % and 53.6 % a partir de la desintegración beta de ^{72}Kr, respectivamente. Por otro lado, el estudio de Collins *et al.* [Col74] donde asignaron 3^{+} basados en alimentación directa a estados 2^{+} and 4^{+} en ^{72}Se a través de la desintegración beta del estado fundamental de ^{72}Br. La alimentación que ellos estiman es de 23.2 % y 20 % a los estados 2^{+} a 862 y 1316.7 keV respectivamente, y un 5 % al estado 4^{+} que está a 1636.8 keV de energía de excitación. Nuestro trabajo descarta esta posibilidad de 3^{+} y mantiene la posibilidad de ser 1^{+} a la vez que añade otros dos posibles valores, 0^{+} y 2^{+}.

- La multipolaridad de 9 transiciones en ^{72}Br han sido establecidas: la transición 30.5-keV ser una E1, la 101.3-keV ser una M2, la 124.4-keV como una M1(E2), la transición 147.2-keV que une los niveles a 310.0 keV y 162.8 keV siendo una M1, la transición 162.7-keV es una M1+E2, la 178.5-keV es M1(E2), la 576.9-keV es M1(E2) y la transición doble (414.5+415.1)-keV donde ambas transiciones por separado se ha encontrado que son M1.

- La multipolaridad de 6 transiciones no han sido firmemente establecidas: la de 38.8-keV pudiendo ser M1+E2, pura M1 o incluso pura E2, la transición 147.2-keV uniendo

los niveles 545.7-keV y 398.5-keV que puede ser M1/M1+E2/E1, la transición 309.9-keV pudiendo ser M1/M1(E2), la 392.7-keV puede ser E3 ó E3(M2), la 398.4-keV pudiendo ser M2 ó M2(E3) y la 559.7-keV que pudiese ser M2/M2(E3).

- Los coeficientes de conversión de las transiciones 454.7-keV en ^{72}Se y 112-keV en ^{76}Br han sido medidos y sus multipolaridades deducidas como E2 ó E2(M1) para la primera y M1+E2 para la segunda.

- La intensidad de dos transiciones E0, la 937-keV en ^{72}Se y la 691-keV en ^{72}Ge han sido medidas y comparadas con la de la transición E2 más intensa de ambos esquemas de desexcitación.

D.5.2 Experimento de Espectroscopía de Absorción Total

La medida de Espectroscopía de Absorción Total ha proporcionado los siguientes resultados:

- La distribución de alimentación β^+ en la desintegración de ^{72}Kr ha sido determinada y la distribución de alimentación total (β^+/CE) ha sido deducida a partir de la anterior hasta una energía de excitación de 2640 keV.

- La distribución de B(GT) acumulado de la desintegración β^+/CE de ^{72}Kr ha sido determinada hasta una energía de excitación de 2640 keV. La incertidumbre experimental de la distribución incluye las componentes sistemática y estadística que han sido estimadas en el análisis.

- La comparación de la distribución de B(GT) acumulada con las predicciones teóricas procedentes de [Sar09] sugiere una deformación predominantemente oblada para el estado fundamental de ^{72}Kr.

- La cantidad total de B(GT) encontrado hasta una energia de excitación de 2640 keV es: $\sum B(GT)_{free} = 0.90^{+0.24}_{-0.09}$ en unidades de $(g_A^2/4\pi)$ siguiendo la convención dada por [BM98].

D.6 Conclusiones

La comparación de la distribución de B(GT) encontrada experimentalmente con las predicciones teóricas que se hacen en [Sar09] para el caso de deformación oblada (azul), prolada (rojo) y dominantemente oblada con 10% de mezcla con prolada (verde) para el estado fundamental de ^{72}Kr se muestra en la figura D.11. La razón de mezcla del 10% con el estado 0^+ a 671(2) keV que es considerado como prolado fue sugerida en [Bou03]. La consideración de esta razón de mezcla en las predicciones teóricas es una aproximación y no es estrictamente correcta ya que lo que se ha hecho es calcular la cantidad de B(GT) acumulado en cada división como la mezcla del 90% del valor predicho para el caso oblado y 10% del valor correspondiente para el caso prolado y no se ha hecho ninguna modificación en el formalismo del cálculo teórico. A pesar de no ser estrictamente correcto esta estimación sirve para guiar el ojo y tener una idea de si la distribución experimental sería compatible con una razón de mezcla de esta cantidad aproximada.

El resultado se ajusta bastante bien a las predicciones para el caso oblado (azul) y también para el caso de estado mezcla 90% oblado y 10% prolado (verde) La predicción para oblado corresponde a un valor del parámetro de deformación cuadrupolar de β_2=-0.1759 cuya forma aproximada se muestra en la figura D.12.

nucleus.

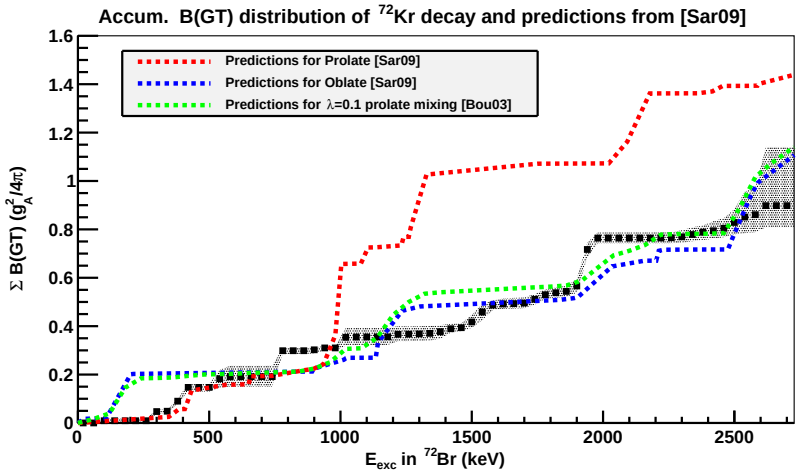

Figure D.11: *Comparación de la distribución experimental de B(GT) acumulado para la desintegración β^+/CE de ^{72}Kr con las predicciones teóricas que aparecen en [Sar09] procedentes del uso de la fuerza SLy4 tipo Skyrme, para el caso oblado (azul), prolado (rojo) y mezcla dominantemente oblado (verde) como deformaciones del estado fundamental del núcleo padre. El caso de mezcla está obtenido utilizando el valor de la razón de mezcla λ=0.1 que se sugirió en [Bou03] con el estado 0^+ a 671(2) keV. El resultado experimental se ajusta bastante bien tanto a la predicción para el caso oblado como para el caso mezcla sugiriendo que la deformación del estado fundamental de ^{72}Kr es dominantemente oblada.*

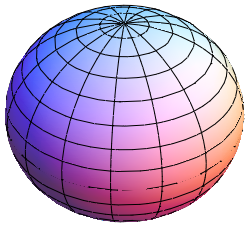

Figure D.12: *Forma del núcleo ^{72}Kr en su estado fundamental obtenida con un parámetro de deformación cuadrupolar β_2=-0.1759 como sugiere P. Sarriguren en [Sar09]. Este estado se corresponde con la deformación oblada cuya distribución de B(GT) teórica se representa en la figura D.11 en azul y que reproduce bastante bien la distribución hallada experimentalmente.*

El esquema de niveles de ^{72}Br ha sido enriquecido con valores de los coeficientes de conversión de las transiciones estudiadas y con las multipolaridades y los espines de los estados deducidos a partir de ellos.

No obstante, el espín y paridad del estado fundamental de ^{72}Br, el cuál había sido previamente discutido [Sch73, Piq03, Col74], no ha podido ser firmemente establecido pero sí se ha restringido sus valores posibles descartando el valor 3^+ que había sido propuesto anteriormente en [Col74].

Bibliography

[Is] Isotope mass Separator On-Line facility (ISOLDE) at CERN, , website: http://isolde.web.cern.ch/ISOLDE.

[Abr10] D. Abriola, Nuclear Data Sheets **111** (2010), 1.

[ANU] ANU - NNDC - Petersburg - ORNL collaboration for the International Network of Nuclear Structure and Decay Data (NSDD) Evaluators, http://physics.anu.edu.au/nuclear/bricc.

[Art96] A. Artna-Cohen, Nuclear Data Sheets **79** (1996), 1.

[Aud12] G. Audi et al., Chinese Physics C **36** (2012), 1157.

[Bas06] M.S. Basunia, Nuclear Data Sheets **107** (2006), 3323.

[Bea95] J. Bea, Estudio de la estructura del núcleo ^{75}Br producido por la desintegración β^+ del ^{75}Kr, Ph.D. thesis, University of Valencia, 1995.

[Bec99] F. Becker et al., Eur. Phys. J. A **4** (1999), 103.

[Bei75] M. Beiner, Nucl. Phys. A **238** (1975), 29.

[Bel] T. Belgya et al., "Handbook for calculations of nuclear reaction data", http://www-nds.iaea.org/ripl2/.

[Ber69] M.J. Berger et al., Nucl. Inst. and Methods **69** (1969), 181.

[Ber82] G.F. Bertsch, Phys. Rev. C **26** (1982), 1323.

[Bet53] H.A. Bethe et al., "passage of radiations through matter" in experimental nuclear physics, vol. 1, John Wiley & Sons, New York, 1953.

[Bla06] K. Blaum, Physics Reports **425** (2006), 1.

[BM98] A. Bohr and B.R. Mottelson, Nuclear structure, World Scientific Publishing Co. Pte. Ltd., 1998.

[Bon85] P. Bonche et al., Nucl. Phys. A **443** (1985), 39.

[Bou03] E. Bouchez et al., Phys. Rev. Lett. **90** (2003), 082502.

[Buc90] S.G. Buccino et al., Phys. Rev. C **41** (1990), 2056.

[Cam68] D.C. Camp et al., Nucl. Phys. A **121** (1968), 561.

[Can99a] D. Cano-Ott et al., Nucl. Inst. and Methods A **430** (1999), 333.

[Can99b] D. Cano-Ott et al., Nucl. Inst. and Methods A **430** (1999), 488.

[Cas00] R. Casten, Nuclear structure from a simple perspective, Second edition, Oxford Science Publications, 2000.

[Cha98] E. Chabanat, Nucl. Phys. A **635** (1998), 231.

[Cle07] E. Clement et al., Phys. Rev. C **75** (2007), 054313.

[Cle11] E. Clement et al., International Journal of Modern Physics E **20** (2011), 415.

[Cob72] A. Coban et al., Nucl. Phys. A **182** (1972), 385.

[Col74] W.E. Collins et al., Phys. Rev. C **9** (1974), 1457.

[D'A95] G. D'Agostini, Nucl. Inst. and Methods A **362** (1995), 487.

[Dam82] A. Damkjaer et al., Nucl. Inst. and Methods **200** (1982), 377.

[Dav73] C.N. Davids et al., Phys. Rev. C **8** (1973), 1029.

[de 97] G. de Angelis et al., Phys. Lett. B **415** (1997), 217.

[Dem77] A.P. Dempster et al., J. R. Statist. Soc. B **39** (1977), 1.

[Dem01] P. Demetriou et al., Nucl. Phys. A **695** (2001), 95.

[Dic72] F. Dickmann et al., Phys. Lett. **38B** (1972), 207.

[Dil73] W. Dilg et al., Nucl. Phys. A **217** (1973), 269.

[Dor70] T.A. Doron and M. Blann, Nucl. Phys. A **161** (1970), 12.

[Dö82] J. Döring et al., Z. Phys A **305** (1982), 365.

[Far99] A.R. Farhan et al., Nuclear Data Sheets **86** (1999), 785.

[Fir96] Richard B. Firestone, Table of isotopes 8^{th} edition, Wiley Interscience, 1996.

[Flo73] H. Flocard et al., Phys. Lett. B **46** (1973), 304.

[Gad05] A. Gade et al., Phys. Rev. Lett. **95** (2005), 022502.

[Gad06] A. Gade et al., Phys. Rev. Lett. **96** (2006), 189901.

[Gaf13] L. Gaffney et al., Nature **497** (2013), 199.

[Gal58] C.J. Gallagher and S.A. Moszkowski, Phys. Rev. **111** (1958), 1282.

[Gal74] W.J. Gallagher et al., Nucl. Inst. and Methods **122** (1974), 405.

[Gar82] G. García Bermúdez et al., Phys. Rev. C **25** (1982), 1396.

[GEA] GEANT4-CERN international collaboration, http://geant4.cern.ch/.

[Gor01] S. Goriely et al., Atomic Data and Nuclear Data Tables **77** (2001), 311.

[Gov71] N.B. Gove and M.J. Martin, Nuclear Data Tables **10** (1971), 205.

[Gri92] A.G. Griffiths et al., Phys. Rev. C **46** (1992), 2228.

[Ham74] J.H. Hamilton et al., Phys. Rev. Lett. **32** (1974), 239.

[Ham95] I. Hamamoto, X.Z. Zhang, Z. Phys A **353** (1995), 145.

[Har77] J.C. Hardy et al., Phys. Lett. B **71** (1977), 307.

[Har09] J.C. Hardy, I.S. Towner, Phys. Rev. C **79** (2009), 055502.

[Her11] F. Herfurth et al., Eur. Phys. J. A **47** (2011), 75.

[Hey11] K. Heyde and J.L. Wood, Reviews of Modern Physics **83** (2011), 1467.

[Jä87] B. Jäckel et al., Nucl. Inst. and Methods A **261** (1987), 547.

[kfa] J. Kopecky et al., "Extensive systematics of global strength function data" kopecky.readme file at, http://www-nds.iaea.org/ripl/gamma.

[Kis98] Z. Kis et al., Nucl. Inst. and Methods A **418** (1998), 374.

[Kop90] J. Kopecky et al., Phys. Rev. C **41** (1990), 1941.

[Kor01] W. Korten et al., Acta Physica Polonica B **32** (2001), 729.

[Kra87] K.S. Krane, Introductory nuclear physics, John Wiley & Sons, Inc., 1987.

[Lan84] K. Lange and R. Carson, J. Comput. Assit. Tomogr. **8** (1984), 306.

[Lie70] R.M. Lieder and J.E. Draper, Phys. Rev. C **2** (1970), 531.

[LK77] K. P. Lieb and J. J. Kolata, Phys. Rev. C **15** (1977), 939.

[Mar93] M.J. Martin, Nuclear Data Sheets **70** (1993), 315.

[Mat09] C.M. Mattoon et al., Phys. Rev. C **80** (2009), 034318.

[Mö95] P. Möller et al., Atomic Data and Nuclear Data Tables **59** (1995), 185.

[Mö09] P. Möller et al., Phys. Rev. Lett. **103** (2009), 212501.

[Naz85] W. Nazarewicz et al., Nucl. Phys. A **435** (1985), 397.

[Nil55] S.G. Nilsson et al., Dan. Mat-Fys. Medd. **29** (1955), 16.

[Nol70] E. Nolte et al., Phys. Lett. **33B** (1970), 4.

[Ná04a] E. Nácher, Beta decay studies in the n≈z and the rare-earth regions using the total absorption spectroscopy techniques, Ph.D. thesis, University of Valencia, 2004.

[Ná04b] E. Nácher et al., Phys. Rev. Lett. **92** (2004), 232501.

[Par73] T. Paradellis et al., Nucl. Phys. A **201** (1973), 113.

[Pet96] A. Petrovici et al., Nucl. Phys. A **605** (1996), 290.

[Pet00] A. Petrovici et al., Nucl. Phys. A **665** (2000), 333.

[Pet09] A. Petrovici et al., Phys. Rev. C **80** (2009), 044319.

[Pet11] A. Petrovici et al., Progress in Particle and Nuclear Physics **66** (2011), 287.

[Piq03] I. Piqueras et al., Eur. Phys. J. A **16** (2003), 313.

[Poi04] E. Poirier et al., Phys. Rev. C **69** (2004), 034307.

[Pre69] J.R. Prescott and G.H. Narayan, Nucl. Inst. and Methods **75** (1969), 51.

[Pé11] A.B. Pérez-Cerdan et al., Phys. Rev. C **84** (2011), 054311.

[Pé13] A.B. Pérez-Cerdan et al., Phys. Rev. C **88** (2013), 014324.

[Que78] P. Quentin et al., Annu. Rev. Nucl. Part. Sci. **28** (1978), 253.

[Rab95] S. Rab, Nuclear Data Sheets **75** (1995), 491.

[Rei77] J. Reisberg et al., Nucl. Phys. A **280** (1977), 13.

[Res71] A.C. Rester et al., Nucl. Phys. A **162** (1971), 481.

[Rod04] D. Rodríguez et al., Phys. Rev. Lett. **93** (2004), 16.

[Roe74] E. Roeckl et al., Z. Phys. **266** (1974), 123.

[Rud97] D. Rudolph et al., Phys. Rev. C **56** (1997), 98.

[Sar99] P. Sarriguren et al., Nucl. Phys. A **668** (1999), 13.

[Sar01] P. Sarriguren et al., Nucl. Phys. A **691** (2001), 631.

[Sar09] P. Sarriguren, Phys. Rev. C **79** (2009), 044315.

[SBNS] IS478 experiment at ISOLDE facility (CERN) Spokeperson: B.S. Nara Singh, http://cds.cern.ch/record/1027564/files/intc-2007-016.pdf.

[Sch73] H. Schmeing et al., Phys. Lett. **44B** (1973), 449.

[Sch06] H. Schatz, International Journal of Mass Spectrometry **251** (2006), 293.

[She82] L.A. Shepp and Y. Vardi, IEEE Trans. Med. Imaging **1** (1982), 113.

[Sin95] B. Singh, Nuclear Data Sheets **74** (1995), 63.

[Sin98] B. et al. Singh, Nuclear Data Sheets **84** (1998), 487.

[Sin06] B. Singh et al., Nuclear Data Sheets **107** (2006), 1923.

[Tai07a] J.L. Tain and D. Cano-Ott, Nucl. Inst. and Methods A **571** (2007), 728.

[Tai07b] J.L. Tain, D. Cano-Ott, Nucl. Inst. and Methods A **571** (2007), 719.

[Twi83] P.J. Twin, Nucl. Phys. A **409** (1983), 343c.

[Van72] J. Van Klinken et al., Nucl. Inst. and Methods **98** (1972), 1.

[Van75] J. Van Klinken et al., Nucl. Inst. and Methods **130** (1975), 427.

[Var87] B.J. Varley et al., Phys. Lett. B **194** (1987), 463.

[Vau72] D. Vautherin et al., Phys. Rev. C **5** (1972), 626.

[Vau73] D. Vautherin, Phys. Rev. C **7** (1973), 296.

[Vis07] C. Visñovezky et al., Spectrochimica Acta Part B **62** (2007), 492.

[Wan12a] M. Wang et al., Chinese Physics C **36** (2012), 1287.

[Wan12b] M. Wang et al., Chinese Physics C **36** (2012), 1603.

[Wei51] V.F. Weisskopf et al., Phys. Rev. **83** (1951), 1073.

[Win90] D.F. Winchell et al., Phys. Rev. C **41** (1990), 1264.

[Yao06] W.M. Yao et al., J. Phys. G **33** (2006), 1.